**Charles University**

**First Faculty of Medicine**

Study programme: Molecular and Cellular Biology, Genetics and Virology


**Mgr. Kateřina Radilová**

# Structural characterization of influenza A polymerase PA subunit domains in complex with novel inhibitors

# Strukturní charakterizace komplexů domén PA podjednotky chřipkové polymerasy s novými inhibitory

**Doctoral dissertation**

Supervisor: RNDr. Milan Kožíšek, Ph.D.

Institute of Organic Chemistry and Biochemistry of the Czech Academy of Sciences

Prague, 2022

Foremost I want to thank my supervisor Milan Kožíšek, for his patient guidance, valuable advice and positive approach, which I have appreciated for several years. Milan's precise, well-planned work greatly impacted me, who was a bit chaotic in the beginning. During my studies, Milan helped me with all the experimental techniques and more importantly, he successfully created a friendly environment.

I would like to thank Jan Konvalinka for a hearty welcome to his group. He encouraged me by saying that science is full of negative results. Even though I was warned, I did not let him repel me. After four years at IOCB, I don't think I could have chosen better. His valuable advice will stay with me for a long time. I hope this is just the end of a chapter, but we will keep in touch.

I am grateful to all past and current colleagues, as well as our collaborators, who contributed to the publications. Many thanks belong to the members who joined our group lately. Namely Michal Král' and Tomáš Kotačka. Michal was fresh air to the team with almost as fast ideas as his English, and Tomáš, who came a few months ago and kindly took over some of my projects. I would also like to thank Joshua Smith, who helped me many times lastly with English corrections, even though he was sick and I did not give him much time.

Thanks to the pandemic of coronavirus disease 2019, I have unintentionally spent over two years with the group of Dr. Maloy Řezáčová. Pavlína's enthusiasm for structural biology has been a great inspiration. I would like to thank all from her group for creating such a nice and friendly atmosphere, even for a "squatting" student. Thanks to Milan Fábry for his advice and quotes, which always enlightened the day and Stefan Djukic for updating me about Serbian culture and political situations. I wish to thank Petr Pachl for being grounded in New Zeland, which enabled me to occupy a spot next to Jiří Brynda for a while, who taught me almost everything about protein crystallography, and whose baking, skiing, cycling, and many other skills will not be forgotten.

Thanks to my friends, not only for keeping my thoughts away from science.

Ráda bych poděkovala Davidovi za jeho podporu posledních pár snadných, i méně snadných let. V neposlední řadě bych chtěla poděkovat své rodině, bez jejichž podpory by tato ani žádná předchozí práce nemohla vzniknout. Díky všem, kteří mi dodávají sílu a inspiraci.

Prohlašuji, že jsem závěrečnou práci zpracovala samostatně a že jsem uvedla všechny použité informační zdroje a literaturu. Tato práce ani její podstatná část nebyla předložena k získání jiného nebo stejného akademického titulu.

V Praze, 24. 11. 2022

_____

IDENTIFIKAČNÍ ZÁZNAM

RADILOVÁ, Kateřina. *Strukturní charakterizace komplexů domén PA podjednotky chřipkové polymerasy s novými inhibitory. [Structural characterization of influenza A polymerase PA subunit domains in complex with novel inhibitors]*. Praha, 2022. 138, 4 příl. Disertační práce (Ph.D.). Univerzita Karlova, 1. lékařská fakulta; Proteázy lidských patogenů, Ústav organické chemie a biochemie AV ČR, v.v.i., vedoucí práce Kožíšek, Milan.

KLÍČOVÁ SLOVA

RNA polymerasa, virus chřipky, protein-proteinová interakce, endonukleasova aktivita, inhibitor, PA podjednotka

KEY WORDS

RNA polymerase, Influenza A virus, protein-protein interaction, endonuclease activity, inhibitor, PA subunit

CONTENTS

ABSTRAKT .....1
ABSTRACT .....2
LIST OF ABBREVATIONS .....3
1. INTRODUCTION .....4
1.1. THE INFLUENZA .....4
1.2. INFLUENZA PANDEMICS .....5
1.3. IAV STRUCTURE .....6
1.4. IAV LIFE CYCLE .....9
1.5. IAV RNA-DEPENDENT RNA POLYMERASE .....12
1.5.1. PB1 SUBUNIT .....14
1.5.2. PB2 SUBUNIT .....14
1.5.3. PA SUBUNIT .....16
1.5.3.1. N-TERMINAL DOMAIN of PA .....17
1.5.3.2. C-TERMINAL DOMAIN of PA .....20
1.6 REPLICATION .....22
1.7 CAP-DEPENDENT vRNA TRANSCRIPTION .....23
1.8 CURRENT ANTI-INFLUENZA TREATMENT .....26
2. RESEARCH AIMS .....29
3. RESULTS .....30
3.1. PUBLICATIONS INCLUDED .....30
3.2. PUBLICATIONS NOT INCLUDED .....31
3.3. PUBLICATION I. .....32
3.3.1. summary .....32
Structural characterization of the interaction between the C-terminal domain of the influenza polymerase PA subunit and an optimized small peptide inhibitor .....35
3.4. PUBLICATION II. .....42
3.4.1. summary .....42
Thermodynamic and structural characterization of an optimized peptide-based inhibitor of the influenza polymerase PA-PB1 subunit interaction .....45
3.5. PUBLICATION III. .....54

3.5.1. summary.....54
Unravelling the anti-influenza effect of flavonoids: experimental validation of luteolin and its congeners as potent influenza endonuclease inhibitors .....56
3.6. PUBLICATION IV. .....79
3.6.1. summary .....79
Synthesis and *in vitro* evaluation of C-7 and C-8 luteolin derivatives as influenza endonuclease inhibitors .....82
4. CONCLUSION AND DISCUSSION .....110
5. SUMMARY .....116
6. SOUHRN .....118
7. REFERENCES .....120
8. SUPPLEMENTARY MATERIAL .....131
8.1. PA SUBUNITS ALIGNMENT.....131
8.2. PB1 SUBUNITS ALIGNMENT .....133
8.3. PB2 SUBUNITS ALIGNMENT.....136

ABSTRAKT

RNA-dependentní RNA polymerasa viru chřipky je heterotrimerický komplex, který má zásadní roli v životním cyklu viru. Je zodpovědná za virovou replikaci a transkripci. Jedna z jejích podjednotek, PA podjednotka, interaguje s PB1 podjednotkou prostřednictvím důležité protein-proteinové interakce na své C-koncové doméně. Tato interakce, která je zprostředkovaná $3_{10}$ helixem, je nutná k utvoření celého heterotrimerického komplexu. N-koncová doména navíc obsahuje místo s endonukleasovou aktivitou se dvěma manganatými ionty. Obě tyto domény jsou považovány za slibné terapeutické cíle. V současnosti jsou přístupy v léčbě a prevenci chřipkového onemocnění limitované na sezónní očkování a existuje pouze několik léků, které ve velké většině cílí na jiné proteiny viru chřipky. U řady z nich však dochází k rychlému vývoji rezistentních mutací, nebo mají závažné vedlejší účinky.

Tato práce nabízí strukturní náhledy na dvě domény PA podjednotky. První část se věnuje charakterizaci a optimalizaci minimálního peptidu odvozeného z PB1 podjednotky, který interaguje s C-koncovou doménou PA podjednotky a brání jejich dimerisaci. Výsledky z této části mohou být považovány za počáteční bod pro racionální vývoj prvních inhibitorů PA-PB1 protein-proteinové interakce proti viru chřipky. V druhé polovině jsme zkoumali rostlinné chemické látky flavonoidy a sloučeniny z nich odvozené jako možné inhibitory endonukleasové domény. Pomocí rentgenové krystalografie jsme popsali vazebné módy těchto látek v aktivním místě PA podjednotky a identifikovali tak cílový protein těchto látek, které jsou hojně používané při chřipkovém onemocnění.

ABSTRACT

Influenza RNA-dependent RNA polymerase is a heterotrimeric complex and has an essential role in the life cycle of the virus. It is responsible for viral replication and transcription. One of its subunits, the polymerase acidic protein, interacts with the PB1 subunit via a crucial protein-protein interaction at its C-terminal domain. This $3_{10}$ helix-mediated intersubunit interaction is required for the whole heterotrimer assembly. The N-terminal domain carries the endonuclease active site with two manganese ions. Both domains are considered promising drug targets. Current strategies to fight the influenza virus are limited to seasonal vaccines, and there are only a few anti-influenza drugs targeting mostly other viral proteins. Many used antivirals are susceptible to rapid resistance mutations development or cause severe side effects.

This thesis provides structural insights into the two domains of the PA subunit. The first part is devoted to the characterization and optimization of a PB1-derived minimal peptide interacting with the C-terminal domain. Results from this part may be considered as a starting point for the rational design of first-in-class anti-influenza inhibitors of the PA-PB1 protein-protein interaction. In the other half, we have explored the inhibitory potency of flavonoids and their derivatives against the endonuclease domain. Using X-ray protein crystallography, we have described the binding modes of those inhibitors in the PA endonuclease active site. Ultimately, we have identified the target protein of those compounds which are being broadly used as supplements during influenza viral infection.

## LIST OF ABBREVATIONS

| | |
|---|---|
| ANP32A | acidic leucine-rich nuclear phosphoprotein 32 A |
| BAM | baloxavir marboxil |
| BXA | baloxavir acid |
| CBD | cap-binding domain |
| CDC | US Centers for Disease Control and Prevention |
| CPA | PA subunit C-terminal domain |
| CRM1 | chromosomal region maintenance 1/exportin-1 |
| cRNA | complementary RNA |
| FDA | US Food and Drug Administration |
| GA | Golgi apparatus |
| HA | hemagglutinin |
| IAV | Influenza A virus |
| IBV | Influenza B virus |
| ICV | Influenza C virus |
| LCAR | acidic (leucine-rich) region |
| mRNA | messenger RNA |
| MTOC | microtubule organizing center |
| NA | neuraminidase |
| NAI | neuraminidase inhibitors |
| NEP/NS2 | nuclear export protein/non-structural protein 2 |
| NES | nuclear export signal |
| NLS | nuclear localization signal |
| NP | nucleoprotein |
| NPA | PA subunit N-terminal domain |
| NPC | nuclear pore complex |
| NS1 | non-structural protein 1 |
| NTP | nucleoside triphosphate |
| PA | polymerase acidic protein |
| PB1 | polymerase basic protein 1 |
| PB2 | polymerase basic protein 2 |
| Pol II | DNA-dependent RNA polymerase II |
| PPI | protein-protein interaction |
| RanGAP | Ran GTPase-activating protein |
| RdRp | RNA-dependent RNA polymerase |
| RIG-I | retinoic acid-inducible gene I |
| RNA | ribonucleic acid |
| RNP | ribonucleoprotein |
| SRP | signal recognition particle |
| UMP | uridine monophosphate |
| vRNA | viral RNA |
| WHO | World Health Organisation |

# 1. INTRODUCTION

## 1. 1. THE INFLUENZA

The influenza virus can cause an acute infection of the upper respiratory system among humans and animals all around the world. There are four circulating species: the influenza A virus (IAV), which has a pandemic potential; the influenza B virus (IBV), responsible together with IAV for seasonal epidemics; the influenza C virus (ICV), generally causing mild illness; and the influenza D virus (IDV), which does not infect humans. The IAV and IBV cause local outbreaks of annually recurring epidemics. They affect up to 30% of the global population and kill 290,000 – 650,000 people each year (Iuliano et al., 2018; WHO, 2019). The ICV has a milder course of the disease. Occasionally, IAVs of animal origin undergo antigenic shift and infect humans causing a pandemic level of influenza infection. There is no doubt about the devastating consequences of pandemic outbreaks in terms of impact on mental health, mortality, and economic loss.

Influenza viruses belong to the family of *Orthomyxoviridae* with seven genera: the *Alphainfluenzavirus*, *Betainfluenzavirus*, *Deltainfluenzavirus*, *Gammainfluenzavirus*, *Isavirus*, *Quaranjavirus*, and *Thogotovirus*. Within the genera, there are influenza virus A-D, *Quaranfil quaranjavirus*, *Salmon isavirus*, *Thogoto thogotovirus*, *Dhori thogotovir*us, and *Johnston Atoll quaranjavirus*. Generally, they differ in morphological characteristics, range of hosts, and ability to cause a pandemic.

Although aquatic birds are the original reservoir of the IAVs, they can infect a diverse range of mammals. The IAV transmits rapidly from person to person, mostly in crowded areas through droplets dispersed in the air. The classification of the influenza virus is based on the host of origin, the “avian influenza” for example. Two major antigens, which are the viral surface proteins, determine further subtypes. So far, there are 18 subtypes of hemagglutinin (HA) and 11 of neuraminidase (NA) for the IAV. The antigen combination is a part of the IAV nomenclature system established by the World Health Organization (WHO) in 1979 (WHO, 1980). Altogether, the strain designation for influenza virus type A contains information on the HA and NA subtypes, host of origin (for strains of non-human sources), geographical origin, strain number, and year of isolation. For example, A/California/07/2009 (H1N1), or A/duck/Fujian/01/2002 (H5N1).

## 1.2. INFLUENZA PANDEMICS

A global outbreak of a new IAV can lead to an influenza pandemic. As IAVs constantly mutate, there is a high probability of non-human influenza viruses shifting and consequently infecting humans. The 18 different HA and 11 NA subtypes can theoretically combine and form a new subtype of influenza virus. However, not all have been found to infect all animals, or humans. There are two different ways the influenza virus can mutate. The "antigenic drift" stands for minor mutations of the influenza virus genome. It is associated with viral replication and may lead to the virus escape from the host immune system. The antigenic drift is the main reason for annual revisions and updates of flu vaccines (Kim et al., 2018). On the other hand, the "antigenic shift" results in major mutations of the influenza virus genome. A genetic reassortment is the combination of two influenza virus strains, which forms a new subtype with mixed surface antigens (R. G. Webster et al., 1982). The newly created subtype may infect humans and have a pandemic potential. This can happen when human IAV reassorts its genes with avian IAV, resulting in novel IAV containing HA and NA from either avian or human influenza virus, or both.

In the past 140 years, there have been five major outbreaks of pandemic influenza. The first one was recorded in 1889-1890 with five years of recurrences. This last pandemic in the nineteenth century, the Asiatic flu, was likely to be of influenza origin (Dowdle, 1999; Valleron et al., 2010).

In 1918, the most serious pandemic in the last century emerged, known as the Spanish flu, and continued in four waves. The first isolation of an influenza virus from human patient was performed much later (Smith et al., 1933). However, this isolation started a speculation about the possible role of a similar virus in 1918. The sequence analyses of the infected lung tissue sample indicated, that the 1918 pandemic was caused by the H1N1 influenza A subtype (Reid et al., 1999; Taubenberger et al., 2005). In two years, it infected 25% of the world's population and killed between 50 – 100 million people (Barry, 2004). Interestingly, there was a higher rate of mortality in young adults and lower mortality peak within elderly (Luk et al., 2001). This is likely accredited to a dysregulated immune response, or insufficient T cell repertoire (Gagnon et al., 2013). Nevertheless, this pandemic occurred at the end of World War II, and the worsened conditions and exhausted personal in hospitals, including the overcrowdedness and poor hygiene connected with subsequent bacterial infection, might have increased the virus spread and overall mortality (Brundage & Shanks, 2007; Hirsch & Mckinney, 1919; Morens & Taubenberger, 2011).

Almost forty years later, the Asian flu emerged in 1957 in southern China. The subtype H2N2 was most probably a recombination of avian and human influenza viruses (Kilbourne, 2006). The anti-influenza vaccine development started in 1942 (Salk et al., 1944), but was ineffective against the H2N2 influenza strain. There was an enormous effort put into the development of a novel pandemic influenza vaccine. A great step forward in dealing with influenza was in 1957 when six pharmaceutical companies licensed the vaccine against Asian flu (Influenza Vaccine, *the New York Times*, 1957).

The H2N2 strain reassorted into the H3N2 subtype, causing the Hong Kong pandemic in late 1968 (Coleman et al., 1968; Robert G. Webster et al., 1993). The vaccine was developed a year later, preventing the majority of deaths and illnesses associated with the emerging pandemic strain. The H3N2 subtype remained in the population and causes seasonal IAV disease.

The last recorded influenza pandemic occurred in April 2009 in North America (influenza A (H1N1)pdm09) and spread around the world by June 2009. It was described to have at least two swine flu ancestors (Trifonov et al., 2009). As the virus was very different from circulating H1N1 viruses, vaccination with seasonal flu vaccines did not offer sufficient cross-protection against (H1N1)pdm09 virus (Garten et al., 2009). According to the Centers for Disease Control and Prevention (CDC), 2009 influenza pandemic caused 150,000-570,000 deaths worldwide (Dawood et al., 2012). Out of that, 80 percent of (H1N1)pdm09 virus-related deaths occurred in people younger than 65 years.

## 1.3. IAV STRUCTURE

The IAV is an enveloped virus containing eight segmented negative-sense single-strand ribonucleic acids (RNAs) (**Figure 1A**). The viral ribonucleoprotein complexes (RNPs) consist of the viral RNA (vRNA), RNA-dependent RNA polymerase (RdRp), and scaffold nucleoproteins (NPs). In the vRNP, the vRNA genome is pseudo-circularized by promoter binding to the viral polymerase with the rest of the RNA forming a supercoiled helical loop coated by NPs (**Figure 1B**) (Arranz et al., 2012). Influenza NPs are believed to bind to 24–26 nucleotides RNA each (Area et al., 2004; Hutchinson et al., 2014; Martín-Benito et al., 2001), although recent studies show that the coating is not uniform and RNA stem-loops may extrude between the NPs (Le Sage et al., 2018; Lee et al., 2017).

The IAV membrane is of host origin and displays several types of viral surface proteins. Hemagglutinin is a homotrimeric glycoprotein coded by 1778 nucleotides. It attaches the viral particle to the sialic acid receptor on the host cell surface and also mediates fusion with the

endosomal membrane. Each of its three monomers is formed by the HA1 and HA2 chains, connected with two disulfide bridges (Wilson et al., 1981). The monomer has a top globular domain and a highly conserved long coiled-coil stalk. When the virus enters the low pH endosome, HA undergoes major conformational changes leading to membrane fusion (Bullough et al., 1994; Chen et al., 1999).

The other viral surface protein is neuraminidase coded by 1413 nucleotides. It releases nascent virions budding from the host cell by enzymatic cleavage of the sialic acid (Itzstein Von, 2007). It is a tetrameric glycoprotein bedded into the viral membrane via its hydrophobic region. The catalytic head has a mushroom-shaped structure of nearly spherical subunits connected to the cytoplasmic tail via the stalk and transmembrane region (Bossart-Whitaker et al., 1993; J. N. Varghese & Colman, 1991). Even though the sequences for NA are different in influenza A and B, their catalytic sites were closely similar (Air, 2012; Ellis et al., 2022). This feature made the NA one of the targets for the influenza treatment.

The last of the viral surface proteins is M2 protein which forms a transmembrane channel. The M2 channel forms a helical homotetrameric pore and mediates the $H^+$ transfer from the endosomal environment to the endocytosed viral particle. It was historically the first-thought anti-influenza drug target. The M2 crystal structure was a starting point for a rational drug design (Joseph N. Varghese et al., 1992), though more details on the inhibitor binding site were described just recently (Thomaston et al., 2018).

The virus also contains nonstructural proteins with various roles within the virus life cycle. By transcribing different reading frames of the vRNA segment for matrix proteins, the M1 protein is synthetized and is involved in the assembly of virions (Ye et al., 1987). The nonstructural protein 1 (NS1) is coded by the same sequence coding the nonstructural protein 2 (NEP/NS2), and is also transcribed from a different reading frame. The NS1 directly interacts with the Retinoic acid-inducible gene I (RIG-I) and consequently prevents induction of the host intracellular pathogen sensor, interferon-β (Guo et al., 2007; Mibayashi et al., 2007). It also prevents the export of host mRNA from the nucleus and therefore contributes to the inhibition of host immunity (K. Zhang et al., 2019). The NS2 protein is involved in the export of nascent vRNPs into the cytosol (Neumann et al., 2000). The PA-X protein, coded by vRNA sequence on the segment for PA, modulates the host response to infection (Hayashi et al., 2015; Jagger et al., 2012). The PA-X selectively degrades host DNA-dependent RNA polymerase II (Pol II) transcripts (Khaperskyy et al., 2016). The last of the viral proteins discovered so far is the PB1-F2 protein. It is a pro-apoptotic protein nonessential for the virus viability (Wise et al., 2009).

Nonetheless, its expression delays the clearance of the virus by the host immune system (Kamal et al., 2017).

Finally, the IAV viral genome codes the essential RNA-dependent RNA polymerase. This large heterotrimeric complex is composed of three subunits, the polymerase basic protein 1 (PB1), the polymerase basic protein 2 (PB2), and the PA polymerase acidic protein (PA). Their cooperation leads to the transcription and replication of the vRNA (see below).

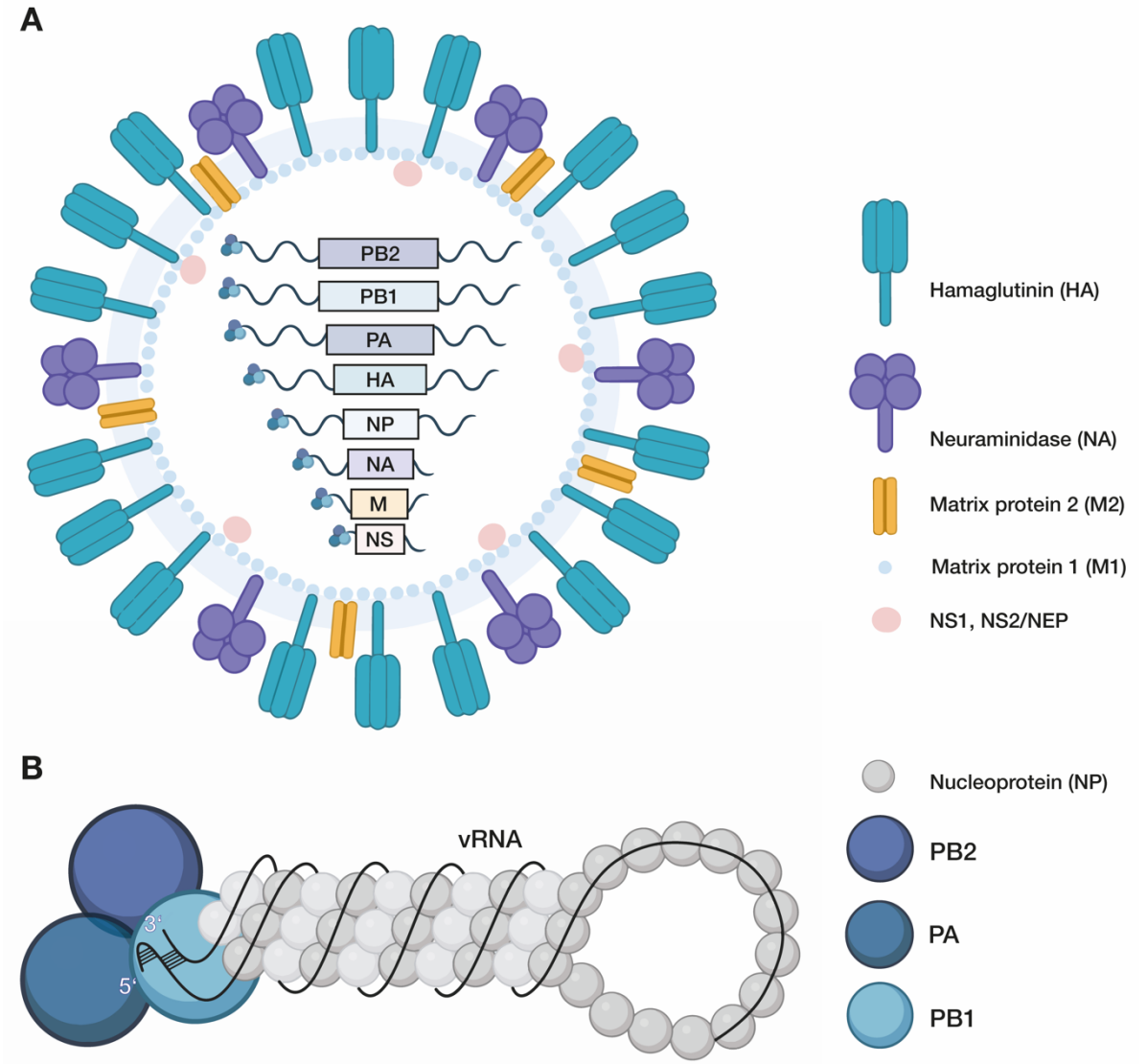


**Figure 1. Schematic illustration of the virus. A)** Particle of the influenza A virus with representations of surface proteins – Hemagglutinin (HA, cyan) and Neuraminidase (NA, violet); proton channel (M2, yellow); non-structural proteins (NS1, NS2/NEP, light pink); and eight vRNP complexes with genes for the viral proteins. **B)** Close-up view onto the viral ribonucleoprotein complex (vRNP). Heterotrimeric RdRp is bound to the viral RNA (vRNA) via PB1 subunit (light blue), PA and PB2 are shown as blue and dark blue spheres respectively; nucleoproteins (NP) are presented as gray spheres. Created with BioRender.com.

## 1.4. IAV LIFE CYCLE

The life cycle of the influenza virus begins with the binding of the surface homotrimeric hemagglutinin to the cellular sialic acid receptor (**Figure 2**). Once bound influenza enters the host cell mostly by clathrin-mediated endocytosis (Rust et al., 2004). The low pH of the endosome triggers an opening of the M2 channel and the translocation of $H^+$ ions. This consequently leads to a conformational change of HA proteins, followed by a fusion of the endosomal membrane with the viral membrane (Cady et al., 2009).

Viral RNPs are released into the cytoplasm and transferred to the nucleus (Banerjee et al., 2013). This energy-dependent mechanism is mediated by the adaptor protein importin-α, which recognizes basic nuclear localization signals (NLS) arginine- and lysine-rich motif of the RdRp PB2 subunit (Tarendeau et al., 2007). Importin-α recruits importin-β, which transports the vRNP complex through the nuclear pore complex (NPC) (Cros et al., 2005; Stewart, 2007). The complex is then dissociated by the activated form of the Ran GTPase, and the vRNP-importin-α complex is released (Eisfeld et al., 2015).

In the nucleus vRNAs are transcribed and replicated (see below), resulting in the synthesis of viral messenger RNA (mRNA), complementary RNA (cRNA), and nascent vRNA. Consequently, the viral mRNA is exported outside the nucleus for the host cell-mediated translation. Viral mRNAs coding the PA, PB1, and PB2 (subunits of RdRp), together with the NP, NS1, NS2 (nuclear export protein, NEP), and M1 coding mRNAs are translated at cytosolic ribosomes. The mRNAs for membrane glycoproteins (HA, NA) and the M2 proton channel contain hydrophobic targeting sequences, which interact with the signal recognition particle (SRP), and are sent to the endoplasmic reticulum-associated ribosomes (Bos et al., 1984; Daniels et al., 2003; Dou et al., 2018; Hull et al., 1988).

The endoplasmic reticulum-associated ribosomes translate the HA0, a precursor of HA, which has to be cleaved into the subunits HA1 and HA2 within the *trans-Golgi* (GA) (Klenk et al., 1975; Stieneke-Grober et al., 1992). Other translated viral proteins are later transported through the Golgi apparatus toward the cell membrane. Moreover, the viral NS1, PB1-F2 and PA-X are involved in the regulation of host cell processes (Ayllon & García-Sastre, 2014), and the NS1 may contribute to the viral mRNA export from the nucleus (Satterly et al., 2007).

Nascent viral proteins required for the vRNP formation are imported back into the nucleus. Translated PA and PB1 are imported as a heterodimer, unlike PB2 and NP, which are translocated into the nucleus independently (Huet et al., 2010). Inside the nucleus, novel vRNPs are formed by binding of NP monomers to the vRNAs and the translated RdRp subunits (Lee et al., 2017).

The M1 and NS2 protein are necessary for the export of vRNPs from the nucleus (Matthew Bui et al., 2000; O'Neill et al., 1998), although the exact mechanism of vRNPs nuclear export is not clear. Conversely, there is a model where M1 serves as an adaptor protein connecting the NS2 to vRNPs (Akarsu et al., 2003; Shimizu et al., 2011). Through the cooperation of established interactions with the CRM1 ('exportin-1') (Huang et al., 2013), NS2 directs the vRNP complex to the CRM1 nuclear export pathway. The NPs contain a leucine-rich nuclear export signal (NES) motif (Elton et al., 2001). The M1 protein blocks the NP, preventing the re-import of vRNPs, and the complex is transported to the cytoplasm (M Bui et al., 1996). Alternatively, vRNPs are associated with chromatin (Matthew Bui et al., 2000; Chase et al., 2011; Sakaguchi et al., 2003) and the M1 protein (Zhirnov & Klenk, 1997), and their interaction is needed for the vRNPs release from the chromatin to proceed with the nuclear export. The complex together with the Ran-GTP is exported outside the nucleus through the NPC. The Ran GTPase-activating protein (RanGAP) hydrolyses Ran-GTP to Ran-GDP. The complex dissociates releasing the vRNPs into the cytoplasm.

The vRNPs move through the cytoplasm most likely via vesicular transport connected to the microtubular network (Momose et al., 2007). After the transportation of vRNPs and vRNAs from the nucleus, their co-localization was detected at the microtubule organizing center (MTOC) and Rab-11, indicating the vRNPs utilize intracellular vesicles via Rab-11 for a transport to the plasma membrane (Amorim et al., 2011; Eisfeld et al., 2011).

The nascent viral particle is formed by the assembly of synthetized viral proteins at the cell plasma membrane. Once the newly assembled IAVs bud, their release is dependent on the sialidase activity of NA. It catalyzes the hydrolysis of the glycosidic linkage, which attaches sialic acid to the sugar molecule in receptors, thus preventing the HA binding to the cell surface (Barman et al., 2004; Gottschalk, 1957).

Even though a considerable effort was made to better understand the influenza virus life cycle, there are still some open questions. Not all the possible viral or cellular phosphorylation targets involved in the virus life cycle were yet discovered, nor the atomic structure of the full-length HA and NA in the membrane, as well as the regulation of the timing and expression levels of the viral mRNA transcription. Moreover, the structure determination of novel influenza anti-virals bound to target protein domains would be a great benefit for further drug development.

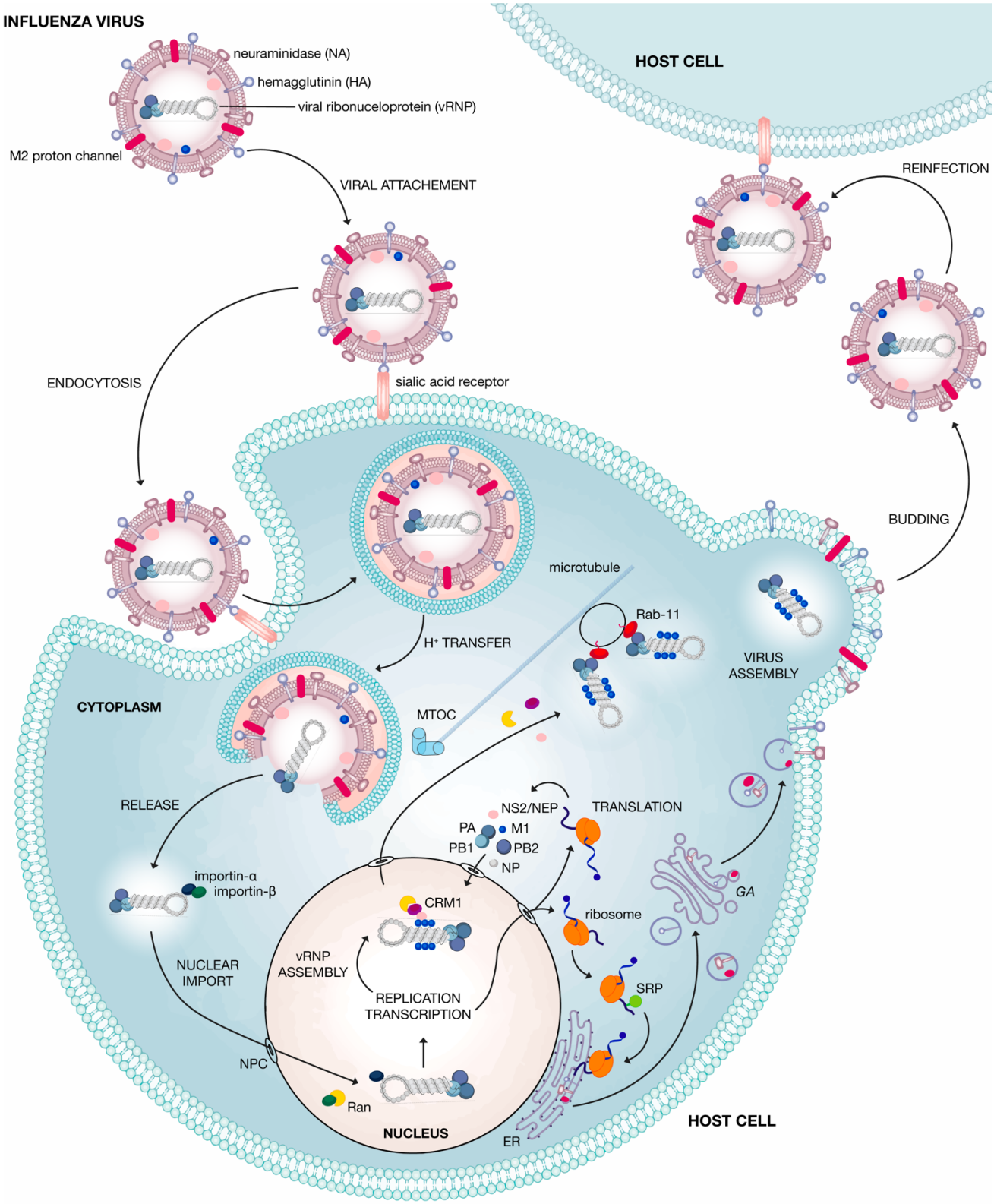


**Figure 2. Influenza virus life cycle.** The influenza virus infects the cell by the attachment of hemagglutinin to the host cell sialic acid receptor. Endosome-mediated endocytosis creates an acidic environment, and the $H^+$ transfer causes a release of viral proteins. Viral RNA is transcribed and replicated in the host cell nucleus, and viral mRNA is translated in the cytoplasm. Viral proteins necessary for the vRNPs formation are translocated to the nucleus,

and the assembled vRNP complex is exported. The Rab-11 linked to vesicles transports vRNPs to the cytoplasmatic membrane, where the viral particle assembles. The final step of the viral budding is the cleavage of the sialic acid by neuraminidase and the nascent viral particle is released.

## 1.5. IAV RNA-DEPENDENT RNA POLYMERASE

The IAV RdRp is responsible for the transcription and replication of vRNA. This multifunctional complex is over 260 kDa, and consists of three heteromeric subunits. The vRNAs for each subunit are located in the viral segments 1 – 3. The activation and consequent cooperation of the whole complex with several host factors, including proteins involved in the host proteosynthesis, leads to the synthesis of nascent viral particles. It is highly conserved among influenza viruses (see Supplementary material **S1**). Especially the PA-PB1 protein-protein interaction (PPI) is almost unmodified across the species.

As the polymerase contains over 2000 amino acids, it was difficult to achieve the entire RdRp structure. In 2014, the inter-subunit interactions were observed in bat-specific influenza virus (bat IAV) as a complete heterotrimeric complex was published (Reich et al., 2014). It revealed a large U-shaped protein complex (**Figure 3A – C**).

The PB1 subunit (polymerase basic protein 1) is in the centre of the polymerase complex containing catalytic residues for RNA synthesis (Fan et al., 2019; Peng et al., 2019; Pflug et al., 2014; Reich et al., 2014; Wandzik et al., 2020). It embodies an internal RNA-binding cavity with three inner narrow-sided tunnels. PB1 is surrounded with two subunits, PA (polymerase acidic protein) and PB2 (polymerase basic protein 2). The PA subunit consists of two domains, the N-terminal endonuclease domain (NPA) and the C-terminal domain (CPA), which creates the bottom-U polymerase part. They are connected by a long linker that wraps around the PB1 and interacts via extensive interface. The PB2 subunit is composed of several domains (**Figure 3D**), and is linked to the PB1 domain via the N-terminus. The C-terminus of PB2 is divided into more domains, all connected by flexible linkers. The PB2 cap-binding domain (PB2) and the NPA form parallel arms facing each other and reach out of the core of the protein complex. There are already several high-resolution RdRp structures of influenza A (human, avian, and bat), influenza B, C, and D (Fan et al., 2019; Hengrung et al., 2015; Keown et al., 2022; Peng et al., 2019; Pflug et al., 2014; Reich et al., 2014). These structural insights revealed that influenza polymerases are flexible macromolecules, adopting several conformational states. Genes coding the viral polymerases are of the most conserved within the influenza viruses.

Therefore, they are ideal targets for the development of influenza antivirals. Besides small molecules targeting different sites within the RdRp complex, recently the single-domain antibodies also known as Nanobodies® were introduced (De Vlieger et al., 2018; Keown et al., 2022).

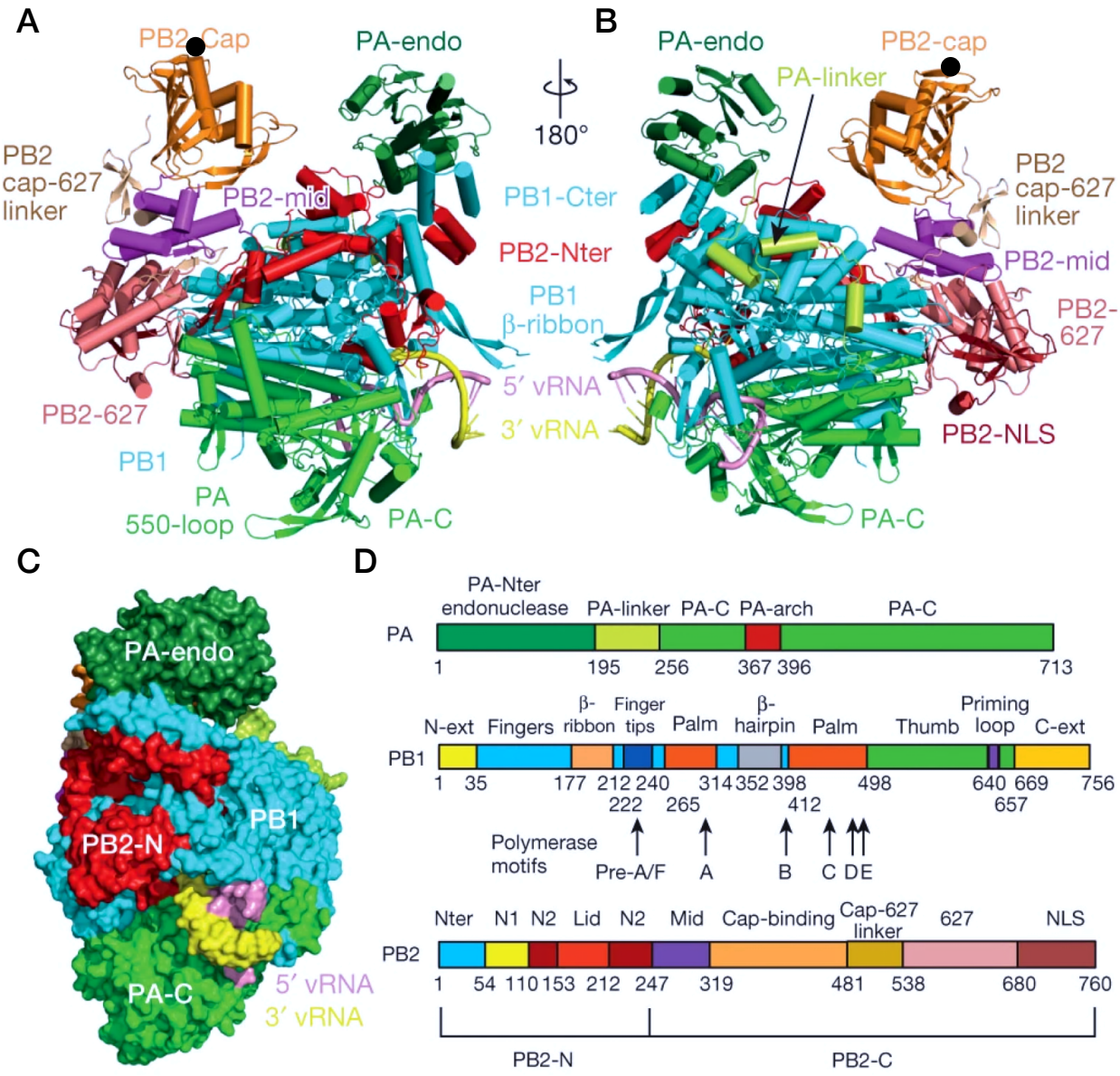


**Figure 3. A)**, **B)** Two views of the IAV RdRp complex. The RdRp is in ribbon representation and color-coded according to the domains in **D)** except that PA-C, PB1, and PB2-N are uniformly green, cyan, and red, respectively. The vRNA 5' and 3'ends are pink and yellow, respectively. The PB2-CBD is indicated as a black circle. **C)** Side-view of the vRNAs emergence at the interface of all three subunits in surface representation. **D)** Subunit domains layout with subdomain names and color scheme, the location of the conserved polymerase motifs in PB1 is indicated below. Reproduced from Pflug et al., 2014.

### 1.5.1. PB1 subunit

The PB1 subunit is an RNA-directed RNA polymerase catalytic subunit. The sequence analyses characterized several motifs within the PB1 subunit before the crystal structure was obtained (Biswas & Nayak, 1994; Bruenn, 2003). The 757 amino acids long sequence encodes the polymerase active site and includes the highly conserved pre-A/F and A-E motifs, which are characteristic for the RdRps and are responsible for the polymerase function. The PB1 overall central structure is formed of the right-handed RdRp fold, with finger domains, fingertips, palm, and thumb (**Figure 3D**).

The pre-A/F motif is located in the fingertips domain and in the loop extending from the fingers domain to the thumb domain. There are a few essential residues for the catalysis within the motifs A and C. The Asp-305 (at motif A) coordinates two divalent metal ions in cooperation with the motif C Asp-445 and Asp-446. The methionine-rich loop of PB1, stabilizing the base pair between entering nucleoside triphosphates (NTPs) and template, is placed in motif B (406-GMMMGMF). Motif D (including residues Lys-480, and Lys-481) is involved in the binding of NTP, and motif E stabilizes the position of substrate or priming NTP.

In PB1, there are four channels leading to the polymerase active site cavity: the NTP channel, which is decorated by positively charged residues, the RNA entry and exit channel, and the product exit channel (Reguera et al., 2016). Every channel is formed by all three subunits of the heterotrimeric complex.

### 1.5.2. PB2 subunit

The IAV PB2 subunit is a multi-domain protein of 760 amino acids. PB2 subunit can be further divided into one third of the N-terminus (PB2-N, residues 1 – 247) and two thirds of the C-terminus (PB2-C, residues 248 – 760), both consisting of several subdomains.

PB2-N is of five subdomains interacting mostly with the PB1 C-terminus via bundles of α-helices. The PB2-Nter is located opposite to the PA linker, enfolding in the PB1 subunit. The amino acid sequence is continued by the helix α4, which interacts with the template in the entry channel. The PB2-N1 domain is structurally supporting the PB1 thumb domain and passes via linker into the PB2-N2 domain. The PB2-Lid domain is composed of another helical bundle (residues 153 – 212), which separates the template-product nucleobases complex during the transcription. The PB2-N ends with the other part of N2 domain, formed by two anti-parallel β-sheets with one inserted helix. It interacts with the PA C-terminus and the thumb and palm domains of PB1 with hydrophobic contacts.

The larger part of PB2 subunit is the arc-shaped PB2-C region. It starts with the Mid domain, composed of four helices with one inter-helical linker, linked to the N2 domain. Connected by a flexible linker, it is followed by the PB2 cap-binding domain (PB2-CBD). This region (residues 319 – 481) has a key role in the viral life cycle. The Cap-627 linker domain precedes the 627 domain of PB2. This domain is bound to the PB1 core in the pre-initiation of transcription (apoform). The Mid domain is partially inserted into the PB2-CBD, preventing the binding of the 5'cap (Hengrung et al., 2015; Thierry et al., 2016). Only after the interaction with the host Pol II, the PB2-CBD is unblocked, and the 5'cap can be bound. The PB2 subunit terminates with the NLS domain (residues 680 – 760), carrying the NLS, Lys-Arg-Lys-Arg (Tarendeau et al., 2007).

During the pre-initiation, the 627 domain of PB2-C is bound to the core region of PB1.

The transcription of vRNA begins with the process "cap snatching", where the polymerase captures the five-prime cap from the host mRNA. This occurs on the PB2 subunit at the CBD. This domain is extremely flexible (Keown et al., 2022), which allows the PB2-CBD to explore the environment for a 5'cap. Moreover, the PB2-CBD orients the cap-bound host mRNA towards the NPA endonuclease and positions the cleaved primer into the polymerase active site, so the initiation of transcription can start.

The PB2-CBD is a well-ordered structure, composed of five antiparallel β-sheet strands (β1 – β5), four α-helices (α1 – α4), and four short β-strands (β8 – β12) (Guilligay et al., 2008). Between the lower end of helical subdomains and the β-sheets is the binding site for the five-prime cap. The binding is mediated by several interactions within the binding cavity. The ribose of 5'cap is positioned via the stacking interactions with a part of hydrophobic cluster, concretely with the Phe-404 (C-terminus of α1), Phe-323 (β1), and the His-357 (β4) (**Figure 4A**). The acidic Glu-361 (β5) forms a key hydrogen bond to the guanine (N1 and N2). Overall, the majority of the 5'cap is buried inside the binding cavity.

There were several attempts to develop a cap-analog inhibitor targeting the PB2-CBD (M. Liu et al., 2017; Pautus et al., 2013). However, the first structure of a PB2-CBD inhibitor, the pimodivir, in complex with the domain was published in 2014 (Clark et al., 2014). From the crystal structure, it is bound at a similar position as the 5'cap (**Figure 4B**). It forms four hydrogen bonds with residues Asn-429, Arg-355, Lys-376, and Glu-361. Alike the 5'cap, it interacts via π-π stacking with the Phe-404, Phe-323, and His-357. The inhibitors' azaindole part interacts with residue Gln-406. As it occupies the PB2-CBD it inhibits the binding of the cap, therefore the transcription of the vRNA.

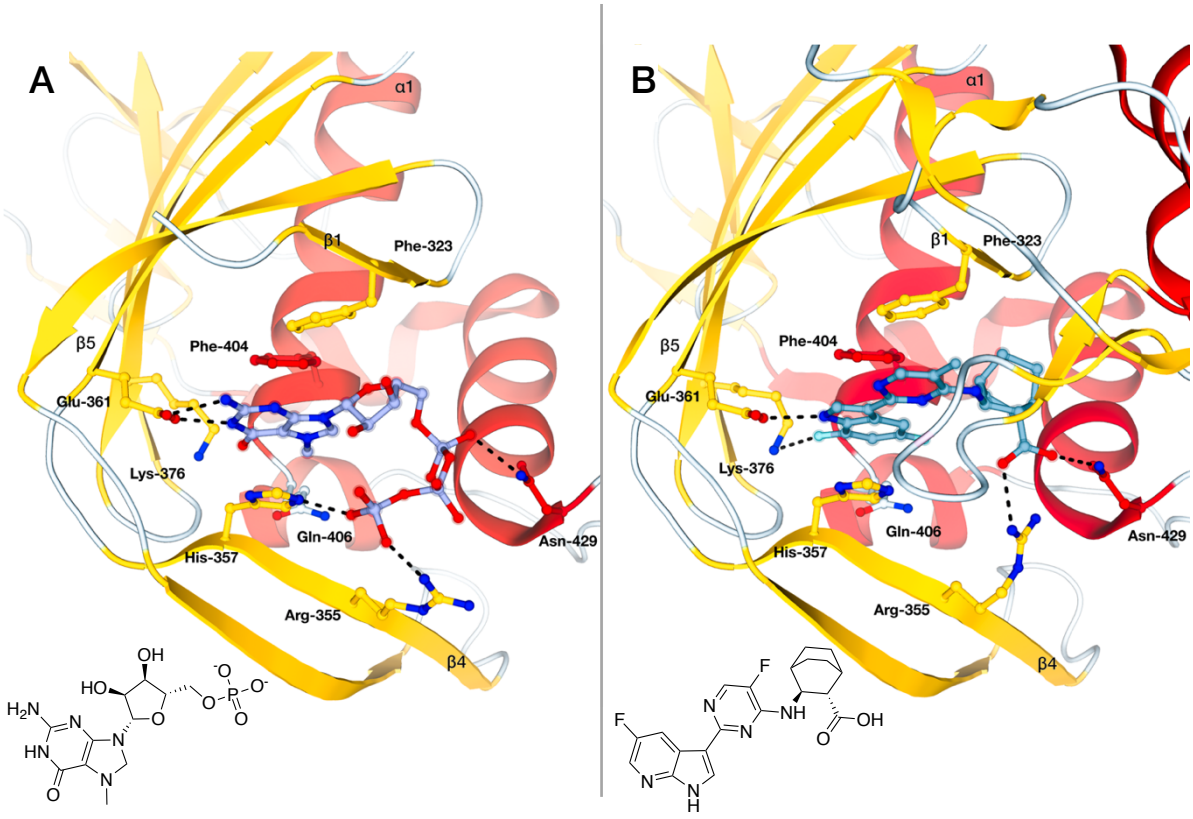


**Figure 4. Detailed view onto the PB2 cap-binding domain. A)** Structure of the CBD binding site with bound 5'cap (light blue). Interacting residues are highlighted in ball-and-stick representation. The PB2 protein is in cartoon representation with α-helices (red) and β-sheets (yellow) in cartoon representation. Hydrogen bonds are indicated as black dashes. Chemical structures are shown in the down-left corner. PDB ID: **2VQZ** (Guilligay et al., 2008). **B)** Structure of the CBD in complex with the pimodivir (teal). The additional loop in front of the pimodivir belongs to the Mid domain, as the crystallized construct was this region longer. Color coding and structure representation is in correspondence with **A)**. PDB ID **6S5V** (McGowan et al., 2019). All structural figures were prepared in Pymol (Schrödinger, LLC, 2015).

### 1.5.3. PA subunit

The complete structure of influenza RdRp revealed two distant major domains of the PA subunit. The NPA endonuclease domain is connected via long PA linker to the CPA domain. The PA subunit shares an extensive interface to the PB1 fingers and palm domains (**Figure 5**), mediated by the three helical segments (Pflug et al., 2014). The NPA (residues 1 – 195) is attached to the PB1 C-terminus. To this region of PB1 also binds the PB2-Nter, so there might be a possible crosstalk between the NPA and the PB2 subunit. The endonuclease active site is exposed to the solvent, opposite the PB2-CBD. The CPA lies on the other side of the PA subunit

(residues 396 – 713). It resembles a dragon's head that clamps the PB1 N-terminal peptide (He et al., 2008; Obayashi et al., 2008). This small inter-subunit interaction is essential for the whole heterotrimer assembly.

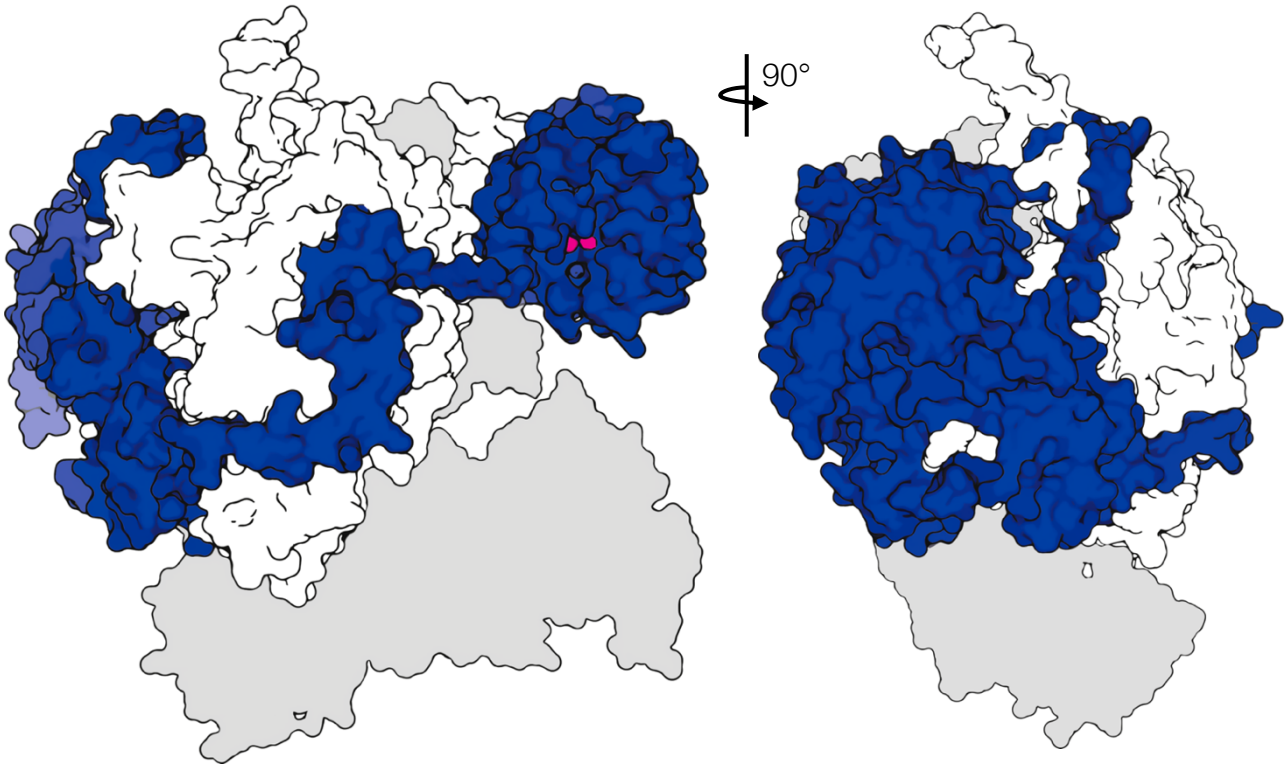


**Figure 5. Two-side view on the IAV PA subunit.** The PA (blue) and the PB1 (white) subunits are shown in the surface representation. The PB2 subunit is shown as gray relief for clarity. Two metal ions within the NPA endonuclease active site are pink spheres. PDB ID: **4WSB** (Reich et al., 2014).

#### 1.5.3.1. N-terminal domain of PA

Until 2009, the endonuclease activity was thought to take place at the PB1 (M. L. Li et al., 2001) or PB2 (Shi et al., 1995). The first crystal structures revealed, that the NPA (residues 1 to 195) carries the endonuclease active site (Dias et al., 2009; P. Yuan et al., 2009). The NPA is approximately 25 kDa domain consisting of seven α-helices surrounding the five central β-sheets. The endonuclease active site contains the (P)DXN(D/E)XK motif, inducing the binding of divalent metal ions. It consists of acidic residues Glu-80, Asp-108, and Glu-119, as well as His-41, and Ile-120. Importantly, Lys-134 is conserved among the type II endonucleases (Dias et al., 2009). This negatively charged pocket embeds two $Mn^{2+}$, or one $Mn^{2+}$ and one $Mg^{2+}$ions (**Figure 6A**). Both metals are coordinated together with water molecules, to the scissile nucleic acid phosphodiester of the host mRNA substrate, together with the apically positioned 3'-O of

ribose (**Figure 6B**) (Xiao et al., 2014). The $Mn^{2+}$ lowers the p$K_a$ of the attacking water molecule, Lys-134, and the adjacent 3'phosphodiester of the substrate. This leads to the activation of nucleophilic water molecule and the cleavage of the substrate. The product of 10-13 nucleotides is inserted inside the polymerase active site cavity in the PB1 and is utilized as a primer for the viral transcription.

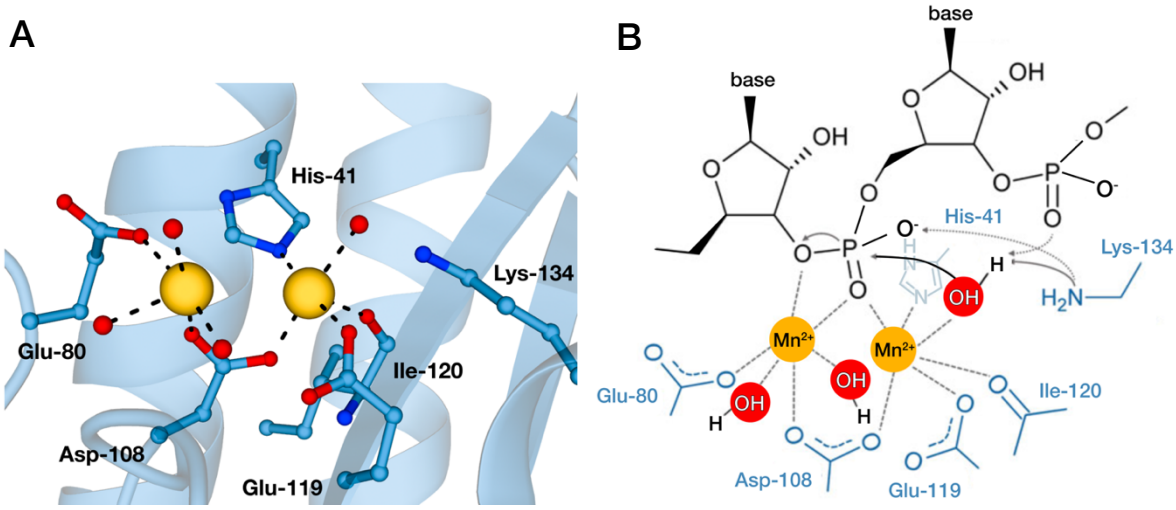


**Figure 6. A)** Close-up view on the NPA endonuclease active site. The NPA is in sky blue cartoon representation, with interacting residues as sticks. Two manganese ions and the water molecules in the active site are yellow and red spheres, respectively. Color coding, nitrogen is blue, oxygen in red. PDB ID: **7NUG** (Reiberger et al., 2021). **B)** A scheme of the RNA substrate NPA-mediated cleavage. Color coding is corresponds to the **A)**. Adapted from Stevaert & Naesens, 2016.

In past years, several compounds targeting the influenza endonuclease were described (Bauman et al., 2013; Cianci et al., 1996; DuBois et al., 2012; Fudo et al., 2016; Kowalinski et al., 2012; Z. Liu et al., 2016; Roch et al., 2015; Song et al., 2016; Stevaert et al., 2013; Xiao et al., 2014; S. Yuan et al., 2016). Even though, not all of them were structurally confirmed to bind the NPA, but showed anti-influenza effect in cell cultures (**Figure 7**) (Tomassini et al., 1996). All of them were designed to target the metal ions within the active site.

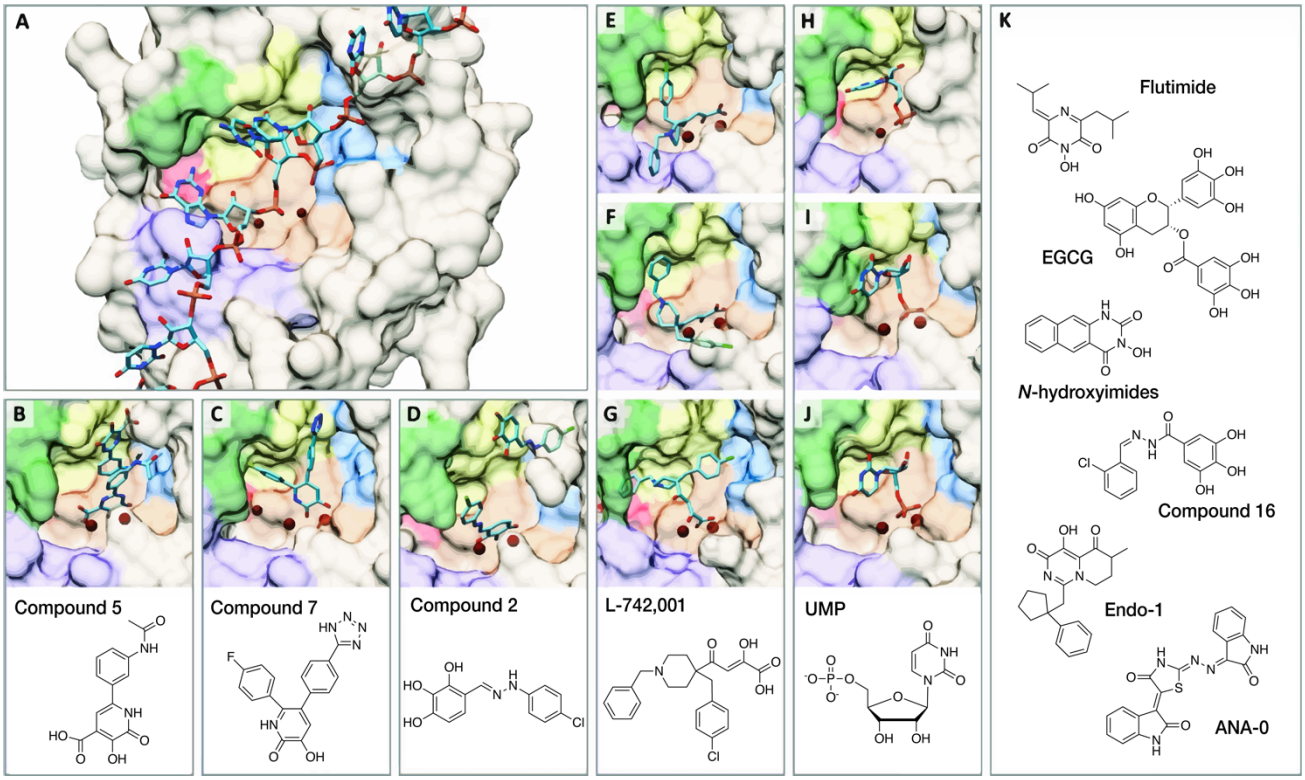


**Figure 7. The NPA active site ligands. A)** Model of the RNA substrate bound to two metal ions in the NPA active site (Xiao et al., 2014). The 3'end of RNA is in the up-right corner. **B)** Crystal structure of NPA with Compound 5 (**4E5J**, DuBois et al., 2012), with the chemical structure below; **D)** Crystal structures of Compound 7 (**4M5U**, Parhi et al., 2013); and crystal structure with Compound 2 (**5I13**, Fudo et al., 2016). E) – G) Different positions of the L-742,001 inhibitor obtained from the co-crystallization experiments (**4E5H** – **E**, DuBois et al., 2012, **5CGV** – **F**, Song et al., 2016), and from the docking studies (Stevaert et al., 2013). **H) – J)** NPA active site with bound uridine monophosphate (UMP), from three published crystal structures (**3HW3**, Zhao et al., 2009; **4AWH**, Kowalinski et al., 2012; **5CL0**, Song et al., 2016; respectively). The UMP in **I)** and **J)** occupy the same position. The protein areas binding ligands are colored. The metal binding and catalytic residues (His-41, Glu-80, Asp-108, Glu-119, Ile-120, and Lys-134) are highlighted in orange. Binding pockets are shown in yellow (P1, residues Ala-37, Ile-38, Leu-42, and Lys-34); blue (P2, residues Thr-40, Val-122, Arg-124, Tyr-130, and Phe-150); purple (P3, Arg-84, Trp-88, Phe-105, and Leu-106); red (P4, Leu-16, and Gly-81), and in green color (P5, Ala-20, Tyr-24, and Glu-26). Compounds, including the RNA are cyan and metals of the active site in dark red. Chemical structures of published inhibitors lacking structural characterization are in panel **K)**. Adapted from Stevaert & Naesens, 2016.

### 1.5.3.2. C-terminal domain of PA

The CPA domain is 767 amino acids long and contains 13 α-helices and 9 β-strands. The domain can be further divided into subdomain I, the dragons' "brain", and subdomain II, the "mouth". The resembling "brain" consists of seven central strands (β1 – β7) and five wrapped around α-helices (α1 – α3, and α6 – α7), together with a small η1-helix (**Figure 8A**, **B**). Subdomain II is formed by nine α-helices (α0, α4 – α5, α8 - α12) and two shorted β-sheets. The α-helices α11 and α10 form a hydrophobic pocket and enclose in between the N-terminal peptide derived from the PB1 subunit. This relatively short peptide adopts the secondary structure of the $3_{10}$ helix (η2). This is a crucial "tail to head" PPI between the PA and PB1 subunit. The interaction is mediated by hydrophobic contacts and a set of hydrogen bonds (**Figure 9A**).

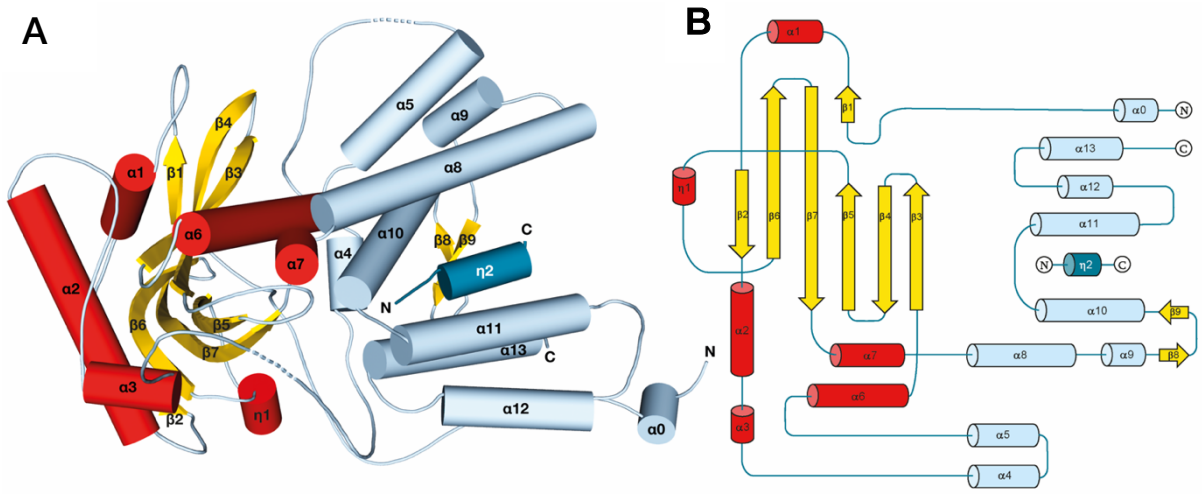


**Figure 8. The CPA dragon's head. A)** The tertiary structure of the CPA. The dragons' "brain" region is on the left with α-helices in red, and β-sheets in yellow. The right side represents the "mouth", with nine α-helices in pale cyan, and two β-sheets in yellow. The PB1-derived peptide is in teal. **B)** Scheme of 2D composition of CPA secondary structures, corresponding to the **A)**. PDB ID: **6SYI** (Hejdánek et al., 2021). Adapted from Radilová et al., 2022.

Residues Asp-2 to Asn-4 of the PB1 bind to the PA residues Ile-621 to Glu-623. More hydrogen bonds are formed between carbonyl oxygens of PB1 residues Asp-2, Val-3, Phe-9, Leu-10, and Val-12 to the PA residues Asn-412, Glu-623, Gln-408, Trp-706, Gln-670, and Arg-673. Moreover, the nitrogen atoms of Asp-2, Val-3, Asn-4, Leu-8, and Ala-14 (PB1) bind to the Glu-623, Asn-412, Ile-621, Pro-620, and Gln-670. Contributing to the peptide binding energy, the hydrophobic interactions were observed within the binding pocket (**Figure 9B**). The PB1 residue Pro-5 interacts with the Phe-411 and Trp-706. The other interaction was characterized

between the Leu-8 and side chains of PA residues Met-595, Trp-619, Val-636, and Leu-640 (He et al., 2008; Obayashi et al., 2008).

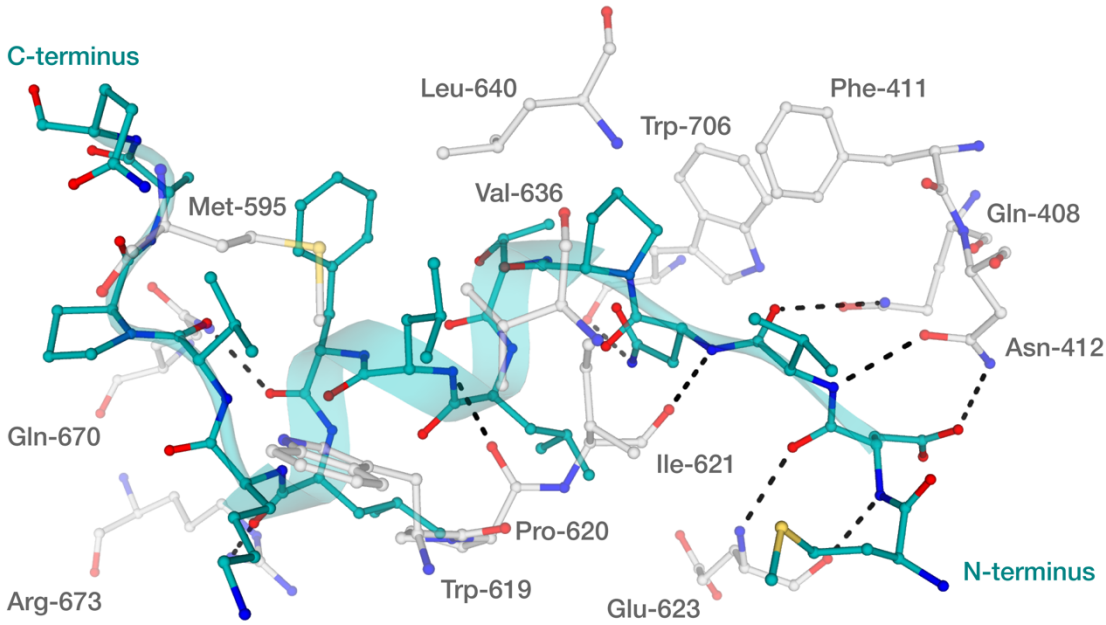


**Figure 9. The PA-PB1 protein-protein interaction hydrophobic pocket.** A close-up view onto the co-crystal structure of the CPA with bound PB1 N-terminal derived peptide. The CPA interacting residues are highlighted with three-code names and shown as gray sticks. The fifteen amino acids long PB1 peptide (teal) is in stick representation, with the $3_{10}$ helix indicated in the background (cartoon representation). Hydrogen bonds are as black dashes. Other color coding; oxygen – red, nitrogen – blue, sulphur – yellow. PDB ID: **2ZNL** (Obayashi et al., 2008).

Shortly after the first structures of CPA was published in 2008 (He et al., 2008; Obayashi et al., 2008), this PPI emerged as a next-generation drug target. The PA-PB1 binding domain is highly conserved among influenza A and B viruses (Wunderlich et al., 2011), and mutations of the residues would negatively affect the polymerase itself (Mänz et al., 2011). The assembly of the whole heterotrimeric RdRp can be inhibited by the disruption of the PA-PB1 PPI. The first PA-PB1 inhibitors were already designed a year before the protein structure was obtained (Ghanem et al., 2007). The inhibitor was a 25 amino acids long peptide, derived from the N-terminus of PB1 subunit. Moreover, using the peptide array, Wunderlich et al., 2011 identified amino acid positions that could be replaced by affinity-enhancing residues.

Several non-peptidic inhibitors of the PA-PB1 interaction were published (Massari et al., 2016). However, they lack structural characterization within the hydrophobic pocket (D'Agostino et al., 2018; Desantis et al., 2017; Lo et al., 2018; Massari et al., 2016; Nannetti et al., 2019; Trist et al., 2016; Watanabe et al., 2017; S. Yuan et al., 2017; J. Zhang et al., 2018, 2020).

## 1.6. REPLICATION

One of two major functions of the IAV RdRp is the replication of the viral genome to synthesize new viral particles. In contrast to viral transcription, replication is not dependent on the 5'cap. It can be divided into two-steps process. The first is the creation of cRNA, a replicative intermediate, and the second is the synthesis of vRNA with cRNA acting as a template. Replication begins with the translocation of the 3'end of vRNA into the polymerase active site (**Figure 10A**).

A terminal initiation follows, which is a formation of pppApG dinucleotide on residues U1 and C2 of the vRNA 3'end (Deng et al., 2006). This *de novo* initiation is structurally supported by a priming loop, especially the conserved proline at the loop tip, providing a stacking platform for the NTP (Te Velthuis et al., 2016).

During elongation, 9-10 nucleotides' nascent strand remains in the polymerase pocket. The 5'end of vRNA must be released from the polymerase active site to be replicated and is recruited together with NP by newly synthesized polymerase to form cRNP (Turrell et al., 2013). The termination of the cRNA synthesis is by yet unclear structural changes of the polymerase.

Next, the vRNA is synthesized using the cRNA as a template. It starts with the internal initiation process, where the pppApG dinucleotide is formed on the 3'end of the cRNA at positions 4 and 5. A second regulatory polymerase binds, creating a symmetrical dimer with replicating polymerase, and most likely causes a priming loop conformation change (Fan et al., 2019; Oymans & te Velthuis, 2018). This leads to a realignment of the dinucleotide to the 3'end of cRNA by backtracking the template (**Figure 10B**).

Nascent vRNA is right away encapsidated during replication, recruited by the polymerase at 5'end together with NPs to form vRNPs. The process is accompanied with another dimerization with cellular host factor acidic leucine-rich nuclear phosphoprotein 32 family member A (ANP32A) (Carrique et al., 2020). By forming an asymmetrical dimer it ideally positions and stabilizes the complex (Long et al., 2016). Moreover, the ANP32A contains the low complexity acidic (leucine-rich) region (LCAR) that could operate as a molecular whip recruiting NPs (Reilly et al., 2014). Different states of dimers and complex structural rearrangements are still not solved.

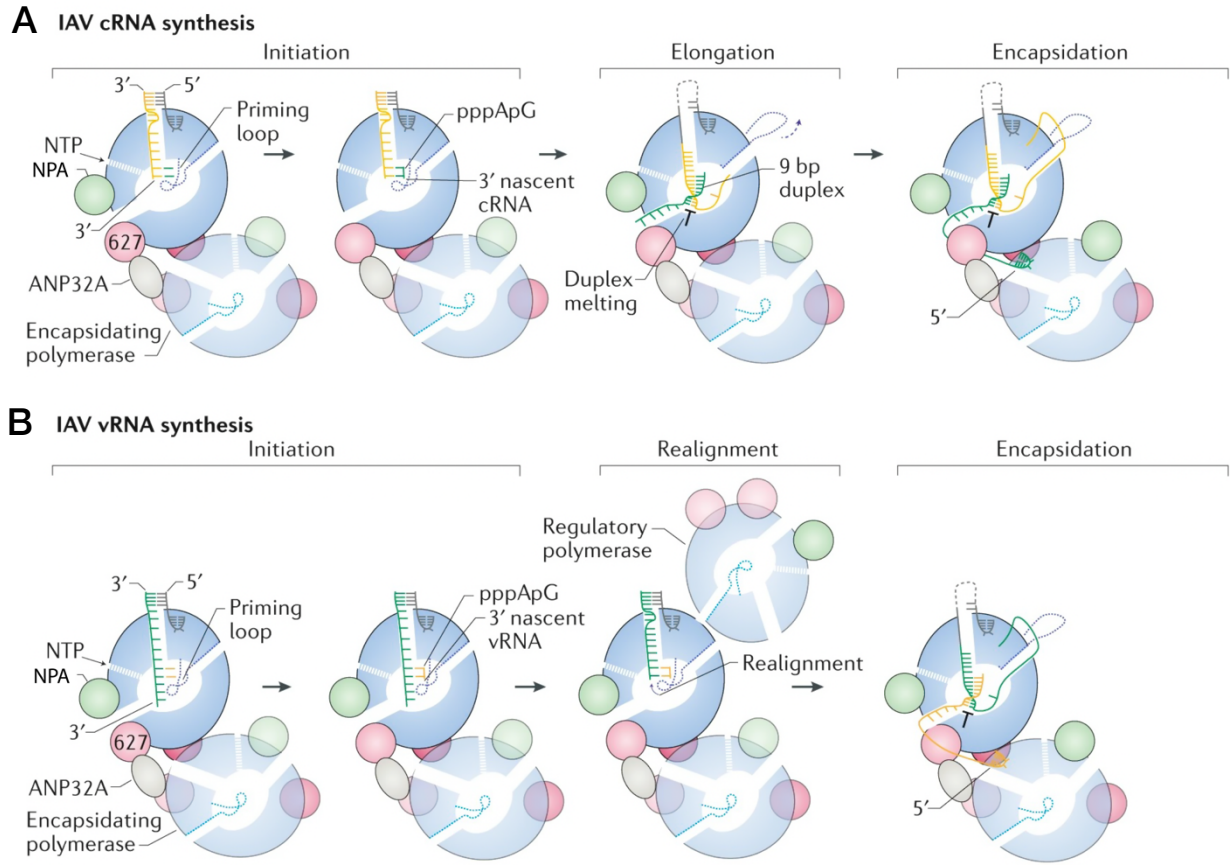


**Figure 10. Influenza A virus RNA synthesis schemes. A)** complementary RNA (cRNA) synthesis; **B)** viral RNA (vRNA) synthesis. Adapted from (te Velthuis et al., 2021).

## 1.7. CAP-DEPENDENT vRNA TRANSCRIPTION

Viral RNA transcription leads to the synthesis of a 5'-capped and 3'-polyadenylated viral mRNA, which is later translated by the host apparatus into viral proteins. Unlike replication of the virus, its transcription requires 5'-capped RNA, but viral RNA does not contain capped vRNA nor codes guanylyl transferase. IAV RdRp gets capped fragments from the nascent host capped RNAs, which serve as primers. The process of taking the host 5'cap is called "cap snatching" and is a result of the collaboration of two IAV RdRp subunits (**Figure 11**).

The transcription is initiated by the binding of the viral polymerase to the serin-5-phosphorylated C-terminal domain of host Pol II. The interaction is mediated by residues of the PB2 627 domain and NLS domain, together with the residues of the PA C-terminal domain (Engelhardt et al., 2005; Kouba et al., 2019; Lukarska et al., 2017; Serna Martin et al., 2018). During the pre-initiation, the 627 domain of PB2-C is bound to the core region of PB1. The binding to the host Pol II stabilizes the CBD. This was affirmed as the transcription of the virus

was sensitive to actinomycin D (transcription inhibitor), and α-amanitin (inhibitor of Pol II) (Mahy et al. 1972; Sugiura et al. 1969). The CBD of PB2 is exposed and can bind the host cellular mRNA. There is some preference for noncoding caps generated by the Pol II seized from small nuclear RNAs (snRNAs), small nucleolar RNAs (snoRNAs), and promoter-associated capped small RNAs (Gu et al., 2015; Koppstein et al., 2015).

The host cap binds to the PB2 CBD at the C-terminus. Following the cap snatching, the endonuclease domain of PA N-terminus located facing the CBD cleaves the 10-13 nucleotides downstream from the 5'cap. Nascent primer is placed into the polymerase active site. This happens by the rotation of the PB2 CBD of approximately 70° and subsequent insertion of the 3' primer end through the exit channel (Kouba et al. 2019; Pflug et al. 2018; Reich et al. 2014). At the same time, the 3'end of the vRNA template transfers from the surface-close position to the polymerase active site through the entry channel.

The transcription is initiated by the addition of G or C nucleotide at the 3'end of primer complementary to the penultimate C (C2) or G (G3) of the vRNA template. Elongating product is separated from the template by the helical PB2 lid domain. Nascent mRNA opens the PB1 thumb domain and pushes the priming loop from the template exit channel. The cap is released from the PB2 CBD and can interact with the host cap-binding complexes during the transcription.

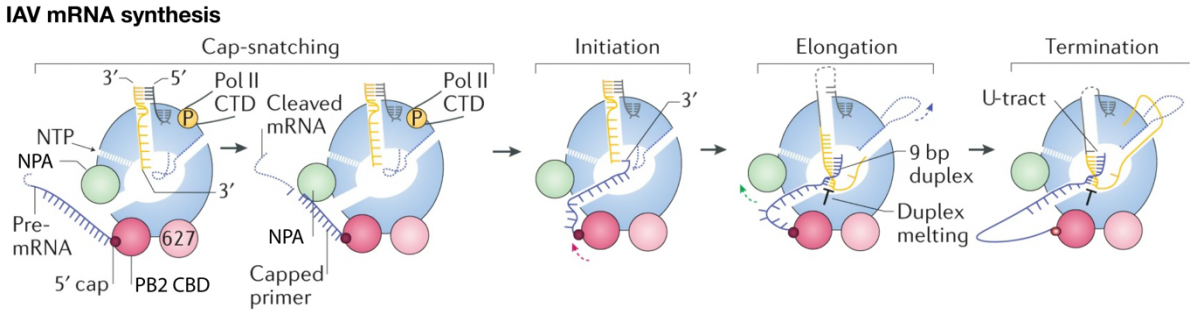


**Figure 11. Influenza A virus mRNA synthesis scheme.** Four processes of viral mRNA synthesis: the cap-snatching, initiation, elongation, and termination. Adapted from (te Velthuis et al., 2021).

While the elongation pulls the vRNA, it peels the template off the NPs and the RNA loop shrinks. After NPs unwind from the nucleobases, they are translocated from the incoming template site and reassociated with the outcoming template (Coloma et al., 2020; Wandzik et al., 2020). From the structural analyses of vRNP, a new mechanism 'processive helical track' was observed (**Figure 12**). Both 3' and 5'ends of the template remain associated with the

transcribing polymerase, and the whole complex slides along the viral genome coiled around NPs. Transcribed template RNA bulges out from a different site of the polymerase, forming a growing loop.

Elongation continues until it reaches the oligo(U) motif starting with U17. This polyadenylation motif is 5-7 nucleotides long. Polymerase stutters, and the U17 flips in and out from the active site chamber and repeatedly incorporates AMPs into the product (X. Li & Palese, 1994; Poon et al., 1999; Wandzik et al., 2020). Termination of polyadenylation might include interactions with host-factors (Landeras-Bueno et al., 2011). The conformation changes of the polymerase probably result in a destabilization of the (U-A)-rich product-template duplex. The nascent capped and polyadenylated viral mRNAs are released.

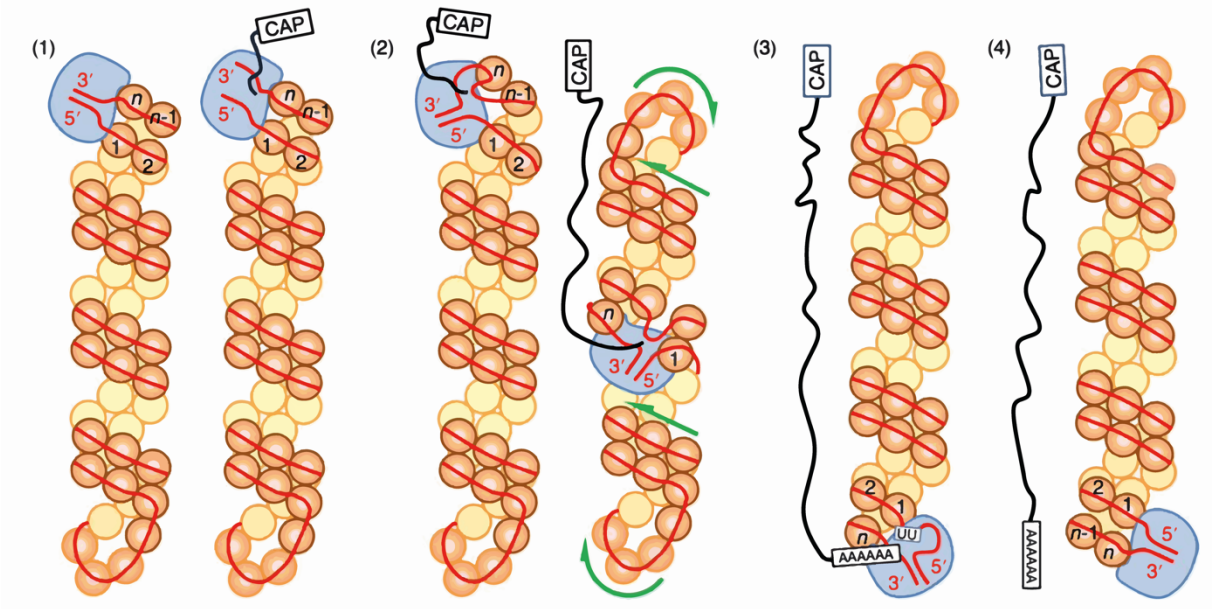


**Figure 12. Processive helical track.** Polymerase (blue) sliding along the vRNA (red) in transcription steps: 1) initiation, 2) elongation, 3) polyadenylation, 4) release of capped, poly(A) tailed -mRNA. Nucleoproteins are orange and yellow spheres and their movement is indicated by green arrows. Reproduced from (Coloma et al., 2020).

## 1.8. CURRENT ANTI-INFLUENZA TREATMENT

Vaccines are the most effective way to fight influenza as well as many other viruses. However, the IAV continuously escapes the immune system by antigenic drift (Kim et al., 2018). Therefore, there is a necessity to reformulate the vaccine composition and annual immunization. Moreover, the vaccines are not effective when the antigenic shift occurs, and the development of specific vaccines is usually delayed weeks after the pandemic outbreak. In such circumstances, antivirals can have an important role in controlling the impact of influenza. In addition, the immune response of the high-risk population groups and the vaccination coverage are suboptimal (Principi et al., 2018; Sano et al., 2017). Naturally, there is an intensive effort to develop anti-influenza drugs to overcome such obstacles. As several targets were described within the influenza virus, a class of viral surface protein inhibitors was among the first ones. These can be divided into two classes, the M2 channel inhibitors, and the neuraminidase inhibitors.

The M2 proton channel inhibitors were the first anti-influenza inhibitors in use, introduced already in the 1960s. Adamantane (Gocovri®), and its derivative rimantadine (Flumadine®) (**Figure 13A**), sterically block the M2 proton channel and therefore restrain the proton translocation needed for a viral intracellular uncoating (Hay et al., 1985; Stouffer et al., 2008; Thomaston et al., 2018; Wang et al., 1993). Their use was limited only to influenza A, had severe side effects, and due to the resistance development, the use of M2 channel inhibitors is not recommended since 2004.

Another viral surface protein neuraminidase is a glycoside hydrolase cleaving the sialic acid residues from the host cell glycoproteins. Its inhibition would prevent the viral particle from being released from the host cell. So far, there are four neuraminidase inhibitors (NAIs) developed (**Figure 13B**). Orally administrated Oseltamivir (Tamiflu®), inhaled Zanamivir (Relenza®), Laninamivir (Inavir®), and intravenously administrated Peramivir (Rapivab®) act on both influenza A and influenza B viruses and have good tolerability (Barroso et al., 2005; Cass et al., 1999; Ishizuka et al., 2010). Among these, oseltamivir discovered by Gilead Sciences in the late 1990s, is most extensively used for the treatment of acute, uncomplicated seasonal influenza (Uyeki et al., 2019). Oseltamivir was introduced in clinical practice together with zanamivir between the years 1999 to 2002. Besides several side effects including nausea (Antipov & Pokryshevskaya, 2019), resistant variants of the virus against NAIs were detected (McKimm-Breschkin et al., 2003).

The other NAI, peramivir, has different structural properties. It was characterized as a tightly-bound inhibitor with slow dissociation (Bantia et al., 2006). However, the intravenous

administration requires medical assistance. The last of the four NAIs is the laninamivir octanoate, precursor of the active form of laninamivir. Like zanamivir, it is administrated by inhalation. It persists in a high concentration of its active form in the lungs for at least five days (Ikematsu & Kawai, 2011). The single dose administration of laninamivir is its major benefit, although the inhalation is not recommended for patients underlying airway diseases (such as asthma). Altogether, NAIs are first-in-hand for the treatment of uncomplicated influenza. However, influenza neuraminidase is affected by antigen drift, which may result in resistant viral variants. The complexity of the NAI-resistance development underlies challenges for surveillance of newly emerging influenza viruses or viruses isolated from the avian/human interface.

Lately, as the structure of the influenza RdRp was published in 2014 (Reich et al., 2014), this protein became a novel target for drug development (**Figure 13C**). Favipiravir (trade name Avigan®), a purine analog, was developed in Japan as an anti-influenza inhibitor (Takahashi et al., 2003). It selectively inhibits the RdRp by incorporation into the nascent RNA strand and consequently causes the vRNA synthesis termination (Furuta et al., 2013; Sangawa et al., 2013). Later it was characterized as a broad-spectrum antiviral as it provided some inhibitory efficacy against other RNA viruses, including phleboviruses or Ebola virus (Shiraki & Daikoku, 2020). It was more efficient than oseltamivir while treating influenza (Tanaka et al., 2017). Nonetheless, influenza has a high intrinsic mutation rate enabling the development of resistance to antivirals (Goldhill et al., 2018; Pauly et al., 2017; Takashita et al., 2016). Also, favipiravir administration raised concerns regarding teratogenic risks (Nagata et al., 2015).

The VX-787 (trade name Pimodivir®) is an azaindole-based compound targeting the unique "cap-snatching" mechanism of influenza RdRp (Clark et al., 2014). It showed significant anti-influenza inhibitory potency, even against influenza pandemic strains. Pimodivir passed two phases of clinical trials, even though some amino acid mutations within the active site occurred (O'Neil et al., 2022; Trevejo et al., 2018; Zhu et al., 2012). However, it did not show added benefits to hospitalized patients with influenza A infection and the drug development program in the phase IIIb (no. NCT03376321) was discontinued by the commercial developer Jannsen Pharmaceutical in September 2020 (www.clinicaltrialsarena.com/news/janssen-pimodivir-development/). Nonetheless, the PB2 CBD and more generally the influenza RdRp remain attractive targets for anti-viral drug development.

It took almost 20 years to develop influenza antivirals with a novel mechanism of action, targeting the endonuclease located on the PA subunit of the RdRp. Baloxavir marboxil (BAM) with the trade name Xofluza® was licensed in Japan in 2018. It is among the four antiviral drugs

approved by the US Food and Drug Administration (FDA) and recommended by the US Centers for Disease Control and Prevention (CDC) for use against circulating influenza viruses this season (2022). It is a precursor for the hydrolyzed active antivirotics, baloxavir acid (BXA). This successful compound is a result of a rational drug design, which was developed based on the structure of dolutegravir, the human immunodeficiency virus inhibitor (Noshi et al., 2018). The BXA chelates two metal ions in the endonuclease active site prohibiting the production of primer, thus the viral transcription. Currently, it is used in Japan and USA in a single dose administrated perorally. In phase II of clinical studies, a significant mutation strain emerged (Hayden et al., 2018). The substitution of Ile-38 to Thr-38 within the endonuclease active site led to 20-40 times reduced susceptibility to the BXA. This mutation removes the methyl group required for the binding of BXA, and lowers the hydrophobicity of the binding surface, which is required for the binding of RNA (Omoto et al., 2018). Nevertheless, the approval of BAM as an anti-influenza drug was a great step forward. Its major advantage is that only one dose is required, it is well tolerated, and is capable of a viral load reduction within 24 hours of the treatment. It opened the door for drug design of a novel target, as well as the possibility of combination therapy of anti-influenza drugs, overcoming the easily arisen resistance mutations.

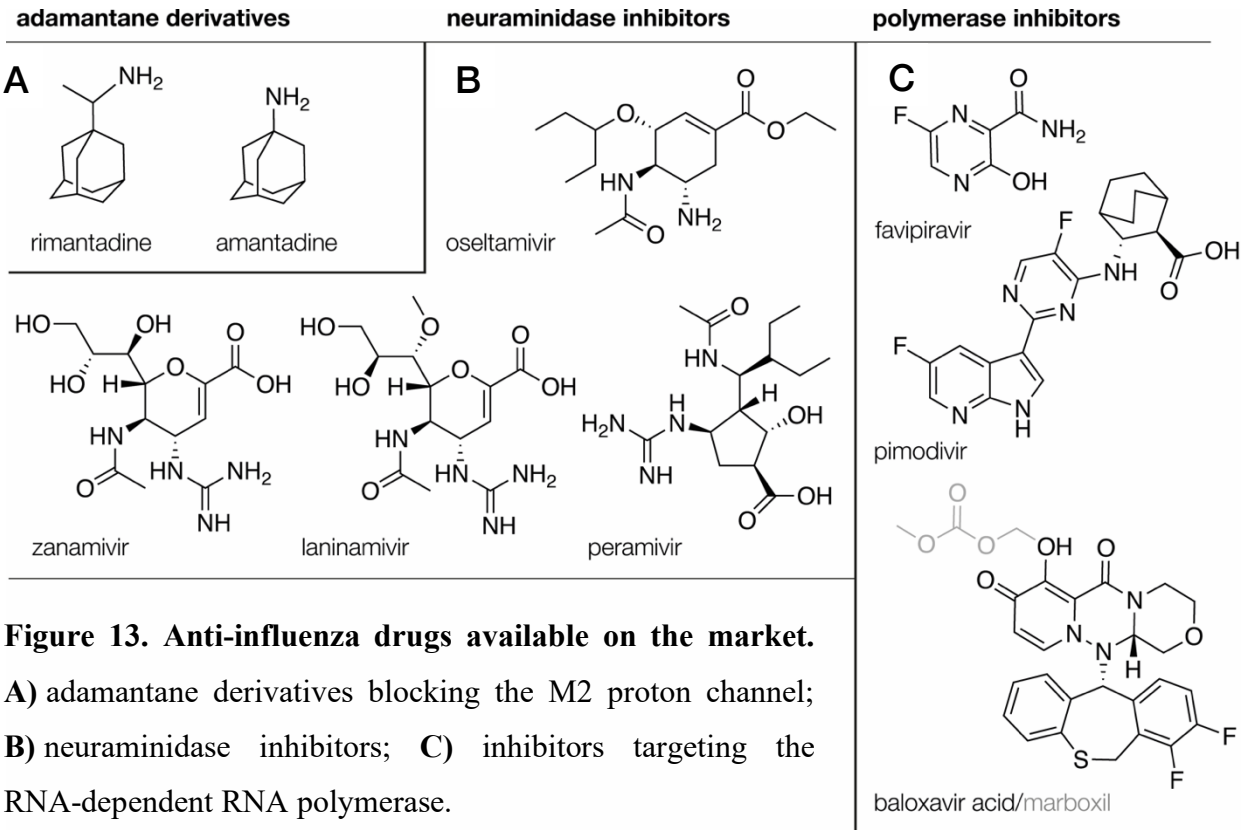


**Figure 13. Anti-influenza drugs available on the market.** **A)** adamantane derivatives blocking the M2 proton channel; **B)** neuraminidase inhibitors; **C)** inhibitors targeting the RNA-dependent RNA polymerase.

## 2. RESEARCH AIMS

In this work, we plan to explore two domains of the PA subunit of influenza A RNA-dependent RNA polymerase and compounds able to bind and inhibit them. Specifically, its C-terminal domain (CPA) bears an essential protein-protein interaction with another RdRp subunit, and the N-terminal domain (NPA), which has endonuclease function.

The first aim of the study is to recombinantly prepare optimized domain of 460 amino-acids, to develop a high-throughput screening assay, and to test a series of peptides for their PPI inhibitory potency. Furthermore, we want to structurally characterize the most promising peptides bound to the CPA using an X-ray protein crystallography and to utilize this for further optimization. Additionally, we intend to improve the peptide stability, intracellular delivery, and to structurally characterize whether those optimizations contribute to the binding.

Furthermore, we set to analyze the second subunit of viral polymerase, the endonuclease, with the aim to decipher the mechanism of action of flavonoids, non-specific antiviral compounds of plant origin. We plan to recombinantly express the endonuclease domain, and to develop an inhibitor-testing assay. With this assay, we want to prove or disapprove our hypothesis that molecules from a polyphenolic class flavonoids target the NPA. If so, to structurally characterize compounds in the endonuclease active site and to utilize this information for further structure-based drug design.

# 3. RESULTS

## 3.1. PUBLICATIONS INCLUDED

**I.** Hejdanek, J., Radilova, K., Pachl, P., Hodek, J., Machara, A., Weber, J., Rezacova, P., Konvalinka, J., and Kozisek, M.; 2021. "**Structural Characterization of the Interaction between the C-Terminal Domain of the Influenza Polymerase PA Subunit and an Optimized Small Peptide Inhibitor**." *Antiviral Research* 185 (January 2021): 104971. doi: 10.1016/j.antiviral.2020.104971. **$IF_{(2021)}$ = 10.19**

**II.** Radilova, K., Zima, V., Kral, M., Machara, A., Majer, P., Hodek, J., Weber, J., Brynda, J., Strmen, T., Konvalinka, J., and Kozisek, M. 2022. "**Thermodynamic and structural characterization of an optimized peptide-based inhibitor of the influenza polymerase PA-PB1 subunit interaction.**" *Antiviral Research* 208 (December 2022): 105449. doi: 10.1016/j.antiviral.2022.105449. **$IF_{(2021)}$ = 10.19**

**III.** Zima, V.*, Radilova, K.*, Kozisek, M., Albinana, C. B., Karlukova, E., Brynda, J., Fanfrlik, J., Flieger, M., Hodek, J., Weber, J., Majer, P., Konvalinka, J., and Machara, A.; 2020. "**Unraveling the Anti-Influenza Effect of Flavonoids: Experimental Validation of Luteolin and Its Congeners as Potent Influenza Endonuclease Inhibitors.**" *European Journal of Medicinal Chemistry* 208:112754. doi: 10.1016/j.ejmech.2020.112754. **$IF_{(2020)}$ = 6.18**

**IV.** Reiberger, R.*, Radilova, K.*, Kral, M., Zima, V., Majer, P., Brynda, J., Dracinsky, M., Konvalinka, J., Kozisek, M., and Machara, A.; 2021. "**Synthesis and In Vitro Evaluation of C-7 and C-8 Luteolin Derivatives as Influenza Endonuclease Inhibitors.**" *International Journal of Molecular Sciences* 22(14):7735. doi: 10.3390/ijms22147735. **$IF_{(2021)}$ = 6.01**

## 3.2. PUBLICATIONS NOT INCLUDED

**I.** Gregor, J., Radilova, K., Brynda, J., Fanfrlik, J., Konvalinka, J., and Kozisek M.; 2021. "**Structural and Thermodynamic Analysis of the Resistance Development to Pimodivir (VX-787), the Clinical Inhibitor of Cap Binding to PB2 Subunit of Influenza A Polymerase.**" *Molecules* 26 (4):1007. doi: 10.3390/molecules26041007. **$IF_{(2021)}$ = 5.56**

## 3.3. PUBLICATION I.

**Structural characterization of the interaction between the C-terminal domain of the influenza polymerase PA subunit and an optimized small peptide inhibitor.**

The heterotrimeric RdRp complex of influenza A is an essential enzyme for viral replication and translation. Two subunits, PA and PB1 share an extensive interface. However, their assembly depends on a relatively small pocket formed by the C-terminus of PA. The PB1 N-terminal domain clicks into the CPA in a form of $3_{10}$ helix (He et al., 2008; Obayashi et al., 2008). Disrupting such an important protein-protein interaction appears to be a promising drug target. The first 14 amino acids peptide from the N-terminus of PB1 were identified as a nanomolar inhibition of the PA-PB1 PPI (Wunderlich et al., 2009). Moreover, the peptide array residue revealed several introduced mutations as advantageous for the peptide binding, though without an X-ray structure (Wunderlich et al., 2011).

### 3.3.1. SUMMARY

To explore the relative importance of the core amino acids PPI between the two subunits (PA-PB1), we have truncated and mutated previously described 14 amino acid long peptide (**PB1-0**). We have developed a new assay based on the AlphaScreen technology to screen inhibitors of the PA-PB2 PPI (**Figure 14**).

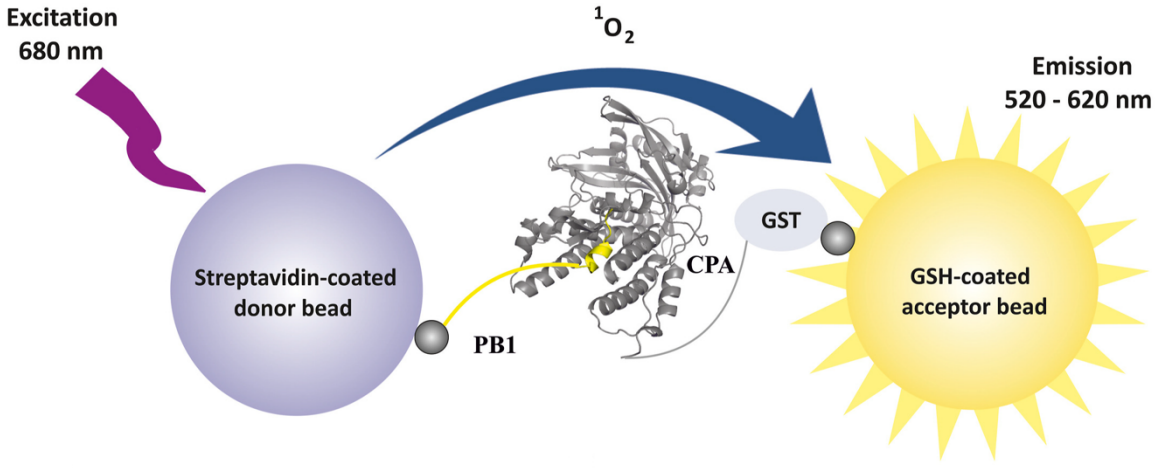


**Figure 14.** Schematic illustration of the AlphaScreen-based assay for PA-PB1 PPI. The streptavidin-coated donor beads are bound to the biotinylated **PB1** peptide. The Glutathione SH (GSH) coated acceptor bead allows the Glutathione-S-transferase (GST) -tagged CPA binding. When the donor bead is excited (λ = 680 nm) and the **PB1** peptide is in proximity with CPA,

the singlet oxygen is transferred and the acceptor bead emits a detectable signal (λ = 520 – 620 nm). If an inhibitor disrupting this interaction is present, the signal is decreased. We tested twelve synthetic peptides to obtain their inhibition potency (**Table 1**).

Truncation of **PB1-0** from both sides resulted in 10 different peptides. None of them exceeded the initial peptide, but it revealed the importance of core amino acids. When truncated from the C-terminus (**PB1-1** to **PB1-5**), the peptides remained fair inhibitory potency until the truncation to Lys-11. The truncation of the N-terminus (**PB1-6** to **PB1-9**) was tolerated only for the two starting amino acids, otherwise led to the loss of inhibition potency. The **PB1-10** peptide was N-terminal Met-1 cut short as well as three C-terminal amino acids. This combination caused a reduction in inhibition with an $IC_{50}$ of 3.4 μM. Finally, inspired by the published peptide array, we introduced two affinity-enhancing substitutions (**PB1-11**) at peptide "hot-spots". The replacement of Val-3 and Trp-6 both with tyrosines vastly improved the binding affinity ($IC_{50}$ of 13 nM). To evaluate the peptides *in vivo* activity we have modified them by the addition of commonly used cell-penetrating Tat peptide to either C-terminus or N-terminus. Unfortunately, the association with cell-penetrating peptide did not provide an effective antiviral *in vivo* effect. To observe the details of this interaction we cocrystallized the complex of CPA and **PB1-11** peptide. A high resolution crystal data were collected at BESSY II (Helmholtz-Zentrum, Berlin) and the structure was solved at 1.6 Å (PDB ID: **6SYI**). Details of this modified peptide within the CPA groove may serve for further structure-based drug design of anti-influenza drug.

| Peptide | Sequence | $IC_{50}(\alpha)$ [nM] |
|---|---|---|
| **PB1-0** | MDVNPTLLFLKIPA | 6 ± 1 |
| **PB1-1** | MDVNPTLLFLKIP | 22 ± 1 |
| **PB1-2** | MDVNPTLLFLKI | 39 ± 4 |
| **PB1-3** | MDVNPTLLFLK | 130 ± 20 |
| **PB1-4** | MDVNPTLLFL | 440 ± 40 |
| **PB1-5** | MDVNPTLLF | 7,200 ± 1,000 |
| **PB1-6** | DVNPTLLFLKIPA | 33 ± 3 |
| **PB1-7** | VNPTLLFLKIPA | 390 ± 50 |
| **PB1-8** | NPTLLFLKIPA | 20,200 ± 1,700 |
| **PB1-9** | PTLLFLKIPA | 36,000 ± 4,000 |
| **PB1-10** | DVNPTLLFLK | 3,400 ± 300 |
| **PB1-11** | D**Y**NP**Y**LLFLK | 13 ± 1 |

**Table 1.** Inhibition potencies of peptide series determined by the AlphaScreen based technology. The $3_{10}$ helix is highlighted in blue. The affinity enhancing "hot-spots" within the **PB1-11** are red bold.

my contribution

I expressed the CPA domain of influenza A RdRp in *E.coli* in high level and purified the protein. I collected the X-ray diffraction data at BESSY II synchrotron Macromolecular X-ray Structure Analysis (MX) beamline 1 (Helmholtz-Zentrum, Berlin). With help from Jiří Brynda I processed the data and solved the protein-peptide structure. Finally, the structure was released under PDB ID: **6SYI**.

"**Structural Characterization of the Interaction between the C-Terminal Domain of the Influenza Polymerase PA Subunit and an Optimized Small Peptide Inhibitor**." *Antiviral Research* 185 (January 2021):104971. doi: 10.1016/j.antiviral.2020.104971.

Antiviral Research 185 (2021) 104971

Contents lists available at ScienceDirect

Antiviral Research

journal homepage: www.elsevier.com/locate/antiviral

Research paper

# structural characterization of the interaction between the C-terminal domain of the influenza polymerase PA subunit and an optimized small peptide inhibitor

Jakub Hejdánek [a], Kateřina Radilová [a,b], Petr Pachl [a], Jan Hodek [a], Aleš Machara [a,c], Jan Weber [a], Pavlína Řezáčová [a,d], Jan Konvalinka [a,e], Milan Kožíšek [a,*]

[a] Institute of Organic Chemistry and Biochemistry of the Czech Academy of Sciences, Gilead Sciences and IOCB Research Center, Flemingovo n. 2, 16610, Prague 6, Czech Republic
[b] First Faculty of Medicine, Charles University, Kateřinská 1660/32, 12108, Prague 2, Czech Republic
[c] Department of Organic Chemistry, Faculty of Science, Charles University, Hlavova 8, 12800, Prague 2, Czech Republic
[d] Institute of Molecular Genetics of the Czech Academy of Sciences, Vídeňská 1083, 14000, Prague 4, Czech Republic
[e] Department of Biochemistry, Faculty of Science, Charles University, Hlavova 8, 12800, Prague 2, Czech Republic

ARTICLE INFO

*Keywords:*
Antiviral peptides
Influenza a polymerase
Protein-protein interaction
AlphaScreen

ABSTRACT

Influenza viruses can cause severe respiratory infections in humans, leading to nearly half a million deaths worldwide each year. Improved antiviral drugs are needed to address the threat of development of novel pandemic strains. Current therapeutic interventions target three key proteins in the viral life cycle: neuraminidase, the M2 channel and RNA-dependent-RNA polymerase. Protein-protein interactions between influenza polymerase subunits are potential new targets for drug development. Using a newly developed assay based on AlphaScreen technology, we screened a peptide panel for protein-protein interaction inhibitors to identify a minimal PB1 subunit-derived peptide that retains high inhibition potential and can be further modified. Here, we present an X-ray structure of the resulting decapeptide bound to the C-terminal domain of PA polymerase subunit from pandemic isolate A/California/07/2009 H1N1 at 1.6 Å resolution and discuss its implications for the design of specific, potent influenza polymerase inhibitors.

## 1. ıntroduction

Influenza virus causes annual epidemics during which older adults, children, and pregnant women are at particularly high risk for developing severe disease. Influenza-related respiratory illnesses cause between 291,000 and 645,000 deaths worldwide each year, according to recent estimate (Iuliano et al., 2018).

Current strategies to fight the influenza virus are limited to seasonal vaccines and a few antiviral drugs. Seasonal influenza vaccine development is a constant struggle, as elaborate analysis must be performed to select the strains for inclusion in each year's vaccine. Current antiviral drugs have certain limitations. First-in-class drugs targeting the M2 proton channel (Symmetrel®, Flumadine®) are no longer used because of rapid resistance development (Deyde et al., 2007). Neuraminidase inhibitors (Tamiflu®, Relenza®) were later introduced to the market, and currently they are also endangered by resistance onset (Lee and Hurt, 2018). Favipiravir (T-705), an RNA-dependent-RNA polymerase inhibitor developed by Toyama Chemical and approved in Japan, is a prodrug that is converted intracellularly to its active form and incorporated into viral RNAs (Baranovich et al., 2013).

The influenza virus polymerase complex offers new viable approaches for viral targeting (Stevaert and Naesens, 2016; Zhou et al., 2018). In 2018, FDA approved baloxavir marboxil, a PA endonuclease inhibitor of host mRNA cleavage, for treatment of acute uncomplicated influenza. Other new antiviral, the compound VX-787 that functions as a PB2 cap-binding inhibitor, is now in late-stage clinical trials (Zhang et al., 2019). Furthermore, another promising drug target was identified by structural analysis of the complex of the N-terminal part of the PB1 subunit with the C-terminal domain of the PA subunit (CPA). These two proteins interact *via* an extensive interface including a well-defined hydrophobic cavity inside CPA interacting the N-terminal PB1 peptide, specifically with core $3_{10}$ helix residues in positions 5–10 (He et al.,

* Corresponding author.
*E-mail address:* milan.kozisek@uochb.cas.cz (M. Kožíšek).

https://doi.org/10.1016/j.antiviral.2020.104971
Received 20 August 2020; Received in revised form 26 October 2020; Accepted 3 November 2020
Available online 6 November 2020
0166-3542/© 2020 The Authors. Published by Elsevier B.V. This is an open access article under the CC BY license (http://creativecommons.org/licenses/by/4.0/).

2008; Obayashi et al., 2008).

Previously, site-directed mutagenesis of the core residues in the PB1 peptide revealed that this peptide is critical for the protein-protein interaction holding the polymerase complex together and that disruption of the PA-PB1 interaction can impair virus infectivity (Manz et al., 2011; Perez and Donis, 2001). Schwemmle and coworkers provided evidence that the N-terminal PB1 peptides block polymerase activity and inhibit viral replication (Ghanem et al., 2007). They identified that the first 14 amino acid peptide from the N-terminus of the PB1 subunit was a nanomolar inhibitor of the PA-PB1 interaction (Wunderlich et al., 2009), and found using a peptide array residues that improved peptide binding after mutations (Wunderlich et al., 2011).

The PA-PB1 subunit interaction is of a major interest in the drug discovery efforts because it is essential for viral replication and is conserved within a broad range of influenza A strains. In the past decade, a number of compounds predicted to inhibit the PA-PB1 interaction have been described (D'Agostino et al., 2018; Desantis et al., 2017; Lo et al., 2018; Massari et al., 2016; Nannetti et al., 2019; Trist et al., 2016; Watanabe et al., 2017; Yuan et al., 2016; Zhang et al., 2020; Zhang et al., 2018). However, there is still no direct structural evidence that they bind into the CPA pocket for PB1.

Here, we set out to describe the relative importance of the core amino acids of the PA-PB1 interaction by peptide truncation and mutational studies. We also provide X-ray structural information that could serve as a starting point for structure-assisted drug design of inhibitors of this challenging drug target.

## 2. Materials and methods

### 2.1. Cloning, expression, and purification of recombinant proteins

DNA encoding CPA from influenza strain A/California/07/2009 (H1N1) (GenBank accession No. CY121685.1) was prepared by PCR amplification from the virus. Two constructs with affinity tags were prepared. The construct for an N-terminally GST-tagged CPA was prepared by PCR amplification of segment coding amino acid region 239–716 that was inserted *via NdeI* and *BamHI* sites into plasmid pGEX1-λT previously modified (having extra *NdeI* restriction site preceding to *BamHI* site), kindly provided to us from Hans-Georg Kräusslich, University of Heidelberg, Germany. Thrombin cleavage site was added to the N-terminus of CPA for potential separation from GST fusion protein. For N-terminally $His_6$-SUMO-tagged variant of CPA, amino acid coding region 257–716 was inserted *via BamHI* and *XhoI* sites into plasmid pETM11-SUMO3 (EMBL Heidelberg).

Both CPA constructs were expressed in *E. coli* BL21 (DE3) RIL. Cells were grown in LB Broth medium (Sigma-Aldrich) at 37 °C to an $OD_{595}$ of 0.2 and then temperature was gradually decreased to 25 °C. When $OD_{595}$ reached approximately 0.8, cells were induced with 0.75 mM IPTG and shaken at 18 °C for 16 h. Cells were harvested, resuspended in lysis buffer [25 mM Tris/HCl, pH 7.5, 150 mM NaCl, 1 mM EDTA (GST) and buffer 50 mM Tris/HCl, pH 8.0, 200 mM NaCl, 10 mM imidazole ($His_6$-SUMO)], and lysed with an Emulsiflex device (Avestin) at a pressure of 1200 bar. For the GST construct, the soluble fraction of proteins was loaded onto a glutathione-agarose column (ThermoScientific) and subsequently eluted with 50 mM Tris/HCl, pH 7.5, 150 mM NaCl, 10 mM reduced L-glutathione, 1 mM EDTA. In the same manner, $His_6$-SUMO-tagged CPA was purified on Ni-NTA Agarose (Roche) and eluted with 50 mM Tris/HCl, pH 8.0, 200 mM NaCl, 250 mM imidazole followed by cleavage of the $His_6$-SUMO tag by ULP1 protease.

Both proteins were further purified by gel filtration chromatography, leading to >95% purity as assessed by SDS-PAGE.

### 2.2. Surface plasmon resonance

SPR measurements were performed as described in Supplemental Material.

### 2.3. AlphaScreen assay

AlphaScreen experiments were performed in 96-well ProxiPlates using a Perkin Elmer Enspire plate reader. Biotinylated peptide PB1 (1–25) was captured on streptavidin-coated donor beads (Perkin Elmer). A second solution contained GST-CPA fusion protein that bound to GSH-coated acceptor beads (Perkin Elmer). Mixtures were incubated for 60 min (RT) in the dark and subsequently mixed together and incubated for another 120 min while mixing. In experiments screening for peptide inhibitors, peptides were mixed with both types of beads prior to the 120-min incubation. Based on optimization experiments, we selected concentrations of 15 nM biotinylated peptide PB1(1–25) and 60 nM GST-CPA for screening experiments. Concentrations of donor and acceptor beads were 5 μg/ml in a 50 μl reaction volume. All experiments were performed in 25 mM Tris-HCl, pH 7.4, 150 mM NaCl, 0.05% Tween20. Assay evaluation was performed with **PB1-0** (MDVNPTLLFLKIPA) as well as the non-inhibitory control CAI peptide (IYDPTLYGLEFD) previously used in an AlphaScreen assay for screening HIV-1 capsid assembly inhibitors (Machara et al., 2016).

### 2.4. Protein crystallography

Purified $CPA_{257\text{-}716}$ was dialyzed into the crystallization buffer (10 mM Tris-HCl, pH 8.0, 1 mM TCEP) and concentrated to 5.5 mg/ml using Amicon 30 kDa centrifugal filter units (Merck). The protein was washed with the excess of solution of 50 μM **PB1-11** (DYNPYLLFLK) in the crystallization buffer and re-concentrated to 5.5 mg/ml in filter unit. The protein sample monodispersity was tested on DLS instrument (Laser-Spectroscatter 201, RiNA Netzwark RNA Technologien GmbH). Initial crystallization trials were performed using 6 commercial screens: Morpheus® (Molecular Dimensions), JBScreen and JCSG$^{++}$ (Jena Bioscience), PEGs Suite (QIAGEN), Crystallization Basic Kit for Proteins and Crystallization Extension Kit for Proteins (Sigma Aldrich), and Index Hampton (Hampton Research) in a vapor-diffusion setup at 18 °C. Sitting drops were made with an Oryx8 instrument (Douglas Instruments) into 96-well plates (MRC 3 well low, Swissci) in 400 nl volume with a 1:1 protein to precipitant ratio. Crystallization plates were observed using a Minstrel™ Gallery DT plate hotel (Rigaku). After several days, crystals appeared in one condition (0.1 M MOPS/HEPES, pH 7.5, 10% PEG, 20000, 20% PEG MME 550, 30 mM NaBr, 30 mM NaF, 30 mM NaI) and were used for microseed matrix-screening (D'Arcy et al., 2007). All 6 screens were used for crystallization microseed screening, and drops were set up in a 4:3:1 ratio of protein to precipitating solution to seed stock. Several conditions resulted in formation of crystals were further optimized. Crystallization optimization experiments were performed in EasyXtal 15-well plates (QIAGEN) by the vapor-diffusion hanging drop method at 18 °C. Drops of 2 μl volume were set up by mixing protein solution, precipitation solution, and seed stock in a 5:4:1 ratio; the reservoir contained 0.5 ml of precipitating solution. A crystal optimal for data collection grew in 0.1 M HEPES, pH 7.5, 35% PEG 3350. The crystal was cryoprotected by soaking in precipitation solution supplemented with 30% ethylene glycol and flash frozen in liquid nitrogen.

### 2.5. Data collection and structure determination

Diffraction data were collected at 100K on the MX14.1 beamline at the BESSY II electron storage ring, operated by the Helmholtz-Zentrum Berlin, Germany (Mueller et al., 2015). The dataset was processed using XDS and its graphical user interface, XDSAPP (Kabsch, 2010; Krug et al., 2012). The crystal parameters and data collection statistics are listed in Table S1. The structure was determined by molecular replacement with the program Molrep (Vagin and Teplyakov, 2000) using protein coordinates from PDB structure 3CM8 as a search model (He et al., 2008). Model refinement was performed using the program REFMAC 5.7.0032 (Murshudov et al., 1997) from the CCP4 package (Bailey, 1994) in

combination with manual building and adjustments in Coot software (Emsley and Cowtan, 2004). **PB1-11** was modeled in the final rounds of structure refinement. The Molprobity server (Lovell et al., 2003) was used to evaluate the final model quality. The final refinement statistics are summarized in Table S1. The structure was analyzed using the programs Lsqkab (superpose) (Krissinel and Henrick, 2004), Baverage, and Contact from the CCP4 package (Bailey, 1994).

Crystallographic model of $CPA_{257-716}$ contains one molecule in the asymmetric unit consisting residues 256–716, the N-terminal Ser256 representing a cloning artifact. Residues 373–396 and 426–440 are missing in the crystallographic model due to their dynamic disorder reflected by missing electron density maps. Additionally, side-chains of following residues could not be unambiguously modeled: Glu300, Lys328, Glu352, Lys353, Arg356, Glu372, Glu399, Met441, Arg442, Arg443, Lys492, Glu493, Arg512, Lys603, Glu604, Lys605, Lys609, Glu610, Asn614, Lys615, Lys626, Glu629, and Lys716. All residues of **PB1-11** were modeled into a well-defined electron density map at the final rounds of structure refinement.

### 2.6. Anti-influenza assays, minireplicon assay, and cell viability determination

Anti-influenza activity was measured by determining the extent to which the test peptides reduced the virus-induced cytopathic effect (CPE) or number of plaques on MDCK cells. To determine the effect of PB1 peptides on polymerase activity *in vivo*, the minireplicon assay was performed. Detailed methods are included in Supplemental Material.

### 2.7. PDB accession code

Atomic coordinates and structure factors have been deposited in the PDB under accession code **6SYI**.

## 3. Results

### 3.1. Development of an AlphaScreen assay to screen inhibitors of the PA-PB1 interaction

To screen peptide inhibitors affecting protein-protein interaction between influenza polymerase PA and PB1 subunits, we developed a new assay based on an amplified luminescent proximity assay system (AlphaScreen). The interaction of the N-terminal part of PB1 peptide on donor beads with CPA on acceptor beads brings the two beads close together. If an acceptor bead coated with glutathione peptide is in proximity upon GST-CPA/PB1-biotin interaction, energy is transferred from donor to the acceptor bead, and a signal is emitted at 520–620 nm (Fig. 1A). In the absence of an acceptor bead due to peptide inhibition of the PA-PB1 interaction, a lower signal is produced. As expected, the interaction was blocked by a peptide corresponding to the first 14 amino acids of the PB1 N-terminus (**PB1-0**) but not by a non-inhibitory control peptide (Fig. 1B). Statistical evaluation of the assay from octaplicates was performed as previously described (Zhang et al., 1999). The Z′ factor, a characteristic parameter of assay quality, was estimated to be in the range of 0.90–0.97, indicating an excellent assay performance and suitability for high-throughput screening. Surface plasmon resonance (SPR) experiments revealed a dissociation constant ($K_d$) of 23 ± 6 nM for the interaction between PB1-biotin and GST-CPA (Fig. 1C). SPR indicated specific binding of PB1-biotin to only the CPA part of the GST-CPA fusion protein (data not shown). These results validated the newly developed AlphaScreen assay for screening of inhibitors of the PA-PB1 protein-protein interaction.

### 3.2. Screening leads to identification of a decapeptide inhibitor

To determine the minimal length of PB1 peptide able to inhibit the PA-PB1 protein-protein interaction, we shortened the peptide corresponding to the first 14 amino acids of the N-terminus of PB1 (**PB1-0**). The truncated peptide sequences and their inhibition activities determined by the new AlphaScreen assay are summarized in Table 1. **PB1-0** acted as a low nanomolar inhibitor of the PA-PB1 interaction with an $IC_{50}$ value of 6 nM. Its truncation by up to four C-terminal amino acids led to a slight decrease in inhibition, with peptides **PB1-1** to **PB1-4** displaying submicromolar $IC_{50}$ values. When shortening from the N-terminus, submicromolar inhibition was observed only for peptides lacking one or two amino acids (**PB1-6** and **PB1-7**), and further truncation led to loss of inhibition potency. Next, we prepared a peptide lacking the N-terminal methionine and three amino acids at the C-terminus (**PB1-10**). However, the combination of both truncations led to further reduction in inhibition, characterized by an $IC_{50}$ of 3.4 μM. Inspired by the peptide array performed by Wunderlich et al. (2011), we

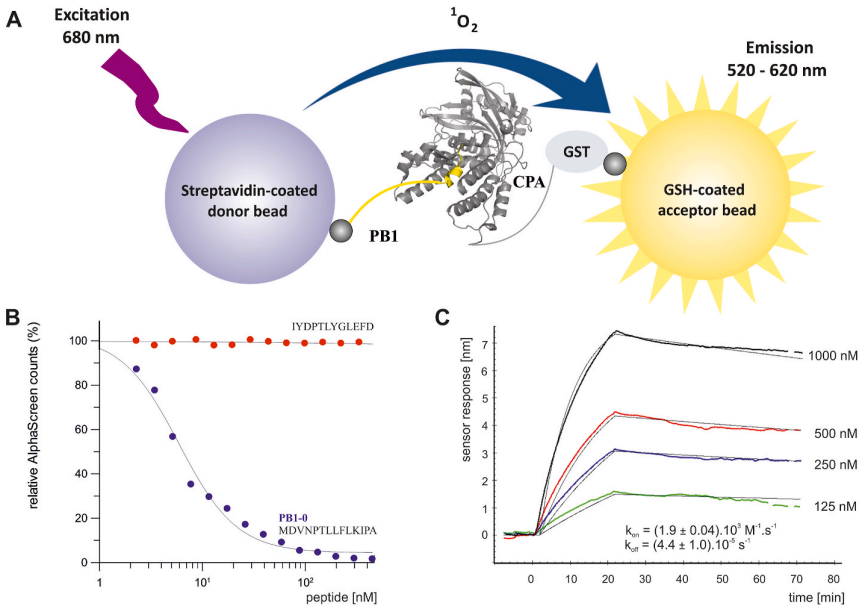


**Fig. 1. A)** Illustration of the AlphaScreen protein-protein interaction assay, using streptavidin-coated donor beads, GSH-coated acceptor beads, biotinylated PB1 peptide, and GST-tagged CPA. **B)** Titration curves of **PB1-0** (in blue) and a non-inhibitory negative control peptide (in red). **C)** Kinetic characterization of the interaction of neutravidin-biotinylated PB1 with GST-CPA measured by SPR. Each curve (in color) corresponds to a certain GST-CPA concentration. The experiment was evaluated in the TraceDrawer v.1.5 software and $k_{cat}$ and $k_{off}$ parameters of interaction were obtained by fitting the experimental curves with one-to-one model of binding (black solid lines).

**Table 1**
Inhibition potencies of truncated PB1-derived peptides ($IC_{50}$ values) determined by AlphaScreen assay. The affinity-enhancing amino acid substitutions in **PB1-11** are in bold.

| Peptide | Sequence | $IC_{50}$(α) [nM] |
|---|---|---|
| **PB1-0** | MDVNPTLLFLKIPA | 6 ± 1 |
| **PB1-1** | MDVNPTLLFLKIP | 22 ± 1 |
| **PB1-2** | MDVNPTLLFLKI | 39 ± 4 |
| **PB1-3** | MDVNPTLLFLK | 130 ± 20 |
| **PB1-4** | MDVNPTLLFL | 440 ± 40 |
| **PB1-5** | MDVNPTLLF | 7,200 ± 1,000 |
| **PB1-6** | DVNPTLLFLKIPA | 33 ± 3 |
| **PB1-7** | VNPTLLFLKIPA | 390 ± 50 |
| **PB1-8** | NPTLLFLKIPA | 20,200 ± 1,700 |
| **PB1-9** | PTLLFLKIPA | 36,000 ± 4,000 |
| **PB1-10** | DVNPTLLFLK | 3,400 ± 300 |
| **PB1-11** | D**Y**NP**Y**LLFLK | 13 ± 1 |

introduced into the **PB1-10** sequence two tyrosine residues into positions 3 and 6 that were reported as the most significantly influencing amino acid substitutions (**PB1-11**). These two substitutions led to substantial improvement in inhibition activity, resulting in an $IC_{50}$ of 13 nM.

### 3.3. X-ray structural analysis shows that the minimal PB1 peptide binds into the CPA pocket

To evaluate whether the binding of the modified **PB1-11** peptide was structurally consistent with previously published structures of the PA-PB1 interface (He et al., 2008; Obayashi et al., 2008), we crystallized a complex of CPA with the peptide (Fig. 2A). Crystals exhibited $P2_12_12_1$ symmetry and diffracted up to 1.6 Å. The asymmetric unit contained one CPA molecule, and all **PB1-11** residues could be modeled into well-defined electron density.

Comparison of the **PB1-11** complex structure with the previously published structure of the 25-residue PB1 peptide bound to CPA (He et al., 2008) revealed a nearly identical binding mode (Fig. 2B). Superposition of **PB1-11** with PB1, both in complex with CPA, gave an RMSD of 0.44 Å for 77 corresponding atoms. The two tyrosine residues newly introduced into the **PB1-11** sequence are involved in interactions that were not observed for PB1. Specifically, the hydroxyl group of Tyr3 forms a water-mediated hydrogen bond with the ε-amino group of Arg638 and the main-chain carboxyl of Cys415 (Fig. 2C). The hydroxyl group of Tyr6 forms one direct hydrogen bond with the δ-amino group of Asn703 and one water-mediated hydrogen bond with the hydroxyl group of Ser659 (Fig. 2D).

### 3.4. Minimal PB1 peptides are active against influenza in vitro

To evaluate the *in vivo* activity of the peptides, we modified them by adding the cell-penetrating Tat peptide to either the C-terminus or N-terminus (Qian et al., 2014; Wunderlich et al., 2009). To assess the effect of Tat addition on the protein-peptide interaction, we used the AlphaScreen method to determine the binding of peptides **PB1-0**, **PB1-10**, **PB1-11**, and their Tat-conjugated variants (Table 2). C-terminal conjugation did not impact peptide binding *in vitro*.

The inhibitory capabilities of the peptides were evaluated with three cell-based approaches. Initially, we tested the ability of the peptides to inhibit influenza RNA polymerase in a minireplicon assay. In this assay, peptides were added to HEK293T cells co-transfected with a plasmid encoding polymerase subunits PA, PB1, and PB2 together with nucleoprotein and a luciferase reporter plasmid containing an influenza viral minigenome. To block viral RNA transcription in the minireplicon assay,

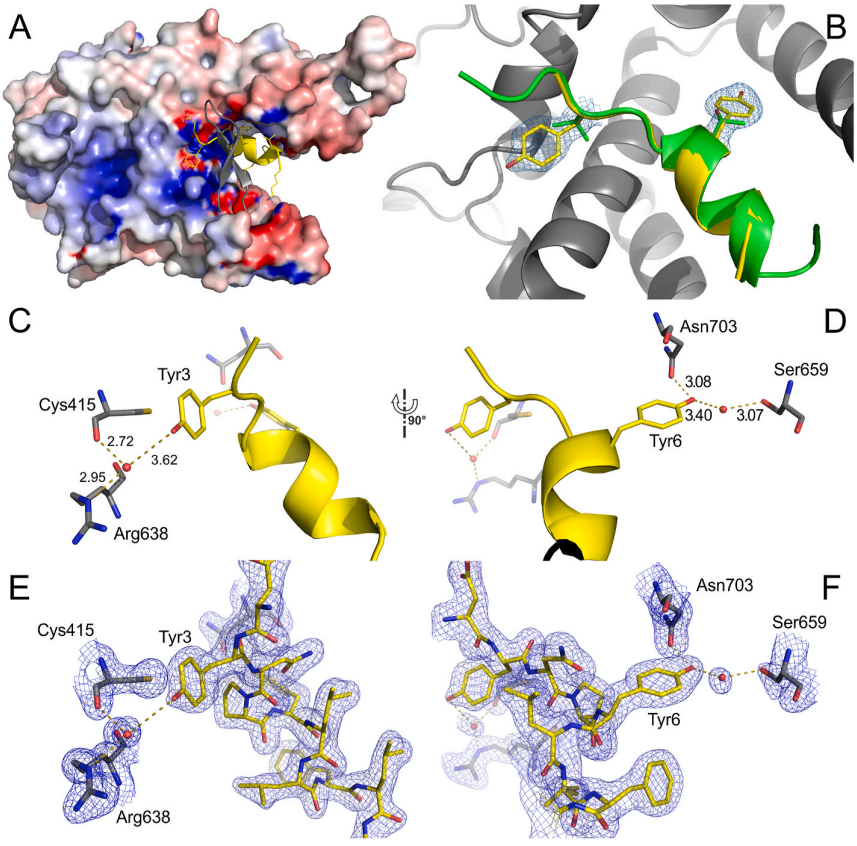


**Fig. 2.** Structure of CPA-binding peptide **PB1-11**. **A)** Overall structure of the CPA and **PB1-11** complex. CPA is shown in a surface representation and colored according to its electrostatic potential (red −10 kT/e, blue +10 kT/e) (Baker et al., 2001; Dolinsky et al., 2004; Unni et al., 2011). The protein flap (sequence 616–633) covering the binding pocket is shown in a gray cartoon representation to allow view on the peptide binding interface. **PB1-11** is colored yellow and shown in a cartoon with side-chains as sticks. **B)** Superposition of **PB1-11** with PB1 (3CM8) (He et al., 2008). The Tyr3 and 6 side chains are highlighted as sticks with the $2F_o$-$F_c$ electron density (contoured at 1σ) shown as a blue mesh. **C), D), E) and F)** Dashed lines indicate direct and water-mediated polar interactions between Tyr side-chains and CPA. Water molecules are shown as red spheres. Numbers indicate the distances in Å between a hydrogen bond donor and acceptor. **PB1-11** peptide represented by cartoon and sticks model is colored yellow. CPA interacting amino acid residues are shown in gray. $2F_o$-$F_c$ electron density contoured at 1σ is shown as a blue mesh.

**Table 2**
Activity and toxicity of PB1 peptides and their Tat-conjugated forms.

| Peptide | Sequence | $IC_{50}$ [μM] AlphaScreen | $EC_{50}$ [μM] minireplicon | $CC_{50}$ [μM] HEK293T | $EC_{50}$ [μM] plaque assay | $EC_{50}$ [μM] CPE assay | $CC_{50}$ [μM] MDCK |
|---|---|---|---|---|---|---|---|
| **PB1-0** | H-MDVNPTLLFLKIPA-$NH_2$ | 0.006 ± 0.001 | >200 | >200 | >200 | >200 | >200 |
| **PB1-0-Tat** | Ac-MDVNPTLLFLKIPA-YGRKKRRQRRRPP-$NH_2$ | 0.010 ± 0.001 | 69 ± 12 | 51 ± 8 | >200 | >200 | >200 |
| **Tat-PB1-0** | Ac-RKKRRQRRR-MDVNPTLLFLKIPA-$NH_2$ | 0.33 ± 0.15 | 9.2 ± 1.2 | 83 ± 2 | 130 ± 15 | >200 | >200 |
| **PB1-10** | H-DVNPTLLFLK-$NH_2$ | 3.4 ± 0.3 | 40 ± 12 | >200 | 100 ± 32 | 23 ± 5 | >200 |
| **PB1-10-Tat** | Ac-DVNPTLLFLK-YGRKKRRQRRRPP-$NH_2$ | 14 ± 1 | 10 ± 2 | 81 ± 6 | 130 ± 45 | 140 ± 13 | >200 |
| **Tat-PB1-10** | Ac-RKKRRQRRR-DVNPTLLFLK-$NH_2$ | >100 | 190 ± 31 | >200 | >200 | >200 | >200 |
| **PB1-11** | H-D**Y**NP**Y**LLFLK-$NH_2$ | 0.013 ± 0.001 | 39 ± 10 | >200 | 160 ± 53 | 87 ± 24 | >200 |
| **PB1-11-Tat** | Ac-D**Y**NP**Y**LLFLK-YGRKKRRQRRRPP-$NH_2$ | 0.011 ± 0.001 | 80 ± 11 | >200 | >200 | >200 | >200 |
| **Tat-PB1-11** | Ac-RKKRRQRRR-D**Y**NP**Y**LLFLK-$NH_2$ | 0.11 ± 0.04 | 96 ± 11 | >200 | 160 ± 30 | >200 | >200 |
| **Favipiravir** | | n.d. | 14 ± 2 | >200 | 2.9 ± 0.6 | 3.4 ± 0.6 | >200 |

the peptides must not only bind efficiently to the PA-PB1 interface but also possess good cellular bioavailability. Indeed, **PB1-0** inhibited viral RNA transcription only after attachment of the cell-penetrating Tat peptide (Table 2). Interestingly, linking Tat to the N-terminus of **PB1-0** increased inhibition potency more than seven-fold, with no increase in cytotoxicity compared with the C-terminal Tat modification. Truncation of **PB1-0** to the decapeptide **PB1-10** yielded higher cellular bioavailability and inhibition of viral RNA transcription. Moreover, attachment of Tat to the C-terminus resulted in an additional four-fold increase in inhibition, resulting in an $EC_{50}$ value comparable to the result from AlphaScreen. Introduction of two tyrosine residues and addition of Tat on either terminus did not considerably improve the inhibition of influenza RNA polymerase in the minireplicon assay.

Next, we analyzed the ability of the peptides to inhibit influenza virus in a plaque reduction assay. In this fully infectious assay, MDCK cells are infected with influenza A H1N1 virus, unbound virus is removed by extensive washing, and peptides are added onto cells. Both **PB1-10** and **PB1-11** were able to reduce the number of plaques, illustrating that inhibition of PA-PB1 interactions results in influenza virus reduction in cell culture (Table 2). Attachment of Tat on either terminus did not improve the inhibition activity of **PB1-10** or **PB1-11**. However, by modifying **PB1-0** with Tat on the N-terminus, we were able to improve influenza virus inhibition to similar moderate levels as for **PB1-10** and **PB1-11**.

Finally, we used an additional infectious assay to confirm the ability of the peptides to inhibit influenza virus in cell culture. In this assay, MDCK cells were pre-treated with the peptides prior to infection with influenza A H1N1 virus. In accord with the plaque reduction assay results, the truncated peptides **PB1-10** and **PB1-11** were able to reduce influenza virus-induced CPE (Table 2). The **PB1-10** peptide exhibited an almost four-fold higher inhibitory effect than **PB1-11.** With an $EC_{50}$ of 23 μM, **PB1-10** exhibited roughly 10-fold weaker inhibition activity than favipiravir, a known inhibitor of influenza virus RNA polymerase used as a control. Addition of Tat to either terminus did not improve the inhibitory activity of **PB1-0**, and the same modifications of **PB1-10** and **PB1-11** reduced inhibition. In contrast to HEK293T cells, uninfected MDCK cells tolerated all modified and unmodified peptides at concentrations up to 200 μM.

## 4. Discussion

Our major aim was to identify the minimal peptide sequence sufficient to inhibit the interaction between the PA and PB1 influenza RNA polymerase subunits. Truncation of **PB1-0** from both N- and C-termini led to the decapeptide **PB1-10** with a low micromolar $IC_{50}$ in the AlphaScreen assay. Introduction of two affinity-enhancing substitutions at positions 3 and 6, yielding **PB1-11**, led to substantial improvement in binding affinity ($IC_{50}$ of 13 nM). Our high-resolution crystal structure revealed a structural basis for the affinity increase: the tyrosine side chains in **PB1-11** form direct and water-mediated hydrogen bonds with Cys415, Arg638, Ser659, and Asn703.

The protein-protein interactions generally represent challenging targets for small-molecule inhibitors, since contact surfaces are usually large and flat. In this work, we have shown that a relatively short peptide is capable of strong interaction within the cavity of the CPA subunit. However, commonly used association with cell-penetrating peptide does not help to deliver the linear short peptide through the cell wall and fails to provide an effective antiviral *in vivo*. Kidney epithelial cells, HEK293T and MDCK, belong in general to more difficult cell lines for cell-penetrating peptide-based delivery (Patel et al., 2019; Zhang et al., 2004). Based on knowledge from the peptidomimetics research, new nanomolar decapeptide inhibitor **PB1-11** could be improved by conversion into peptidomimetics with better metabolic stability and membrane permeability. The incorporation of unnatural amino acids into a peptide, further hot-spots optimization and peptide cyclization could improve its *in vivo* efficacy, and might open up new directions for following research.

In summary, we developed a new assay to screen inhibitors of the

protein-protein interaction between two influenza polymerase subunits and used it to determine a minimal PB1 peptide sequence with nanomolar binding affinity for CPA. We co-crystallized this minimal peptide in complex with CPA and determined the crystal structure at high resolution. This active peptide can serve as a lead for structure-based drug design of a new type of anti-influenza drug.

## Declaration of competing interest

The authors declare that there is no conflict of interest regarding the publication of this paper.

## Acknowledgements

The authors wish to thank Iva Flaisigová for technical assistance and Hillary Hoffman for proofreading of the manuscript. Diffraction data were collected on BL14.1 at the BESSY II electron storage ring operated by the Helmholtz-Zentrum Berlin. This work was supported by the European Regional Development Fund; OP RDE; Project: "Chemical biology for drugging undruggable targets (ChemBioDrug)" (No. CZ.02.1.01/0.0/0.0/16_019/0000729) and The Czech National Node to the European Infrastructure for Translational Medicine EATRIS-CZ, grant No. LM2018133.

## Appendix A. Supplementary data

Supplementary data to this article can be found online at https://doi.org/10.1016/j.antiviral.2020.104971.

## References

Bailey, S., 1994. The Ccp4 suite - programs for protein crystallography. Acta Crystallogr. Sect. D Biol. Crystallogr. 50, 760–763.
Baker, N.A., Sept, D., Joseph, S., Holst, M.J., McCammon, J.A., 2001. Electrostatics of nanosystems: application to microtubules and the ribosome. Proc. Natl. Acad. Sci. U. S. A. 98, 10037–10041.
Baranovich, T., Wong, S.S., Armstrong, J., Marjuki, H., Webby, R.J., Webster, R.G., Govorkova, E.A., 2013. T-705 (favipiravir) induces lethal mutagenesis in influenza A H1N1 viruses in vitro. J. Virol. 87, 3741–3751.
D'Agostino, I., Giacchello, I., Nannetti, G., Fallacara, A.L., Deodato, D., Musumeci, F., Grossi, G., Palu, G., Cau, Y., Trist, I.M., Loregian, A., Schenone, S., Botta, M., 2018. Synthesis and biological evaluation of a library of hybrid derivatives as inhibitors of influenza virus PA-PB1 interaction. Eur. J. Med. Chem. 157, 743–758.
D'Arcy, A., Villard, F., Marsh, M., 2007. An automated microseed matrix-screening method for protein crystallization. Acta Crystallogr D Biol Crystallogr 63, 550–554.
Desantis, J., Nannetti, G., Massari, S., Barreca, M.L., Manfroni, G., Cecchetti, V., Palu, G., Goracci, L., Loregian, A., Tabarrini, O., 2017. Exploring the cycloheptathiophene-3-carboxamide scaffold to disrupt the interactions of the influenza polymerase subunits and obtain potent anti-influenza activity. Eur. J. Med. Chem. 138, 128–139.
Deyde, V.M., Xu, X., Bright, R.A., Shaw, M., Smith, C.B., Zhang, Y., Shu, Y., Gubareva, L. V., Cox, N.J., Klimov, A.I., 2007. Surveillance of resistance to adamantanes among influenza A(H3N2) and A(H1N1) viruses isolated worldwide. J. Infect. Dis. 196, 249–257.
Dolinsky, T.J., Nielsen, J.E., McCammon, J.A., Baker, N.A., 2004. PDB2PQR: an automated pipeline for the setup of Poisson-Boltzmann electrostatics calculations. Nucleic Acids Res. 32, W665–W667.
Emsley, P., Cowtan, K., 2004. Coot: model-building tools for molecular graphics. Acta Crystallogr. D 60, 2126–2132.
Ghanem, A., Mayer, D., Chase, G., Tegge, W., Frank, R., Kochs, G., Garcia-Sastre, A., Schwemmle, M., 2007. Peptide-mediated interference with influenza A virus polymerase. J. Virol. 81, 7801–7804.
He, X.J., Zhou, J., Bartlam, M., Zhang, R.G., Ma, J.Y., Lou, Z.Y., Li, X.M., Li, J.J., Joachimiak, A., Zeng, Z.H., Ge, R.W., Rao, Z.H., Liu, Y.F., 2008. Crystal structure of the polymerase PA(C)-PB1(N) complex from an avian influenza H5N1 virus. Nature 454, 1123–U1151.
Iuliano, A.D., Roguski, K.M., Chang, H.H., Muscatello, D.J., Palekar, R., Tempia, S., Cohen, C., Gran, J.M., Schanzer, D., Cowling, B.J., Wu, P., Kyncl, J., Ang, L.W., Park, M., Redlberger-Fritz, M., Yu, H., Espenhain, L., Krishnan, A., Emukule, G., van Asten, L., Pereira da Silva, S., Aungkulanon, S., Buchholz, U., Widdowson, M.A., Bresee, J.S., Global Seasonal Influenza-associated Mortality Collaborator, N, 2018. Estimates of global seasonal influenza-associated respiratory mortality: a modelling study. Lancet 391, 1285–1300.
Kabsch, W., 2010. Xds. Acta Crystallogr D Biol Crystallogr 66, 125–132.
Krissinel, E., Henrick, K., 2004. Secondary-structure matching (SSM), a new tool for fast protein structure alignment in three dimensions. Acta Crystallogr. D 60, 2256–2268.
Krug, M., Weiss, M.S., Heinemann, U., Mueller, U., 2012. XDSAPP: a graphical user interface for the convenient processing of diffraction data using XDS. J. Appl. Crystallogr. 45, 568–572.
Lee, N., Hurt, A.C., 2018. Neuraminidase inhibitor resistance in influenza: a clinical perspective. Curr. Opin. Infect. Dis. 31, 520–526. https://doi.org/10.1097/QCO.0000000000000498. https://pubmed.ncbi.nlm.nih.gov/30299356/.
Lo, C.Y., Li, O.T., Tang, W.P., Hu, C., Wang, G.X., Ngo, J.C., Wan, D.C., Poon, L.L., Shaw, P.C., 2018. Identification of influenza polymerase inhibitors targeting C-terminal domain of PA through surface plasmon resonance screening. Sci. Rep. 8, 2280.
Lovell, S.C., Davis, I.W., Adrendall, W.B., de Bakker, P.I.W., Word, J.M., Prisant, M.G., Richardson, J.S., Richardson, D.C., 2003. Structure validation by C alpha geometry: phi,psi and C beta deviation. Proteins Struct. Funct. Genet. 50, 437–450.
Machara, A., Lux, V., Kozisek, M., Saskova, K.G., Stepanek, O., Kotora, M., Parkan, K., Pavova, M., Glass, B., Sehr, P., Lewis, J., Mueller, B., Kraeusslich, H.-G., Konvalinka, J., 2016. Specific inhibitors of HIV capsid assembly binding to the C-terminal domain of the capsid protein: evaluation of 2-arylquinazolines as potential antiviral compounds. J. Med. Chem. 59, 545–558.
Manz, B., Gotz, V., Wunderlich, K., Eisel, J., Kirchmair, J., Stech, J., Stech, O., Chase, G., Frank, R., Schwemmle, M., 2011. Disruption of the viral polymerase complex assembly as a novel approach to attenuate influenza A virus. J. Biol. Chem. 286, 8414–8424.
Massari, S., Goracci, L., Desantis, J., Tabarrini, O., 2016. Polymerase acidic protein-basic protein 1 (PA-PB1) protein-protein interaction as a target for next-generation anti-influenza therapeutics. J. Med. Chem. 59, 7699–7718.
Mueller, U., Forster, R., Hellmig, M., Huschmann, F.U., Kastner, A., Malecki, P., Puhringer, S., Rower, M., Sparta, K., Steffien, M., Uhlein, M., Wilk, P., Weiss, M.S., 2015. The macromolecular crystallography beamlines at BESSY II of the Helmholtz-Zentrum Berlin: current status and perspectives. Eur Phys J Plus 130.
Murshudov, G.N., Vagin, A.A., Dodson, E.J., 1997. Refinement of macromolecular structures by the maximum-likelihood method. Acta Crystallogr. D 53, 240–255.
Nannetti, G., Massari, S., Mercorelli, B., Bertagnin, C., Desantis, J., Palu, G., Tabarrini, O., Loregian, A., 2019. Potent and broad-spectrum cycloheptathiophene-3-carboxamide compounds that target the PA-PB1 interaction of influenza virus RNA polymerase and possess a high barrier to drug resistance. Antivir. Res. 165, 55–64. https://doi.org/10.1016/j.antiviral.2019.03.003. https://pubmed.ncbi.nlm.nih.gov/30885750/.
Obayashi, E., Yoshida, H., Kawai, F., Shibayama, N., Kawaguchi, A., Nagata, K., Tame, J. R., Park, S.Y., 2008. The structural basis for an essential subunit interaction in influenza virus RNA polymerase. Nature 454, 1127–1131.
Patel, S.G., Sayers, E.J., He, L., Narayan, R., Williams, T.L., Mills, E.M., Allemann, R.K., Luk, L.Y.P., Jones, A.T., Tsai, Y.H., 2019. Cell-penetrating peptide sequence and modification dependent uptake and subcellular distribution of green florescent protein in different cell lines. Sci. Rep. 9, 6298.
Perez, D.R., Donis, R.O., 2001. Functional analysis of PA binding by influenza a virus PB1: effects on polymerase activity and viral infectivity. J. Virol. 75, 8127–8136.
Qian, Z., LaRochelle, J.R., Jiang, B., Lian, W., Hard, R.L., Selner, N.G., Luechapanichkul, R., Barrios, A.M., Pei, D., 2014. Early endosomal escape of a cyclic cell-penetrating peptide allows effective cytosolic cargo delivery. Biochemistry 53, 4034–4046.
Stevaert, A., Naesens, L., 2016. The influenza virus polymerase complex: an update on its structure, functions, and significance for antiviral drug design. Med. Res. Rev. 36, 1127–1173.
Trist, I.M., Nannetti, G., Tintori, C., Fallacara, A.L., Deodato, D., Mercorelli, B., Palu, G., Wijtmans, M., Gospodova, T., Edink, E., Verheij, M., de Esch, I., Viteva, L., Loregian, A., Botta, M., 2016. 4,6-Diphenylpyridines as promising novel anti-influenza agents targeting the PA-PB1 protein-protein interaction: structure-activity relationships exploration with the aid of molecular modeling. J. Med. Chem. 59, 2688–2703.
Unni, S., Huang, Y., Hanson, R.M., Tobias, M., Krishnan, S., Li, W.W., Nielsen, J.E., Baker, N.A., 2011. Web servers and services for electrostatics calculations with APBS and PDB2PQR. J. Comput. Chem. 32, 1488–1491.
Vagin, A., Teplyakov, A., 2000. An approach to multi-copy search in molecular replacement. Acta Crystallogr D Biol Crystallogr 56, 1622–1624.
Watanabe, K., Ishikawa, T., Otaki, H., Mizuta, S., Hamada, T., Nakagaki, T., Ishibashi, D., Urata, S., Yasuda, J., Tanaka, Y., Nishida, N., 2017. Structure-based drug discovery for combating influenza virus by targeting the PA-PB1 interaction. Sci. Rep. 7, 9500.
Wunderlich, K., Juozapaitis, M., Ranadheera, C., Kessler, U., Martin, A., Eisel, J., Beutling, U., Frank, R., Schwemmle, M., 2011. Identification of high-affinity PB1-derived peptides with enhanced affinity to the PA protein of influenza A virus polymerase. Antimicrob. Agents Chemother. 55, 696–702.
Wunderlich, K., Mayer, D., Ranadheera, C., Holler, A.S., Manz, B., Martin, A., Chase, G., Tegge, W., Frank, R., Kessler, U., Schwemmle, M., 2009. Identification of a PA-binding peptide with inhibitory activity against influenza A and B virus replication. PloS One 4, e7517.
Yuan, S., Chu, H., Zhao, H., Zhang, K., Singh, K., Chow, B.K., Kao, R.Y., Zhou, J., Zheng, B.J., 2016. Identification of a small-molecule inhibitor of influenza virus via disrupting the subunits interaction of the viral polymerase. Antivir. Res. 125, 34–42.
Zhang, J., Hu, Y., Musharrafieh, R., Yin, H., Wang, J., 2019. Focusing on the influenza virus polymerase complex: recent progress in drug discovery and assay development. Curr. Med. Chem. 26, 2243–2263.
Zhang, J., Hu, Y., Wu, N., Wang, J., 2020. Discovery of influenza polymerase PA-PB1 interaction inhibitors using an in vitro split-luciferase complementation-based assay. ACS Chem. Biol. 15, 74–82.

Zhang, J.H., Chung, T.D.Y., Oldenburg, K.R., 1999. A simple statistical parameter for use in evaluation and validation of high throughput screening assays. J. Biomol. Screen 4, 67–73.

Zhang, J.T., Hu, Y.M., Foley, C., Wang, Y.X., Musharrafieh, R., Xu, S.T., Zhang, Y.T., Ma, C.L., Hulme, C., Wang, J., 2018. Exploring ugi-azide four-component reaction products for broad-spectrum influenza antivirals with a high genetic barrier to drug resistance. Sci. Rep. 8.

Zhang, X., Wan, L., Pooyan, S., Su, Y., Gardner, C.R., Leibowitz, M.J., Stein, S., Sinko, P. J., 2004. Quantitative assessment of the cell penetrating properties of RI-Tat-9: evidence for a cell type-specific barrier at the plasma membrane of epithelial cells. Mol. Pharm. 1, 145–155.

Zhou, Z., Liu, T., Zhang, J., Zhan, P., Liu, X., 2018. Influenza A virus polymerase: an attractive target for next-generation anti-influenza therapeutics. Drug Discov. Today 23, 503–518. https://doi.org/10.1016/j.drudis.2018.01.028. https://pubmed.ncbi.nlm.nih.gov/29339107/.

## 3.4. PUBLICATION II.

**Thermodynamic and structural characterization of an optimized peptide-based inhibitor of the influenza polymerase PA-PB1 subunit interaction**

In the light of recent years, there is no need to say that pandemic influenza outbreak caused by newly reassortment viruses could have disastrous global impact. Any effort for novel antiviral drugs as well as improved vaccines is necessary. The influenza RdRp heterotrimer is considered one of the anti-influenza drug targets. It was described that its assembly depends on highly conserved protein-protein interaction between the PA and PB1 subunit. At 2008 ((He et al., 2008; Obayashi et al., 2008)) the first structure of PA C-terminal domain (CPA) with a small peptide derived from the N-terminus of PB1 subunit was solved. The interaction became a potential drug target. It is particularly formed by the peptide core $3_{10}$ helix at positions 5-10. Disrupting such a small interaction with any compound and therefore prohibiting the whole heterotrimeric complex to assemble would be one small step ahead to a successful drug development.

### 3.4.1. SUMMARY

Predate to this manuscript we have published a decapeptide able to bind in the CPA cleft at nanomolar affinity (see manuscript **I.**). Within the PB1 N-terminal-derived peptide, three "hot-spots" were described. Their substitution could lead to better inhibitory potency as well as peptide solubility. To explore this hypothesis, we have further optimized decapeptide "hot-spots" and used the AlphaScreen assay for measurement of inhibitory potency. Compared to the previously published peptide DYNPYLLFLK (**PB1-11**), the final sequence DYNPYLLYLK (**PB1-19**, "hot-spots" underlined) had two times lower half maximal inhibitory concentration. However, the main advantage of this peptide was its highly improved solubility. This enabled the first thermodynamic characterization of **PB1-19** to the CPA. The dissociation constant of **PB1-19** binding to CPA was estimated to be 1.7 nM. To get details of the decapeptide-protein interaction, we have co-crystallized CPA with **PB1-19**. Finally, we achieved protein crystals diffracting at 1.9 Å resolution. The intracellular delivery of peptides is usually quite difficult. Therefore, we have used recently published bicyclic strategy which improved the inhibition in the cell-based assay (**Figure 15**). One part of the bicyclic peptide contains the cell-penetrating peptide (CPP). The whole complex is via CPP endosomally internalized. The bicyclic peptide then escapes the early endosome and intracellular glutathione reduces disulfide bonds. With this, the linear peptide **PB1-19** with CPP at N-terminus

is released into the cytosol and can inhibit the PA-PB1 assembly. Also, the bicyclic strategy prolonged the peptide stability in human plasma and increased biovailibility. We have characterized the bicyclic **PB1-19B** peptide as a low micromolar inhibitor in CPE antiviral testing.

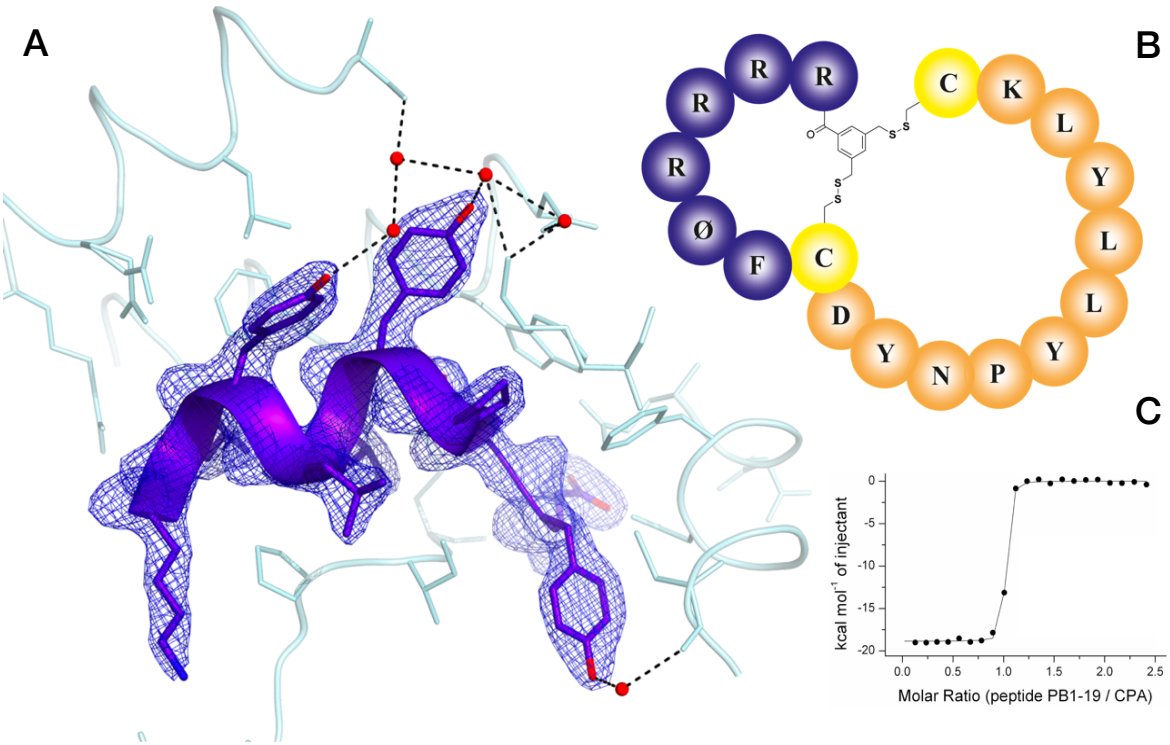


**Figure 15. A)** Crystal structure of decapeptide **PB1-19** in the CPA cleft. Water molecules forming hydrogen bonds with the protein and decapeptide are shown as red spheres. **B)** Schematic representation of bicyclic strategy for intracellular delivery. CPP sequence is shown in dark-blue beads; **PB1-19** is presented as orange beads. **C)** The calorimetric titration curve from integrated peaks of CPA with **PB1-19** in Tris-HCl buffer.

my contribution

I expressed the CPA domain of influenza A RdRp in *E.coli*, purified the protein and set up initial crystallization conditions. I optimized crystallization conditions in several steps. In few days to two weeks, small crystals grew and I obtained larger protein crystals (~200 μm). I collected X-ray diffraction data at BESSY II synchrotron Macromolecular X-ray Structure Analysis (MX) beamline 1 (Helmholtz-Zentrum, Berlin), processed the data and solved the protein-peptide structure. After several steps of refinement, the structure was released under PDB ID: **7ZPY**. I compared two CPA structures with either **PB1-11** and **PB1-19**.

**"Thermodynamic and structural characterization of an optimized peptide-based inhibitor of the influenza polymerase PA-PB1 subunit interaction.**" *Antiviral Research 208* (December 2022): 105449. doi: 10.1016/j.antiviral.2022.105449.

Antiviral Research 208 (2022) 105449

Contents lists available at ScienceDirect

Antiviral Research

journal homepage: www.elsevier.com/locate/antiviral

# Thermodynamic and structural characterization of an optimized peptide-based inhibitor of the influenza polymerase PA-PB1 subunit interaction

Kateřina Radilová [a,b], Václav Zima [a,c], Michal Kráľ [a,b], Aleš Machara [a,*], Pavel Majer [a], Jan Hodek [a], Jan Weber [a], Jiří Brynda [a], Timotej Strmeň [a], Jan Konvalinka [a,d], Milan Kožíšek [a,*]

[a] Institute of Organic Chemistry and Biochemistry of the Czech Academy of Sciences, Flemingovo n. 2, 16610, Prague 6, Czech Republic
[b] First Faculty of Medicine, Charles University, Kateřinská 1660/32, 12108, Prague, 2, Czech Republic
[c] Department of Organic Chemistry, Faculty of Science, Charles University, Hlavova 8, 12800, Prague, 2, Czech Republic
[d] Department of Biochemistry, Faculty of Science, Charles University, Hlavova 8, 12800, Prague, 2, Czech Republic

ARTICLE INFO

*Keywords:*
Antiviral peptides
Influenza A polymerase
Protein-protein interaction
AlphaScreen
Isothermal titration calorimetry

ABSTRACT

Influenza virus causes severe respiratory infection in humans. Current antivirotics target three key proteins in the viral life cycle: neuraminidase, the M2 channel and the endonuclease domain of RNA-dependent-RNA polymerase. Due to the development of novel pandemic strains, additional antiviral drugs targetting different viral proteins are still needed. The protein-protein interaction between polymerase subunits PA and PB1 is one such possible target. We recently identified a modified decapeptide derived from the N-terminus of the PB1 subunit with high affinity for the C-terminal part of the PA subunit. Here, we optimized its amino acid hotspots to maintain the inhibitory potency and greatly increase peptide solubility. This allowed thermodynamic characterization of peptide binding to PA. Solving the X-ray structure of the peptide-PA complex provided structural insights into the interaction. Additionally, we optimized intracellular delivery of the peptide using a bicyclic strategy that led to improved inhibition in cell-based assays.

## 1. Introduction

Influenza virus is a major human pathogen, easily spread from person to person during seasonal epidemics, that causes disease of the upper respiratory tract. Influenza-related respiratory illnesses cause up to 640,000 deaths worldwide each year (Iuliano et al., 2018). Due to its high virulence and mutation rate, influenza virus remains a major threat to public health. Annual vaccines targeting the seasonal flu cannot replace anti-influenza drugs, especially in the event of unexpected influenza pandemics.

Currently, several antiviral drugs are available, but certain limitations remain. Drugs targeting the M2 proton channel (Symmetrel®, Flumadine®) are no longer in clinical use, due to rapid resistance development (Jalily et al., 2020; Wang et al., 2015; Deyde et al., 2007). Other commercial antivirals inhibit viral release from the host cells by targeting neuraminidase (Tamiflu®, Relenza®), although their usefulness can be compromised by the emergence and spread of a drug-resistant virus (Lee and Hurt, 2018). Favipiravir (T-705) is approved in Japan to treat influenza and infections caused by other RNA viruses (Shiraki and Daikoku, 2020). However, due to evidence suggesting that favipiravir shows teratogenicity and embryo toxicity (Agrawal et al., 2020; Hurt, 2019), its more widespread use is unlikely (Duwe et al., 2021).

As influenza virus RNA-dependent RNA polymerase (RdRp) is a heterotrimeric complex, it offers many potential approaches for pharmaceutical targeting (Stevaert and Naesens, 2016; Zhou et al., 2018; Zhang et al., 2019). Each subunit of the RdRp is crucial for both viral replication and transcription. The FDA-approved drug baloxavir marboxil inhibits the RdRp polymerase acidic (PA) subunit. It prevents the cleavage of host mRNA by the PA endonuclease and is recommended for treatment of acute and uncomplicated influenza (Ng, 2019). Another compound targeting RdRp, VX-787, acts as a polymerase basic 2 (PB2) subunit cap-binding inhibitor (Zhang et al., 2019), although clinical trials were terminated in 2021, due to insufficient effect compared to currently available standard care.

In 2008, determination of the structure of the C-terminal domain of

** Corresponding authors. Institute of Organic Chemistry and Biochemistry of the Czech Academy of Sciences, Czech Republic.
*E-mail addresses:* ales.machara@uochb.cas.cz (A. Machara), milan.kozisek@uochb.cas.cz (M. Kožíšek).

https://doi.org/10.1016/j.antiviral.2022.105449
Received 24 August 2022; Received in revised form 10 October 2022; Accepted 13 October 2022
Available online 17 October 2022
0166-3542/© 2022 The Authors. Published by Elsevier B.V. This is an open access article under the CC BY license (http://creativecommons.org/licenses/by/4.0/).

PA (CPA) in complex with a fragment of the PB1 subunit illustrated a novel target for drug development (He et al., 2008; Obayashi et al., 2008). These two proteins interact via an extensive interface, including a hydrophobic cavity in CPA and the N-terminal PB1 peptide (Fig. 1). This interaction, including a $3_{10}$ helix, is necessary for complex assembly, and its disruption leads to reduced virus infectivity (Perez and Donis, 2001; Manz et al., 2011). The first peptide capable of preventing heterotrimer assembly and inhibiting viral replication at nanomolar concentrations was derived from the PB1 subunit (Wunderlich et al., 2009).

The protein-protein interaction (PPI) between the RdRp PA and PB1 subunits is also promising as a target for drug development because of its high conservation among influenza strains. Numerous compounds have been predicted to inhibit heterotrimer assembly at the PA-PB1 interaction site (D'Agostino et al., 2018; Desantis et al., 2017; Lo et al., 2018; Massari et al., 2016; Nannetti et al., 2019; Trist et al., 2016; Watanabe et al., 2017; Yuan et al., 2017; Zhang et al., 2020; Zhang et al., 2018), but no structure of a protein-compound complex has been reported.

We previously developed an assay suitable for PPI inhibition screening based on AlphaScreen technology (Hejdanek et al., 2021) and identified a decapeptide derived from the N-terminus of the PB1 subunit that inhibits RdRp at micromolar concentrations. Furthermore, we optimized the amino-acid "hotspots", which improved the interaction affinity (Wunderlich et al., 2011).

Here, we optimized the decapeptide sequence, which vastly improved its solubility and preserved inhibitory potency. This enabled us to determine the thermodynamics of protein-peptide binding by isothermal titration calorimetry (ITC). The optimized decapeptide was characterized as a high affinity nanomolar inhibitor. We also employed a bicyclic peptide strategy to assess peptide-based cytosolic delivery (Qian et al., 2015, 2017). We used a cell-penetrating peptide (CPP) coupled with a fluorescently labelled inhibitory decapeptide to visualize peptide pharmacodynamics.

Additionally, we solved the crystal structure of the principal part of the RdRp PA subunit in complex with the inhibitory peptide used in our detailed thermodynamics analysis. This crystal structure may assist structure-inspired drug design efforts to inhibit this heterotrimer of major interest.

## 2. Results

### 2.1. Identification of a PA-PB1 peptide inhibitor suitable for thermodynamic analysis

Previously, we developed a screening assay for inhibitors of the PPI between the PA and PB1 subunits of influenza A RdRp based on AlphaScreen technology (Hejdanek et al., 2021). We identified a decapeptide derived from the N-terminus of PB1 as a micromolar PPI inhibitor (peptide **PB1-10**). PPI peptide inhibitors contain hotspot amino acids that affect the affinity of the interaction substantially. **PB1-10** contains hotspots at three positions, denoted A, B and C (Fig. 2). These positions were determined based on the structure with decapeptide (Hejdanek et al., 2021), from the results of the peptide array

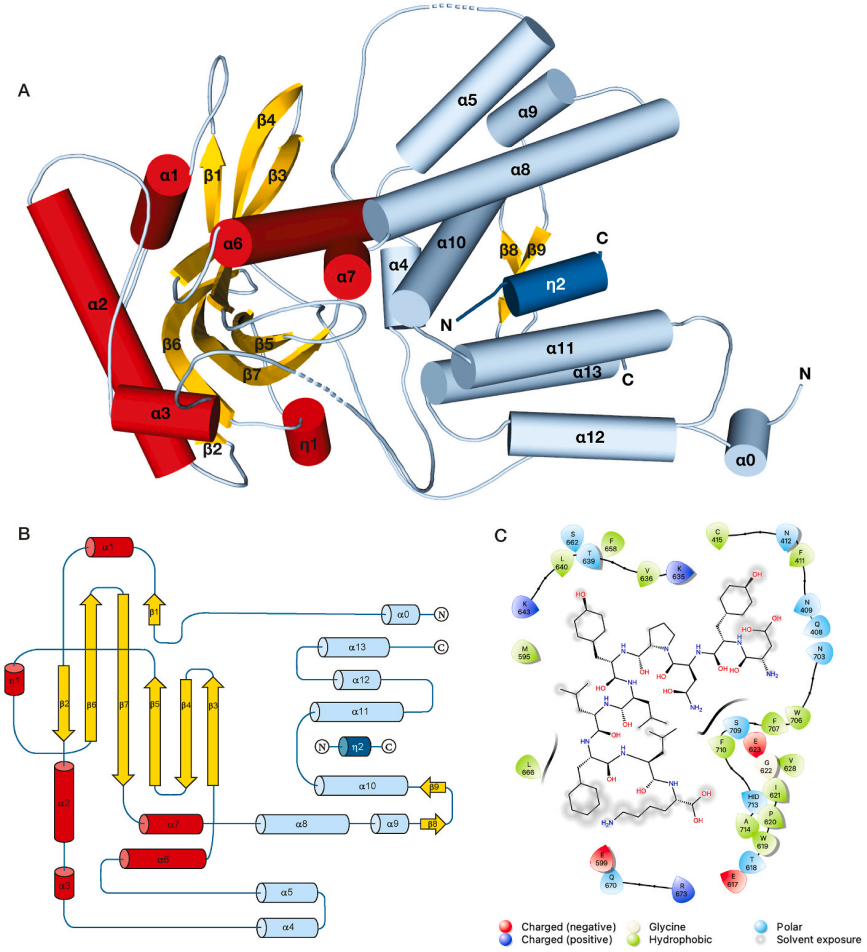


**Fig. 1. A)** The overall structure of CPA in complex with a PB1 decapeptide ($3_{10}$ helix, η2, teal) (Hejdanek et al., 2021). Helices are shown as cylinders, and CPA is divided into the red "brain" domain and light blue "mouth" domain; β-sheets are yellow and loops in blue. **B)** Topology diagram of CPA; coloring is consistent with the overall structure. Inspired by He et al. (2008). **C)** 2D pose for the interaction of **PB1-11** peptide into the CPA PPI site. Ligand plot created via Maestro from the Schrödinger suite (Schrödinger Release, 2021, 2022).

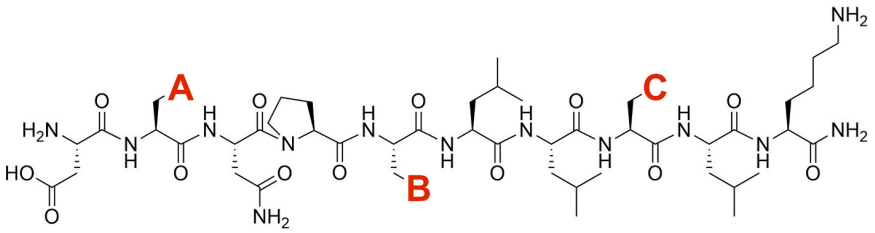


| Peptide | Hot-spots A | B | C | $IC_{50}$ [nM] | Maximal solubility [μM] |
|---|---|---|---|---|---|
| **PB1-10** | | OH | | 3 400 ± 300 | 25 |
| **PB1-11** | OH | OH | | 13 ± 1 | 66 |
| **PB1-12** | $CH_2$–OH | OH | | 6.8 ± 0.2 | 97 |
| **PB1-13** | COOH | OH | | 4.7 ± 0.3 | 66 |
| **PB1-14** | OH | $CH_2$–OH | | 54 ± 2 | 34 |
| **PB1-15** | OH | COOH | | 450 ± 30 | 95 |
| **PB1-16** | OH | OH | | 4.0 ± 0.1 | 12 |
| **PB1-17** | OH | OH | | 4.8 ± 0.1 | 18 |
| **PB1-18** | OH | OH | | 7.8 ± 0.2 | 175 |
| **PB1-19** | OH | OH | OH | 5.5 ± 0.1 | >200 |
| **PB1-20** | OH | OH | COOH | 4.9 ± 0.3 | 176 |

**Fig. 2.** Inhibition characteristics of PB1-derived decapeptides ($IC_{50}$ values) determined by AlphaScreen assay. It is a proximity assay involving reduced glutathione-coated acceptor beads with bound GST-CPA, and a streptavidin-coated donor beads with biotinylated peptide **PB1(1–25)** that binds to the active site of the GST-CPA. Upon excitation of the donor bead, a singlet oxygen species is released and mediates energy transfer between the excited donor and acceptor bead, which can be detected as emission signal. If a potent inhibitor of the PA-PB1 interaction is present, however, this interaction is disrupted, resulting in reduced emission signal.

(Wunderlich et al., 2011) and based on the knowledge of helix mimicking inhibitors of protein-protein interaction (Ernst et al., 2003; Bullock et al., 2011). By replacing the amino acids at the A and B positions with tyrosines, we obtained a low nanomolar PPI inhibitor (**PB1-11**) (Hejdanek et al., 2021).

Thermodynamic profiles of inhibitor binding, together with structural characterization, provide an important guide for optimization of medically relevant biomolecules. However, it was not possible to determine the thermodynamic interaction profile of these PA-PB1 inhibitors due to their limited solubility. Thus, we prepared a series of **PB1-11** analogs with various substitutions at hotspots, aiming to identify a variant that would maintain nanomolar affinity for CPA. Substitution of hotspot A with homo-tyrosine or *p*-carboxyphenylalanine (**PB1-12** and **PB1-13**) led to affinity retention, but did not significantly improve solubility. Substitution of hotspot B with more polar residues led to a decrease in affinity, and solubility did not improve (**PB1-14** and **PB1-15**). Subsequently, we replaced the phenylalanine in hotspot C with *L*-biphenylalanine and *L*-2-naphtylalanine. The resulting peptides, **PB1-16** and **PB1-17**, were strong inhibitors, but their solubility decreased. Substitution with tryptophan (**PB1-18**), tyrosine (**PB1-19**) and *p*-carboxyphenylalanine (**PB1-20**) led to improved inhibition as well as increased solubility. We selected peptide **PB1-19**, the most soluble of this series, as a candidate for thermodynamic characterization by isothermal titration calorimetry.

### 2.2. *Isothermal titration calorimetry of the optimized peptide inhibitor PB1-19*

The thermodynamics of **PB1-19** binding to CPA were monitored at 25 °C using a VP-ITC microcalorimeter (MicroCal Inc./Malvern Instruments Ltd., UK).

Titrations performed in buffers with different enthalpies of ionization yielded similar binding enthalpies ($-18.8 \pm 0.1$ kcal mol$^{-1}$ for Tris-HCl, $-18.9 \pm 0.1$ kcal mol$^{-1}$ for HEPES), indicating that under the experimental conditions there is no net proton transfer coupled to **PB1-19** binding to CPA (Klebe, 2017). The titration was characterized by a high parameter c-value of 3400 and served to determine the enthalpic contribution only (Fig. 3A). Because the parameter c-value was higher than 1000, determination of the dissociation constant ($K_d$) would be inaccurate under these conditions (Leavitt and Freire, 2001). Displacement titration using a weak competitive inhibitor is commonly used to determine the dissociation constants of high-affinity inhibitors.

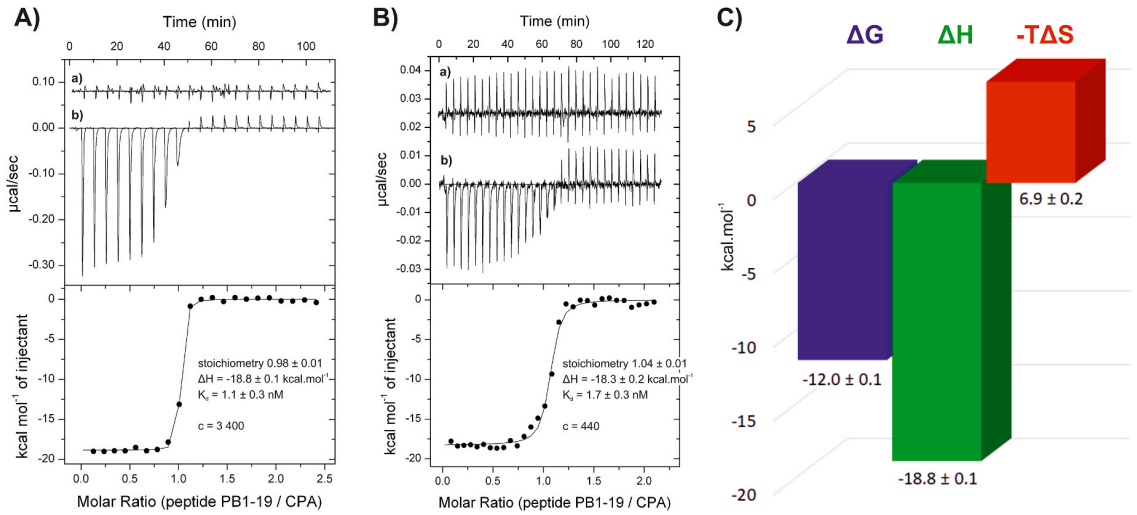


**Fig. 3.** Calorimetric titrations of CPA with **PB1-19** in Tris-HCl buffer characterized by a parameter c-value of 3400 **(A)** or 440 **(B)**. The upper panels show raw data from the following experiments: (a) heats of injection of **PB1-19** into buffer and (b) heats of injection of an identical peptide solution into a calorimetric cell containing CPA solution. The lower panels show the integrated peaks plotted as a binding isotherm. **C)** Graphical comparison of the thermodynamic parameters of **PB1-19** binding to CPA.

Unfortunately, there is no such weak inhibitor of PA-PB1 PPI that is sufficiently soluble for titration experiments. However, the enthalpy-dominant interaction allowed us to use low concentrations of interactants and titrate 7 µM **PB1-19** into 0.7 µM CPA, thus obtaining a titration curve with a low parameter c-value of 440, at which an accurate determination of the $K_d$ value was feasible (Fig. 3B). The dissociation constant of **PB1-19** binding to CPA was estimated to be 1.7 nM, corresponding to a Gibbs energy of binding of −12 kcal mol$^{-1}$. The peptide bound to CPA with a large favorable enthalpic contribution of −18.8 kcal mol$^{-1}$ and an unfavorable entropic contribution of 6.9 kcal mol$^{-1}$ (Fig. 3C). This dominant low enthalpy change suggests a large number of van der Waals and favorable hydrogen bonding interactions between **PB1-19** and CPA. The unfavorable entropy change implies conformational changes in either or both of the biomolecules (O' Brien and Haq, 2004).

### 2.3. *X-ray structural analysis of PB1-19 binding to the CPA subunit*

To observe structural changes within the hydrophobic pocket of CPA, we crystallized CPA in complex with **PB1-19** (Fig. 4A, PDB accession number **7ZPY**). The crystals exhibited *P* $2_12_12_1$ symmetry, which is consistent with the structure of CPA in complex with the peptide inhibitor **PB1-11** (PDB accession number **6SYI**) (Hejdanek et al., 2021). The crystal diffracted up to 1.9 Å and contained one CPA molecule in the asymmetric unit, and all **PB1-19** residues could be modelled into a well-defined electron density map (Fig. 4B). The binding modes of the decapeptides in **6SYI** (DYNPYLLFLK) and **7ZPY** (DYNPYLLYLK) were nearly identical, similarly to the native PB1 N-terminal peptide in **2ZNL** (Fig. S7). Superposition of peptides **PB1-11** and **PB1-19** in the CPA hydrophobic pocket gave an RMSD of 0.21 Å for 81 corresponding atoms. The mutation of Phe-9 to Tyr-9 yielded two additional water-mediated hydrogen bonds with O$^{\gamma}$Ser-662 in the α13 helix (Fig. 4C and D) and created a water net (w1-w4) connecting Tyr-9 and Tyr-6 with O$^{\delta1}$Asn-703 from helix α13. This resulted in the shift of residues ranging from Ala-651 (α11 helix) to Leu-694 (α12 helix) of RMSD of 0.84 Å for corresponding 332 atoms (Fig. 4E and D). The hydroxyl group of Tyr-3 forms a water-mediated hydrogen bond (w5) with the main chain carboxyl of Cys-415, as previously observed (Hejdanek et al., 2021).

### 2.4. *Bicyclic peptide delivery*

Intracellular peptide inhibitors are sensitive to degradation, rapid plasma clearance and low plasma membrane permeability. These poor pharmacokinetic properties are challenging to overcome even using cell-penetrating peptide (CPP) sequences such as Tat, which also decreases the antiviral effect. We used a recently described reversible bicyclization strategy (Qian et al., 2017) that yields enhanced proteolytic stability and efficient escape from the early endosome into the cytosol, providing protection from proteolysis in the endosome/lysosome (Qian et al., 2015).

Peptide **PB1-11** with 3,5-bis(mercaptomethyl)benzoyl (BMB) was fused via cysteines with a short CPP motif (RRRRØF), and modified into a bicyclic peptide by formation of two disulfide bonds. Based on previous work (Qian et al., 2017), we expected the bicyclic peptide **PB1–11B** to enter cells by endocytosis and escape from the early endosome into the cytosol, where intracellular glutathione would reduce the pair of disulfide bonds (Fig. 5). The released linear peptide, **PB1-21**, could then inhibit the intracellular PA-PB1 interaction. Results from AlphaScreen indicated that **PB1-21** retained inhibitory efficacy ($IC_{50}$ = 10 nM).

To observe the peptides' intracellular delivery and escape from the early endosome into the cytosol, we labelled both linear and bicyclic peptides with naphthofluorescein (NF) and rhodamine B (RB) (Fig. 6).

HeLa cells were treated with 5 µM NF- and RB-labelled peptides (**PB1-11**, **PB1–11B**) for 2 h and visualized using confocal microscopy (Fig. 7). Peptides labelled with the pH-insensitive RB were visible intracellularly across the entire pH range, giving a fluorescent signal both in cytosol and inside endosomes. On the other hand, NF-labelled **PB1–11B** exhibited diffuse fluorescence only in the cytosol, as the label is pH-sensitive. Consistent with previous work (Hejdanek et al., 2021), the addition of a cell-penetrating sequence increased the peptide's cytosolic delivery. Compared to the linear **PB1-11**, the bicyclic **PB1–11B** showed greater fluorescence in both labelled variants. This suggests not only increased transmembrane transport, but also enhanced escape from the early endosome.

### 2.5. *Effect of bicyclic peptides targeting the PA/PB1 interaction in cell culture*

The effect of linear peptides **PB1-11** and **PB1-19** and their bicyclic variants was evaluated with two cell-based approaches: a minireplicon

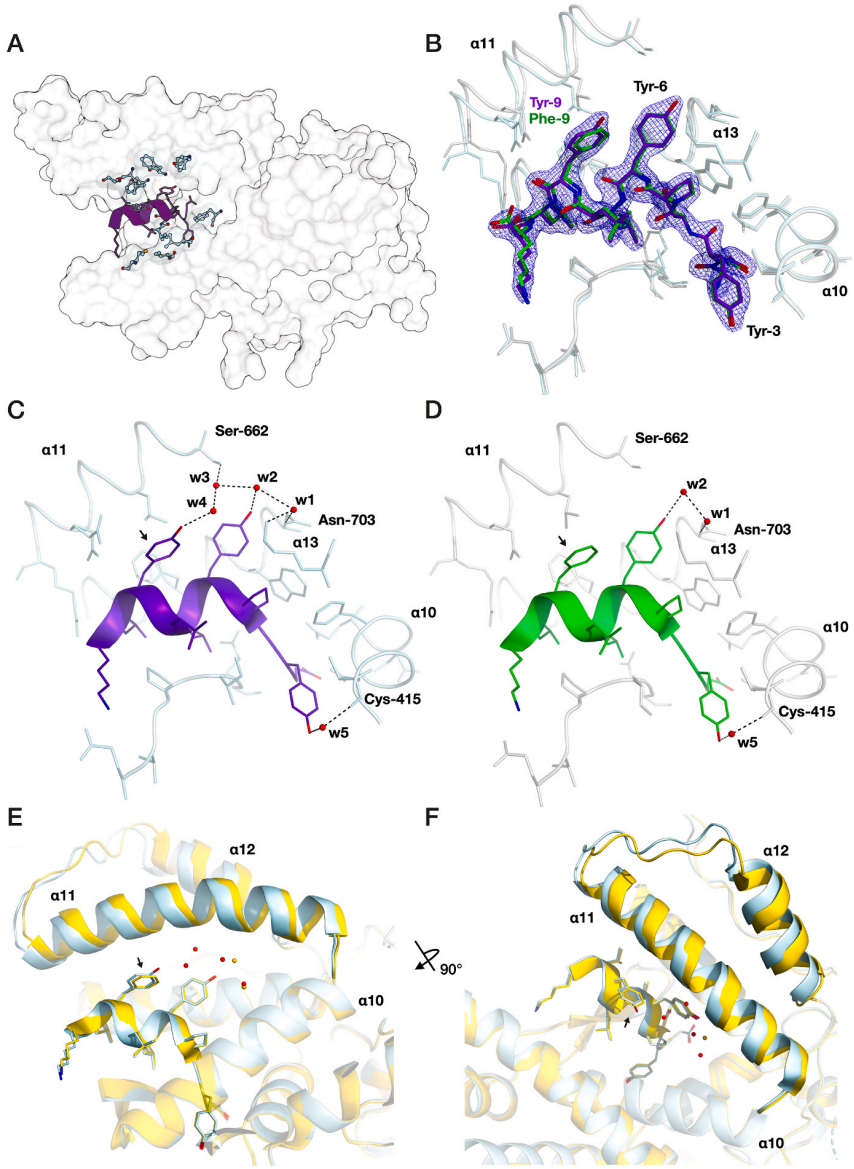


**Fig. 4.** Structure of CPA with the inhibiting peptide **PB1-19**. **(A)** Overall structure of CPA in complex with the peptide. CPA is shown in surface representation. The peptide (purple-blue) is shown in cartoon representation with side chains as sticks. Hydrophobic residues within 5 Å of the decapeptide are highlighted in pale cyan ball-and-stick representation. Other colour coding: oxygen – red, nitrogen – blue, sulphur – orange; **(B)** Close-up view of the hydrophobic binding pocket of CPA with aligned peptides **PB1-11** (green) and **PB1-19** (purple-blue) both in stick representation. Three "hotspots" (Tyr-3, Tyr-6 and Tyr-9/Phe-9) are highlighted. The 2*Fo* - *Fc* electron density map (contoured at 1.5σ) of **PB1-19** is shown as blue mesh; **(C)** and **(D)** polar interactions between CPA and decapeptides. Dashed lines represent hydrogen bonds between **PB1-19** (purple-blue) or **PB1-11** (green), water molecules (w1-w5) and CPA. The Phe-9 to Tyr-9 mutation site is indicated with an arrow. Side chains are shown as sticks and water molecules as red spheres; **(E)** and **(D)** alignment of **7ZPY** (light blue) and **6SYI** (yellow). Helices are in cartoon representation, **PB1-11** and **PB1-19** side chains are shown as sticks, water molecules as red spheres; Gln-415 (**7ZPY**) was modelled in two alternative conformations to better explain the electron density map.

assay and a cytopathic effect (CPE) reduction assay.

In the minireplicon assay, **PB1-11** barely inhibited RdRp ($EC_{50}$ of 64 μM, Table 1) and **PB1-19** did not have any effect. Although the replacement of phenylalanine with tyrosine in hotspot C improved the inhibitory ability, lower lipophilicity led to a decrease in cellular bioavailability. However, our bicyclic strategy significantly improved the properties of the peptide inhibitors in cell-based assays. **PB1–11B** showed a six-fold increase in influenza A RdRp inhibition. Considerable improvement was also seen for the bicyclic peptide **PB1–19B**, which was determined to be a low micromolar polymerase inhibitor ($EC_{50}$ of 1 μM).

To confirm the ability of bicyclic peptides to inhibit influenza virus in cell culture, we used a CPE reduction assay. MDCK cells were treated with peptides before infection with influenza A H1N1 virus. In accord with the minireplicon assay results, **PB1-11** had only a weak effect on viral replication, and **PB1-19** did not have any effect (Table 1). The bicyclic peptide **PB1–11B** exhibited a two-fold higher inhibitory effect than linear **PB1-11**. We observed a significant effect of bicyclic peptide delivery for **PB1–19B**, which had an $EC_{50}$ value of 2 μM in the infectious assay. Both HEK293T and MDCK cells tolerated all peptides at concentrations up to 100 μM. Favipiravir, baloxavir marboxil and pimodivir were used as controls.

In addition, we determined the effect of bicyclization on peptide stability in human plasma. Both linear peptides, **PB1-11** and **PB1-19**, underwent rapid proteolytic degradation in human plasma with half-lives of 12 and 13 min, respectively (Table 1). In contrast, bicyclic peptides **PB1–11B** and **PB1–19B** had half-lives of about 175 and 123 min, respectively.

The results from these assays indicate that suitable peptide modification together with reversible bicyclization led to significant improvements in pharmacokinetic characteristics and inhibitory potency in cell-based assays.

## 3. Conclusion

The PPI between the PA and PB1 subunits of influenza A polymerase is an important target for antiviral development. Here, we optimized a recently identified decapeptide derived from the N-terminus of the PB1 subunit. By modifying hotspot amino acid residues, we obtained a

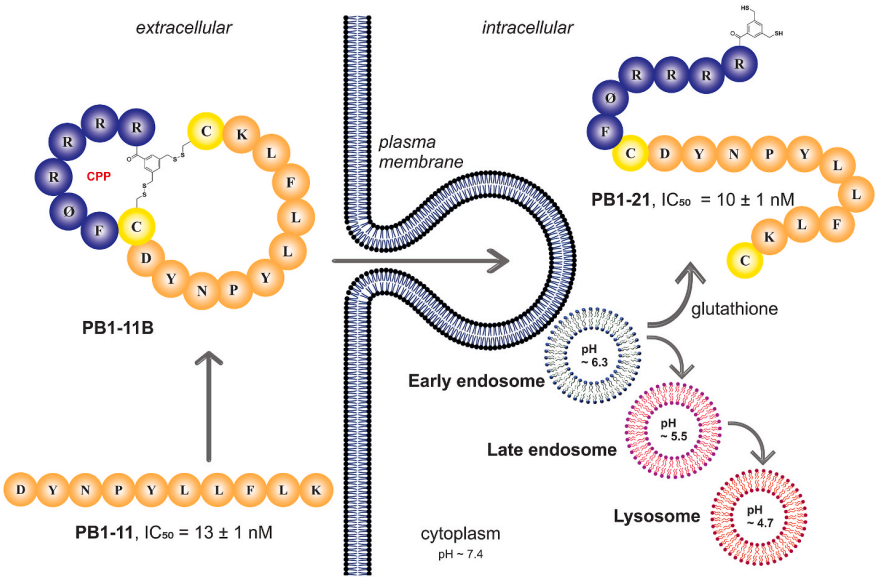


**Fig. 5.** Bicyclic peptide strategy for efficient delivery of **PB1-11** into cells.

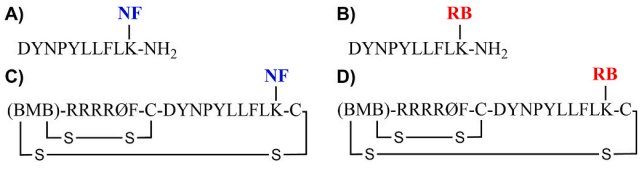


**Fig. 6.** Schematic presentation of labelled linear a bicyclic peptides: **PB1-11-NF** (A), **PB1-11-RB** (B), **PB1–11B–NF** (C) and **PB1–11B-RB** (D). BMB = 3,5-bis (mercaptomethyl)benzoyl; Ø = L-2-naphthylalanine.

peptide with better inhibitory potency and solubility. This enabled the first detailed thermodynamic analysis of PA/PB1 interaction inhibitor binding. **PB1-19** binds to CPA with high affinity, with a $K_d$ of 1.7 nM. It is an enthalpy-driven inhibitor, suggesting a high degree of van der Waals and favorable hydrogen bonding interactions between **PB1-19** and CPA. The unfavorable entropy change indicates conformational changes coupled to the binding process in either or both of the biomolecules. A detailed structural characterization of the **PB1-19**/CPA complex by X-ray crystallography revealed additional water-mediated hydrogen bonds between the protein and the modified peptide, compared to the original decapeptide **PB1-11**.

Although **PB1-11** and **PB1-19** are potent inhibitors of the PA/PB1 interaction, their peptide nature precludes their use in cell-based assays. Both peptides were unstable in human plasma, were not active in a polymerase minireplicon assay, and did not show any antiviral activity. To circumvent this, we applied a recently described strategy for efficient peptide delivery based on bicyclic peptides that are converted intracellularly into linear peptides. The corresponding bicyclic peptides **PB1–11B** and **PB1–19B** exhibited greater stability in human plasma, increased bioavailability, and the ability to escape from the endosome into the cytosol. These qualities led to a significant improvement in inhibition in cell-based assays, where **PB1–19B** was characterized as a low micromolar inhibitor in minireplicon and CPE antiviral testing.

## 4. Materials and methods

### 4.1. Cloning, expression, and purification of recombinant proteins

The expression and purification of amino acid region 257–716 of C-terminal domain of PA subunit (CPA) was performed as previously described (Hejdanek et al., 2021). CPA cloned in pETM11-SUMO3 (EMBL, Heidelberg, Germany) was expressed in *E. coli* BL21 (DE3) RIL. Cells were harvested and resuspended in lysis buffer (50 mM Tris/HCl, pH 8.0, 200 mM NaCl, 10 mM imidazole) and lysed with EmulsiFlex (Avestin). $His_6$-SUMO-tagged CPA was purified on Ni-NTA Agarose (Roche) and eluted with elution buffer (50 mM Tris/HCl, pH 8.0, 200 mM NaCl, 250 mM imidazole), followed by cleavage of the $His_6$-SOMO tag by ULP1 protease.

### 4.2. Inhibitor screening assay based on AlphaScreen technology and maximal solubility testing

AlphaScreen experiments were performed as described (Hejdanek et al., 2021). The assay conditions are described in the supplemental information. The maximal solubility of prepared peptides in the screening assay buffer was estimated by UV spectral analysis after centrifugation. The degree of precipitation was estimated by comparing the spectra of precipitates dissolved in DMSO with the spectra of compounds in DMSO of known concentration.

### 4.3. Isothermal titration calorimetry

The binding of peptide **PB1-19** to CPA was monitored at 25 °C using a VP-ITC microcalorimeter (MicroCal Inc./Malvern Instruments Ltd., UK). Reactant solutions were prepared in 20 mM Tris-HCl, pH 7.5, containing 150 mM NaCl, 5 mM 2-mercaptoethanol and 2% DMSO. The exact concentrations of peptide and protein were determined by HPLC amino acid analysis. Typically, 9 μl aliquots of 59.5 μM **PB1-19** were injected stepwise into a sample cell containing 1.43 mL of 3.9–4.8 μM CPA until saturation was achieved. For a titration curve with a parameter c-value of 440, the aliquotes of 7 μM **PB1-19** were injected into 0.7 μM CPA. To estimate whether inhibitor binding was accompanied by proton transfer, titrations in two buffers with different ionization enthalpies (Fukada and Takahashi, 1998; Krimmer and Klebe, 2015) (Tris-HCl, HEPES) were performed. Experimental titrations were accompanied by a corresponding control experiment, where solely ligand was injected into the buffer. The thermodynamic parameters were determined by MicroCal software implemented in Origin 7.0 (MicroCal Inc./Malvern Instruments Ltd., UK).

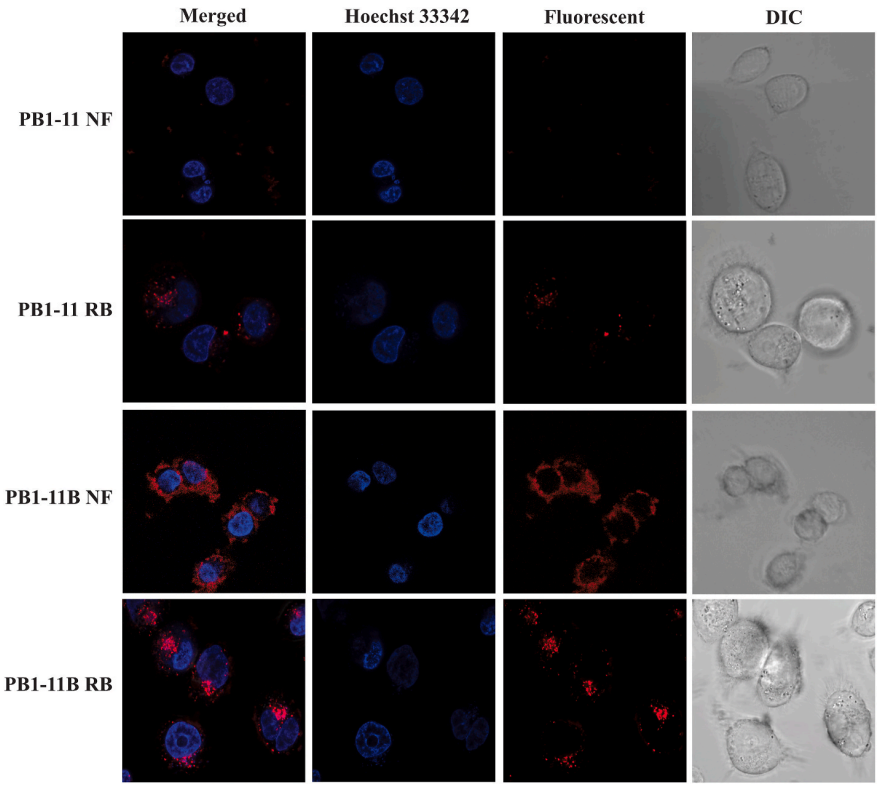


**Fig. 7.** Live-cell confocal microscopy snapshots of HeLa cells after 2 h of treatment with rhodamine B- and naphthofluorescein-labelled peptides **PB1-11** and **PB1–11B**. Rhodamine B was captured at 561 nm, 3% laser power and an exposure time of 100 ms; naphthofluorescein at 633 nm, 3% laser power and an exposure time of 100 ms. Localization of NF- and RB-labelled peptides is shown in red; cell nuclei were visualized using Hoechst 33342 dye (blue). All snapshots were taken at 63x magnification.

**Table 1**
Activity, toxicity and plasma half-life of PB1 peptides and their bicyclic forms. BMB = 3,5-bis(mercaptomethyl)benzoyl; Ø = *L*-2-naphthylalanine.

| Peptide | Peptide sequence | $EC_{50}$ [μM] minireplicon | $CC_{50}$ [μM] HEK293T | $EC_{50}$ [μM] CPE assay | $CC_{50}$ [μM] MDCK | plasma half-life [min] |
|---|---|---|---|---|---|---|
| PB1-11 | DYNPYLLFLK-NH2 | 64 ± 13 | >100 | 66 ± 9 | >100 | 12 |
| PB1–11B | (BMB)-RRRRØF-C-DYNPYLLFLK-C | 11 ± 1 | >100 | 29 ± 4 | >100 | 175 |
| PB1-19 | DYNPYLLYLK-NH2 | > 100 | >100 | >100 | >100 | 13 |
| PB1–19B | (BMB)-RRRRØF-C-DYNPYLLYLK-C | 0.99 ± 0.11 | >100 | 1.9 ± 0.3 | >100 | 123 |
| **Controls** | | | | | | |
| Favipiravir | | 20 ± 10 | >100 | 5.8 ± 1.0 | >100 | |
| Baloxavir marboxil | | 0.022 ± 0.006 | >100 | 0.053 ± 0.011 | >100 | |
| Pimodivir (VX-787) | | 0.0042 ± 0.0009 | >100 | 0.0029 ± 0.0004 | >100 | |

### *4.4. Protein crystallography*

Purified $CPA_{257\text{-}716}$ was dialyzed into crystallization buffer (10 mM Tris-HCl, pH 8.0, 1 mM TCEP) and concentrated to 15 mg/ml using Amicon 30 kDa centrifugal filter units (Merck). Concentrated protein was mixed with a solution of 50 μM **PB1-19** in crystallization buffer and re-concentrated to 15 mg/ml. Crystallization experiments were performed in EasyXtal 15-well plates (QIAGEN) using the vapor-diffusion hanging drop method at 18 °C. Crystallization drops (2 μl) were set up by mixing protein solution, precipitating solution and seed stock in a 5 : 4: 1 ratio. Approximately 100 μm crystals grew after several days in conditions containing 0.1 M MOPS/HEPES, pH 7.5, 15% PEG 3350. Crystals were cryoprotected by soaking in the precipitation solution supplemented with 40% PEG 3350 and flash frozen in liquid nitrogen.

### *4.5. Data collection and structure determination*

Diffraction data were collected at 100K on the MX14.1 beamline at the BESSY II synchrotron, operated by the Helmholtz-Zentrum Berlin, Germany (Mueller et al., 2015). The crystal of the CPA-**PB1-19** complex diffracted up to 1.9 Å. The diffraction data were processed using XDS and its GUI XDSAPP (Krug et al., 2012; Kabsch, 2010). The crystal

belonged to the *P* $2_12_12_1$ space group and contained one molecule in the asymmetric unit, with a solvent content of approximately 55%. The crystal parameters and data collection statistics are listed in Table S1. The structure was determined by molecular replacement with Molrep (Vagin and Teplyakov, 2000) using protein coordinates from structure **6SYI** (Hejdanek et al., 2021). Model refinement was performed using the program REFMAC 7.1.018 (Murshudov et al., 1997) from the CCP4 package (Collaborative Computational Project, 1994) in combination with manual building and adjustments in Coot software (Emsley and Cowtan, 2004). **PB1-19** was modelled in the final rounds of the structure refinement. The Molprobity server was used to evaluate the final model quality (Lovell et al., 2003). Final refinement statistics are summarized in Table S1. All figures showing structural representations were prepared with PyMOL (Delano, 2002). Atomic coordinates and structure factors were deposited in the PDB under accession code **7ZPY**.

### 4.6. Confocal microscopy

HeLa cells were grown in DMEM complete growth medium (10% FBS, 4 mM L-glutamine, 100U/100 μg/mL penicillin/streptomycin). Each of the labelled peptides was prepared as a 5 μM solution in phenol-red-free, high-glucose DMEM supplied with 4 mM L-glutamine. HeLa cells were seeded in a 35 mm, glass bottomed microwell dish (5x10 (Deyde et al., 2007) cells per well) and cultured overnight at 37 °C, 5% $CO_2$. Aliquots (100 μl) of the prepared 5 μM labelled-peptide solutions (**PB1-11-RB**; **PB1-11-NF**; **PB1–11B-RB** and **PB1–11B–NF**) were added to the cells and incubated for 2 h at 37 °C, 5% $CO_2$. After washing with PBS, cells were treated with Hoechst 33342 nucleic acid stain solution (5 μg/ml), incubated for 10 min, washed with PBS, and imaged on a confocal microscope. Rhodamine B was captured at a wavelength of 561 nm; naphthofluorescein was captured at a wavelength of 633 nm.

### 4.7. Anti-influenza assays, minireplicon assay and cell viability determination

Anti-influenza activity was measured by determining the extent to which the test peptides reduced the virus-induced cytopathic effect (CPE) on MDCK cells. To determine the effect of PB1 peptides on polymerase activity in cells, minireplicon assays were performed. Detailed methods are included in Supplemental Data.

### 4.8. Peptide and bicyclic peptide syntheses

General procedures for peptides synthesis and their bicyclization are described in the Supplementary Data.

## Declaration of competing interest

The authors declare that they have no known competing financial interests or personal relationships that could have appeared to influence the work reported in this paper.

## Data availability

Atomic coordinates and structure factors were deposited in the PDB database (www.rcsb.org) under accession code 7ZPY.

## Acknowledgements

The authors thank František Sedlák for help with confocal microscopy measurements, Helena Mertlíková-Kaiserová for help with stability testing of peptides in human plasma, Miloš Buděšínský for NMR measurements, and Hillary Hoffman for proofreading of the manuscript. Diffraction data were collected on BL14.1 at the BESSY II electron storage ring operated by the Helmholtz-Zentrum Berlin. This work was supported by the European Regional Development Fund, OP RDE, Project: "Chemical biology for drugging undruggable targets (ChemBioDrug)" (No. CZ.02.1.01/0.0/0.0/16_019/0000729) and the European Union - Next Generation EU, The project National Institute of Virology and Bacteriology (Programme EXCELES, ID Project No. LX22NPO5103).

## Appendix A. Supplementary data

Supplementary data to this article can be found online at https://doi.org/10.1016/j.antiviral.2022.105449.

## References

Agrawal, U., Raju, R., Udwadia, Z.F., 2020. Favipiravir: a new and emerging antiviral option in COVID-19. Med. J. Armed Forces India 76, 370–376.
Bullock, B.N., Jochim, A.L., Arora, P.S., 2011. Assessing helical protein interfaces for inhibitor design. J. Am. Chem. Soc. 133, 14220–14223.
Collaborative Computational Project, N., 1994. The CCP4 suite: programs for protein crystallography. Acta Crystallogr D Biol Crystallogr 50, 760–763.
D'Agostino, I., Giacchello, I., Nannetti, G., Fallacara, A.L., Deodato, D., Musumeci, F., Grossi, G., Palu, G., Cau, Y., Trist, I.M., Loregian, A., Schenone, S., Botta, M., 2018. Synthesis and biological evaluation of a library of hybrid derivatives as inhibitors of influenza virus PA-PB1 interaction. Eur. J. Med. Chem. 157, 743–758.
Delano, W.L., 2002. The PyMOL Molecular Graphics System. *http://www.pymol.org*.
Desantis, J., Nannetti, G., Massari, S., Barreca, M.L., Manfroni, G., Cecchetti, V., Palu, G., Goracci, L., Loregian, A., Tabarrini, O., 2017. Exploring the cycloheptathiophene-3-carboxamide scaffold to disrupt the interactions of the influenza polymerase subunits and obtain potent anti-influenza activity. Eur. J. Med. Chem. 138, 128–139.
Deyde, V.M., Xu, X., Bright, R.A., Shaw, M., Smith, C.B., Zhang, Y., Shu, Y., Gubareva, L. V., Cox, N.J., Klimov, A.I., 2007. Surveillance of resistance to adamantanes among influenza A(H3N2) and A(H1N1) viruses isolated worldwide. J. Infect. Dis. 196, 249–257.
Duwe, S.C., Schmidt, B., Gartner, B.C., Timm, J., Adams, O., Fickenscher, H., Schmidtke, M., 2021. Prophylaxis and treatment of influenza: options, antiviral susceptibility, and existing recommendations. GMS Infect. Dis. 9, Doc02.
Emsley, P., Cowtan, K., 2004. Coot: model-building tools for molecular graphics. Acta Crystallogr. D 60, 2126–2132.
Ernst, J.T., Becerril, J., Park, H.S., Yin, H., Hamilton, A.D., 2003. Design and application of an alpha-helix-mimetic scaffold based on an oligoamide-foldamer strategy: antagonism of the Bak BH3/Bcl-xL complex. Angew Chem. Int. Ed. Engl. 42, 535–539.
Fukada, H., Takahashi, K., 1998. Enthalpy and heat capacity changes for the proton dissociation of various buffer components in 0.1 M potassium chloride. Proteins 33, 159–166.
He, X.J., Zhou, J., Bartlam, M., Zhang, R.G., Ma, J.Y., Lou, Z.Y., Li, X.M., Li, J.J., Joachimiak, A., Zeng, Z.H., Ge, R.W., Rao, Z.H., Liu, Y.F., 2008. Crystal structure of the polymerase PA(C)-PB1(N) complex from an avian influenza H5N1 virus. Nature 454, 1123–1126.
Hejdanek, J., Radilova, K., Pachl, P., Hodek, J., Machara, A., Weber, J., Rezacova, P., Konvalinka, J., Kozisek, M., 2021. Structural characterization of the interaction between the C-terminal domain of the influenza polymerase PA subunit and an optimized small peptide inhibitor. Antiviral. Res. 185, 104971.
Hurt, A.C., 2019. Antiviral therapy for the next influenza pandemic. Trav. Med. Infect. Dis. 4, 67.
Iuliano, A.D., Roguski, K.M., Chang, H.H., Muscatello, D.J., Palekar, R., Tempia, S., Cohen, C., Gran, J.M., Schanzer, D., Cowling, B.J., Wu, P., Kyncl, J., Ang, L.W., Park, M., Redlberger-Fritz, M., Yu, H., Espenhain, L., Krishnan, A., Emukule, G., van Asten, L., Pereira da Silva, S., Aungkulanon, S., Buchholz, U., Widdowson, M.A., Bresee, J.S., 2018. Estimates of global seasonal influenza-associated respiratory mortality: a modelling study. Lancet 391, 1285–1300.
Jalily, P.H., Duncan, M.C., Fedida, D., Wang, J., Tietjen, I., 2020. Put a cork in it: plugging the M2 viral ion channel to sink influenza. Antiviral. Res. 178, 104780.
Kabsch, W., 2010. XDS. Acta Crystallogr D Biol Crystallogr 66, 125–132.
Klebe, 2017. Profiling Drug Binding by Thermodynamics: Key to Understanding, pp. 1–36.
Krimmer, S.G., Klebe, G., 2015. Thermodynamics of protein-ligand interactions as a reference for computational analysis: how to assess accuracy, reliability and relevance of experimental data. J. Comput. Aided Mol. Des. 29, 867–883.
Krug, M., Weiss, M.S., Heinemann, U., Mueller, U., 2012. XDSAPP: a graphical user interface for the convenient processing of diffraction data using XDS. J. Appl. Crystallogr. 45, 568–572.
Leavitt, S., Freire, E., 2001. Direct measurement of protein binding energetics by isothermal titration calorimetry. Curr. Opin. Struct. Biol. 11, 560–566.
Lee, N., Hurt, A.C., 2018. Neuraminidase inhibitor resistance in influenza: a clinical perspective. Curr. Opin. Infect. Dis. 31, 520–526.
Lo, C.Y., Li, O.T., Tang, W.P., Hu, C., Wang, G.X., Ngo, J.C., Wan, D.C., Poon, L.L., Shaw, P.C., 2018. Identification of influenza polymerase inhibitors targeting C-terminal domain of PA through surface plasmon resonance screening. Sci. Rep. 8, 2280.
Lovell, S.C., Davis, I.W., Arendall 3rd, W.B., de Bakker, P.I., Word, J.M., Prisant, M.G., Richardson, J.S., Richardson, D.C., 2003. Structure validation by Calpha geometry: phi,psi and Cbeta deviation. Proteins 50, 437–450.

Manz, B., Gotz, V., Wunderlich, K., Eisel, J., Kirchmair, J., Stech, J., Stech, O., Chase, G., Frank, R., Schwemmle, M., 2011. Disruption of the viral polymerase complex assembly as a novel approach to attenuate influenza A virus. J. Biol. Chem. 286, 8414–8424.
Massari, S., Goracci, L., Desantis, J., Tabarrini, O., 2016. Polymerase acidic protein-basic protein 1 (PA-PB1) protein-protein interaction as a target for next-generation anti-influenza therapeutics. J. Med. Chem. 59, 7699–7718.
Mueller, U., Forster, R., Hellmig, M., Huschmann, F.U., Kastner, A., Malecki, P., Puhringer, S., Rower, M., Sparta, K., Steffien, M., Uhlein, M., Wilk, P., Weiss, M.S., 2015. The macromolecular crystallography beamlines at BESSY II of the Helmholtz-Zentrum Berlin: current status and perspectives. Eur. Phys. J. E 130, 141.
Murshudov, G.N., Vagin, A.A., Dodson, E.J., 1997. Refinement of macromolecular structures by the maximum-likelihood method. Acta Crystallogr. D 53, 240–255.
Nannetti, G., Massari, S., Mercorelli, B., Bertagnin, C., Desantis, J., Palu, G., Tabarrini, O., Loregian, A., 2019. Potent and broad-spectrum cycloheptathiophene-3-carboxamide compounds that target the PA-PB1 interaction of influenza virus RNA polymerase and possess a high barrier to drug resistance. Antiviral. Res. 165, 55–64.
Ng, K.E., 2019. Xofluza (baloxavir marboxil) for the treatment of acute uncomplicated influenza. P T 44, 9–11.
Obayashi, E., Yoshida, H., Kawai, F., Shibayama, N., Kawaguchi, A., Nagata, K., Tame, J. R., Park, S.Y., 2008. The structural basis for an essential subunit interaction in influenza virus RNA polymerase. Nature 454, 1127–1131.
O' Brien, R., Haq, I., 2004. Applications of biocalorimetry: binding. Stability and Enzyme Kinetics 3–34.
Perez, D.R., Donis, R.O., 2001. Functional analysis of PA binding by influenza a virus PB1: effects on polymerase activity and viral infectivity. J. Virol. 75, 8127–8136.
Qian, Z., Dougherty, P.G., Pei, D., 2015. Monitoring the cytosolic entry of cell-penetrating peptides using a pH-sensitive fluorophore. Chem. Commun. 51, 2162–2165.
Qian, Z., Rhodes, C.A., McCroskey, L.C., Wen, J., Appiah-Kubi, G., Wang, D.J., Guttridge, D.C., Pei, D., 2017. Enhancing the cell permeability and metabolic stability of peptidyl drugs by reversible bicyclization. Angew Chem. Int. Ed. Engl. 56, 1525–1529.
Schrödinger Release 2022-3, 2021. Maestro, S., LLC, New York, NY.
Shiraki, K., Daikoku, T., 2020. Favipiravir, an anti-influenza drug against life-threatening RNA virus infections. Pharmacol. Ther. 209, 107512.
Stevaert, A., Naesens, L., 2016. The influenza virus polymerase complex: an update on its structure, functions, and significance for antiviral drug design. Med. Res. Rev. 36, 1127–1173.
Trist, I.M., Nannetti, G., Tintori, C., Fallacara, A.L., Deodato, D., Mercorelli, B., Palu, G., Wijtmans, M., Gospodova, T., Edink, E., Verheij, M., de Esch, I., Viteva, L., Loregian, A., Botta, M., 2016. 4,6-Diphenylpyridines as promising novel anti-influenza agents targeting the PA-PB1 protein-protein interaction: structure-activity relationships exploration with the aid of molecular modeling. J. Med. Chem. 59, 2688–2703.
Vagin, A., Teplyakov, A., 2000. An approach to multi-copy search in molecular replacement. Acta Crystallogr D Biol Crystallogr 56, 1622–1624.
Wang, J., Li, F., Ma, C., 2015. Recent progress in designing inhibitors that target the drug-resistant M2 proton channels from the influenza A viruses. Biopolymers 104, 291–309.
Watanabe, K., Ishikawa, T., Otaki, H., Mizuta, S., Hamada, T., Nakagaki, T., Ishibashi, D., Urata, S., Yasuda, J., Tanaka, Y., Nishida, N., 2017. Structure-based drug discovery for combating influenza virus by targeting the PA-PB1 interaction. Sci. Rep. 7, 9500.
Wunderlich, K., Mayer, D., Ranadheera, C., Holler, A.S., Manz, B., Martin, A., Chase, G., Tegge, W., Frank, R., Kessler, U., Schwemmle, M., 2009. Identification of a PA-binding peptide with inhibitory activity against influenza A and B virus replication. PLoS One 4, e7517.
Wunderlich, K., Juozapaitis, M., Ranadheera, C., Kessler, U., Martin, A., Eisel, J., Beutling, U., Frank, R., Schwemmle, M., 2011. Identification of high-affinity PB1-derived peptides with enhanced affinity to the PA protein of influenza A virus polymerase. Antimicrob. Agents Chemother. 55, 696–702.
Yuan, S., Chu, H., Ye, J., Singh, K., Ye, Z., Zhao, H., Kao, R.Y., Chow, B.K., Zhou, J., Zheng, B.J., 2017. Identification of a novel small-molecule compound targeting the influenza A virus polymerase PB1-PB2 interface. Antiviral. Res. 137, 58–66.
Zhang, J.T., Hu, Y.M., Foley, C., Wang, Y.X., Musharrafieh, R., Xu, S.T., Zhang, Y.T., Ma, C.L., Hulme, C., Wang, J., 2018. Exploring ugi-azide four-component reaction products for broad-spectrum influenza antivirals with a high genetic barrier to drug resistance. Sci. Rep. 8, 4653.
Zhang, J., Hu, Y., Musharrafieh, R., Yin, H., Wang, J., 2019. Focusing on the influenza virus polymerase complex: recent progress in drug discovery and assay development. Curr. Med. Chem. 26, 2243–2263.
Zhang, J., Hu, Y., Wu, N., Wang, J., 2020. Discovery of influenza polymerase PA-PB1 interaction inhibitors using an in vitro split-luciferase complementation-based assay. ACS Chem. Biol. 15, 74–82.
Zhou, Z., Liu, T., Zhang, J., Zhan, P., Liu, X., 2018. Influenza A virus polymerase: an attractive target for next-generation anti-influenza therapeutics. Drug Discov. Today 23, 503–518.

## 3.5. PUBLICATION III.

**Unraveling the Anti-Influenza Effect of Flavonoids: Experimental Validation of Luteolin and its Congeners as Potent Influenza Endonuclease Inhibitors.**

A large group of polyphenolic phytochemicals called flavonoids was described to have a beneficial impact on human health. They are present in daily diet and beside many other effects have a role in cancer and bone loss prevention. One flavonoid – the quercetin was discussed for its antiviral effect on influenza. The exact mode-of-action was unknown even though number of *in vitro* and *in vivo* experiments were published. There was no consensus on influenza target protein. Several studies including molecular docking simulations suggested the binding of quercetin to the viral surface enzymes the hemagglutinin or neuraminidase, thus preventing the viral entry/escape (Choi et al., 2009; Z. Liu et al., 2016). One publication described the PB2 subunit of the RdRp to be the targeted by quercetin (Gansukh et al., 2016). We were already concerned about the PA subunit of influenza RdRp, and the collaboration with chemists from Pavel Majer group at the Institute of Organic Chemistry and Biochemistry allowed us to widen our study target. With the theory of flavonoids binding to the endonuclease site, we could focus also on the N-terminal domain of PA subunit (NPA) and therefore complete both sides suitable as drug development targets.

### 3.5.1. SUMMARY

As the NPA bears two metal ions in the active site and quercetin and other flavonoids are known to have the ability to coordinate metal ions, we hypothesized the PA N-terminal domain as the potential inhibitory target. There were two thinkable binding modes dependent on the molecule structure (**Figure 16**). The binding mode A is analogous to the EGCG binding to the active site of NPA endonuclease. Binding mode B utilizes the 3,5-dihydroxyflavone moiety. These were called for simplification the bidentate (two hydroxyls; **A**) and the tridentate (three hydroxyls; **B**) binding mode, respectively. To investigate a wide range of these polyols against the influenza endonuclease, we have developed an assay based on the AlphaScreen technology supported by data the from gel-based endonuclease assay. Out of the 83 tested compounds, three were selected for protein X-ray crystallography: luteolin, quambalarine B and myricetin. Out of those, two protein-inhibitor structures were obtained. Clear structure of myricetin in the active site was not achieved, as only partial electron density for the inhibitor was visible. To understand its flexibility, we employed the molecular modelling based on rough estimates from the protein crystallography. Finally, unlike all previously published data concerning the

neuraminidase, hemagglutinin, or the PB2 domain, we disclose the PA endonuclease domain of the RdRp to be the target protein for flavonoids during the influenza virus infection. The NPA structure in complex with luteolin at 2.0 Å revealed the bidentate motif as an advantage for the inhibitory activity. Hydroxyl presented at position C7 enhanced the binding of the inhibitor to the protein active site via an additional hydrogen bond to the $O^{\varepsilon 2}$ Glu-26. Moreover, we have structurally characterized the unfavoured novel binding mode B of compound quambalarine B at 2.5 Å. Combination of two different assays together with the X-ray crystallography, the molecular binding mode-of-action of flavonoids within influenza was elucidated for the first time.

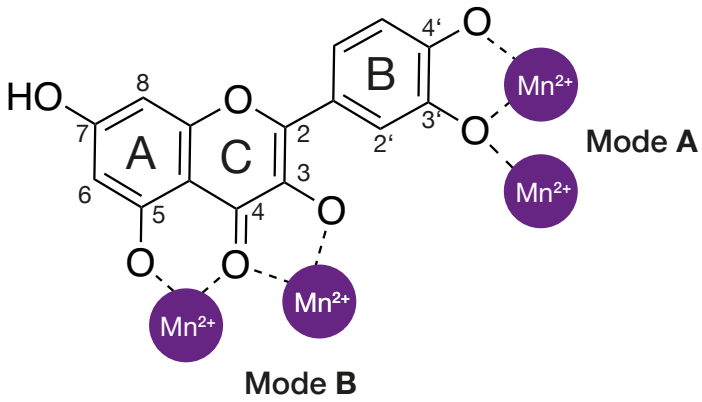


**Figure 16.** Schematic representation of quercetin including the numbering system and the binding modes to the $Mn^{2+}$ ions in the endonuclease active site. The bidentate binding mode **A** utilizes the 3',4'-dihydroxyphenyl moiety on ring B. The binding mode **B** possesses the 3,5-dihydroxyflavone moiety, also named as the tridentate mode.

my contribution

I expressed the NPA domain of influenza A RdRp in *E.coli*, purified the protein and set up initial crystallization conditions. After several optimization steps, I soaked the selected ligands into protein crystals. With a help from Jiří Brynda, I collected all the data using X-ray crystallography for the first time, processed them, solved their structures, and refined them resulting in two protein-ligand complexes (PDB IDs: **6YA5**, **6YEM**). In collaboration with the computational chemist Jindřich Fanfrlík, we compared the obtained X-ray structures to the molecular model.

"**Unraveling the Anti-Influenza Effect of Flavonoids: Experimental Validation of Luteolin and Its Congeners as Potent Influenza Endonuclease Inhibitors.**" *European Journal of Medicinal Chemistry* 208:112754. doi: 10.1016/j.ejmech.2020.112754.

European Journal of Medicinal Chemistry 208 (2020) 112754

Contents lists available at ScienceDirect

European Journal of Medicinal Chemistry

journal homepage: http://www.elsevier.com/locate/ejmech

# Unraveling the anti-influenza effect of flavonoids: Experimental validation of luteolin and its congeners as potent influenza endonuclease inhibitors

Václav Zima [a, b, 1], Kateřina Radilová [b, c, 1], Milan Kožíšek [b, *], Carlos Berenguer Albiñana [a, b], Elena Karlukova [b], Jiří Brynda [b, d], Jindřich Fanfrlík [b], Miroslav Flieger [e], Jan Hodek [b], Jan Weber [b], Pavel Majer [b], Jan Konvalinka [b, f], Aleš Machara [a, b, **]

[a] Department of Organic Chemistry, Faculty of Science, Charles University, Hlavova 8, 128 00, Prague 2, Czech Republic
[b] Institute of Organic Chemistry and Biochemistry of the Czech Academy of Sciences, Gilead Sciences and IOCB Research Center, Flemingovo n. 2, 166 10, Prague 6, Czech Republic
[c] First Faculty of Medicine, Charles University, Kateřinská 1660, 121 08, Prague 2, Czech Republic
[d] Institute of Molecular Genetics of the Czech Academy of Sciences, Vídeňská 1083, 140 00, Prague 4, Czech Republic
[e] Institute of Microbiology of the Czech Academy of Sciences, Vídeňská 1083, 140 00, Prague 4, Czech Republic
[f] Department of Biochemistry, Faculty of Science, Charles University, Hlavova 8, 128 00, Prague 2, Czech Republic

ARTICLE INFO

*Article history:*
Received 22 June 2020
Received in revised form
20 July 2020
Accepted 9 August 2020
Available online 22 August 2020

*Keywords:*
Influenza
Neuraminidase
Polyphenols
$PA_N$ endonuclease Inhibitors
RNA polymerase

ABSTRACT

The biological effects of flavonoids on mammal cells are diverse, ranging from scavenging free radicals and anti-cancer activity to anti-influenza activity. Despite appreciable effort to understand the anti-influenza activity of flavonoids, there is no clear consensus about their precise mode-of-action at a cellular level. Here, we report the development and validation of a screening assay based on AlphaScreen technology and illustrate its application for determination of the inhibitory potency of a large set of polyols against PA N-terminal domain (PA-Nter) of influenza RNA-dependent RNA polymerase featuring endonuclease activity. The most potent inhibitors we identified were luteolin with an $IC_{50}$ of 72 ± 2 nM and its 8-*C*-glucoside orientin with an $IC_{50}$ of 43 ± 2 nM. Submicromolar inhibitors were also evaluated by an *in vitro* endonuclease activity assay using single-stranded DNA, and the results were in full agreement with data from the competitive AlphaScreen assay. Using X-ray crystallography, we analyzed structures of the PA-Nter in complex with luteolin at 2.0 Å resolution and quambalarine B at 2.5 Å resolution, which clearly revealed the binding pose of these polyols coordinated to two manganese ions in the endonuclease active site. Using two distinct assays along with the structural work, we have presumably identified and characterized the molecular mode-of-action of flavonoids in influenza-infected cells.

© 2020 The Author(s). Published by Elsevier Masson SAS. This is an open access article under the CC BY-NC-ND license (http://creativecommons.org/licenses/by-nc-nd/4.0/).

## 1. Introduction

Influenza is a serious viral infection of the upper respiratory tract that can spread easily from person to person during seasonal epidemics and cause respiratory infections in other mammals and birds. The virus remains a major threat to public health because of its high virulence and mutation rate. Several human influenza pandemics have occurred in the last century, each caused by a new

*Abbreviations:* QM, quantum mechanics; MM, molecular mechanics; PDB, protein data bank; PA-Nter, N-terminal part of PA subunit; SAR, structure-activity relationship; SPR, surface plasmon resonance.

* Corresponding author. Institute of Organic Chemistry and Biochemistry, Academy of Sciences of the Czech Republic, Gilead Sciences and IOCB Research Center, Flemingovo n. 2, 166 10, Prague 6, Czech Republic.
** Corresponding author. Department of Organic Chemistry, Faculty of Science, Charles University, Hlavova 8, 128 00, Prague 2, Czech Republic.
*E-mail addresses:* milan.kozisek@uochb.cas.cz (M. Kožíšek), ales.machara@uochb.cas.cz (A. Machara).
[1] These authors contributed equally to this work.

https://doi.org/10.1016/j.ejmech.2020.112754
0223-5234/© 2020 The Author(s). Published by Elsevier Masson SAS. This is an open access article under the CC BY-NC-ND license (http://creativecommons.org/licenses/by-nc-nd/4.0/).

**Abbreviation used**

| | |
|---|---|
| DCM | dichloromethane |
| DMF | *N*,*N*-dimethylformamide |
| EtOAc | ethyl acetate |
| $IC_{50}$ | half-maximal inhibitory concentration |
| THF | tetrahydrofuran |
| TLC | thin layer chromatography |

strain of the virus. The most severe of these, the 1918 "Spanish flu" caused by an H1N1 virus, resulted in more than 50 million deaths worldwide over a two-year period. Seasonal influenza epidemics typically lead to 3 to 5 million cases of severe disease and up to 650,000 deaths worldwide annually [1].

Vaccination and antiviral therapies are two of the treatment methods used to control influenza infections. Three classes of antivirals that target different influenza virus enzymes are clinically available. Oseltamivir and zanamivir are neuraminidase inhibitors that block the release of viral particles from the host cell and consequently stop the infection from spreading [2]. Unfortunately, continually emerging resistant strains have undermined their effectiveness and compromised further development of neuraminidase inhibitors. The other two drug classes are RNA polymerase inhibitors with different modes of action. The prodrug baloxavir marboxil [3–5], which is metabolized to baloxavir acid (BXA), blocks initiation of mRNA synthesis, thus preventing viral replication. The drug not only features a distinct mechanism of action, but also is superior to neuraminidase inhibitors because it is active against a wide range of influenza viruses, including oseltamivir-resistant strains and avian strains (H7N9, H5N1). Another RNA-polymerase targeting drug, favipiravir [6], was approved with an indication limited for treatment of influenza insufficiently responsive to current drugs and is being evaluated in clinical trials in other countries. Favipiravir acts as a pseudo purine nucleic acid in virus-infected cells and targets a different enzyme site than BXA.

Influenza virus contains a single-stranded, negative sense RNA genome in complex with RNA-dependent RNA polymerase. After infection, the viral polymerase-RNA complex is transported into the host cell, where it plays an essential role in viral replication and transcription. Influenza RNA-polymerase is a heterotrimeric enzyme comprising subunits PA, PB1 and PB2. It is unable to synthesize the 5′-mRNA cap required for eukaryotic translation. The initiation of transcription of viral mRNA depends on primers—short oligomers of host pre-mRNA—gained by a unique "cap-snatching" mechanism. This process begins with the PB2 subunit binding the 5′-cap ($m^7$GTP) of the host pre-mRNA. Subsequently, the PA subunit cleaves the RNA strain approximately 10–13 nucleotides downstream from the 5′-cap to acquire the primer. PB1 uses this detached RNA segment as a template by subunit for viral mRNA synthesis. The RNA-dependent RNA polymerase is highly conserved across all influenza strains, the "cap-snatching" mechanism has been observed in all viruses of the *Orthomyxoviridae* family. These features make the RNA-dependent RNA polymerase an exceptionally promising target for drug development [7–10].

The PA subunit is bridged dinuclear metalloenzyme, which does not have a human counterpart, and is further subdivided into a C-terminal domain (PA-Cter) tethered by a long peptide chain to an N-terminal domain (PA-Nter) featuring the endonuclease active site. PA-Cter forms an interface for binding of the N-terminal domain of the PB1 subunit. The endonuclease active site of PA-Nter is a negatively charged pocket consisting of His-41, Lys-134, and a triad of acidic residues (Glu-80, Asp-108 and Glu-119) that can bind either $Mg^{2+}$ or $Mn^{2+}$ ions, with stronger affinity for the latter [11]. Two ions positioned in the deep cleft of PA-Nter are critical for endonuclease activity. Understandably, any inhibitor designed to interfere with the PA-Nter active site must be able to chelate these two ions efficiently. In theory, tight coordination provided by such a compound would block the active site and prevent the enzyme from executing its biological function.

Intensive effort has been made to develop PA-Nter inhibitors by SAR-guided drug design. Several promising lead compounds with metal-binding pharmacophores have been reported, including BXA-like-compounds, diketo acid derivatives, hydroxylated heterocycles, flutimide congeners, catechol derivatives, and other scaffolds [12–15].

BXA was developed by rational drug design using a two-metal pharmacophore concept similar to that used to develop the HIV-1 integrase inhibitor dolutegravir. Screening of metal-chelating compounds by enzymatic assay and subsequent optimization of the chemical structure culminated in discovery of baloxavir marboxil, which features enhanced oral absorption compared to BXA (Fig. 1, left) [16]. BXA shows strong inhibitory potency against the endonuclease activity of various RNA polymerases from influenza A and B viruses with mean $IC_{50}$ values of 1.4–3.1 nM and 4.5–8.9 nM, respectively [4].

L-742,001 (**2**) is a typical example of the α,γ-diketo acid class. This compound possesses a piperidinyl moiety, which bears two benzyl substituents that occupy different hydrophobic pockets. According to an X-ray analysis of **2** bound to PA-Nter, the first $Mn^{2+}$ ion coordinates a carboxylate and an α-oxygen atom of **2**, while the second ion binds both α and γ-oxo groups of the chelator (Fig. 1, center). Compound **2** is one of the most potent inhibitors from this class, with an inhibition potency in the submicromolar range ($IC_{50}$ = 0.43 μM, $EC_{50}$ = 0.35 μM) [17]. Different substitutions on the nitrogen atom of the piperidinyl moiety do not dramatically change its inhibitory potency, allowing for further modification of **2**.

Promising PA-Nter inhibitors from the catechol derivatives class include the phytochemicals (−)-epigallocatechin gallate (**3**, EGCG; Fig. 1, right) and its congener epicatechin gallate (not shown), which are the major polyphenol components of green tea [18,19]. EGCG inhibited the endonuclease activity in a plaque inhibition assay using MDCK cells with an $EC_{50}$ = 28.4 μM. Notably, the galloyl moiety (3′,4′,5′-trihydroxyphenyl motif) proved to be necessary for anti-influenza activity. An X-ray structure of influenza PA-Nter with EGCG clearly showed the binding pose of EGCG in PA-Nter and the coordination of $Mn^{2+}$ ions to the two hydroxyl groups of galloyl moiety [11].

Flavonoids are a large group of polyphenolic phytochemicals prominent in pharmacognosy (Fig. 2, left). Flavonoids are an integral part of daily diets; most humans consume approximately 1 g of flavonoids and their glycosides daily. Many studies have suggested that intake of flavonoids might have health benefits, due to their role in prevention of cancer [20–23], bone loss [24], and other age-related diseases [25]. Numerous reports have documented the anti-inflammatory properties [26], as well as the antibacterial [27,28] and antiviral activity, of flavonoids [29,30]. One flavonoid in particular—quercetin (4)—has attracted attention due to its inhibitory effect on viruses (Fig. 2, right).

Quercetin (3,3′,4′,5,7-pentahydroxyflavone) is one of the most ubiquitous flavonoids in the plant kingdom. It is a common component of green tea, various berries, vegetables such as onions and raw capers, and fruits such as pomegranates and apples [31]. Quercetin may have a beneficial effect on liver injury and fibrosis, as found in animal studies [32]. Numerous publications have reported its anti-inflammatory activity [33,34] and its antibacterial [35], anticancer [36–40], and antiviral effects [30,41–46]. Some reports

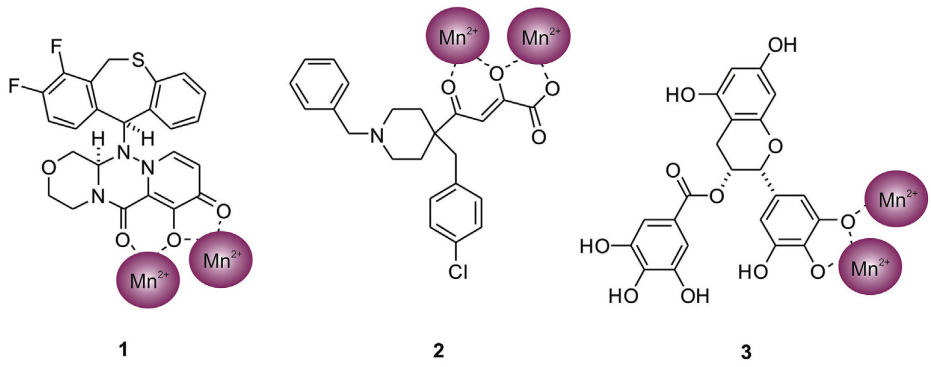


**Fig. 1.** Structures of reported $Mn^{2+}$ binding inhibitors of PA endonuclease. Left: Baloxavir acid (BXA, 1) binding manganese ions. Center: Two ions coordinated to L-742,001 (2) [17]. Right: Two manganese ions coordinated to EGCG (3).

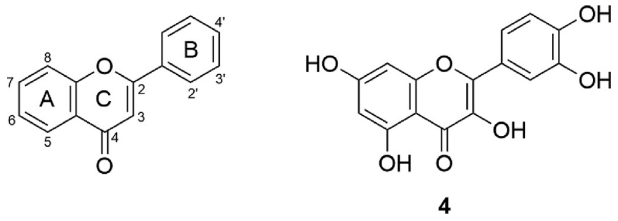


**Fig. 2.** Left: Molecular structure of the flavonoid backbone including the numbering system. Right: Structure of quercetin (4).

also suggest that quercetin [47–49] or its glycoside exhibit anti-influenza activity [50–53].

The precise anti-influenza mode-of-action of quercetin has not been elucidated to date despite numerous *in vitro* experiments and experiments in mice [54,55]. These *in vivo* experiments showed that treatment with quercetin or its glycosides leads to a reduction in influenza-induced cytopathic effect and also reduces lung damage and inflammation induced by viral infection [55]. Additionally, numerous docking simulation analyses have been performed to explore the potential mechanism of quercetin's anti-influenza activity. Nearly all reports linked quercetin's anti-influenza activity with inhibition of the surface enzymes hemagglutinin and neuraminidase. In contrast, one paper concluded that the inhibitory effects are due to interaction with PB2 of the viral RNA polymerase [56]. Furthermore, there seems to be no consensus on whether the flavonoid intervenes with influenza infection in its early or in its late phase [57]. Mechanisms that may explain quercetin's anti-influenza activity include the following:

a) Hemagglutinin inhibitor. A mechanistic investigation suggested that quercetin interacts with the HA2 subunit [58]. This hypothesis arose from SPR and microscale thermophoresis experiments; the interaction with HA2 has not been confirmed by structural analysis.
b) Neuraminidase inhibitor. *In vitro* inhibitory activities of flavonoids were based on experiments with infected MDCK cells. $IC_{50}$ values were additionally determined by a fluorometric assay (MUNANA) that mimics the cleavage of sialic acid in infected cells [49,59,60]. In this assay the inhibition is examined by measuring the fluorogenic product 4-methylumbelliferone (4-MU) cleaved from 2′-*O*-(4-methylumbelliferyl) α-D-*N*-acetylneuraminic acid (4-MUNANA). The amount of 4-MU is inversely proportional to the inhibitory activity of the tested compound. However, conclusions about the anti-influenza activities of flavonoids determined by the fluorometric assay deserve careful interpretation because flavonoids have a strong quenching effect on 4-MU fluorescence [61,62]. Reported $IC_{50}$ values range from 20 to 90 μM (quercetin had $IC_{50}$ = 58 μM against H1N1) [49].
c) PB2 cap-binding inhibitor. Quercetin and its glycoside have been proposed to block RNA polymerase by occupying the binding site of $m^7GTP$ [56]. The antiviral mechanism was investigated by time-dependent incubation assay and molecular docking studies. In an *in vitro* assay with infected MDCK cells, quercetin glycoside exhibited a 3- to 8-times higher anti-influenza activity than oseltamivir. Results from a series of experiments indicated that quercetin glycoside does not inhibit hemagglutinin and pre-incubation of the virus does not alter its infectivity. The same authors also performed a neuraminidase activity inhibition assay (NA-Star® Influenza NA Inhibitor Resistance Detection Kit). Interestingly, the neuraminidase activity of the virus was 90% when 10 μg/mL (22 μM) glycoside was present. However, 1 μg/mL (3.5 μM) oseltamivir treatment had a potent blocking effect. This indicates that potential neuraminidase inhibition by quercetin cannot account for the inhibitory effect observed in infected MDCK cells.

We hypothesized that the anti-influenza effect of flavonoids may stem from their ability to coordinate metal ions, as documented by various quercetin-metal ion complexes reported in the literature [63–70]. We tentatively proposed two potential binding modes for quercetin and the two $Mn^{2+}$ ions in the endonuclease active site (Fig. 3). Binding mode A is analogous to the binding of

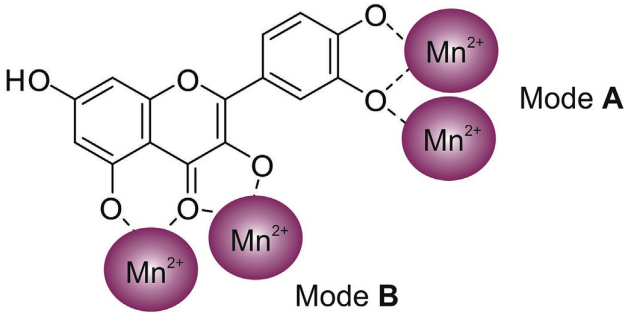


**Fig. 3.** Schematic representation of potential binding modes of quercetin with two $Mn^{2+}$ ions in the endonuclease active site. Binding mode A utilizes the 3′,4′-dihydroxyphenyl moiety on ring B, whereas binding mode B exploits the 3,5-dihydroxyflavone moiety.

the ions to EGCG at the PA-Nter active site. Proposed endonuclease inhibition based on binding mode B is supported by a [Mn(quercetin)$_2$($H_2O$)$_2$] complex [71] that utilizes the 3,5-dihydroxyflavone moiety of quercetin. The metal binding properties of flavonoids have generally been attributed to the 3,5-dihydroxyflavone moiety rather than to the 3′,4′-dihydroxyphenyl moiety of the B ring. However, the actual binding mode remains unsolved, as the complexes characterized in the literature were prepared by combining dissociated metal ions with quercetin and thus do not reflect the complex binding interactions common in the active site of enzymes.

The discovery of quercetin derivatives with potent anti-hepatitis C virus (HCV) activity substantially supports our hypothesis that the anti-influenza activity of flavonoids is associated with the inhibition of the PA endonuclease [72,73]. HCV also has an RNA polymerase (protein NS5B) with two divalent ions ($Mg^{2+}$ or $Mn^{2+}$) that play a pivotal role in the active site by mediating ligation of ribonucleotide triphosphate substrates. The authors also performed molecular docking calculations and concluded that binding mode B (see Fig. 3) is most likely to occur.

Based on these assumptions we decided to conduct a thorough investigation to account for the inhibitory potency of various polyols, namely flavonoids, against influenza endonuclease. Furthermore, we also set out to evaluate flavonoids as potential inhibitors of influenza neuraminidase using an assay recently developed in our laboratory [74] based on a cutting-edge DIANA technology [75].

## 2. Results and discussion

### 2.1. Development and validation of the binding assay

We set to develop a new assay for screening PA-Nter inhibitors based on the amplified luminescent proximity assay system (AlphaScreen). In this competitive binding assay, the binding interaction of a derivative of **2** tethered to donor beads with PA-Nter bound to acceptor beads effectively brings the two beads into proximity, resulting in a robust signal. The metal-binding motif of **2** was decorated with an ω-biotinylated flexible linker, and this adduct was noncovalently bound to donor beads coated with streptavidin. PA-Nter was expressed in *E.coli* with an N-terminal GST-tag, purified, and bound to acceptor beads coated with glutathione. Upon excitation of the donor, molecules of oxygen are converted to singlet oxygen, which diffuses approximately 200 nm within its half-life. If an acceptor bead is present within this 200-nm perimeter, the generated singlet oxygen mediates energy transfer from excited donor beads to acceptor beads, and an emission signal can be detected (Fig. 4A). On the other hand, presence of potent PA-Nter inhibitor disrupts the binding interaction of a tethered derivative of **2** with PA-Nter and reduces emission signal.

As replacement of the benzyl moiety in **2** with fluorescein did not compromise the binding potency of this fluorescent adduct [76], we assumed that the introduction of a suitable linker instead of benzyl would be tolerated as well. Our hypothesis was also supported by a meticulous study investigating a 2009H1N1 PA-Nter complex with **2**. Thus, we designed a ω-biotinylated linker based on 4-hydroxyisophthalate that partially mimics fluorescein and is equipped with a short ethylene glycol linker bearing biotin.

Preparation of the linker started from the *tert*-butyl ester of hydroxyisophthalic acid **5**, which was prepared from the corresponding dimethyl ester using reported conditions (Scheme 1) [77]. In the next step, its free phenol moiety was alkylated with $N_3$-PEG4-Ts reagent (see Supplementary Data). This was followed by saponification of the methyl ester in the *para* position of adduct **6** and catalytic hydrogenation of the azide into an amino group. The resulting crude product was protected with Boc to provide intermediate **8**, which was converted to corresponding NHS ester **9** using the TBTU coupling reagent.

Preparation of the key intermediate **10** followed a reported procedure for the synthesis of **2** [78]. However, we introduced several modifications based on different building blocks; these modified procedures are provided in Supplementary Data. The assembly of the probe for the competition assay (AlphaScreen) started with selective *N*-Boc-deprotection of the piperidine moiety of **10**. Then, the reaction mixture was evaporated and intermediate **9** was added along with an excess of base. Adduct **11** was fully deprotected with trifluoroacetic acid and reacted with biotin-PEG6-NHS ester, furnishing **12**, which was purified by preparative HPLC.

A Surface Plasmon Resonance (SPR) analysis was performed to test the binding parameters of the L-742,001-like probe **12** prior to its usage in the AlphaScreen experiment (Fig. S1). The biotinylated probe was attached to the chip through the interaction with neutravidin. Different concentrations of GST-PA-Nter were injected into corresponding channels. SPR indicated binding of the modified probe **12** to the protein and revealed a dissociation constant ($K_d$) less than 9.3 nM.

Then the AlphaScreen assay was developed to screen inhibitors affecting the GST-PA-Nter–**12** interaction (Fig. 4A). A statistical evaluation of the assay from octuplicates was performed as previously described [79]. The Z' factor, a characteristic parameter of assay quality, was estimated to be in the range of 0.83–0.87, indicating excellent assay performance and suitability for high-throughput screening. The assay was validated with **1** and **2**, revealing an $IC_{50}$ value of 24 ± 1 nM and 26 ± 1 nM, respectively. Quercetin exhibited an $IC_{50}$ value of 0.67 μM (Fig. 4B), validating our hypothesis linking the therapeutic effect of flavonoids to inhibition of influenza endonuclease.

These results from the AlphaScreen assay were subsequently evaluated by a gel-based endonuclease inhibitory assay based on monitoring endonuclease-catalyzed cleavage of a single-stranded DNA plasmid in the presence of an inhibitor [13]. Findings from this assay further validated quercetin's ability to inhibit the endonuclease (Fig. 4C).

### 2.2. Compound synthesis

We aimed to thoroughly study the SAR of flavonoids and their analogues. Methylations are the simplest way to access quercetin congeners. Unfortunately, selective and facile mono-, di- and trimethylations of quercetin have not been described in the literature. Therefore, we performed tetra- and pentamethylation of quercetin to obtain **13** and **14**, respectively [80]. Many flavonoids are commercially available, but to access particular flavones with carefully selected polyhydroxylation on the A and B rings, we carried out a three-step synthesis [81]. Aldol condensations of *ortho*-hydroxyacetophenones with *meta*-methoxybenzaldehydes under basic conditions yielded corresponding 2′-hydroxychalcones **15**–**19** (Scheme 2). Subsequent cyclization and oxidation was accomplished by reaction with 2,3-dichloro-5,6-dicyano-1,4-benzoquinone (DDQ) at elevated temperatures overnight [82]. This one-pot protocol provided methoxylated flavones **20**–**24** in acceptable yields. Treatment of **20**–**24** with concentrated hydrobromic acid under reflux furnished O-demethylated products **25**–**29**.

We also took the opportunity to study the chemistry and biology of the aza-analogues of flavonoids. Replacement of an oxygen atom at position 1 with a nitrogen atom could in theory change the electron density of the metal-binding groups and affect the inhibitory potency. The synthesis of two azaflavonoids (Scheme 3) followed a previously reported procedure with some modifications

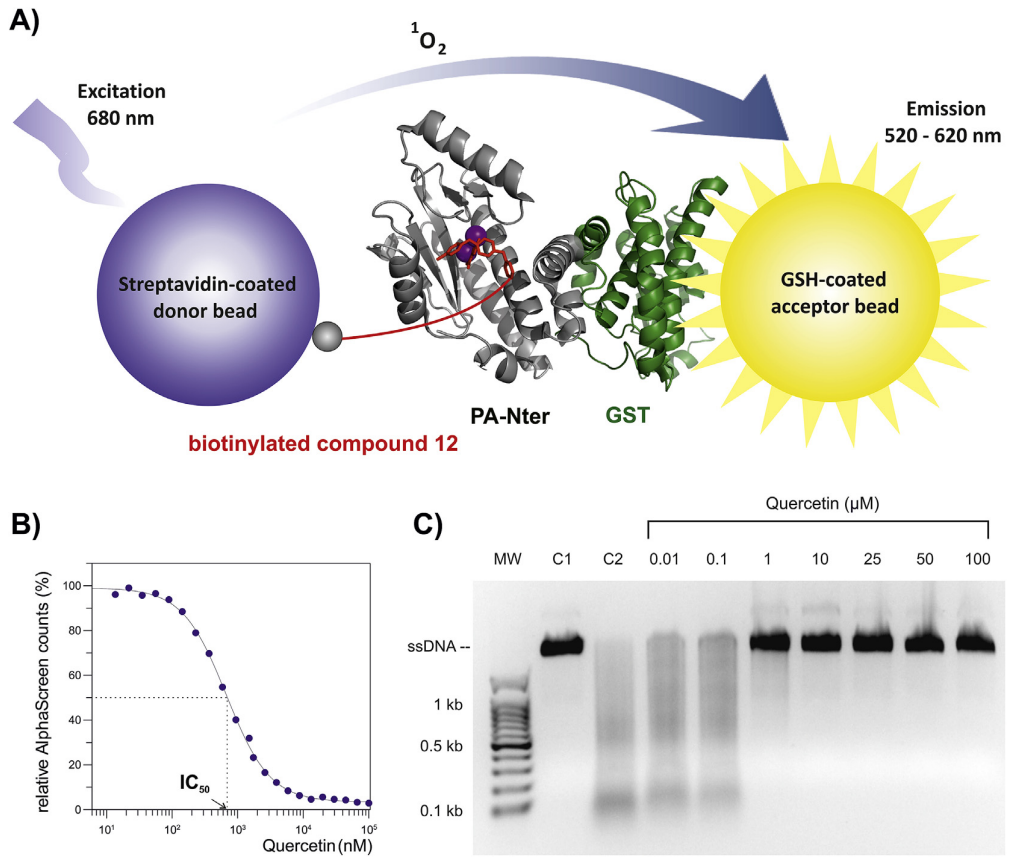


**Fig. 4.** A) Illustration of the AlphaScreen protein-protein interaction assay, using streptavidin-coated donor beads, GSH-coated acceptor beads, a biotinylated congener of L-742,001 (**12**), and GST-PA-Nter. B) Titration curve of quercetin using the AlphaScreen assay, revealing an $IC_{50}$ value of 0.67 μM. C) Inhibition of endonuclease activity by quercetin, documented by a gel-based endonuclease inhibitory assay. The single-stranded circular DNA M13mp18 was used as substrate (lane C1). The substrate fully cleaved by endonuclease in the absence of inhibitor (lane C2) was used as a control. The GelPilot 100bp Plus Ladder molecular weight marker (lane MW) is shown for reference.

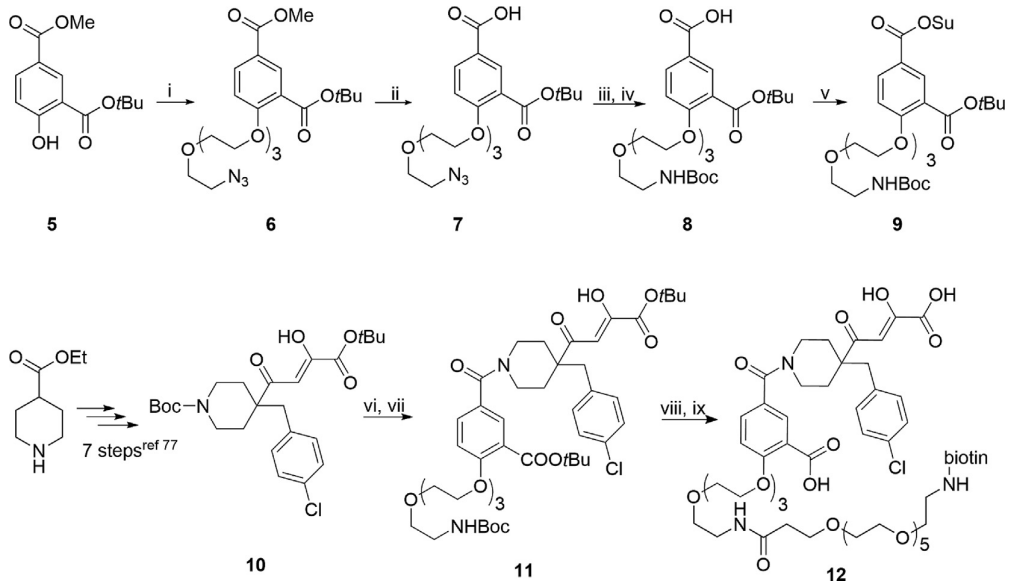


**Scheme 1.** *Reagents and conditions*. (i) azide-PEG4-Ts, $K_2CO_3$, DMF, 60 °C, 24 h, 94% yield; (ii) NaOH 0.5 M, 1,4-dioxane, 24 h, r.t., 97% yield; (iii) Lindlar catalyst, $H_2$ (1 atm), MeOH, 60 min, r.t. (iv) $Boc_2O$, $Et_3N$, DCM, 24 h, r.t., 64% yield. (v) TBTU, THF, $Et_3N$, *N*-hydroxysuccinimide, 16 h, r.t., 81% yield; (vi) TFA/DCM (1:5), 15 min, r.t.; (vii) **9**, $Et_3N$, DCM, 24 h, r.t., 68% yield; (viii) TFA/DCM (1:5), 15 min, r.t.; (ix) biotin-PEG6-NHS ester, $Et_3N$, DCM, 24 h, r.t., 15% yield over two steps.

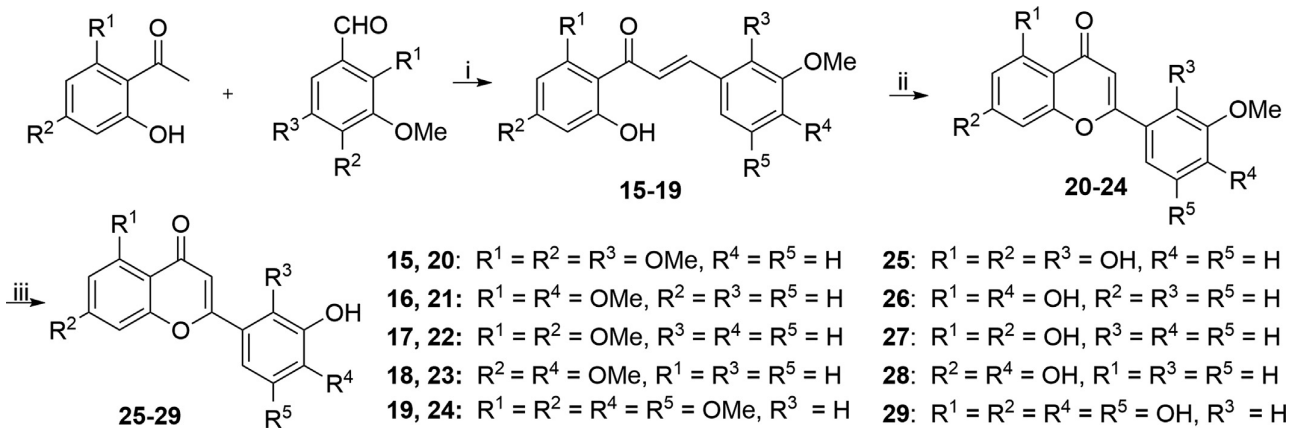


**Scheme 2.** Reagents and conditions: (i) KOH, 24 h, r.t.; (ii) 2,3-dichloro-5,6-dicyano-1,4-benzoquinone (DDQ), 1,4-dioxane, 12 h, 80 °C; (iii) 40% HBr in $H_2O$, 4–12 h, reflux.

[83]. Preparation of **30** and **31** from dimethoxyaniline was challenging, and subsequent acylation with dimethoxybenzoyl chloride required elevated temperatures but furnished **32** and **33** in satisfactory yields. We then attempted to cyclize these acyl derivatives in the presence of sodium ethoxide, but this resulted in low yields. Replacing ethoxide with potassium *tert*-butoxide [84] led to significantly improved yields. In the last step, intermediates **34** and **35** were subjected to O-demethylation in refluxing hydrobromic acid, affording the desired compounds **36** and **37**.

### 2.3. Relationship between chemical structure and inhibitory potency

The inhibition activities of purchased compounds and those synthesized in our laboratory were assessed by AlphaScreen binding assay (Table 1). Flavone and flavonol congeners displayed a relatively wide spread of inhibitory potencies with $IC_{50}$ values ranging from submicromolar to higher than 50 μM, calling for a thorough SAR study.

Quercetin, the parental compound of the series, inhibited endonuclease with an $IC_{50}$ of 0.67 μM. Tetra- and pentamethylated quercetin analogues **13** and **14** exhibited complete loss of inhibition. Diosmetin (**39**), a 4′-monomethylated quercetin congener lacking the C3 hydroxyl group, was also non-inhibitory, indicating that either an unsubstituted 3′,4′-dihydroxyphenyl motif or the presence of a hydroxyl group at C3 are crucial for inhibition. The moderate inhibitory activity of 3′,4′-dihydroxyflavone (**40**) pointed to the key role of the 3′,4′-dihydroxyphenyl motif. The structurally similar luteolin (**41**) was more potent than other compounds in the series ($IC_{50}$ = 0.072 μM), clearly demonstrating the positive effect of the two additional hydroxyl groups at C5 and C7 on inhibitory activity. This finding fits well with literature data. Luteolin and its 5-*O*-glucosides galuteolin have been already recognized as anti-influenza drugs but its mode of action has never been associated with the RNA polymerase. Their effect were determined by an *in vitro* antiviral assay using a cytopathic effect reduction assay in MDCK cells [85,86].

Guaijaverin (**42**), a quercetin 3-*O*-glycoside, had a more than two-order-of-magnitude weaker binding potency than **41** but

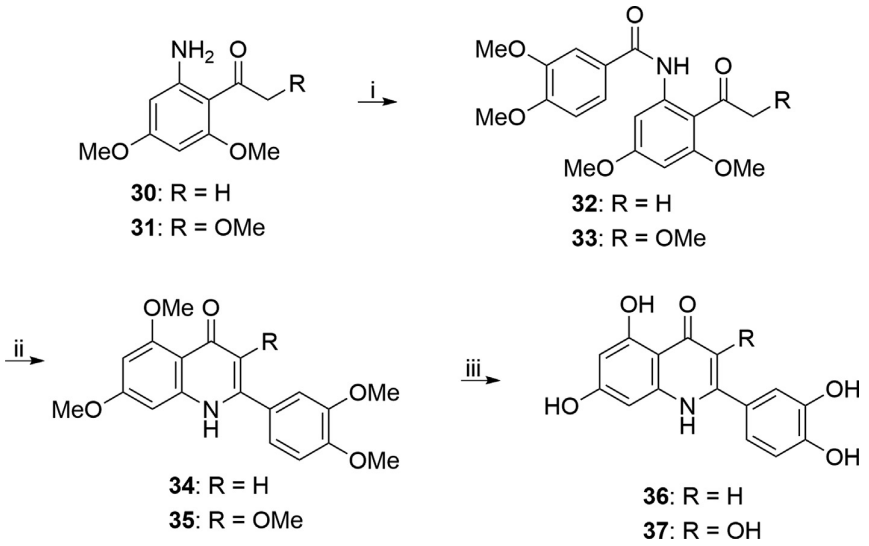


**Scheme 3.** Reagents and conditions: (i) 3,4-dimethoxybenzoyl chloride, DIPEA, DMAP, toluene, 12 h, 80 °C; (ii) potassium *tert*-butoxide, *t*-BuOH, 16 h, 80 °C, sealed tube; (iii) 40% aqueous HBr in $H_2O$, 4–12 h, reflux.

**Table 1**
Inhibition assay of influenza endonuclease. Structure-activity relationship of quercetin congeners.

| Compound | Structure | Trivial name | $IC_{50}$ (μM) (AlphaScreen) |
|---|---|---|---|
| **4** | 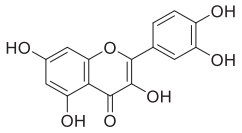 | quercetin | 0.67 ± 0.02 |
| **13** | 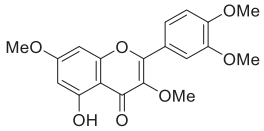 | N/A | >50 |
| **14** | 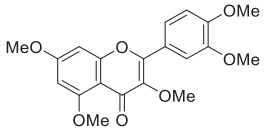 | N/A | >50 |
| **39** | 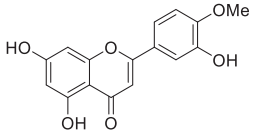 | diosmetin | >50 |
| **40** | 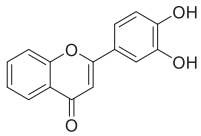 | 3′,4′-dihydroxy-flavone | 2.4 ± 0.3 |
| **41** | 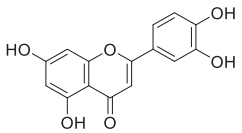 | luteolin | 0.072 ± 0.002 |
| **42** | 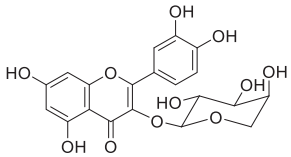 | guaijaverin | 17 ± 2 |
| **43** | 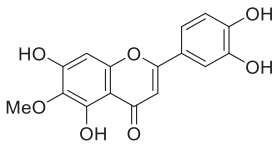 | nepetin | 0.93 ± 0.03 |
| **44** | 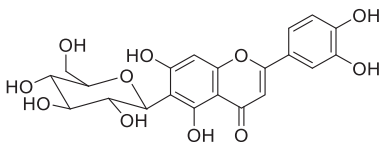 | isoorientin | >50 |
| **45** | 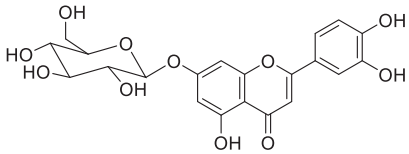 | cynaroside | 32 ± 3 |

(*continued on next page*)

**Table 1** (*continued*)

| Compound | Structure | Trivial name | $IC_{50}$ (μM) (AlphaScreen) |
|---|---|---|---|
| **46** | 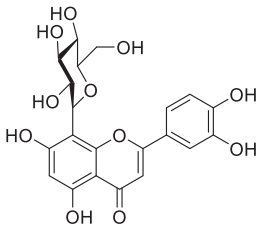 | orientin | 0.043 ± 0.002 |
| **24** | 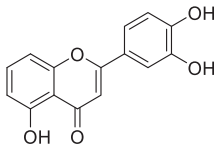 | N/A | 1.8 ± 0.1 |
| **26** | 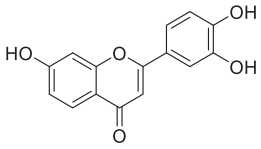 | N/A | 1.3 ± 0.1 |
| **47** | 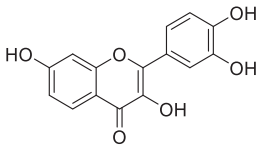 | fisetin | 0.96 ± 0.05 |
| **29** | 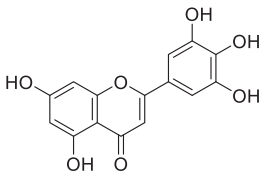 | N/A | 0.16 ± 0.02 |
| **48** | 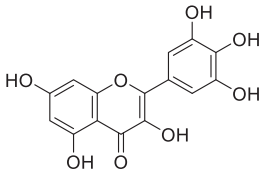 | myricetin | 0.76 ± 0.03 |
| **49** | 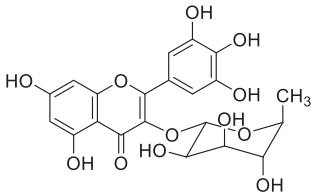 | myricitrin | 1.8 ± 0.1 |
| **25** | 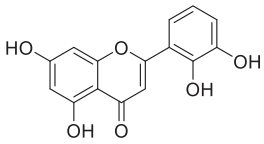 | N/A | 17 ± 2 |
| **50** | 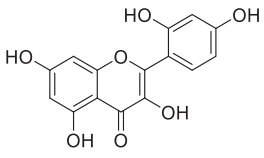 | morin | 9 ± 1 |

**Table 1** (*continued*)

| Compound | Structure | Trivial name | $IC_{50}$ (μM) (AlphaScreen) |
|---|---|---|---|
| **51** | 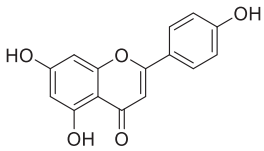 | apigenin | >50 |
| **52** | 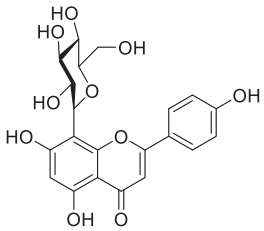 | vitexin | 1.9 ± 0.1 |
| **53** | 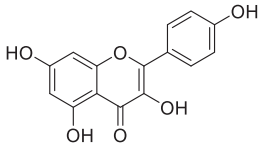 | kaempferol | 16 ± 3 |
| **27** | 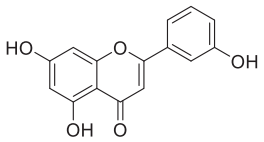 | N/A | >50 |
| **54** | 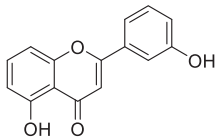 | N/A | >50 |
| **55** | 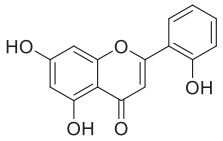 | N/A | >50 |
| **36** | 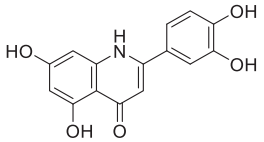 | azaluteolin | 0.068 ± 0.002 |
| **37** | 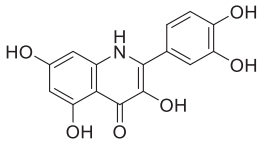 | azaquercetin | 0.2 ± 0.02 |

demonstrated that substitution at C3 is tolerated. The introduction of a methoxy group at C6 of the luteolin scaffold led to nepetin (**43**), which exhibited an inhibition activity comparable to that of quercetin ($IC_{50}$ = 0.93 μM *versus* $IC_{50}$ = 0.67 μM). However, the introduction of a bulky glucose residue at the same position led to a loss of inhibition (see 6-*C*-β-D-glucoside isoorientin **44**), which may indicate an unfavorable steric hindrance. Cynaroside (**45**), a luteolin 7-*O*-β-D-glucoside, showed an acceptable inhibitory potency ($IC_{50}$ = 32 μM). Likely, the C7 position is not as sensitive to modification as C6. Orientin (**46**), originally chosen as another luteolin glucoside to ensure comprehensive SAR data, unexpectedly surpassed the inhibition potency of luteolin ($IC_{50}$ = 0.043 μM *versus* $IC_{50}$ = 0.072 μM of luteolin).

Constitutional isomers **24** and **26**, along with fisetin (**47**), exhibited a relatively flat SAR. This could be because the 3′,4′-dihydroxyflavone scaffold of **40** is the actual pharmacophore, and the introduction of a hydroxyl group at C5 or C7 is unable to significantly improve the inhibitory potency. On the other hand, the presence of a free hydroxyl group at both C5 and C7 on the 3′,4′-dihydroxyflavone scaffold led to the most potent compound (see **4**

and **41** *versus* **40**). The $IC_{50}$ values determined for **29** and its C3−OH congener **48** (myricetin) fit into this hypothesis. Our data also showed the luteolin congener **29** to be slightly more active than quercetin congener **48**, in agreement with the trend observed for parent compounds **4** and **41**. Glycosidation of myricetin at C3 is well-tolerated, as evidenced by the inhibitory potency of myricitrin (**49**). This finding fits with the data provided for **4** and its glycoside **42**.

We next set out to elucidate the effect of the 3′,4′-dihydroxy motif on the activity. Compounds **25** and **50** carry two hydroxyl groups on the B ring, although the 3′,4′-dihydroxy pattern is lacking, and both exhibit a significantly decreased inhibitory activity compared to luteolin. The presence of only one hydroxyl group on ring B, regardless of dihydroxylation at C5 and C7, appeared insufficient for binding potency, as is seen with apigenin (**51**). Surprisingly, vitexin (**52**), an apigenin-8-*C*-glucoside, had an $IC_{50} = 1.9$ μM. Clearly, the introduction of a glycoside residue at C8 to some extent counterbalanced the lack of the 3′,4′-dihydroxy motif on ring B. We observed a similar effect of the 8-*C*-glucoside in the case of orientin (**46**). Kaempferol (**53**), with an $IC_{50} = 16$ μM, also indicated the positive effect of C3−OH on a substrate lacking the otherwise required 3′,4′-dihydroxy motif. Compounds **27** and **54**, **55** are other apigenin congeners that are monohydroxylated on ring B and, accordingly, did not exhibit any activity in the assay. Compounds **36** and **37**, aza-analogues of luteolin and quercetin, share structural features with the corresponding flavonoids and showed a comparable inhibitory potency.

Having identified the inhibitory potency of flavones and flavonols, we set out to explore analogues with a saturated double bond between C2 and C3 in the C-ring (Table 2). Eiodictyol (**56**), taxifolin (**57**), and dihydromyricetin (**58**) belong to a subgroup of compounds with an (*S*)-configuration on stereocenter C2 and possess at least four hydroxyl groups at C3', C4', C5, and C7. Both **57** and **58** have an additional hydroxyl group at C3, and **58** has one more at C5'. Therefore, it shares similar structural features with myricetin and EGCG (**3**). All three compounds exhibited reduced inhibition, indicating that saturation of the flavonoid scaffold led to decreased inhibitory potency. The purchased enantiomers of catechin (**59** and **60**) and their stereoisomer (−)-epicatechin (**61**) displayed even more reduced effects, with $IC_{50}$ values close to or greater than 50 μM. On the other hand, epigallocatechin (**62**) and its gallate ester EGCG (**3**) proved to be good inhibitors of influenza endonuclease ($IC_{50} = 3.3$ μM and $IC_{50} = 0.87$ μM, respectively). Our results are consistent with the literature data [12]. The inhibition potencies indicated a favorable effect of the galloyl moiety of ring-B in **62** and **3**. However, this moiety is not capitalized on in the case of structurally similar **58**. This could be attributed to $sp^2$ hybridization of C4 in the structure of **58** rather than to a different spatial orientation of the hydroxyl group at C3, as changes at this position are well-tolerated. The 3-hydroxyflavanone derivatives silybin (**63**), silychristin (**64**), and silydianin (**65**) were inactive in the AlphaScreen assay. This confirms our hypothesis that a lack of the 3′,4′-dihydroxy motif effectively suppresses the inhibition effect.

With two well-established assays at our disposal, we next evaluated several structurally diverse classes of compounds featuring potential metal-binding moieties. From a set of selected polyols, ten showed significant activity against endonuclease ($IC_{50} < 50$ μM, Table 3). The isoflavonoid genistein (**66**) proved to be completely inactive. This finding supported our hypothesis regarding the essential 3′,4′-dihydroxyphenyl motif and pointed to the need for a particular spatial orientation. Isocoumarin thunberginol A (**67**) exhibited comparable inhibitory potency to flavone **24**. A copper(II)-mediated rearrangement of **4** furnished polyol **68** with a contracted C-ring [87]. Obviously, **68** features some of quercetin structural motifs, which seems to account for its moderate activity against PA endonuclease. Compounds **69**−**71** did not display inhibitory activity, although they possess a potential metal-binding motif. Acid **71** was previously reported as an anti-influenza agent but the mechanism of action was not fully elucidated [88]. Clearly, it does not seem to interfere with the PA-Nter domain of RNA-polymerase. The moderate inhibitory activities of gossypol (**72**) and fenoldam mesylate (**73**) could be attributed to the presence of a dihydroxyphenyl moiety. Purpurogallin's structure (**74**) is a textbook example of an efficient metal-binding aromatic polyol, and its strong inhibitory activity ($IC_{50} = 1.5$ μM) was not surprising. Both nalidixic acid (**75**) and narciclasine (**76**) have a structurally rigid and well-arranged assembly of hydroxyl and oxy groups, which apparently do not meet the structural requirements of an endonuclease inhibitor. Both compounds were completely inactive. On the other hand, the structurally similar lapachol (**77**), mompain (**78**), and quambalarine B (**79**) inhibited endonuclease. Lapachol had moderate activity ($IC_{50} = 19$ μM), and the other two were potent submicromolar inhibitors ($IC_{50} = 0.43$ μM and $IC_{50} = 0.29$ μM, respectively). Hence 2,5,7,8-tetrahydroxynaphthoquinone motif in compounds **78** and **79** is another metal-binding pharmacophore described in this work, and its binding mode in the endonuclease calls for further investigation. In addition to aromatic polyols, we also evaluated the inhibitory potency of curcumins, which represent a privileged class of natural compounds with diverse biological effects. Among the curcumin derivatives, only bisdemethylcurcumin (**83**) possessed appreciable inhibitory potencies with $IC_{50}$ value of 1.7 μM. A brief SAR study of congeners **80**−**83** clearly revealed the importance of the dihydroxyphenyl moiety in their structures.

We verified the inhibition effects of the compounds listed in Tables 1−3 with a complementary gel-based endonuclease inhibitory assay. This assay confirmed results gained from AlphaScreen testing in all cases; Fig. S2 (Supplementary Data) shows a representative gel with selected endonuclease inhibitors (potent inhibitors **3**, **4**, **36**, **41**, **48**, **79**, and **83**). Compounds **50** and **76** lacking inhibitory potency were used as negative controls.

The antiviral activities of flavonoids are well documented. However, for the most potent endonuclease inhibitors **4, 37, 41, 74** we analyzed their antiviral activity using an assay based on the prevention of cytopathic activity and tested their cytotoxicity (Fig. S7 in Supplementary Data). These experiments showed rather weak antiviral activities of the tested compounds and confirmed that they show very little if any cytotoxicity.

### *2.4. Crystal structure of the PA-Nter domain in complex with luteolin and quambalarine B*

To understand binding of mentioned polyols to the influenza endonuclease enzyme, we selected two compounds for X-ray crystallographic studies of protein-ligand complexes, taking into account inhibitory potency and aqueous solubility. Luteolin (PDBe ligand LU2) and quambalarine B (PDBe ligand OOH) were soaked into unoccupied protein crystals. The structure of PA-Nter in complex with luteolin was refined to 2.0 Å resolution; quambalarine B was refined up to 2.5 Å, likely due to a prolonged soaking time. In the final crystallographic models, each asymmetric unit consisted of one PA-Nter molecule.

Two octahedrally coordinated metal ions were embedded in the active site (Fig. 5). Due to a strong anomalous signal observed up to 2.3 Å, we determined the proximal ion at site 1 to be fully occupied by a $Mn^{2+}$ cation. The octahedral coordination sphere is formed by the central $Mn^{2+}$ ion, four protein atoms of $N^{\varepsilon 2}$ His-41, $O^{\delta 2}$ Asp-108, $O^{\varepsilon 2}$Glu-119, O Ile-120, and two hydroxyl groups of luteolin. The distal cation at site 2 exhibited lower anomalous scattering, in agreement with a previously reported structural analysis of PA-Nter complexes [11]. This indicates partial occupation of the site

**Table 2**
Structure-activity relationship of flavanones, flavanonols and flavanols.

| Compound | Structure | Trivial name | $IC_{50}$ (μM) (AlphaScreen) |
|---|---|---|---|
| **56** | 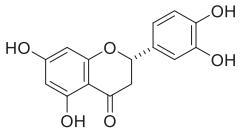 | eriodictyol | 18 ± 3 |
| **57** | 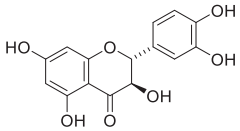 | taxifolin | ~50 |
| **58** | 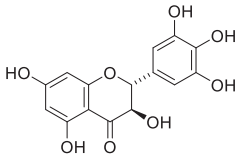 | dihydromyricetin | 22 ± 1 |
| **59** | 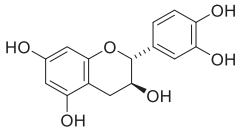 | (+)-catechin | 42 ± 5 |
| **60** | 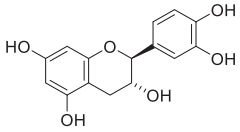 | (−)-catechin | >50 |
| **61** | 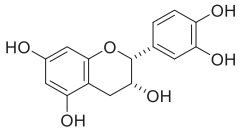 | (−)-epicatechin | >50 |
| **62** | 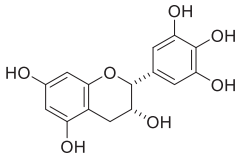 | (−)-epigallo-catechin | 3.3 ± 0.6 |
| **3** | 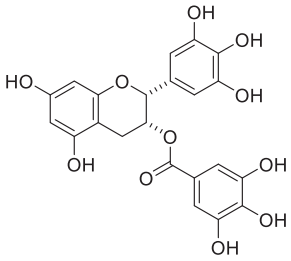 | (−)-epigallo-catechin gallate (EGCG) | 0.87 ± 0.07 |
| **63** | 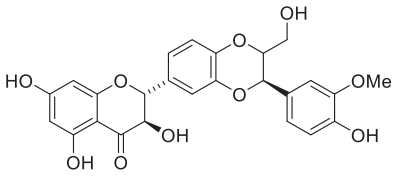 | silybin | >50 |

(*continued on next page*)

**Table 2** (*continued*)

| Compound | Structure | Trivial name | $IC_{50}$ (μM) (AlphaScreen) |
|---|---|---|---|
| **64** | 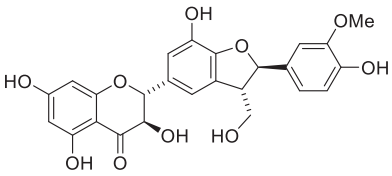 | silychristin | >50 |
| **65** | 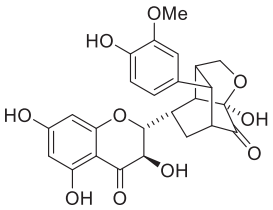 | silydianin | >50 |

with a $Mg^{2+}$ cation, which is coordinated by $O^{\varepsilon 2}$ Glu-80, $O^{\delta}$ Asp-108[1], the C3' hydroxyl group of luteolin, and three water molecules (W1, W2, W3).

Metal ions in enzymatically active PA-Nter (PDB entry 5DES) coordinate two molecules of water (not shown). In the luteolin complex, these waters are replaced with the two hydroxyl groups of the flavonoid's B ring. Clearly, binding to the endonuclease active site utilizes binding mode A (by the 3′,4′-dihydroxyphenyl moiety; see Fig. 3). The flavone scaffold of luteolin creates van der Waals interactions within the pocket between helices α2 and α3 (for sequence and structural alignment of PA-Nter, see Figs. S5 and S6 in Supplementary Data). Additionally, the hydroxyl group at position C7 creates a hydrogen bond with $O^{\varepsilon 2}$ Glu-26 (Figs. 5 and 6A). We can attribute the high affinity of the ligand to the surface complementarity and strong hydrogen bonding network. This satisfactory binding is demonstrated by the well-defined electron density map of luteolin in our crystal structure.

Quambalarine B acts as a tridentate ligand bound to PA-Nter *via* its 7,8-dihydroxynaphthoquinone moiety (Fig. 6B). The ligand affinity is improved by the ketone moiety which contributes to van der Waals interaction with water molecule in first solvation shell of protein. The rest of the ligand molecule is not engaged in direct interactions with protein residues and is oriented towards the solvent. Compared to mompain lacking ketone extension this lipophilic residue slightly enhances affinity.

### 2.5. Molecular modelling of myricetin complex with PA-Nter domain

We also attempted X-ray crystallographic characterization of a PA-Nter complex with myricetin (**48**). However, the electron density of the flavonol was of poor quality; its position in the active site was ambiguous and data did not meet requirements for their deposition into PDB database. Thus, we applied molecular modeling to the acquired data. Initially, we compared the stability of four possible protonation states of bound myricetin in the cluster model. The most favorable state was deprotonated myricetin at C3—OH. Dideprotonated myricetin (i.e., at C3—OH and C5—OH) was less stable by 2.0 kcal/mol. The other two considered protonation states—myricetin deprotonated at C5—OH and the neutral molecule—were also considerably less stable (by 7.1 and 11.2 kcal/mol, respectively). These results indicate that the C3—OH group of myricetin should be deprotonated in the model. The C3—OH group forms close contacts at 2.2 and 2.9 Å with $Mn^{2+}$ and the ε-amino group of Lys-115, respectively. Deprotonated myricetin was further used to evaluate its flexibility while bound in the enzymatic site (Graph S1 in Supplementary Data), indicating that the B ring (3′,4′,5′-trihydroxyphenyl) of myricetin has limited space available for thermal motion. The dihedral angle varied from approximately 30 to 55°, which corresponds to a relative 'free' energy under 0.3 kcal/mol (approximately equal to the energy of the thermal motion at 150 K). This range might represent the lower limit of myricetin's flexibility, as the crystallization and soaking were performed at 291 K. We also modelled a hypothetical complex with a flipped myricetin molecule, in which the positions of C3—OH and C5—OH were exchanged and the C5—OH group was deprotonated (Fig. 7). Interestingly, the energy of the obtained structure was comparable to that of the original model; the energy of the complex with flipped myricetin was less negative by 0.5 kcal/mol. Myricetin coordinated to the PA-Nter cations by binding mode B could likely adopt two different poses, which may account for the deficient electron density map of myricetin, a potent PA endonuclease inhibitor.

### 2.6. Comparison of the binding modes of flavonoids and quambalarine B to the PA-Nter domain

Two binding modes were observed for flavonoids—a bidentate mode (A), which was ascertained in the luteolin complex, and a tridentate mode (B) in the myricetin complex, which was supported by a combination of crystallographic data and molecular modelling. Both binding modes allow the inhibition of endonuclease activity at submicromolar concentrations. Quambalarine B binds to PA-Nter using a tridentate binding mode similar to mode B exploited by flavonols. In general, this mode is advantageous over the bidentate binding mode employing the 3′,4′-dihydroxyphenyl moiety. However, luteolin is able to interact with PA-Nter at both ends. At one end, it coordinates the metal ions (binding mode A) and at the other end the C7 hydroxyl group forms a hydrogen bond with $O^{\varepsilon 2}$ Glu-26. This increases the ligand affinity to an $IC_{50}$ (AlphaScreen) of around 70 nM.

### 2.7. Evaluation of flavonoids as potential influenza neuraminidase inhibitors

To determine the inhibitory potency of flavonoids against influenza neuraminidase, we performed a DNA-linked inhibitor antibody assay (DIANA, see Fig. S3) [74], which allowed

**Table 3**
Inhibition assay of influenza endonuclease using a panel of various natural and synthetic compounds that could potentially bind metal ions.

| Compound | Structure | Trivial name | $IC_{50}$ (μM) (AlphaScreen) |
|---|---|---|---|
| **66** | 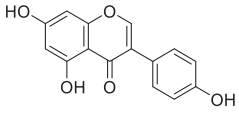 | genistein | >50 |
| **67** | 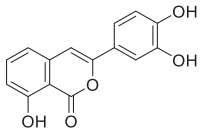 | thunberginol A | 1.4 ± 0.2 |
| **68** | 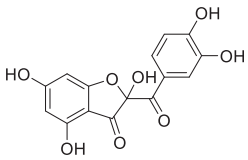 | N/A | 9.8 ± 0.5 |
| **69** | 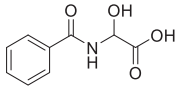 | α-hydroxyhippuric acid | >50 |
| **70** | 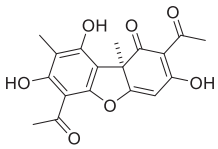 | (+)-usnic acid | >50 |
| **71** | 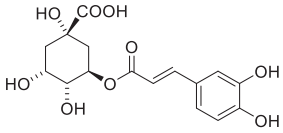 | chlorogenic acid | >50 |
| **72** | 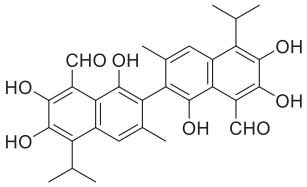 | gossypol | 13 ± 2 |
| **73** | 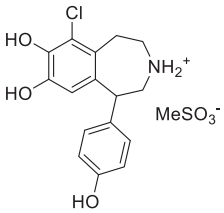 | fenoldam mesylate | 31 ± 6 |
| **74** | 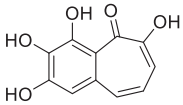 | purpurogallin | 1.5 ± 0.04 |
| **75** | 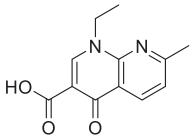 | nalidixic acid | >50 |

(*continued on next page*)

**Table 3** (*continued*)

| Compound | Structure | Trivial name | $IC_{50}$ (μM) (AlphaScreen) |
|---|---|---|---|
| **76** | 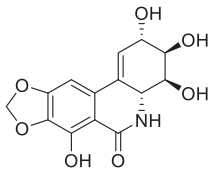 | narciclasine | >50 |
| **77** | 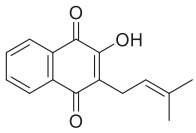 | lapachol | 19 ± 1.5 |
| **78** | 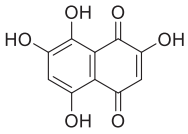 | mompain | 0.43 ± 0.02 |
| **79** | 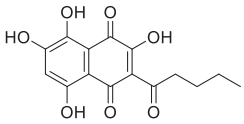 | quambalarine B | 0.29 ± 0.01 |
| **80** | 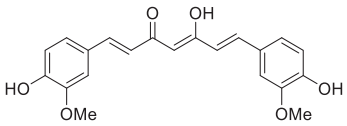 | curcumin | 25 ± 2 |
| **81** | 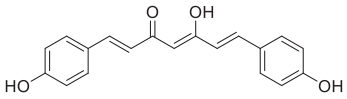 | bisdemethoxycurcumin | >50 |
| **82** | 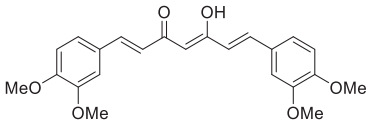 | dimethylcurcumin | >50 |
| **83** | 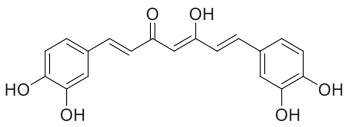 | bisdemethylcurcumin | 1.7 ± 0.3 |

determination of dissociation constants ($K_d$). Screening of a set of representative compounds ruled out any neuraminidase inhibitory activity of flavonoids (**3**, **4**, **41**, **48**, **52**), chlorogenic acid (**71**), quambalarine B (**79**), and bisdemethylcurcumin (**83**). None of these compounds showed inhibition even at 400 μM concentration. Oseltamivir carboxylate (OST), used as a control, exhibited an inhibition constant of 39 ± 8 nM, which is in agreement with recently reported values [74,89].

## 3. Conclusion

Our findings do not support the notion that flavonoids might be inhibitors of influenza neuraminidases [53,54,59,85,90–92]. The data we present confirm some other previous reports suggesting that neuraminidase is not a target for flavonoid inhibitors [56,61,62].

Instead, we identified the N-terminus of the PA subunit of influenza RNA-dependent-RNA polymerase as a target of several flavonoids. Using a novel assay based on AlphaScreen technology and gel-based endonuclease inhibitory assay we identified luteolin (**41**) and its 8-*C*-glycoside orientin (**46**) as the potent inhibitors of the endonuclease.

We determined X-ray structures of the PA-Nter in complex with luteolin at 2.0 Å resolution. We found that the 3′,4′-dihydroxyflavone motif is important for the inhibitory activity. The presence of hydroxyl groups in positions C5 and C7 were highly advantageous for the anti-influenza activity. Our SAR study also, indicate that the presence of the C3 hydroxyl group of flavonoids is only crucial for derivatives lacking a 3′-hydroxyl group. Apigenin (**51**) and its congeners are inactive unless a hydroxyl group is introduced at C3, which results in moderate inhibitory activity (see **50** and **53**). A combination of protein crystallography and molecular modeling revealed that flavonoids with a 3,5-dihydroxyflavone motif can bind PA-Nter through these two hydroxyl groups (binding mode B). In contrast, the introduction of a hydroxyl group at position C3 in 3′,4′-dihydroxyflavone derivatives and their aza-analogues either does not alter their half maximal inhibitory concentration

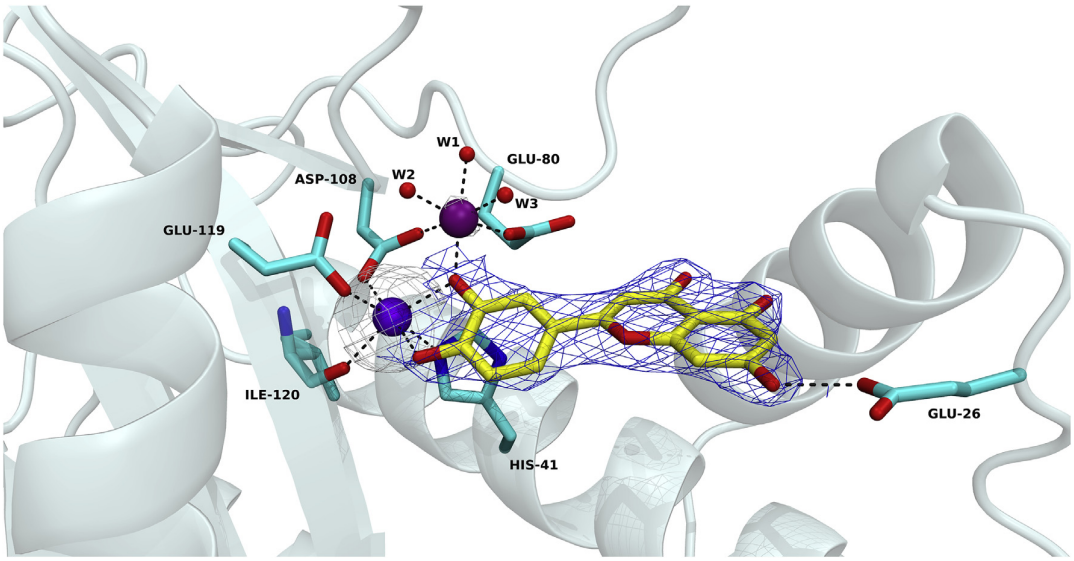


**Fig. 5.** Polar interactions in the PA-Nter active site with bound luteolin (PDB entry 6YA5). The manganese ion at proximal site 1 is shown as a purple-blue sphere and the magnesium ion at site 2 is in purple. The 3′,4′-dihydroxyphenyl moiety of luteolin coordinates the manganese ion, and the hydroxyl group at C7 forms a hydrogen bond with $O^{\varepsilon 2}$ Glu-26. Details of the $2F_o - F_c$ electron density map (contoured at 1.5$\sigma$) are in blue, and electron density for anomalous scattering ($Mn^{2+}$) shown as grey mesh (contoured at 3.5$\sigma$).

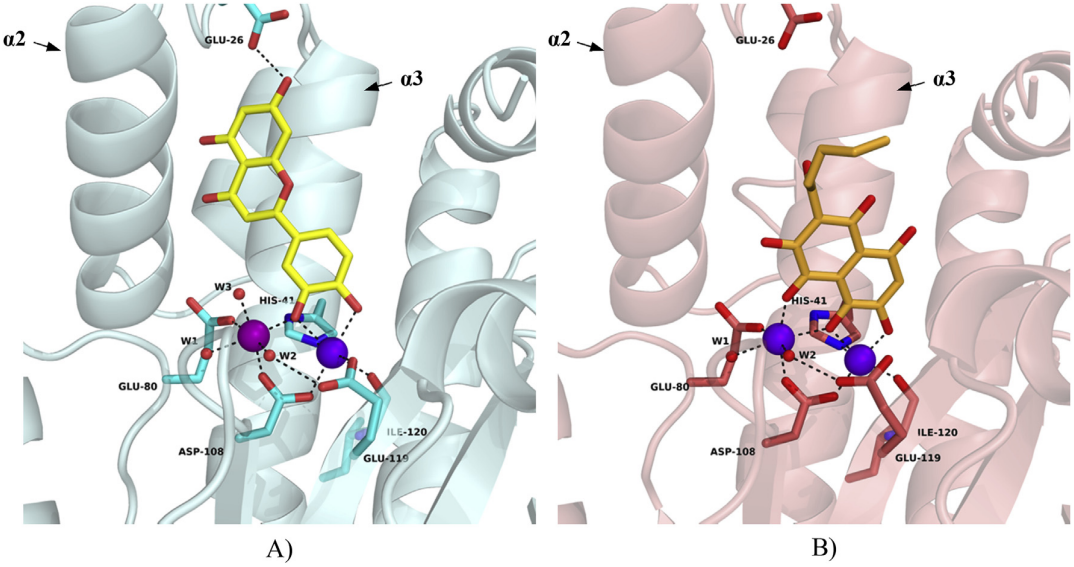


**Fig. 6.** A) Luteolin coordinates ions with the 3′,4′-dihydroxyphenyl moiety (PDB entry 6YA5). Luteolin coordinates metal ions in the protein active site in bidentate mode *via* two hydroxyl groups. On the opposite side of the molecule, the hydroxyl group at C7 forms a hydrogen bond with $O^{\varepsilon 2}$ Glu-26. B). Quambalarine B acts as a tridentate ligand coordinating two manganese ions with a pair of hydroxyls at C7 and C8 and the carbonyl of C1 (PDB entry 6YEM). PA-Nter is shown in cartoon representation; coordinating amino acid residue side chains are in stick representation. Colour coding: Carbon of protein residues cyan (panel A) and salmon (panel B); oxygen, red; nitrogen, blue; manganese ion, purple-blue; magnesium ion, purple.

significantly (compare **26** and **47**) or it leads to reduced inhibitory potency (compare **41** and **4**, **36** and **37**, and **29** and **48**). A substitution at C8 was not only well-tolerated but resulted in increased inhibition potency when a *C*-glycoside was introduced.

In addition, we described a new metal-binding motif in PA endonuclease inhibitors featuring a tetrahydroxynaphthoquinone moiety and structurally characterized quambalarine B in complex with the PA-Nter domain.

Through the use of two different assays, along with structural analysis of the complexes of PA-Nter with luteolin and myricetin, we identified and characterized the molecular mode-of-action of flavonoids in influenza-infected cells. Our findings reveal two distinct binding modes for flavonoids and identified an additional point of interaction at C7 that could play a pivotal role in the design of next-generation PA endonuclease inhibitors.

## 4. Experimental section

### *4.1. Cloning, expression, and purification of recombinant proteins*

DNA encoding the N-terminal domain of influenza polymerase acidic subunit (PA-Nter) from viral strain A/California/07/2009

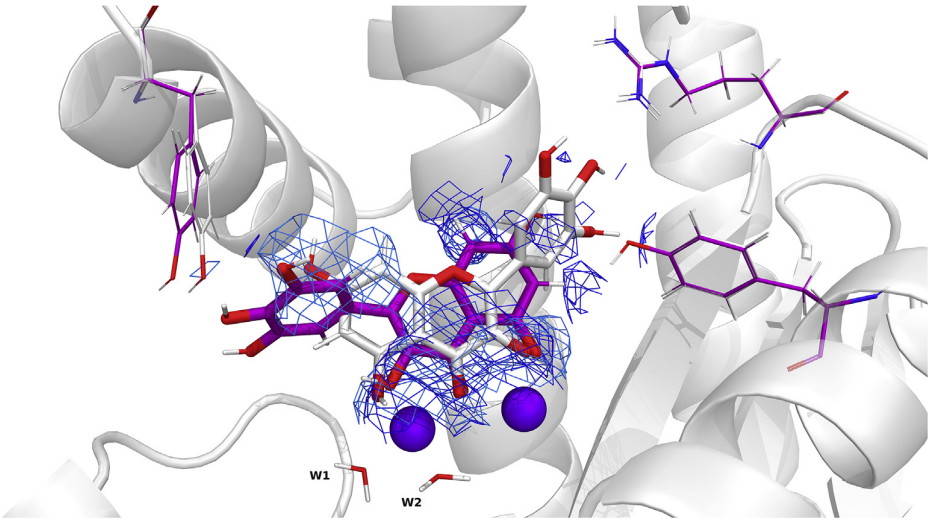


**Fig. 7.** Comparison of the two modelled optimized QM/MM structures of myricetin bound to the N-terminus of PA. Two orientations are based on rough estimates of the myricetin from the X-ray structure analyses. Carbon atoms of myricetin in its "native" binding mode are in white. Carbon atoms of the "hypothetical" complex with flipped myricetin are in purple. Colour coding: oxygen, red; nitrogen, blue; manganese ion, purple-blue.

(H1N1) (GenBank accession No. CY121685.1) with the flexible loop (residues 51–72) replaced with a GGS linker was prepared by GenScript USA Inc [13]. Two constructs with affinity tags, GST-PA-Nter and $His_6$-SUMO-PA-Nter, were prepared. PA-Nter was inserted into a plasmid pGEX-1λT. Second, PA-Nter with a $(GS)_4$ linker N-terminal extension was inserted between the *Bam*HI and *Xho*I sites of plasmid pETM11-SUMO3. Both tagged PA-Nter constructs were expressed in *E. coli* BL21 (DE3) RIL cells. Cells were harvested and resuspended in lysis buffer [25 mM Tris/HCl, pH 7.5, 150 mM NaCl, 1 mM EDTA (GST) or 50 mM Tris/HCl, pH 8.0, 200 mM NaCl, 10 mM imidazole ($His_6$-SUMO)] and lysed with an Emulsiflex device (Avestin) at a pressure of 1200 bar. For the GST construct, soluble proteins were loaded onto a glutathione-agarose column (ThermoScientific) and subsequently eluted with 50 mM Tris/HCl, pH 7.5, 150 mM NaCl, 10 mM reduced L glutathione, 1 mM EDTA. In the same manner, $His_6$-SUMO-tagged PA-Nter was purified on Ni-NTA Agarose (Roche) and eluted with 50 mM Tris/HCl, pH 8.0, 200 mM NaCl, 250 mM imidazole. The $His_6$-SUMO tag was removed with ULP1 protease. Both proteins were further purified by gel filtration chromatography, yielding >95% purity as assessed by SDS-PAGE.

### 4.2. AlphaScreen assay

AlphaScreen experiments were performed using a Perkin Elmer Enspire plate reader in 96 well ProxiPlates. Biotinylated **12** was captured on Streptavidin-coated donor beads (Perkin Elmer). Separately, GST-PA-Nter fusion protein was bound to GSH-coated acceptor beads (Perkin Elmer). These solutions were incubated for 60 min at RT in the dark and subsequently mixed together and incubated for an additional 120 min. In experiments screening for endonuclease inhibitors, compounds were mixed with both types of beads prior to the 120-min incubation. We first evaluated the optimal concentrations of GST-PA-Nter and biotinylated **12**. For further screening experiments, 15 nM biotinylated **12** and 50 nM GST-PA-Nter were used. The concentrations of donor and acceptor beads were 5 μg/mL in a 50 μL reaction volume. All experiments were performed in 25 mM Tris-HCl, pH 7.4, 150 mM NaCl, 0.05% Tween20, 1 mM $MnCl_2$, 10 mM $MgCl_2$, 1 mM 2-mercaptoethanol.

### 4.3. Gel-based endonuclease inhibitory assay

The endonuclease inhibitory activities of selected flavonoids were verified by *in vitro* cleavage of single-stranded DNA substrate M13mp18 (New England Biolabs). Each 10-μL reaction contained 1 μM GST-PA-Nter in digestion buffer (25 mM Tris-HCl, pH 7.4, 150 mM NaCl, 0.05% Tween20, 1 mM $MnCl_2$, 10 mM $MgCl_2$, 1 mM 2-mercaptoethanol) incubated with 10 μM flavonoid and initiated by addition of 0.2 μg M13mp18 plasmid. Reactions were incubated at 37 °C for 4 h, stopped by adding 1 μL of 0.2 M EDTA, and visualized by agarose electrophoresis using a 1% agarose gel stained with GelRed.

### 4.4. Crystallization and diffraction data collection

Hexagonal bifrustum crystals (Fig. S1) of the PA-Nter subunit without ligand were obtained by the hanging-drop vapour diffusion technique at 291 K by mixing 1 μL protein solution (19.2 $mg \cdot mL^{-1}$) with 1 μL crystallization reservoir solution (12.5% w/v MDP, 12.5% w/v PEG 1000, 12.5% w/v PEG 3350, 0.1% M MOPS/HEPES-Na pH 7.5, 0.06 M magnesium chloride, 0.06 M calcium chloride) and 0.2 μL PA seed. Crystals appeared in 2 days and grew up to 200 μm in diameter within one week. Crystals were soaked for 2 h with luteolin or 12 h with quambalarine B in reservoir solution supplemented with 100 mM ligand solution (final 10% DMSO concentration). Crystals were flash-cooled by plunging into liquid nitrogen and were stored in liquid nitrogen.

Diffraction data were collected at 100 K on a home diffractometer (MicroMax-007 HF microfocus equipped with a PILATUS 300 K detector, Rigaku). The crystal of PA-Nter soaked with luteolin (LU2) diffracted to a resolution of up to 2.0 Å and the quambalarine B crystal (OOH) up to 2.5 Å. Diffraction data were processed, integrated, and reduced using XDS [93] and scaled using XSCALE from XDS suite [94]. The crystals belonged to the $P6_422$ space group and contained one molecule in the asymmetric unit, with a solvent content of approximately 47%. There were clear anomalous signals up to resolution of 2.3 Å and 3.7 Å, respectively; therefore, data were processed with unmerged Friedel pairs. Crystal parameters and data-collection statistics are given in Table S1.

### 4.5. Structure determination and analyses

Structures of PA-Nter were determined by molecular replacement with MOLREP [95] from the CCP4 package [96] interspersed with manual adjustments in Coot [97], using a previously determined PA-Nter structure as template (PDB entry 5CGV [98]). Refinement was carried out using REFMAC 5.8.0103 [99].

The quality of the final models was validated with MolProbity [100]. Refinement statistics are given in Table S1. All figures showing structural representations were prepared with PyMOL. Atomic coordinates and experimental structure factors have been deposited in the Protein Data Bank under codes 6YA5 and 6YEM for PA-Nter−LU2 and PA-Nter−OOH, respectively.

### 4.6. Molecular modelling

#### 4.6.1. Structure preparation

To study the flexibility of myricetin in the active site of the PA-Nter domain computationally, we used rough estimates of the myricetin position from the X-ray structure analyses. Hydrogens were added with the Reduce and LeaP modules in the AMBER 14 package [101]. Protonation of histidines was assigned individually based on visual inspection of their surroundings; histidine residues 41 and 109 were protonated at ND1 and histidine residues 55, 125, and 127 at NE2. The protein N-terminus, lysines, and arginines were positively charged, while the C-terminus, glutamates, and aspartates were negatively charged. The protonation state of myricetin was determined at the DFT-D3/B-LYP/DZVP [102] level with the implicit solvent COSMO model [103] on a cluster model that contained residues His41, Glu61, Asp89, Glu100, Ile101, Lys115, two $Mn^{2+}$ ions, two water molecules (Wat1 and Wat2), and myricetin (186 atoms in total). To keep the number of atoms and charge constant, we added the sum of the DFT-D3/B-LYP/DZVP energy and experimental solvation free energy [104,105] of two $H_2O$ molecules for neutral myricetin, of $H_2O$ and $H_3O^+$ for deprotonated myricetin, and of two $H_3O^+$ for dideprotonated myricetin. The most favorable protonation state of myricetin was further used in a model with the entire protein receptor. The added hydrogen atoms were relaxed by annealing (10 ps) from 600 to 10 K and by gradient optimization in the SANDER module of the AMBER 14 package [101].

#### 4.6.2. Methodology used

A hybrid QM/MM methodology was utilized. The QM part was treated with the DFT-D/B-LYP/DZVP method [102] and comprised residues within 3 Å of myricetin and 2.5 Å of $Mn^{2+}$ ions. The rest of the system was described at the MM level. We used the parm14SB force field [106] for the protein. The MM parameters for $Mn^{2+}$ were adopted from UFF [107]. The ligand atoms were described by the General Amber Force Field (GAFF) [106]. The partial charges on the ligand atoms were assigned according to the Restricted Electrostatic Potential (RESP) procedure calculated on the HF/6−31G level [108]. The protein surroundings were modelled using the IGB7 implicit solvent model implemented in AMBER 14. Crystallographic water molecules Wat1 and Wat2 were also considered. The coupling between the QM and MM parts was performed with the CUBY4 program [109], which called Turbomole 7.0 [110] for QM and AMBER 14 [101] for MM. A harmonic potential applied on the C3−C2−C1′-C2' dihedral angle of myricetin was utilized to study the conformational space of the bound molecule. Myricetin, Tyr24, Arg105, Tyr111, and all hydrogen atoms were optimized during gradient optimizations; the remaining atoms were frozen in crystallographic positions.

### 4.7. Chemistry

Unless otherwise noted, all reactions were carried out under argon in oven-dried glassware. Solvents were distilled from drying agents as indicated and transferred under argon: THF (Na/benzophenone), toluene (Na/benzophenone), MeCN ($CaH_2$), and DCM ($CaH_2$). Chromatography was performed using Fluka silica gel 60 (0.040−0.063 mm) or Merck silica gel 60; RP-18 $F_{254}$ −coated aluminum sheets were used. Spots were detected both by UV light and a solution of $Ce(SO_4)_2 \cdot 4H_2O$ (1%) and $H_3P(Mo_3O_{10})_4$ (2%) in 10% sulfuric acid. All starting materials were used as purchased (Sigma Aldrich, Alfa Aesar, Strem Chemicals), unless otherwise indicated. All inhibitors were purified using a Jasco preparative HPLC (flow rate 10 mL/min; gradient 2−100% ACN in 50 min), with a Waters SunFire C18 OBD Prep Column, 5 μm, 19 × 150 mm. The purity of compounds was tested on an analytical Jasco PU-1580 HPLC (flow rate 1 mL/min, invariable gradient 2−100% ACN in 30 min) with a Watrex C18 Analytical Column, 5 μm, length 250 mm. The final inhibitors were of at least 95% purity. $^1$H NMR spectra were recorded on Bruker instruments at 300, 400, or 600 MHz; $^{13}$C NMR spectra at were recorded at 75, 100, or 150 MHz. Chemical shifts are provided in $\delta$-scale; coupling constants $J$ are given in Hz. The EI mass spectra were determined at an ionizing voltage of 70 eV; $m/z$ values are given alone with their relative intensities (%). ESI mass spectra were recorded using a ZQ micromass mass spectrometer (Waters) equipped with an ESCi multimode ion source and controlled by MassLynx software. Methanol was used as the solvent.

Compounds **67** [111], **68** [87], **74** [112], and **83** were prepared according to literature procedures. Analytical data for these compounds were in agreement with published data. Mompain (**78**) and quambalarine B (**79**) were isolated from the fungus *Quambalaria cyanescens* [113]. Compounds **3**, **4**, **39**, **41**, **46**, **48**, **49**, **50**, **51**, **52**, **53**, **59**, **60**, **61**, **62**, **66**, **69**, **72**, **73**, **75**, and **77** were purchased from Sigma Aldrich; **54** and **55** from BroadPharm; **44**, **45**, **56**, and **58** from MedChemExpress; **42** and **43** from BOC Sciences; and **40**, **47**, **70**, **71**, **80**, and **81** from TCI Europe.

### 4.8. Probe synthesis

#### 4.8.1. 3-(tert-Butyl) 1-methyl 4-(2-(2-(2-(2-azidoethoxy)ethoxy) ethoxy)ethoxy)isophthalate (**6**)

The linker 11-azido-3,6,9-trioxa-undecanyl *p*-toluenesulfonate (0.93 g, 2.5 mmol) was added to a solution of 3-(*tert*-butyl) 1-methyl 4-hydroxyisophthalate (0.57 g, 2.2 mmol) and potassium carbonate (0.62 g, 5.0 mmol) in DMF (10 mL). The reaction mixture was stirred at 60 °C for 24 h. The reaction was quenched with water (100 mL), and the mixture was extracted with EtOAc (3 × 30 mL). The combined organic layers were washed with water (2 × 15 mL) and brine (10 mL), evaporated to dryness, and purified by flash chromatography (hexane/EtOAc 1:1) to yield **6** (0.96 g, 94%). $^1$H NMR (300 MHz, $CDCl_3$) δ 8.32 (d, $J$ = 2.3 Hz, 1H), 8.06 (dd, $J$ = 8.8, 2.3 Hz, 1H), 6.96 (d, $J$ = 8.8 Hz, 1H), 4.23 (dd, $J$ = 5.6, 4.4 Hz, 2H), 3.93−3.84 (m, 2H), 3.88 (s, 3H), 3.77−3.69 (m, 2H), 3.68−3.61 (m, 8H), 3.36 (dd, $J$ = 5.6, 4.6 Hz, 2H), 1.57 (s, 9H). $^{13}$C NMR (75 MHz, $CDCl_3$) δ 166.3, 165.2, 161.3, 134.2, 132.9, 129.9, 128.1, 122.4, 112.7, 81.7, 71.1, 70.9, 70.8, 70.2, 69.5, 68.7, 52.2, 50.8, 28.3 (3x). HRMS (ESI) $m/z$ calcd for $C_{21}H_{31}N_3O_8Na$ $[M+Na]^+$ 476.2003, found 476.2003.

#### 4.8.2. 4-(2-(2-(2-(2-Azidoethoxy)ethoxy)ethoxy)ethoxy)-3-(tert-butoxycarbonyl)benzoic acid (**7**)

An aqueous solution of sodium hydroxide (8.2 mL, 0.5 M) was added to a solution of **6** (0.93 g, 2.05 mmol) in 1,4-dioxane (10 mL). The reaction mixture was stirred for 24 h at room temperature

under an inert atmosphere. Consumption of the starting material was monitored by TLC. Once the reaction was complete, the pH of the reaction was neutralized by addition of amberlite IR 120. Amberlite was filtered out and the beads were rinsed with methanol several times. The filtrate was then evaporated to dryness under reduced pressure, and the remaining product was purified by flash chromatography to afford the desired free acid **7** (0.90 g, 97%). $^1$H NMR (300 MHz, $CDCl_3$) δ 8.38 (d, $J$ = 2.3 Hz, 1H), 8.11 (dd, $J$ = 8.8, 2.3 Hz, 1H), 6.98 (d, $J$ = 8.9 Hz, 1H), 4.24 (t, $J$ = 4.9 Hz, 2H), 3.90 (dd, $J$ = 5.6, 4.2 Hz, 2H), 3.73 (dt, $J$ = 5.2, 2.0 Hz, 2H), 3.69–3.58 (m, 8H), 3.35 (t, $J$ = 5.0 Hz, 2H), 1.57 (s, 9H). $^{13}$C NMR (75 MHz, $CDCl_3$) δ 170.7, 164.9, 161.9, 134.8, 133.6, 123.0, 121.5, 112.7, 81.7, 71.0, 70.8, 70.7, 70.7, 70.1, 69.4, 68.7, 50.7, 28.3. HRMS (ESI) *m/z* calcd for $C_{20}H_{29}N_3O_8Na$ $[M+Na]^+$ 462.1847, found 462.1848.

#### 4.8.3. 3-(tert-Butoxycarbonyl)-4-((2,2-dimethyl-4-oxo-3,8,11,14-tetraoxa-5-azahexadecan-16-yl)oxy)benzoic acid (**8**)

Compound **7** (0.64 g, 1.46 mmol) and Lindlar catalyst (0.19 g, 30 wt%) were suspended in methanol (15 mL). The flask was first purged with argon, and hydrogen gas was bubbled through the solution for 1 h. The catalyst was filtered out and the filtrate was evaporated to dryness under reduced pressure. The resulting crude product was dissolved in DCM (15 mL), the reaction was cooled down in an ice bath, and triethylamine (0.4 mL, 2.92 mmol) and di-*tert*-butyl dicarbonate (0.38 g, 1.75 mmol) were added. After stirring the reaction for 24 h at room temperature, the mixture was diluted with DCM (20 mL) and the organic phase was washed with a saturated solution of ammonium chloride (2 × 5 mL) and brine (5 mL). The organic layer was then evaporated to dryness and purified by flash chromatography (DCM/MeOH 20:1) to yield **8** (0.48 g, 64%). $^1$H NMR (300 MHz, $CDCl_3$) δ 8.36 (d, $J$ = 2.3 Hz, 1H), 8.09 (dd, $J$ = 8.8, 2.3 Hz, 1H), 6.96 (d, $J$ = 8.9 Hz, 1H), 5.11 (s, 1H), 4.24 (dd, $J$ = 5.7, 4.2 Hz, 2H), 3.90 (dd, $J$ = 5.5, 4.3 Hz, 2H), 3.74 (dt, $J$ = 4.5, 3.1 Hz, 2H), 3.68–3.55 (m, 6H), 3.52 (t, $J$ = 5.2 Hz, 2H), 3.36–3.19 (m, 2H), 1.57 (s, 9H), 1.42 (s, 9H). $^{13}$C NMR (75 MHz, $CDCl_3$) δ 170.1, 165.0, 161.7, 149.5, 134.8, 133.5, 122.9, 122.0, 112.6, 81.7, 79.3, 71.0, 70.7, 70.6, 70.3 ( × 2), 69.5, 68.7, 40.5, 28.5 ( × 3), 28.3 ( × 3). HRMS (ESI) *m/z* calcd for $C_{25}H_{40}NO_{10}$ $[M+H]^+$ 514.2647, found 514.2646.

#### 4.8.4. 3-(tert-Butyl) 1-(2,5-dioxopyrrolidin-1-yl) 4-((2,2-dimethyl-4-oxo-3,8,11,14-tetraoxa-5-azahexadecan-16-yl)oxy)isophthalate (**9**)

Compound **8** (0.48 g, 0.94 mmol) was dissolved in THF (17 mL) under an inert atmosphere followed by addition of *O*-(benzotriazol-1-yl)-*N*,*N*,*N*′,*N*′-tetramethyl-uronium tetrafluoroborate (0.39 g, 1.22 mmol) and triethylamine (0.26 mL, 0.22 mmol). The reaction was stirred for 10 min at room temperature, and *N*-hydroxysuccinimide (0.016 g, 1.88 mmol) was added. After stirring for 16 h at room temperature, the solvent was evaporated under reduced pressure and the resulting mixture was purified by flash chromatography (DCM/MeOH 20:1) to afford the activated ester **9** (0.47 g, 81%). $^1$H NMR (300 MHz, $CDCl_3$) δ 8.40 (d, $J$ = 2.3 Hz, 1H), 8.13 (dd, $J$ = 8.8, 2.2 Hz, 1H), 7.02 (d, $J$ = 8.9 Hz, 1H), 5.01 (bs, 1H), 4.24 (t, $J$ = 5.0 Hz, 2H), 3.88 (q, $J$ = 5.1 Hz, 2H), 3.71 (dd, $J$ = 6.1, 3.5 Hz, 2H), 3.60 (dd, $J$ = 14.6, 3.6 Hz, 6H), 3.49 (t, $J$ = 5.3 Hz, 2H), 3.26 (q, $J$ = 5.5 Hz, 2H), 2.86 (s, 4H), 1.54 (s, 9H), 1.39 (s, 9H). $^{13}$C NMR (75 MHz, $CDCl_3$) δ 169.4 (x2), 164.3, 162.8, 161.0, 156.0, 135.2, 134.0, 123.4, 116.8, 113.0, 81.9, 79.1, 71.0, 70.6, 70.6, 70.2, 70.2, 69.3, 68.8, 40.4, 28.45 ( × 3), 28.2 ( × 3), 25.7 ( × 2). HRMS (ESI) *m/z* calcd for $C_{29}H_{42}N_2O_{12}Na$ $[M+Na]^+$ 633.2630, found 633.2630.

#### 4.8.5. tert-Butyl (Z)-5-(4-(4-(tert-butoxy)-3-hydroxy-4-oxobut-2-enoyl)-4-(4-chlorobenzyl)- piperidine-1-carbonyl)-2-((2,2-dimethyl-4-oxo-3,8,11,14-tetraoxa-5-azahexadecan-16-yl)oxy) benzoate (**11**)

Compound **10** (0.065 g, 0.136 mmol) was dissolved in DCM (1 mL), and the resulting solution was cooled down in an ice bath. Trifluoroacetic acid (100%, 0.2 mL) was added, and the reaction was stirred for 15 min at room temperature. Once TLC showed total consumption of the starting material, the solvents were evaporated under reduced pressure, and the resulting oil was dried under high vacuum for 2 h. The dried mixture was then dissolved in DCM (1.5 mL) followed by addition of triethylamine (0.3 mL) and **9** (0.082 g, 0.136 mmol). The reaction mixture was stirred overnight at room temperature. The solvents were removed under reduced pressure, and the residue was purified by flash chromatography (DCM/MeOH 20:1) to yield the desired amide **11** (0.080 g, 68%). $^1$H NMR (400 MHz, $CDCl_3$) δ 14.76 (s, 1H), 7.73 (d, $J$ = 2.3 Hz, 1H), 7.44 (dd, $J$ = 8.6, 2.3 Hz, 1H), 7.20 (d, $J$ = 8.4 Hz, 2H), 6.95 (d, $J$ = 8.6 Hz, 1H), 6.93–6.86 (m, 2H), 6.37 (s, 1H), 5.02 (s, 1H), 4.20 (t, $J$ = 5.0 Hz, 2H), 3.90 (t, $J$ = 5.0 Hz, 2H), 3.78–3.69 (m, 2H), 3.69–3.57 (m, 8H), 3.53 (t, $J$ = 5.1 Hz, 2H), 3.34–3.25 (m, 2H), 3.05 (bs, 2H), 2.84 (s, 2H), 2.25–2.02 (bs, 2H), 1.72 (bs, 2H), 1.56 (s, 9H), 1.56 (s, 9H), 1.43 (s, 9H). $^{13}$C NMR (100 MHz, $CDCl_3$) δ 205.2, 169.6, 169.1, 165.1, 161.0, 159.1, 134.6, 133.8, 133.4, 133.2, 132.0, 131.3 ( × 2), 130.7, 128.6 ( × 2), 127.6, 122.8, 113.3, 99.0, 84.3, 81.7, 71.1, 70.8, 70.7, 70.3, 70.3, 69.6, 68.8, 49.7 ( × 2), 45.7, 40.5, 38.7 ( × 2), 32.9, 28.6 ( × 3), 28.4 ( × 3), 27.9 ( × 3).

#### 4.8.6. 5-(4-((Z)-3-Carboxy-3-hydroxyacryloyl)-4-(4-chlorobenzyl) piperidine-1-carbonyl)-2-((13,35-dioxo-39-((3aR,4R,6aS)-2-oxohexahydro-1H-thieno[3,4-d]imidazole-4-yl)-3,6,9,16,19,22,25,28,31-nonaoxa-12,34-diazanonatriacontyl)oxy) benzoic acid (**12**)

Compound **11** (0.020 g, 0.023 mmol) was dissolved in DCM (1 mL), and the solution was cooled down in an ice bath. Neat trifluoroacetic acid (0.2 mL) was added dropwise, and the reaction was stirred for 15 min. Once TLC showed complete consumption of the starting material, the solvents were evaporated under reduced pressure, and the remaining oil was dried for 3 h under high vacuum. The dried product was dissolved in DCM (1 mL) followed by addition of triethylamine (0.3 mL) and biotin-PEG6-NHS ester (0.016 g, 0.023 mmol). After stirring the reaction for 24 h at room temperature, the solvent was removed under reduced pressure and the remaining mixture dried under high vacuum for 2 h. The crude mixture was dissolved in DCM (1 mL), trifluoroacetic acid (0.5 mL) was added, and the reaction was stirred for 1 h at room temperature. After removing the solvents under reduced pressure, the mixture was purified by preparative HPLC to yield the desired compound **12** (0.004 g, 15%). $^1$H NMR (600 MHz, Methanol-$d_4$) δ 7.87 (d, $J$ = 2.3 Hz, 1H), 7.59 (dd, $J$ = 8.6, 2.3 Hz, 1H), 7.29–7.20 (m, 4H), 7.07–6.99 (m, 2H), 4.49 (ddd, $J$ = 7.9, 5.0, 1.0 Hz, 1H), 4.39–4.25 (m, 4H), 3.94–3.88 (m, 2H), 3.79–3.73 (m, 2H), 3.71 (t, $J$ = 6.2 Hz, 3H), 3.69–3.55 (m, 26H), 3.53 (td, $J$ = 5.5, 4.1 Hz, 4H), 3.35 (td, $J$ = 5.5, 2.5 Hz, 4H), 3.20 (ddd, $J$ = 8.9, 6.0, 4.6 Hz, 1H), 3.06 (bs, 2H), 2.96 (s, 2H), 2.92 (dd, $J$ = 12.7, 5.0 Hz, 1H), 2.70 (d, $J$ = 12.7 Hz, 1H), 2.44 (t, $J$ = 6.2 Hz, 2H), 2.27–2.12 (m, 4H), 1.78–1.55 (m, 6H), 1.49–1.38 (m, 2H). $^{13}$C NMR (150 MHz, Methanol-$d_4$) δ 207.3, 176.1, 174.0, 171.2, 168.6, 167.7, 166.1, 164.7, 160.7, 135.9, 133.9, 133.9, 133.1, 132.7 ( × 2), 132.0, 129.2 ( × 2), 129.2, 129.0, 121.9, 114.9, 71.9, 71.6, 71.6 ( × 7), 71.5, 71.5, 71.4, 71.3, 71.3, 70.6, 70.5, 70.4, 70.3, 68.3, 63.4, 61.6, 57.0, 51.1, 46.6, 45.7, 41.1, 40.4, 40.4, 37.6, 36.7, 34.0, 33.4, 29.8, 29.5, 26.9. HRMS (ESI) *m/z* calcd for $C_{57}H_{82}ClN_5O_{20}S$ $[M+H]^+$ 1224.5035, found 1224.5035.

### 4.9. General procedure I: preparation of chalcone

Potassium hydroxide (3 eq.) was added to a solution of aldehyde (1.2–1.4 eq.) and ketone (1 eq.) in ethanol (7 mL) at 0 °C. The reaction mixture was stirred overnight at room temperature under an inert atmosphere. The reaction mixture was acidified by addition of aqueous hydrogen chloride (5%) and extracted with DCM (3 × 12 mL). The combined organic layers were washed with brine (10 mL), dried over $MgSO_4$, and evaporated to dryness under reduced pressure. The products were purified by column chromatography and crystallized if needed.

#### 4.9.1. (E)-3-(2,3-dimethoxyphenyl)-1-(2-hydroxy-4,6-dimethoxyphenyl)prop-2-en-1-one (**15**)

The title compound was synthesized from 1-(2-hydroxy-4,6-dimethoxyphenyl)ethan-1-one (0.20 g, 1.00 mmol) and 2,3-dimethoxybenzaldehyde (0.20 g, 1.20 mmol) following general procedure I. The product was purified by column chromatography (cyclohexane/EtOAc 2:1) to furnish the chalcone **15** (0.26 g, 75%). $^1$H NMR (400 MHz, $CDCl_3$) δ 14.33 (s, 1H), 8.08 (d, $J$ = 15.8 Hz, 1H), 7.96 (d, $J$ = 15.8 Hz, 1H), 7.23 (dd, $J$ = 8.0, 1.4 Hz, 1H), 7.08 (t, $J$ = 8.0 Hz, 1H), 6.95 (dd, $J$ = 8.1, 1.5 Hz, 1H), 6.11 (d, $J$ = 2.3 Hz, 1H), 5.96 (d, $J$ = 2.3 Hz, 1H), 3.91 (s, 3H), 3.89 (s, 6H), 3.84 (s, 3H). $^{13}$C NMR (100 MHz, $CDCl_3$) δ 193.0, 168.5, 166.3, 162.7, 153.4, 149.0, 137.3, 129.9, 129.0, 124.3, 119.9, 113.8, 106.6, 93.9, 91.4, 61.4, 56.0, 56.0, 55.7. HRMS (ESI) *m/z* calcd for $C_{19}H_{21}O_6$ $[M+H]^+$ 345.1332, found 345.1333.

#### 4.9.2. (E)-3-(3,4-dimethoxyphenyl)-1-(2-hydroxy-6-methoxyphenyl)prop-2-en-1-one (**16**)

The title compound was synthesized from 1-(2-hydroxy-6-methoxyphenyl)ethan-1-one (0.50 g, 3.01 mmol) and 3,4-dimethoxybenzaldehyde (0.70 g, 4.21 mmol) following general procedure I. The product was purified by column chromatography (cyclohexane/EtOAc 2:1) and crystallized from ethanol to furnish the chalcone **16** (0.70 g, 73%). $^1$H NMR (400 MHz, $CDCl_3$) δ 13.20 (s, 1H), 7.88–7.68 (m, 2H), 7.35 (t, $J$ = 8.3 Hz, 1H), 7.24 (dd, $J$ = 8.3, 2.0 Hz, 1H), 7.14 (d, $J$ = 2.0 Hz, 1H), 6.91 (d, $J$ = 8.3 Hz, 1H), 6.62 (dd, $J$ = 8.4, 1.0 Hz, 1H), 6.43 (dd, $J$ = 8.3, 1.0 Hz, 1H), 3.95 (s, 3H), 3.94 (s, 3H), 3.94 (s, 3H). $^{13}$C NMR (100 MHz, $CDCl_3$) δ 194.3, 165.0, 161.0, 151.4, 149.3, 143.4, 135.8, 128.5, 125.6, 123.0, 112.2, 111.3, 111.2, 110.6, 101.7, 56.2, 56.1, 56.0. HRMS (ESI) *m/z* calcd for $C_{18}H_{18}O_5Na$ $[M+Na]^+$ 337.1046, found 337.1047.

#### 4.9.3. (E)-1-(2-hydroxy-4,6-dimethoxyphenyl)-3-(3-methoxyphenyl)prop-2-en-1-one (**17**)

The title compound was synthesized from 1-(2-hydroxy-4,6-dimethoxyphenyl)ethan-1-one (0.32 g, 1.61 mmol) and 3-methoxybenzaldehyde (0.285 g, 2.10 mmol) following general procedure I. The product was purified by column chromatography (toluene) to obtain the chalcone **17** (0.20 g, 38%). $^1$H NMR (400 MHz, $CDCl_3$) δ 14.27 (s, 1H), 7.88 (d, $J$ = 15.6 Hz, 1H), 7.74 (d, $J$ = 15.6 Hz, 1H), 7.32 (t, $J$ = 7.9 Hz, 1H), 7.23–7.19 (m, 1H), 7.12 (dd, $J$ = 2.6, 1.6 Hz, 1H), 6.94 (ddd, $J$ = 8.2, 2.6, 1.0 Hz, 1H), 6.11 (d, $J$ = 2.4 Hz, 1H), 5.96 (d, $J$ = 2.4 Hz, 1H), 3.92 (s, 3H), 3.85 (s, 3H), 3.84 (s, 3H). $^{13}$C NMR (100 MHz, $CDCl_3$) δ 192.7, 168.5, 166.4, 162.6, 160.0, 142.3, 137.1, 130.0, 128.0, 121.1, 115.7, 113.8, 106.5, 93.9, 91.4, 56.0, 55.8, 55.4. HRMS (ESI) *m/z* calcd for $C_{18}H_{19}O_5$ $[M+H]^+$ 315.1227, found 315.1228.

#### 4.9.4. (E)-3-(3,4-dimethoxyphenyl)-1-(2-hydroxy-4-methoxyphenyl)prop-2-en-1-one (**18**)

The title compound was synthesized from 1-(2-hydroxy-4-methoxyphenyl)ethan-1-one (0.75 g, 4.51 mmol) and 3,4-dimethoxybenzaldehyde (0.97 g. 5.87 mmol) following general procedure I. The product was purified by column chromatography (cyclohexane/EtOAc 2:1) and crystallized from ethanol to furnish the chalcone **18** (0.18 g, 13%). $^1$H NMR (400 MHz, $CDCl_3$) δ 13.53 (s, 1H), 7.89–7.85 (m, 1H), 7.83 (s, 1H), 7.44 (dd, $J$ = 15.3, 0.5 Hz, 1H), 7.26 (dd, $J$ = 8.2, 2.2 Hz, 1H), 7.16 (d, $J$ = 2.0 Hz, 1H), 6.91 (d, $J$ = 8.3 Hz, 1H), 6.52–6.46 (m, 2H), 3.97 (s, 3H), 3.94 (s, 3H), 3.86 (s, 3H). $^{13}$C NMR (100 MHz, $CDCl_3$) δ 191.9, 166.8, 166.2, 151.7, 149.4, 144.7, 131.3, 127.9, 123.5, 118.2, 114.3, 111.3, 110.4, 107.8, 101.2, 56.2, 56.2, 55.7. HRMS (ESI) *m/z* calcd for $C_{18}H_{18}O_5Na$ $[M+Na]^+$ 337.1046, found 337.1047.

#### 4.9.5. (E)-1-(2-hydroxy-4,6-dimethoxyphenyl)-3-(3,4,5-trimethoxyphenyl)prop-2-en-1-one (**19**)

The title compound was synthesized from 3,4,5-trimethoxybenzaldehyde (0.57 g, 2.91 mmol) and 1-(2-hydroxy-4,6-dimethoxyphenyl)ethan-1-one (0.48 g, 2.43 mmol) following general procedure I. The product was purified by column chromatography (cyclohexane/EtOAc from 3:1 to 1:1) to furnish the chalcone **19** (0.35 g, 38%). $^1$H NMR (300 MHz, $CDCl_3$) δ 14.32 (s, 1H), 7.81 (d, $J$ = 15.5 Hz, 1H), 7.75–7.66 (m, 1H), 6.84 (d, $J$ = 0.4 Hz, 2H), 6.12 (d, $J$ = 2.4 Hz, 1H), 5.97 (d, $J$ = 2.4 Hz, 1H), 3.91 (s, 6H), 3.91 (s, 3H), 3.90 (s, 3H), 3.84 (s, 3H). $^{13}$C NMR (75 MHz, $CDCl_3$) δ 192.5, 168.6, 166.3, 162.5, 153.5, 142.5, 131.3, 127.1, 106.4, 105.7, 100.1, 94.0, 91.5, 61.2, 56.3, 55.9, 55.8. HRMS (ESI) *m/z* calcd for $C_{20}H_{22}O_7Na$ $[M+Na]^+$ 397.1257, found 397.1258.

### 4.10. General procedure II: cyclization of chalcones

2,3-Dichloro-5,6-dicyano-1,4-benzoquinone (2.0 eq) was added to a solution of chalcone (1.0 eq) in dry 1,4-dioxane (0.1 M). The solution was stirred in a sealed tube at 80 °C for 12 h. The reaction mixture was quenched by addition of water or saturated sodium bicarbonate (10 mL) and extracted with EtOAc (3 × 10 mL). The combined organic layers were washed with brine (10 mL), dried over $MgSO_4$, and evaporated to dryness under reduced pressure. The products were purified by column chromatography.

#### 4.10.1. 2-(2,3-Dimethoxyphenyl)-5,7-dimethoxy-4H-chromen-4-one (**20**)

Compound **15** (0.061 g, 0.17 mmol) was cyclized using general procedure II. Column chromatography (DCM/MeOH 20:1) of the residue furnished the flavone **20** (0.058 g, 95%). $^1$H NMR (400 MHz, $CDCl_3$) δ 7.32 (dd, $J$ = 7.9, 1.5 Hz, 1H), 7.17 (t, $J$ = 8.0 Hz, 1H), 7.05 (dd, $J$ = 8.2, 1.6 Hz, 1H), 6.85 (s, 1H), 6.52 (d, $J$ = 2.3 Hz, 1H), 6.38 (d, $J$ = 2.3 Hz, 1H), 3.95 (s, 3H), 3.92 (s, 3H), 3.90 (s, 3H), 3.88 (s, 3H). $^{13}$C NMR (100 MHz, $CDCl_3$) δ 178.2, 164.3, 161.1, 160.3, 159.4, 153.5, 127.7, 126.4, 124.3, 120.8, 115.0, 113.7, 96.3, 92.9, 67.2, 61.1, 56.5, 56.2, 55.9. HRMS (ESI) *m/z* calcd for $C_{19}H_{19}O_6$ $[M+H]^+$ 343.1176, found 343.1178.

#### 4.10.2. 2-(3,4-Dimethoxyphenyl)-5-methoxy-4H-chromen-4-one (**21**)

Compound **16** (0.20 g, 0.63 mmol) was cyclized using general procedure II. Column chromatography (DCM/MeOH 20:1) of the residue furnished the flavone **21** (0.13 g, 66%). $^1$H NMR (400 MHz, $CDCl_3$) δ 7.58–7.47 (m, 2H), 7.32 (d, $J$ = 2.1 Hz, 1H), 7.11 (dd, $J$ = 8.4, 1.0 Hz, 1H), 6.95 (d, $J$ = 8.5 Hz, 1H), 6.80 (dd, $J$ = 8.3, 0.9 Hz, 1H), 6.65 (s, 1H), 3.98 (s, 3H), 3.95 (s, 3H), 3.93 (s, 3H). $^{13}$C NMR (100 MHz, $CDCl_3$) δ 178.4, 161.1, 159.8, 158.3, 151.9, 149.3, 133.7, 124.0, 119.8, 114.6, 111.2, 110.2, 108.7, 108.1, 106.5, 56.6, 56.2 (2 ×). HRMS (ESI) *m/z* calcd for $C_{18}H_{17}O_5$ $[M+H]^+$ 313.1070, found 313.1071.

#### 4.10.3. 5,7-Dimethoxy-2-(3-methoxyphenyl)-4H-chromen-4-one (**22**)

Compound **17** (0.10 g, 0.32 mmol) was cyclized using general procedure II. Column chromatography (DCM/MeOH 20:1) of the

residue furnished the flavone **22** (0.095 g, 94%). $^1$H NMR (400 MHz, $CDCl_3$) δ 7.45 (dt, $J$ = 7.8, 1.3 Hz, 1H), 7.40 (d, $J$ = 8.0 Hz, 1H), 7.37 (dd, $J$ = 2.5, 1.5 Hz, 1H), 7.03 (ddd, $J$ = 8.0, 2.6, 1.1 Hz, 1H), 6.66 (s, 1H), 6.56 (d, $J$ = 2.3 Hz, 1H), 6.37 (d, $J$ = 2.3 Hz, 1H), 3.95 (s, 3H), 3.90 (s, 3H), 3.87 (s, 3H). $^{13}$C NMR (100 MHz, $CDCl_3$) δ 177.8, 164.2, 161.0, 160.6, 160.1, 160.0, 133.0, 130.1, 118.5, 117.0, 111.4, 109.4, 109.4, 96.3, 92.9, 56.6, 55.9, 55.6. HRMS (ESI) *m/z* calcd for $C_{18}H_{16}O_5Na$ $[M+Na]^+$ 335.0889, found 335.0890.

#### 4.10.4. 2-(3,4-Dimethoxyphenyl)-7-methoxy-4H-chromen-4-one (**23**)

Compound **18** (0.18 g, 0.57 mmol) was cyclized using general procedure II. Column chromatography (cyclohexane/EtOAc 1:1) of the residue furnished the flavone **23** (0.074 g, 41%). $^1$H NMR (400 MHz, $CDCl_3$) δ 8.16 (dd, $J$ = 8.7, 0.5 Hz, 1H), 7.57 (dd, $J$ = 8.5, 2.1 Hz, 1H), 7.40 (d, $J$ = 2.2 Hz, 1H), 7.03 (d, $J$ = 2.6 Hz, 1H), 7.00 (q, $J$ = 2.4 Hz, 2H), 6.73 (s, 1H), 4.01 (s, 3H), 3.99 (s, 3H), 3.97 (s, 3H). $^{13}$C NMR (100 MHz, $CDCl_3$) δ 178.0, 164.2, 163.2, 158.1, 152.1, 149.4, 127.2, 124.5, 120.0, 118.0, 114.4, 111.3, 108.9, 106.6, 100.6, 56.3, 56.2, 56.0. HRMS (ESI) *m/z* calcd for $C_{18}H_{17}O_5$ $[M+H]^+$ 313.1070, found 313.1071.

#### 4.10.5. 5,7-Dimethoxy-2-(3,4,5-trimethoxyphenyl)-4H-chromen-4-one (**24**)

Compound **19** (0.37 g, 0.94 mmol) was cyclized using general procedure II. Column chromatography (EtOAc/MeOH 50:1) of the residue furnished the flavone **24** (0.21 g, 57%). $^1$H NMR (300 MHz, $CDCl_3$) δ 7.07 (s, 2H), 6.63 (s, 1H), 6.56 (d, $J$ = 2.2 Hz, 1H), 6.39 (d, $J$ = 2.3 Hz, 1H), 3.97 (s, 3H), 3.95 (m, 6H), 3.93–3.90 (m, 6H). $^{13}$C NMR (100 MHz, $CDCl_3$) δ 177.8, 164.4, 161.1, 160.9, 160.0, 153.7, 141.1, 126.8, 109.2, 108.8, 103.6, 96.4, 93.0, 61.2, 56.6, 56.5, 56.0. HRMS (ESI) *m/z* calcd for $C_{20}H_{21}O_7$ $[M+H]^+$ 373.1281, found 373.1282.

### 4.11. General procedure III: O-demethylation

An aqueous solution of hydrogen bromide (48%; 1 mL per 0.10 mmol of substrate) was mixed with flavone. The reaction mixture was refluxed for 6–9 h, during which the reaction progress was monitored by UPLC-MS. After the disappearance of partially *O*-demethylated intermediates, the reaction mixture was evaporated under reduced pressure.

#### 4.11.1. 2-(2,3-Dihydroxyphenyl)-5,7-dihydroxy-4H-chromen-4-one (**25**)

Compound **25** was obtained from **20** (0.047 g, 0.18 mmol) using general procedure III. The residue was purified by column chromatography (DCM/MeOH 10:1), and crystallized from chloroform/acetone to furnish the flavone **25** (0.012 g, 30%). $^1$H NMR (400 MHz, DMSO-$d_6$) δ 12.89 (s, 1H), 10.85 (s, 1H), 10.02 (s, 1H), 9.62 (s, 1H), 7.31 (dd, $J$ = 8.1, 1.6 Hz, 1H), 7.03 (s, 1H), 6.99 (dd, $J$ = 7.8, 1.6 Hz, 1H), 6.82 (t, $J$ = 8.0 Hz, 1H), 6.45 (d, $J$ = 2.1 Hz, 1H), 6.20 (d, $J$ = 2.1 Hz, 1H). $^{13}$C NMR (100 MHz, DMSO-$d_6$) δ 181.9, 164.3, 161.7, 161.4, 157.5, 145.9, 145.5, 119.2, 118.4, 117.8, 117.7, 109.1, 103.7, 98.8, 93.9. HRMS (ESI) *m/z* calcd for $C_{15}H_{10}O_6Na$ $[M+Na]^+$ 309.0369, found 309.0367.

#### 4.11.2. 2-(3,4-Dihydroxyphenyl)-5-hydroxy-4H-chromen-4-one (**26**)

Compound **26** was obtained from **21** (0.13 g, 0.42 mmol) using general procedure III. The residue was purified by column chromatography (DCM/MeOH 100:3) and crystallized from ethanol to obtain the flavone **26** (0.040 g, 35%). $^1$H NMR (400 MHz, DMSO-$d_6$) δ 12.84 (s, 1H), 10.01 (bs, 1H), 9.44 (bs, 1H), 7.65 (t, $J$ = 8.3 Hz, 1H), 7.48 (dd, $J$ = 8.3, 2.3 Hz, 1H), 7.46 (d, $J$ = 2.3 Hz, 1H), 7.14 (dd, $J$ = 8.4, 0.9 Hz, 1H), 6.91 (d, $J$ = 8.3 Hz, 1H), 6.83 (s, 1H), 6.80 (dd, $J$ = 8.2, 0.9 Hz, 1H). $^{13}$C NMR (100 MHz, DMSO-$d_6$) δ 182.9, 164.8, 159.9, 155.8, 150.1, 145.8, 135.7, 121.3, 119.4, 116.0, 113.6, 110.9, 109.9, 107.3, 103.4. HRMS (ESI) *m/z* calcd for $C_{15}H_{11}O_5$ $[M+H]^+$ 271.0601, found 271.0599.

#### 4.11.3. 5,7-Dihydroxy-2-(3-hydroxyphenyl)-4H-chromen-4-one (**27**)

Compound **27** was obtained from **22** (0.10 g, 0.32 mmol) using general procedure III. The residue was purified by preparative HPLC to obtain the flavone **27** (0.030 g, 34%). $^1$H NMR (400 MHz, DMSO-$d_6$) δ 12.84 (s, 1H), 10.92 (s, 1H), 9.90 (s, 1H), 7.53–7.47 (m, 1H), 7.42–7.33 (m, 2H), 7.01 (ddd, $J$ = 8.3, 2.6, 1.0 Hz, 1H), 6.86 (s, 1H), 6.50 (d, $J$ = 2.1 Hz, 1H), 6.23 (d, $J$ = 2.1 Hz, 1H). $^{13}$C NMR (100 MHz, DMSO-$d_6$) δ 181.8, 164.4, 163.3, 161.5, 157.9, 157.4, 132.0, 130.3, 119.1, 117.3, 112.8, 105.1, 104.0, 99.0, 94.0. HRMS (ESI) *m/z* calcd for $C_{15}H_{11}O_5$ $[M+H]^+$ 271.0601, found 271.0599.

#### 4.11.4. 2-(3,4-Dihydroxyphenyl)-7-hydroxy-4H-chromen-4-one (**28**)

Compound **28** was obtained from **23** (0.074 g, 0.23 mmol) using general procedure III. The residue was purified by preparative HPLC to obtain the flavone **28** (0.044 g, 68%). $^1$H NMR (400 MHz, DMSO-$d_6$) δ 10.75 (bs, 1H), 9.80 (bs, 1H), 9.38 (bs, 1H), 7.85 (d, $J$ = 8.6 Hz, 1H), 7.43–7.35 (m, 2H), 6.93–6.86 (m, 3H), 6.60 (s, 1H). $^{13}$C NMR (100 MHz, DMSO-$d_6$) δ 176.2, 162.6, 162.5, 157.3, 149.1, 145.7, 126.5, 122.1, 118.5, 116.1, 116.0, 114.8, 113.2, 104.5, 102.4. HRMS (ESI) *m/z* calcd for $C_{15}H_{10}O_5Na$ $[M+Na]^+$ 293.0420, found 293.0418.

#### 4.11.5. 5,7-Dihydroxy-2-(3,4,5-trihydroxyphenyl)-4H-chromen-4-one (**29**)

Compound **29** was obtained from **24** (0.21 g, 0.56 mmol) using general procedure III. The residue was purified by preparative HPLC to obtain the flavone **29** (0.060 g, 28%). $^1$H NMR (400 MHz, DMSO-$d_6$) δ 6.96 (s, 2H), 6.51 (s, 1H), 6.39 (d, $J$ = 2.1 Hz, 1H), 6.17 (d, $J$ = 2.1 Hz, 1H). $^{13}$C NMR (100 MHz, DMSO-$d_6$) δ 182.0, 164.9, 164.5, 161.9, 157.7, 146.8, 138.5, 120.7, 106.1, 104.0, 103.3, 99.3, 94.2. HRMS (ESI) *m/z* calcd for $C_{15}H_{11}O_7$ $[M+H]^+$ 303.0499, found 303.0498.

### 4.12. Synthesis of aza-flavones

#### 4.12.1. N-(2-Acetyl-3,5-dimethoxyphenyl)-3,4-dimethoxybenzamide (**32**)

*N*,*N*-Diisopropylethylamine (1.00 mL, 5.93 mmol) and 4-dimethylaminopyridine (0.024 g, 0.19 mmol) were added to a solution of **30** (0.38 g, 1.97 mmol) and 3,4-dimethoxybenzoyl chloride (0.44 g, 2.17 mmol) in toluene (3 mL). The reaction mixture was stirred overnight at 80 °C in a sealed tube. The reaction was quenched by addition of water and extracted with DCM (3 × 20 mL). The combined organic layers were dried over $MgSO_4$ and evaporated to dryness under reduced pressure. The residue was crystallized from ethanol to obtain the amide **32** (0.70 g, 95%). $^1$H NMR (400 MHz, $CDCl_3$) δ 12.88 (s, 1H), 8.25 (d, $J$ = 2.4 Hz, 1H), 7.66 (dd, $J$ = 8.4, 2.2 Hz, 1H), 7.63 (d, $J$ = 2.1 Hz, 1H), 6.97 (d, $J$ = 8.4 Hz, 1H), 6.22 (d, $J$ = 2.4 Hz, 1H), 3.99 (s, 3H), 3.95 (s, 3H), 3.92 (s, 3H), 3.89 (s, 3H), 2.63 (s, 3H). $^{13}$C NMR (100 MHz, $CDCl_3$) δ 203.1, 166.1, 164.9, 162.9, 152.3, 149.2, 144.3, 127.6, 120.5, 110.8, 110.7, 108.7, 96.6, 94.4, 56.2, 56.2, 55.8, 55.7, 34.4. HRMS (ESI) *m/z* calcd for $C_{19}H_{21}O_6NNa$ $[M+Na]^+$ 382.1272, found 382.1267.

#### 4.12.2. N-(3,5-dimethoxy-2-(2-methoxyacetyl)phenyl)-3,4-dimethoxybenzamide (**33**)

*N*,*N*-Diisopropylethylamine (1.00 mL, 5.93 mmol) and 4-dimethylaminopyridine (0.044 g, 0.36 mmol) were added to a solution of **31** (0.40 g, 1.80 mmol) and 3,4-dimethoxybenzoyl chloride (0.38 g, 1.90 mmol) in DCM (4 mL). The reaction mixture was stirred overnight at 80 °C in a sealed tube. The reaction was quenched by

addition of water and extracted with DCM (3 × 20 mL). The combined organic layers were dried over $MgSO_4$ and evaporated to dryness under reduced pressure. The residue was crystallized from ethanol to obtain the amide **33** (0.50 g, 67%). $^1$H NMR (400 MHz, $CDCl_3$, mixture of two rotamers) δ 13.23 (bs, 1H), 8.37 (d, $J$ = 2.4 Hz, 1H), 7.75 (dd, $J$ = 8.4, 2.2 Hz, 1H), 7.65 (d, $J$ = 2.1 Hz, 1H), 6.95 (d, $J$ = 8.4 Hz, 1H), 6.21 (d, $J$ = 2.4 Hz, 1H), 4.62 (s, 2H), 3.98 (s, 3H), 3.95 (s, 3H), 3.93 (s, 3H), 3.90 (s, 3H), 3.50 (s, 3H). $^{13}$C NMR (100 MHz, $CDCl_3$) δ 200.4, 166.2, 165.5, 163.0, 152.3, 149.1, 145.6, 127.3, 120.6, 110.8, 110.6, 110.5, 105.8, 96.7, 96.7, 94.0, 79.6, 59.3, 59.2, 56.1, 56.1, 56.0, 56.0, 55.8, 55.7, 55.7, 55.6. HRMS (ESI) *m/z* calcd for $C_{20}H_{23}O_7NNa$ $[M+Na]^+$ 412.1377, found 412.1379.

#### 4.12.3. 2-(3,4-Dimethoxyphenyl)-5,7-dimethoxyquinolin-4(1H)-one (**34**)

Compound **32** (0.074 g, 0.205 mmol) and potassium *tert*-butoxide (0.12 g, 1.03 mmol) were suspended in *tert*-butanol (4 mL), and the reaction mixture was stirred overnight at 80 °C in a sealed tube. The reaction mixture was quenched by addition of water (20 mL) and extracted with EtOAc (3 × 20 mL). The combined organic layers were extracted with brine (20 mL), dried over $MgSO_4$, and evaporated to dryness under reduced pressure. The product was purified by column chromatography (DCM/MeOH 20:1) to furnish the flavone **34** (0.060 g, 84%). $^1$H NMR (400 MHz, $CDCl_3$) δ 7.67 (d, $J$ = 2.1 Hz, 1H), 7.55 (dd, $J$ = 8.4, 2.1 Hz, 1H), 7.02 (d, $J$ = 2.2 Hz, 1H), 6.98 (s, 1H), 6.95 (d, $J$ = 8.4 Hz, 1H), 6.42 (d, $J$ = 2.2 Hz, 1H), 4.01 (s, 2H), 4.00 (s, 3H), 3.93 (s, 3H), 3.91 (s, 3H). $^{13}$C NMR (100 MHz, $CDCl_3$) δ 161.3, 161.2, 157.5, 156.2, 154.6, 150.4, 149.2, 149.2, 119.9, 111.0, 110.2, 106.5, 103.1, 97.0, 91.1, 56.3, 56.0, 56.0, 55.6. HRMS (ESI) *m/z* calcd for $C_{19}H_{20}O_5N$ $[M+H]^+$ 342.1336, found 342.1336.

#### 4.12.4. 2-(3,4-Dimethoxyphenyl)-3,5,7-trimethoxyquinolin-4(1H)-one (**35**)

Compound **33** (0.20 g, 0.51 mmol) and potassium *tert*-butoxide (0.29 g, 2.60 mmol) were suspended in *tert*-butanol (4 mL). The reaction mixture was stirred overnight in a sealed tube at 80 °C. The reaction mixture was quenched by addition of saturated ammonium chloride (25 mL) and extracted with DCM/propan-2-ol 5:1 (3 × 15 mL). The combined organic layers were evaporated to dryness under reduced pressure. The residue was purified by column chromatography (DCM/MeOH 20:1) and crystallized from methanol to furnish the flavone **35** (0.15 g, 78%). $^1$H NMR (400 MHz, DMSO-$d_6$) δ 10.95 (bs, 1H), 7.28–7.02 (m, 4H), 6.67 (d, $J$ = 2.3 Hz, 1H), 6.26 (d, $J$ = 2.3 Hz, 1H), 3.83 (s, 3H), 3.83 (s, 3H), 3.80 (s, 3H), 3.78 (s, 3H), 3.60 (s, 3H). $^{13}$C NMR (100 MHz, DMSO-$d_6$) δ 171.8, 161.5, 160.8, 149.7, 148.2, 142.8, 139.7, 139.1, 124.3, 121.7, 112.5, 111.4, 111.0, 93.8, 91.2, 59.0, 55.6, 55.6, 55.2, 48.6. HRMS (ESI) *m/z* calcd for $C_{20}H_{22}O_6N$ $[M+H]^+$ 372.1441, found 372.1440.

#### 4.12.5. 2-(3,4-Dihydroxyphenyl)-5,7-dihydroxyquinolin-4(1H)-one (**36**)

Compound **36** was obtained from **34** (0.074 g, 0.23 mmol) using general procedure III. The reaction mixture was neutralized with aqueous sodium bicarbonate and extracted with DCM/propan-2-ol 5:1 (3 × 15 mL). The combined organic layers were evaporated to dryness under reduced pressure, and the residue was purified by preparative HPLC to obtain the flavone **36** (0.026 g, 42%). $^1$H NMR (400 MHz, DMSO-$d_6$) δ 11.55 (s, 1H), 10.20 (s, 1H), 9.35 (s, 1H), 7.15 (d, $J$ = 2.3 Hz, 1H), 7.11 (dd, $J$ = 8.2, 2.3 Hz, 1H), 6.89 (d, $J$ = 8.2 Hz, 1H), 6.50 (d, $J$ = 2.1 Hz, 1H), 6.05 (d, $J$ = 1.7 Hz, 1H), 6.00 (d, $J$ = 2.1 Hz, 1H). $^{13}$C NMR (100 MHz, DMSO-$d_6$) δ 181.3, 162.9, 162.6, 151.6, 148.6, 146.1, 143.1, 125.0, 119.5, 116.3, 115.0, 106.8, 104.0, 97.7, 92.7. HRMS (ESI) *m/z* calcd for $C_{15}H_{12}O_5N$ $[M+H]^+$ 286.0710, found 286.0707.

#### 4.12.6. 2-(3,4-Dihydroxyphenyl)-3,5,7-trihydroxyquinolin-4(1H)-one (**37**)

Compound **37** was obtained from **35** (0.074 g, 0.23 mmol) using general procedure III. After complete consumption of the starting material, the reaction mixture was neutralized with aqueous sodium bicarbonate, and a precipitate appeared. The precipitate was collected, washed with water, and crystallized from methanol to obtain the flavone **37** (0.030 g, 50%). $^1$H NMR (500 MHz, DMSO-$d_6$) δ 14.11 (s, 1H), 11.31 (s, 1H), 10.04 (s, 1H), 9.40 (s, 1H), 9.24 (s, 1H), 8.24 (s, 1H), 7.20 (d, $J$ = 2.2 Hz, 1H), 7.05 (dd, $J$ = 8.2, 2.2 Hz, 1H), 6.88 (d, $J$ = 8.2 Hz, 1H), 6.44 (d, $J$ = 2.1 Hz, 1H), 5.97 (d, $J$ = 2.1 Hz, 1H). $^{13}$C NMR (125 MHz, DMSO-$d_6$) δ 172.3, 161.2, 146.8, 144.6, 140.0, 134.6, 133.6, 122.8, 120.7, 116.7, 115.3, 105.5, 96.2, 91.1, 39.5. HRMS (ESI) *m/z* calcd for $C_{15}H_{12}O_6N$ $[M+H]^+$ 302.0659, found 302.0660.

## Declaration of competing interest

The authors declare that they have no known competing financial interest or personal relationship that could have appeared to influence the work reported in the paper.

## Acknowledgements

The authors thank Radko Souček for HPLC, Kateřina Čermáková for performing the DIANA assay, the company Mihulka for providing narciclasine, Dr. Ladislav Cvak for providing four flavonoids (taxifolin, silybin, silychristin, and silydianin), and Hillary Hoffman for proofreading of the manuscript. This work was supported by the Czech National Node to the European Infrastructure for Translational Medicine EATRIS-CZ, grant No. LM2018133, from the Ministry of Education, Youth and Sports of the Czech Republic and by the European Regional Development Fund; OP RDE; Project: "Chemical biology for drugging undruggable targets (ChemBioDrug)" (No. CZ.02.1.01/0.0/0.0/16_019/0000729).

## Appendix A. Supplementary data

Supplementary data to this article can be found online at https://doi.org/10.1016/j.ejmech.2020.112754.

## References

[1] https://www.who.int/en/news-room/detail/14-12-2017-up-to-650-000-people-die-of-respiratory-diseases-linked-to-seasonal-flu-each-year.
[2] M. von Itzstein, The war against influenza: discovery and development of sialidase inhibitors, Nat. Rev. Drug Discov. 6 (2007) 967–974.
[3] F.G. Hayden, N. Sugaya, N. Hirotsu, N. Lee, M.D. de Jong, A.C. Hurt, T. Ishida, H. Sekino, K. Yamada, S. Portsmouth, K. Kawaguchi, T. Shishido, M. Arai, K. Tsuchiya, T. Uehara, A. Watanabe, B.M. Investigators, Baloxavir marboxil for uncomplicated influenza in adults and adolescents, N. Engl. J. Med. 379 (2018) 913–923.
[4] T. Noshi, M. Kitano, K. Taniguchi, A. Yamamoto, S. Omoto, K. Baba, T. Hashimoto, K. Ishida, Y. Kushima, K. Hattori, M. Kawai, R. Yoshida, M. Kobayashi, T. Yoshinaga, A. Sato, M. Okamatsu, Y. Sakoda, H. Kida, T. Shishido, A. Naito, In vitro characterization of baloxavir acid, a first-in-class cap-dependent endonuclease inhibitor of the influenza virus polymerase PA subunit, Antivir. Res. 160 (2018) 109–117.
[5] T. Kikuchi, A. Watanabe, Baloxavir heralds a new era in influenza virus biology, Respir Investig 57 (2019) 1–2.
[6] Y. Furuta, B.B. Gowen, K. Takahashi, K. Shiraki, D.F. Smee, D.L. Barnard, Favipiravir (T-705), a novel viral RNA polymerase inhibitor, Antivir. Res. 100 (2013) 446–454.
[7] F.G. Hayden, N. Shindo, Influenza virus polymerase inhibitors in clinical development, Curr. Opin. Infect. Dis. 32 (2019) 176–186.
[8] E.J. Mifsud, F.G. Hayden, A.C. Hurt, Antivirals targeting the polymerase complex of influenza viruses, Antivir. Res. 169 (2019) 104545.
[9] L. Naesens, A. Stevaert, E. Vanderlinden, Antiviral therapies on the horizon for influenza, Curr. Opin. Pharmacol. 30 (2016) 106–115.
[10] J.T. Zhang, Y.M. Hu, R. Musharrafieh, H. Yin, J. Wang, Focusing on the influenza virus polymerase complex: recent progress in drug discovery and assay development, Curr. Med. Chem. 26 (2019) 2243–2263.
[11] E. Kowalinski, C. Zubieta, A. Wolkerstorfer, O.H.J. Szolar, R.W.H. Ruigrok,

S. Cusack, Structural analysis of specific metal chelating inhibitor binding to the endonuclease domain of influenza pH1N1 (2009) polymerase, PLoS Pathog. 8 (2012) e1002831.
[12] H. Ju, J. Zhang, B.S. Huang, D.W. Kang, B. Huang, X.Y. Liu, P. Zhan, Inhibitors of influenza virus polymerase acidic (PA) endonuclease: contemporary developments and perspectives, J. Med. Chem. 60 (2017) 3533–3551.
[13] R.M. DuBois, P.J. Slavish, B.M. Baughman, M.K. Yun, J. Bao, R.J. Webby, T.R. Webb, S.W. White, Structural and biochemical basis for development of influenza virus inhibitors targeting the PA endonuclease, PLoS Pathog. 8 (2012) e1002830.
[14] Y.X. Liao, Y.L. Ye, S.M. Li, Y.L. Zhuang, L.Y. Chen, J.X. Chen, Z.N. Cui, L.J. Huo, S.W. Liu, G.P. Song, Synthesis and SARs of dopamine derivatives as potential inhibitors of influenza virus PA(N) endonuclease, Eur. J. Med. Chem. 189 (2020) 112048.
[15] M. Carcelli, D. Rogolino, A. Gatti, L. De Luca, M. Sechi, G. Kumar, S.W. White, A. Stevaert, L. Naesens, N-acylhydrazone inhibitors of influenza virus PA endonuclease with versatile metal binding modes, Sci. Rep. 6 (2016) 31500.
[16] S. Omoto, V. Speranzini, T. Hashimoto, T. Noshi, H. Yamaguchi, M. Kawai, K. Kawaguchi, T. Uehara, T. Shishido, A. Naito, S. Cusack, Characterization of influenza virus variants induced by treatment with the endonuclease inhibitor baloxavir marboxil, Sci. Rep. 8 (2018) 9633.
[17] J.C. Hastings, H. Selnick, B. Wolanski, J.E. Tomassini, Anti-influenza virus activities of 4-substituted 2,4-dioxobutanoic acid inhibitors, Antimicrob. Agents Chemother. 40 (1996) 1304–1307.
[18] T. Kuzuhara, Y. Iwai, H. Takahashi, D. Hatakeyama, N. Echigo, Green tea catechins inhibit the endonuclease activity of influenza A virus RNA polymerase, PLoS Curr 1 (2009) RRN1052.
[19] S. Mori, S. Miyake, T. Kobe, T. Nakaya, S.D. Fuller, N. Kato, K. Kaihatsu, Enhanced anti-influenza A virus activity of (-)-epigallocatechin-3-O-gallate fatty acid monoester derivatives: effect of alkyl chain length, Bioorg. Med. Chem. Lett 18 (2008) 4249–4252.
[20] J. Garcia-Tirado, C. Rieger-Reyes, P. Saz-Peiro, Effect of flavonoids in the prevention of lung cancer: systematic review, Med. Clin. 139 (2012) 358–363.
[21] H. Yao, W.Z. Xu, X.L. Shi, Z. Zhang, Dietary flavonoids as cancer prevention agents, J. Environ Sci. Heal. 29 (2011) 1–31.
[22] M.L. Neuhouser, Flavonoids and cancer prevention: what is the evidence in humans? Pharm. Biol. 42 (2004) 36–45.
[23] U. Wenzel, H. Daniel, Flavonoids and their possible role in colon cancer prevention and therapy, Falk Symp. 128 (2003) 264–274.
[24] A.A. Welch, A.C. Hardcastle, The effects of flavonoids on bone, Curr. Osteoporos. Rep. 12 (2014) 205–210.
[25] J.K. Prasain, S.H. Carlson, J.M. Wyss, Flavonoids and age-related disease: risk, benefits and critical windows, Maturitas 66 (2010) 163–171.
[26] A.R. Tapas, D.M. Sakarkar, R.B. Kakde, Flavonoids as nutraceuticals: a review, Trop. J. Pharmaceut. Res. 7 (2008) 1089–1099.
[27] S. Kumar, A.K. Pandey, Chemistry and Biological Activities of Flavonoids: an Overview, ScientificWorldJournal, 2013, p. 162750.
[28] Y.X. Xie, W.J. Yang, F. Tang, X.Q. Chen, L.C. Ren, Antibacterial activities of flavonoids: structure-activity relationship and mechanism, Curr. Med. Chem. 22 (2015) 132–149.
[29] A. Ahmad, M. Kaleem, Z. Ahmed, H. Shafiq, Therapeutic potential of flavonoids and their mechanism of action against microbial and viral infections-A review, Food Res. Int. 77 (2015) 221–235.
[30] T.N. Kaul, E. Middleton, P.L. Ogra, Antiviral effect of flavonoids on human viruses, J. Med. Virol. 15 (1985) 71–79.
[31] J.M. Harnly, R.F. Doherty, G.R. Beecher, J.M. Holden, D.B. Haytowitz, S. Bhagwat, S. Gebhardt, Flavonoid content of US fruits, vegetables, and nuts, J. Agric. Food Chem. 54 (2006) 9966–9977.
[32] X. Li, Q.W. Jin, Q.Y. Yao, B.L. Xu, L.X. Li, S.C. Zhang, C.T. Tu, The flavonoid quercetin ameliorates liver inflammation and fibrosis by regulating hepatic macrophages activation and polarization in mice, Front. Pharmacol. 9 (2018) 72.
[33] M. Lesjak, I. Beara, N. Simin, D. Pintac, T. Majkic, K. Bekvalac, D. Orcic, N. Mimica-Dukic, Antioxidant and anti-inflammatory activities of quercetin and its derivatives, J. Funct. Foods 40 (2018) 68–75.
[34] Y. Li, J.Y. Yao, C.Y. Han, J.X. Yang, M.T. Chaudhry, S.N. Wang, H.N. Liu, Y.L. Yin, Quercetin, inflammation and immunity, Nutrients 8 (2016) 167.
[35] M.Y. Li, Z.T. Xu, Quercetin in a lotus leaves extract may be responsible for antibacterial activity, Arch Pharm. Res. (Seoul) 31 (2008) 640–644.
[36] S.M. Tang, X.T. Deng, Q.P. Li, X.X. Ge, L. Miao, Anticancer effects of quercetin on cholangiocarcinoma, Gastroenterology 154 (2018) S1122–S1123.
[37] Y.J. Kim, Y.H. Lee, Y.J. Choi, H. Chung, Quercetin enhanced the apoptotic effect of anticancer drug, N-(4-Hydroxyphenyl) retinamide (4hpr) via depletion of gsh in human leukemia cell line, Ann. Oncol. 20 (2009), 37-37.
[38] X. Gao, B.L. Wang, X.W. Wei, K. Men, F.J. Zheng, Y.F. Zhou, Y. Zheng, M.L. Gou, M.J. Huang, G. Guo, N. Huang, Z.Y. Qian, Y.Q. Wei, Anticancer effect and mechanism of polymer micelle-encapsulated quercetin on ovarian cancer, Nanoscale 4 (2012), 7883-7883.
[39] F. Dajas, Life or death: neuroprotective and anticancer effects of quercetin, J. Ethnopharmacol. 143 (2012) 383–396.
[40] J.K. Kim, S.U. Park, Quercetin and its role in biological functions: an updated review, EXCLI J 17 (2018) 856–863.
[41] H.J. Choi, J.H. Kim, C.H. Lee, Y.J. Ahn, J.H. Song, S.H. Baek, D.H. Kwon, Antiviral activity of quercetin 7-rhamnoside against porcine epidemic diarrhea virus, Antivir. Res. 81 (2009) 77–81.
[42] H.D. Gravina, N.F. Tafuri, A. Silva, J.L.R. Fietto, T.T. Oliveira, M.A.N. Diaz, M.R. Almeida, In vitro assessment of the antiviral potential of trans-cinnamic acid, quercetin and morin against equid herpesvirus 1, Res. Vet. Sci. 91 (2011) E158–E162.
[43] N.T. Lu, C.M. Crespi, N.M. Liu, J.Q. Vu, Y. Ahmadieh, S. Wu, S. Lin, A. McClune, F. Durazo, S. Saab, S. Han, D.C. Neiman, S. Beaven, S.W. French, A phase I dose escalation study demonstrates quercetin safety and explores potential for bioflavonoid antivirals in patients with chronic hepatitis C, Phytother Res. 30 (2016) 160–168.
[44] K. Zandi, B.T. Teoh, S.S. Sam, P.F. Wong, M.R. Mustafa, S. AbuBakar, Antiviral activity of four types of bioflavonoid against dengue virus type-2, Virol. J. 8 (2011) 560.
[45] M. Wleklik, M. Luczak, W. Panasiak, M. Kobus, E. Lammerzarawska, Structural basis for antiviral activity of flavonoids - naturally-occurring compounds, Acta Virol. 32 (1988) 522–525.
[46] G. Matthee, A.D. Wright, G.M. Konig, HIV reverse transcriptase inhibitors of natural origin, Planta Med. 65 (1999) 493–506.
[47] B. Vaidya, S.Y. Cho, K.S. Oh, S.H. Kim, Y.O. Kim, E.H. Jeong, T.T. Nguyen, S.H. Kim, I.S. Kim, J. Kwon, D. Kim, Effectiveness of periodic treatment of quercetin against influenza A virus H1N1 through modulation of protein expression, J. Agric. Food Chem. 64 (2016) 4416–4425.
[48] J.M. Davis, E.A. Murphy, J.L. McClellan, M.D. Carmichael, J.D. Gangemi, Quercetin reduces susceptibility to influenza infection following stressful exercise, Am. J. Physiol.-Reg I 295 (2008) R505–R509.
[49] A.L. Liu, H.D. Wang, S.M.Y. Lee, Y.T. Wang, G.H. Du, Structure-activity relationship of flavonoids as influenza virus neuraminidase inhibitors and their in vitro anti-viral activities, Bioorg. Med. Chem. 16 (2008) 7141–7147.
[50] N. Uchide, H. Toyoda, Antioxidant therapy as a potential approach to severe influenza-associated complications, Molecules 16 (2011) 2032–2052.
[51] H.J. Choi, J.H. Song, K.S. Park, D.H. Kwon, Inhibitory effects of quercetin 3-rhamnoside on influenza A virus replication, Eur. J. Pharmaceut. Sci. 37 (2009) 329–333.
[52] Y.J. Kim, S. Narayanan, K.O. Chang, Inhibition of influenza virus replication by plant-derived isoquercetin, Antivir. Res. 88 (2010) 227–235.
[53] P. Mehrbod, S.N. Ebrahimi, F. Fotouhi, F. Eskandari, J.N. Eloff, L.J. McGaw, F.O. Fasina, Experimental validation and computational modeling of anti-influenza effects of quercetin-3-O-alpha-L-rhamnopyranoside from indigenous south African medicinal plant Rapanea melanophloeos, BMC Compl. Alternative Med. 19 (2019) 346.
[54] Z.K. Liu, J.P. Zhao, W.C. Li, L. Shen, S.B. Huang, J.J. Tang, J. Duan, F. Fang, Y.L. Huang, H.Y. Chang, Z. Chen, R. Zhang, Computational screen and experimental validation of antiinfluenza effects of quercetin and chlorogenic acid from traditional Chinese medicine, Sci. Rep. 6 (2016) 19095.
[55] H.J. Choi, J.H. Song, D.H. Kwon, Quercetin 3-rhamnoside exerts antiinfluenza A virus activity in mice, Phytother Res. 26 (2012) 462–464.
[56] E. Gansukh, Z. Kazibwe, M. Pandurangan, G. Judy, D.H. Kim, Probing the impact of quercetin-7-O-glucoside on influenza virus replication influence, Phytomedicine 23 (2016) 958–967.
[57] E. Gansukh, M. Muthu, D. Paul, G. Ethiraj, S. Chun, J. Gopal, Nature nominee quercetin's anti-influenza combat strategy Demonstrations and remonstrations, Rev. Med. Virol. 27 (2017) e1930.
[58] W.J. Wu, R.C. Li, X.L. Li, J. He, S.B. Jiang, S.W. Liu, J. Yang, Quercetin as an antiviral agent inhibits influenza A virus (IAV) entry, Viruses-Basel 8 (2016).
[59] C. Rakers, S.M. Schwerdtfeger, J. Mortier, S. Duwe, T. Wolff, G. Wolber, M.F. Melzig, Inhibitory potency of flavonoid derivatives on influenza virus neuraminidase, Bioorg. Med. Chem. Lett 24 (2014) 4312–4317.
[60] H.J. Jeong, Y.B. Ryu, S.J. Park, J.H. Kim, H.J. Kwon, J.H. Kim, K.H. Park, M.C. Rho, W.S. Lee, Neuraminidase inhibitory activities of flavonols isolated from Rhodiola rosea roots and their in vitro anti-influenza viral activities, Bioorg. Med. Chem. 17 (2009) 6816–6823.
[61] J. Kongkamnerd, A. Milani, G. Cattoli, C. Terregino, I. Capua, L. Beneduce, A. Galotta, P. Pengo, G. Fasina, O. Monthakantirat, K. Umehara, W. De-Eknamkul, S. Miertus, The quenching effect of flavonoids on 4-methylumbelliferone, a potential pitfall in fluorimetric neuraminidase inhibition assays, J. Biomol. Screen 16 (2011) 755–764.
[62] S. Chamni, W. De-Eknamkul, Recent progress and challenges in the discovery of new neuraminidase inhibitors, Expert Opin. Ther. Pat. 23 (2013) 409–423.
[63] A. Torreggiani, M. Tamba, A. Trinchero, S. Bonora, Copper(II)-quercetin complexes in aqueous solutions: spectroscopic and kinetic properties, J. Mol. Struct. 744 (2005) 759–766.
[64] Y.Z. Liu, M.Q. Guo, Studies on transition metal-quercetin complexes using electrospray ionization tandem mass spectrometry, Molecules 20 (2015) 8583–8594.
[65] L. Mira, M.T. Fernandez, M. Santos, R. Rocha, M.H. Florencio, K.R. Jennings, Interactions of flavonoids with iron and copper ions: a mechanism for their antioxidant activity, Free Radic. Res. 36 (2002) 1199–1208.
[66] T. Muthurajan, P. Rammanohar, N.P. Rajendran, S. Sethuraman, U.M. Krishnan, Evaluation of a quercetin-gadolinium complex as an efficient positive contrast enhancer for magnetic resonance imaging, RSC Adv. 5 (2015) 86967–86979.
[67] N. Ghosh, T. Chakraborty, S. Mallick, S. Mana, D. Singha, B. Ghosh, S. Roy, Synthesis, characterization and study of antioxidant activity of quercetin-magnesium complex, Spectrochim. Acta 151 (2015) 807–813.
[68] J. Zhou, L.F. Wang, J.Y. Wang, N. Tang, Antioxidative and anti-tumour

activities of solid quercetin metal(II) complexes, Transit. Metal. Chem. 26 (2001) 57–63.
[69] J. Tan, L.C. Zhu, B.C. Wang, GC (Guanine-Cytosine)-Selective DNA-binding and antitumor activity of a quercetin-manganese(II) complex, Chem. Biodivers. 8 (2011) 1550–1559.
[70] A. Bravo, J.R. Anacona, Metal complexes of the flavonoid quercetin: antibacterial properties, Transit. Metal. Chem. 26 (2001) 20–23.
[71] J. Tan, B.C. Wang, L.C. Zhu, Hydrolytic cleavage of DNA by quercetin manganese(II) complexes, Colloids Surf., B 55 (2007) 149–152.
[72] D.W. Zhong, M.M. Liu, Y. Cao, Y.L. Zhu, S.H. Bian, J.Y. Zhou, F.J. Wu, K.C. Ryu, L. Zhou, D.Y. Ye, Discovery of metal ions chelator quercetin derivatives with potent anti-HCV activities, Molecules 20 (2015) 6978–6999.
[73] M.M. Liu, L. Zhou, P.L. He, Y.N. Zhang, J.Y. Zhou, Q. Shen, X.W. Chen, J.P. Zuo, W. Li, D.Y. Ye, Discovery of flavonoid derivatives as anti-HCV agents via pharmacophore search combining molecular docking strategy, Eur. J. Med. Chem. 52 (2012) 33–43.
[74] M. Kozisek, V. Navratil, K. Rojikova, J. Pokorna, C.B. Albinana, P. Pachl, J. Zemanova, A. Machara, P. Sacha, J. Hudlicky, I. Cisarova, P. Rezacova, J. Konvalinka, DNA-linked inhibitor antibody assay (DIANA) as a new method for screening influenza neuraminidase inhibitors, Biochem. J. 475 (2018) 3847–3860.
[75] V. Navratil, J. Schimer, J. Tykvart, T. Knedlik, V. Vik, P. Majer, J. Konvalinka, P. Sacha, DNA-linked Inhibitor Antibody Assay (DIANA) for sensitive and selective enzyme detection and inhibitor screening, Nucleic Acids Res. 45 (2017) e10.
[76] B.M. Baughman, P.J. Slavish, R.M. DuBois, V.A. Boyd, S.W. White, T.R. Webb, Identification of influenza endonuclease inhibitors using a novel fluorescence polarization assay, ACS Chem. Biol. 7 (2012) 526–534.
[77] I.G.C. Coutts, M. Edwards, D.J. Richards, Mild selective hydrolysis of the methyl-esters of some ortho-substituted aromatic carboxylic-acids, Synthesis-Stuttgart (1981) 487–489.
[78] A. Stevaert, S. Nurra, N. Pala, M. Carcelli, D. Rogolino, C. Shepard, R.A. Domaoal, B. Kim, M. Alfonso-Prieto, S.A.E. Marras, M. Sechi, L. Naesens, An integrated biological approach to guide the development of metal-chelating inhibitors of influenza virus PA endonuclease, Mol. Pharmacol. 87 (2015) 323–337.
[79] J.H. Zhang, T.D.Y. Chung, K.R. Oldenburg, A simple statistical parameter for use in evaluation and validation of high throughput screening assays, J. Biomol. Screen 4 (1999) 67–73.
[80] G.J. Pan, K. Yang, Y.T. Ma, X. Zhao, K. Lu, P. Yu, Synthesis of 6-or 8-bromo flavonoids by regioselective mono-bromination and deprotection protocol from flavonoid alkyl ethers, Bull. Kor. Chem. Soc. 36 (2015) 1460–1466.
[81] M. Freitas, D. Ribeiro, S.M. Tome, A.M.S. Silva, E. Fernandes, Synthesis of chlorinated flavonoids with anti-inflammatory and proapoptotic activities in human neutrophils, Eur. J. Med. Chem. 86 (2014) 153–164.
[82] M. Iinuma, Y. Matoba, T. Tanaka, M. Mizuno, Flavonoids synthesis .1. Synthesis and spectroscopic properties of flavones with 2 hydroxy and 5 methoxy groups at C-2',3',4',5,6,6',7 and C-2',3,4',5,5',6,7, Chem. Pharm. Bull. 34 (1986) 1656–1662.
[83] Z.H. Sui, V.N. Nguyen, J. Altom, J. Fernandez, J.J. Hilliard, J.I. Bernstein, J.F. Barrett, K.A. Ohemeng, Synthesis and topoisomerase inhibitory activities of novel aza-analogues of flavones, Eur. J. Med. Chem. 34 (1999) 381–387.
[84] M. Hadjeri, E.L. Peiller, C. Beney, N. Deka, M.A. Lawson, C. Dumontet, A. Boumendjel, Antimitotic activity of 5-hydroxy-7-methoxy-2-phenyl-4-quinolones, J. Med. Chem. 47 (2004) 4964–4970.
[85] A.L. Liu, B. Liu, H.L. Qin, S.M.Y. Lee, Y.T. Wang, G.H. Du, Anti-influenza virus activities of flavonoids from the medicinal plant Elsholtzia rugulosa, Planta Med. 74 (2008) 847–851.
[86] H.Y. Yan, L.L. Ma, H.Q. Wang, S. Wu, H. Huang, Z.Y. Gu, J.D. Jiang, Y.H. Li, Luteolin decreases the yield of influenza A virus in vitro by interfering with the coat protein I complex expression, J. Nat. Med. 73 (2019) 487–496.
[87] I. Kubo, K. Nihei, K. Shimizu, Oxidation products of quercetin catalyzed by mushroom tyrosinase, Bioorg. Med. Chem. 12 (2004) 5343–5347.
[88] Y. Ding, Z.Y. Cao, L. Cao, G. Ding, Z.Z. Wang, W. Xiao, Antiviral activity of chlorogenic acid against influenza A (H1N1/H3N2) virus and its inhibition of neuraminidase, Sci. Rep. 7 (2017) 45723.
[89] V. Zima, C.B. Albinana, K. Rojikova, J. Pokorna, P. Pachl, P. Rezacova, J. Hudlicky, V. Navratil, P. Majer, J. Konvalinka, M. Kozisek, A. Machara, Investigation of flexibility of neuraminidase 150-loop using tamiflu derivatives in influenza A viruses H1N1 and H5N1, Bioorg. Med. Chem. 27 (2019) 2935–2947.
[90] Z.K. Liu, J.P. Zhao, W.C. Li, X.K. Wang, J.X. Xu, J. Xie, K. Tao, L. Shen, R. Zhang, Molecular docking of potential inhibitors for influenza H7N9, Comput. Math. Method Med. (2015) 480764.
[91] A.S. Chintakrindi, D.J. Gohil, A.S. Chowdhary, M.A. Kanyalkar, Design, synthesis and biological evaluation of substituted flavones and aurones as potential anti-influenza agents, Bioorg. Med. Chem. 28 (2020) 115191.
[92] S.M. Sadati, N. Gheibi, S. Ranjbar, M.S. Hashemzadeh, Docking study of flavonoid derivatives as potent inhibitors of influenza H1N1 virus neuraminidase, Biomed. Rep. 10 (2019) 33–38.
[93] W. Kabsch, Xds, Acta Crystallogr. D 66 (2010) 125–132.
[94] W. Kabsch, Integration, scaling, space-group assignment and post-refinement, Acta Crystallogr. D Biol. Crystallogr. 66 (2010) 133–144.
[95] A. Vagin, A. Teplyakov, MOLREP: an automated program for molecular replacement, J. Appl. Crystallogr. 30 (1997) 1022–1025.
[96] M.D. Winn, C.C. Ballard, K.D. Cowtan, E.J. Dodson, P. Emsley, P.R. Evans, R.M. Keegan, E.B. Krissinel, A.G. Leslie, A. McCoy, S.J. McNicholas, G.N. Murshudov, N.S. Pannu, E.A. Potterton, H.R. Powell, R.J. Read, A. Vagin, K.S. Wilson, Overview of the CCP4 suite and current developments, Acta Crystallogr. D Biol. Crystallogr. 67 (2011) 235–242.
[97] P. Emsley, K. Cowtan, Coot: model-building tools for molecular graphics, Acta Crystallogr. D Biol. Crystallogr. 60 (2004) 2126–2132.
[98] M.S. Song, G. Kumar, W.R. Shadrick, W. Zhou, T. Jeevan, Z. Li, P.J. Slavish, T.P. Fabrizio, S.W. Yoon, T.R. Webb, R.J. Webby, S.W. White, Identification and characterization of influenza variants resistant to a viral endonuclease inhibitor, Proc. Natl. Acad. Sci. U. S. A. 113 (2016) 3669–3674.
[99] G.N. Murshudov, P. Skubak, A.A. Lebedev, N.S. Pannu, R.A. Steiner, R.A. Nicholls, M.D. Winn, F. Long, A.A. Vagin, REFMAC5 for the refinement of macromolecular crystal structures, Acta Crystallogr. D Biol. Crystallogr. 67 (2011) 355–367.
[100] V.B. Chen, W.B. Arendall 3rd, J.J. Headd, D.A. Keedy, R.M. Immormino, G.J. Kapral, L.W. Murray, J.S. Richardson, D.C. Richardson, MolProbity: all-atom structure validation for macromolecular crystallography, Acta Crystallogr. D Biol. Crystallogr. 66 (2010) 12–21.
[101] D.A. Case, I.Y. Ben-Shalom, S.R. Brozell, D.S. Cerutti, T.E. Cheatham III, V.W.D. Cruzeiro, T.A. Darden, R.E. Duke, G. Giambasu, M.K. Gilson, H. Gohlke, A.W. Goetz, R. Harris, S. Izadi, K. Kasava- jhala, A. Kovalenko, R. Krasny, T. Kurtzman, T.S. Lee, S. LeGrand, P. Li, C. Lin, J. Liu, T. Luchko, R. Luo, V. Man, K.M. Merz, Y. Miao, O. Mikhailovskii, G. Monard, H. Nguyen, A. Onufriev, F. Pan, S. Pantano, R. Qi, D.R. Roe, A. Roitberg, C. Sagui, S. Schott-Verdugo, J. Shen, C.L. Simmerling, N. Skrynnikov, J. Smith, J. Swails, R.C. Walker, J. Wang, L. Wilson, R.M. Wolf, X. Wu, D.M. York, P.A. Kollman, AMBER 2020, K. B, University of California, San Francisco, 2020.
[102] J. Hostas, J. Rezac, Accurate DFT-D3 calculations in a small basis set, J. Chem. Theor. Comput. 13 (2017) 3575–3585.
[103] A. Klamt, G. Schuurmann, Cosmo - a new approach to dielectric screening in solvents with explicit expressions for the screening energy and its gradient, J. Chem. Soc. PT 2 (1993) 799–805.
[104] A.V. Marenich, R.M. Olson, C.P. Kelly, C.J. Cramer, D.G. Truhlar, Self-consistent reaction field model for aqueous and nonaqueous solutions based on accurate polarized partial charges, J. Chem. Theor. Comput. 3 (2007) 2011–2033.
[105] C.P. Kelly, C.J. Cramer, D.G. Truhlar, Aqueous solvation free energies of ions and ion-water clusters based on an accurate value for the absolute aqueous solvation free energy of the proton, J. Phys. Chem. B 110 (2006) 16066–16081.
[106] J.M. Wang, R.M. Wolf, J.W. Caldwell, P.A. Kollman, D.A. Case, Development and testing of a general amber force field, J. Comput. Chem. 25 (2004) 1157–1174.
[107] A.K. Rappe, C.J. Casewit, K.S. Colwell, W.A. Goddard, W.M. Skiff, Uff, a full periodic-table force-field for molecular mechanics and molecular-dynamics simulations, J. Am. Chem. Soc. 114 (1992) 10024–10035.
[108] C.I. Bayly, P. Cieplak, W.D. Cornell, P.A. Kollman, A well-behaved electrostatic potential based method using charge restraints for deriving atomic charges - the resp model, J. Phys. Chem. 97 (1993) 10269–10280.
[109] J. Rezac, Cuby: an integrative framework for computational chemistry, J. Comput. Chem. 37 (2016) 1230–1237.
[110] R. Ahlrichs, M. Bar, M. Haser, H. Horn, C. Kolmel, Electronic-structure calculations on workstation computers - the program system Turbomole, Chem. Phys. Lett. 162 (1989) 165–169.
[111] K. Okuma, K. Hirano, Y. Tanabe, R. Itoyama, A. Miura, N. Nagahora, K. Shioji, Novel one-pot synthesis of polysubstituted isocoumarins from arynes and trifluoroacetylated beta-diketones, Chem. Lett. 43 (2014) 492–494.
[112] G. Nonaka, F. Hashimoto, I. Nishioka, Tannins and related-compounds XXXVI.: isolation and structures of theaflagallins, new red pigments from black tea, Chem. Pharm. Bull. 34 (1986) 61–65.
[113] E. Stodulkova, I. Cisarova, M. Kolarik, M. Chudickova, P. Novak, P. Man, M. Kuzma, B. Pavlu, J. Cerny, M. Flieger, Biologically active metabolites produced by the basidiomycete Quambalaria cyanescens, PloS One 10 (2015) e011891.

## 3.6. PUBLICATION IV.

**Synthesis and In Vitro Evaluation of C-7 and C-8 Luteolin Derivatives as Influenza Endonuclease Inhibitors.**

As mentioned above, PA subunit carries the endonuclease active site at its N-terminus with two metal ions embedded. Depending on the environment, those are either two $Mn^{2+}$ ions or mixed $Mn^{2+}$ and $Mg^{2+}$ ions. It is responsible for the host mRNA segment cleavage, necessary for the viral transcription initiation. The NPA endonuclease inhibitors must be a metal-binding pharmacophore able to bind either $Mn^{2+}$ or $Mg^{2+}$. Only few of all inhibitors approved by the FDA target metalloenzymes and those lack of structural diversity. For the treatment of influenza, there is only one FDA-approved inhibitor targeting the NPA endonuclease. The baloxavir marboxil (BXA) is administrated as a prodrug under a trade name Xofluza. During the clinical studies of BXA a key mutation within the endonuclease active site occurred. The post-treatment monitoring of patients detected Ile-38 substitution to Thr-38 (I38T). This one-point mutation reduced susceptibility to BXA up to 30- to 50-fold. Viruses with the I38T mutation possess impaired endonuclease activity *in vitro*. The crystal structures of I38T variant in complex with BXA confirmed reduced van der Waals contacts with the inhibitor (Omoto et al., 2018). To consider any efficient NPA endonuclease inhibitor, this emerging mutation should be surveyed.

### 3.6.1. SUMMARY

In our preceding work, we have characterized the molecular mode-of-action of flavonoids and developed a high-throughput screening assay based on AlphaScreen technology. This we utilized to evaluate a series of compounds from the flavonoid polyols and its derivatives. From the previous study, we learned that the hydroxyl group of luteolin at position C-7 forms a hydroxyl bond with the Glu-26 residue of NPA and its two hydroxyls from ring **B** chelate two metal ions in the endonuclease active site. This made luteolin a starting scaffold for its derivate compounds (**Figure 17**). To explore the structure-activity relationship (SAR) of luteolin derivatives, we have prepared 21 compounds with different groups at C-7 and 33 compounds of C-8 introduced moieties. We tested them using two different assays, the AlphaScreen and the gel-based endonuclease assay. No compound of the C-7 derivatives was better inhibitor than luteolin ($IC_{50}$ = 73 nM ± 3 nM). Out of the C-8 series one compound, orientin containing glucose at position C-8 turned out to be a potent inhibitor of the NPA endonuclease ($IC_{50}$ = 42 nM ± 2 nM). However, vitexin lacking the requisite 3',4'-dihydroxyphenyl motif, retained

some inhibitory potency ($IC_{50}$ = 1.9 µM ± 0.1). That indicated additional protein-ligand interactions of the glucose moiety. To get the answers for the actual chemical space of these inhibitors, we have crystallized both the wild type and the I38T mutant variant in complex with orientin, best of our series. Glucose moiety from orientin molecule forms supplementary interactions in the NPA active site via water-mediated net of hydrogen bonds while maintaining the luteolin binding mode. The I38T mutation revealed an additional water molecule in the endonuclease active site compared to the wild type. Nonetheless, the I38T mutation which was observed in BXA clinical trials should not influence the binding mode of orientin to the NPA active site.

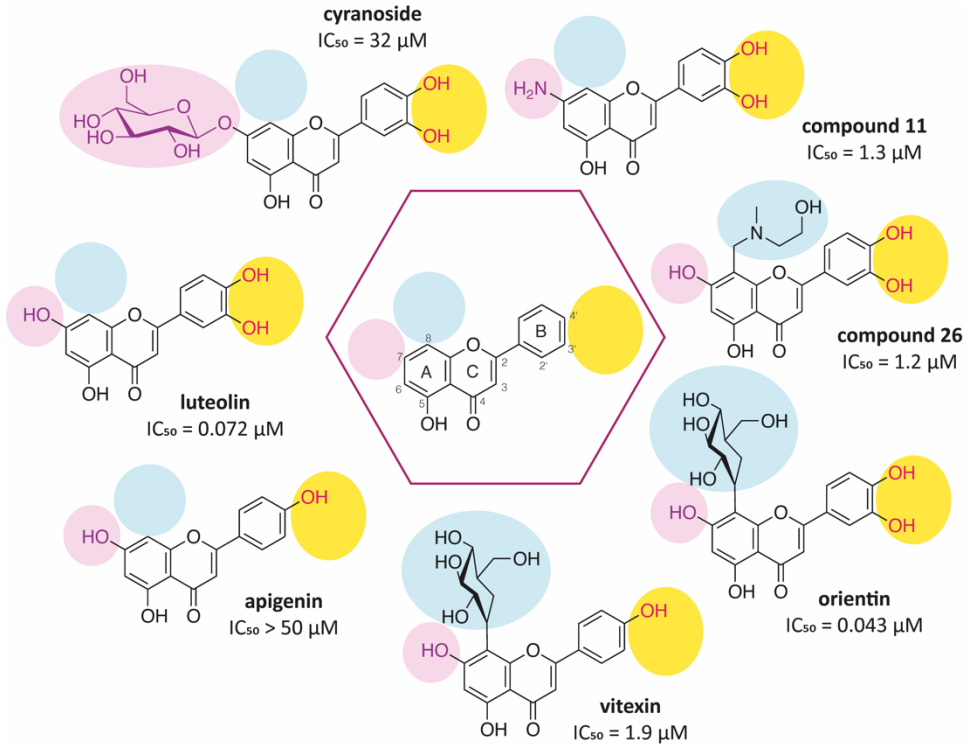


**Figure 17.** Overview of selected compounds from the SAR study of luteolin derivatives. The hydroxyl group at C-7 position was characterized as advantageous compared to other reactive groups at this position. On the other hand, moiety introduced at the C-8 position of flavone backbone enhanced the inhibitory potency (orientin). This C-8 addition led to moderate inhibition even when the 3',4'-dihydroxyphenyl motif was missing (vitexin), unlike the solely 4'-hydroxyphenyl motif (apigenin) which lost its inhibitory potency completely.

my contribution

I expressed the wild-type and I38T mutant variant of NPA domain of influenza A RdRp in *E.coli*. I purified proteins and crystallized both variants without any ligand for further ligand soaking. The hexagonal bifrustum crystals were then soaked in several time points with orientin. I tested several crystals at BESSY II, collected all the data at home diffractometer, processed them, and solved their structures. After refining them two protein-ligand complexes (PDB IDs: **7NUG**, **7NUH**) diffracted at 1.9 Å and 2.2 Å respectively. I compared the obtained structures and characterized an additional water-mediated hydrogen bond of the I38T mutant variant with the orientin molecule. To confirm the data from the AlphaScreen assay, I performed the gel-based endonuclease assay (see Supplementary Material for more information).

"**Synthesis and In Vitro Evaluation of C-7 and C-8 Luteolin Derivatives as Influenza Endonuclease Inhibitors.**" *International Journal of Molecular Sciences* 22(14):7735. doi: 10.3390/ijms22147735.

International Journal of
*Molecular Sciences*

MDPI

*Article*

# Synthesis and In Vitro Evaluation of C-7 and C-8 Luteolin Derivatives as Influenza Endonuclease Inhibitors

**Robert Reiberger [1,2,†], Kateřina Radilová [1,3,†], Michal Kráľ [1,3], Václav Zima [1,2], Pavel Majer [1], Jiří Brynda [1,4], Martin Dračínský [1], Jan Konvalinka [1,5], Milan Kožíšek [1,*] and Aleš Machara [1,*]**

1 Institute of Organic Chemistry and Biochemistry of the Czech Academy of Sciences, Gilead Sciences and IOCB Research Center, Flemingovo n. 2, 166 10 Prague, Czech Republic; robert.reiberger@uochb.cas.cz (R.R.); katerina.radilova@uochb.cas.cz (K.R.); michal.kral@uochb.cas.cz (M.K.); vaclav.zima@uochb.cas.cz (V.Z.); pavel.majer@uochb.cas.cz (P.M.); jiri.brynda@uochb.cas.cz (J.B.); martin.dracinsky@uochb.cas.cz (M.D.); jan.konvalinka@uochb.cas.cz (J.K.)
2 Department of Organic Chemistry, Faculty of Science, Charles University, Hlavova 8, 128 00 Prague, Czech Republic
3 First Faculty of Medicine, Charles University, Kateřinská 1660, 121 08 Prague, Czech Republic
4 Institute of Molecular Genetics of the Czech Academy of Sciences, Vídeňská 1083, 140 00 Prague, Czech Republic
5 Department of Biochemistry, Faculty of Science, Charles University, Hlavova 8, 128 00 Prague, Czech Republic
* Correspondence: milan.kozisek@uochb.cas.cz (M.K.); ales.machara@uochb.cas.cz (A.M.); Tel.: +420-220-183-479 (A.M.)
† These authors contributed equally to this work.

**Abstract:** The part of the influenza polymerase PA subunit featuring endonuclease activity is a target for anti-influenza therapies, including the FDA-approved drug Xofluza. A general feature of endonuclease inhibitors is their ability to chelate $Mg^{2+}$ or $Mn^{2+}$ ions located in the enzyme's catalytic site. Previously, we screened a panel of flavonoids for PA inhibition and found luteolin and its C-glucoside orientin to be potent inhibitors. Through structural analysis, we identified the presence of a 3′,4′-dihydroxyphenyl moiety as a crucial feature for sub-micromolar inhibitory activity. Here, we report results from a subsequent investigation exploring structural changes at the C-7 and C-8 positions of luteolin. Experimental $IC_{50}$ values were determined by AlphaScreen technology. The most potent inhibitors were C-8 derivatives with inhibitory potencies comparable to that of luteolin. Bio-isosteric replacement of the C-7 hydroxyl moiety of luteolin led to a series of compounds with one-order-of-magnitude-lower inhibitory potencies. Using X-ray crystallography, we solved structures of the wild-type PA-N-terminal domain and its I38T mutant in complex with orientin at 1.9 Å and 2.2 Å resolution, respectively.

**Keywords:** bio-isosterism; cross-coupling; endonuclease inhibitor; flavonoids; influenza; Mannich reaction; RNA polymerase

check for updates

**Citation:** Reiberger, R.; Radilová, K.; Kráľ, M.; Zima, V.; Majer, P.; Brynda, J.; Dračínský, M.; Konvalinka, J.; Kožíšek, M.; Machara, A. Synthesis and In Vitro Evaluation of C-7 and C-8 Luteolin Derivatives as Influenza Endonuclease Inhibitors. *Int. J. Mol. Sci.* **2021**, *22*, 7735. https://doi.org/10.3390/ijms22147735

Academic Editors: Mattia Mori and Ilaria Vicenti

Received: 26 May 2021
Accepted: 17 July 2021
Published: 20 July 2021

**Publisher's Note:** MDPI stays neutral with regard to jurisdictional claims in published maps and institutional affiliations.

**Copyright:** © 2021 by the authors. Licensee MDPI, Basel, Switzerland. This article is an open access article distributed under the terms and conditions of the Creative Commons Attribution (CC BY) license (https://creativecommons.org/licenses/by/4.0/).

## 1. Introduction

Influenza viruses cause illness in a variety of species, including humans. Despite the availability of vaccines and antiviral drugs, influenza remains a serious threat to human health, causing 290,000–650,000 deaths worldwide annually [1]. Influenza virus RNA-dependent RNA polymerase (RdRP) lacks proof-reading activity, which leads to an accumulation of point mutations known as antigenic drift. This is responsible for the emergence of new viral variants causing seasonal flu, which requires the flu vaccine to be reformulated every year. Antigenic drift also contributes to increasing viral resistance against antiviral drugs. Additionally, antigenic shift—the reassortment of viral RNA segments from two or more different influenza strains in animals or humans—could lead to a new pandemic strain. In fact, various zoonotic strains are considered "ticking time bombs", as these pathogens have the potential to mutate to facilitate human transmission given enough

time and infected organisms. Generally, vaccination is the best intervention against viral pathogens including influenza. However, the last influenza pandemic in 2009 reminded us that effective vaccines are often not available at the onset of a pandemic. Reformulation of vaccines is time-consuming, and many human lives can be taken by the disease during this process. The intricacies of vaccine development, in combination with influenza's genomic variability, makes the development of novel anti-influenza therapeutics imperative.

Influenza viruses contain a single-stranded, negative-sense RNA genome in complex with RdRP [2–4]. RdRP comprises the subunits PA (polymerase acidic protein), PB1 and PB2 (polymerase basic protein 1 and 2). The virus itself is unable to synthesize the 5′-mRNA cap required for eukaryotic translation; this represents the "Achillies heel" of influenza virus. The virus obtains host primers—short oligomers of host pre-mRNA that initiate transcription—by a unique "cap-snatching" mechanism [5–9], which serves as a target for pharmaceutical intervention. The process begins with binding of the PB2 subunit to the 5′-cap ($m^7$GTP) of the host pre-mRNA. Subsequently, the PA subunit cleaves the RNA strain approximately 10–13 nucleotides downstream from the 5′-cap to acquire the cap/primer [10]. The PB1 subunit uses this detached RNA segment as a template for viral mRNA synthesis. RdRP is highly conserved across influenza strains, and the three subunits involved in the cap-snatching mechanism have been recognized as attractive targets for drug development in the past decade [11–18].

The PA subunit is a bridged binuclear metalloenzyme with an N-terminal domain (PA-Nter) harboring the endonuclease active site that carries out cleavage of the RNA segment. The active site is a negatively charged pocket that accommodates either $Mg^{2+}$ or $Mn^{2+}$ ions, with stronger affinity for the latter [19]. These ions are critical for endonuclease activity. Evidence suggests that PA-Nter endonuclease inhibitors must possess a metal-binding pharmacophore with the ability to bind either $Mg^{2+}$ or $Mn^{2+}$ ions efficiently [9].

Even though metalloenzymes comprise more than one-third of all known enzymes, clinical development of metalloenzyme inhibitors is rather limited and few such inhibitors have been approved by the Food and Drug Administration (FDA) [9,20–22]. Less than 5% of all FDA-approved drugs target metalloenzymes [23]. Unsurprisingly, metal-binding pharmacophores exhibit a lack of structural diversity.

There is currently only one FDA-approved influenza endonuclease inhibitor: baloxavir marboxil (trade name Xofluza), which is administrated as a prodrug [24,25]. Successful antiviral drugs must be able to block at least the existing variant of the target enzyme and should have a high resistance barrier. One key mutation in the influenza A/H1N1 2009 pandemic (A/H1N1pdm) and A/H3N2 viruses is Ile-38 to Thr-38 in PA-Nter. This mutation reduced patient susceptibility to baloxavir marboxil and impaired the virus' replicative fitness in cells [26]. Resistance development could eventually lead to the loss of the clinical relevance of Xofluza. Furthermore, fewer than a dozen PA-Nter endonuclease inhibitor classes have been reported in the literature to date. These classes include diketo acids [27], dopamine derivatives [28], hydroxylated heterocycles [29–31], flutimide congeners [32], green tea catechins [33,34], catechol derivatives [35], hydroxylated *N*-acyl-hydrazones [36] and others [18]. Recently, we identified the molecular mode of action of flavonoids in influenza-infected cells [37]. We developed a screening assay based on AlphaScreen technology and determined the inhibitory potency of 38 flavonoids, of which luteolin ($IC_{50}$ of 73 ± 3 nM) and its 8-*C*-glucoside orientin ($IC_{50}$ of 42 ± 2 nM) were the most potent inhibitors (Figure 1). A gel-based endonuclease inhibitory assay confirmed our findings from the competition assay. Finally, we performed structural analysis of complexes of PA-Nter with luteolin and myricetin and described various binding poses of flavonoids in the PA-Nter active site.

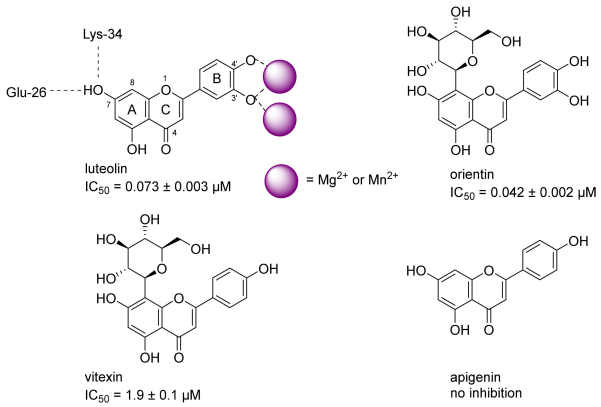


**Figure 1.** Selected hits from previous screening campaigns are shown. The tight coordination of metal ions and interactions with PA-Nter residues are indicated on the structure of luteolin.

In the current study, we aimed to pursue structure-assisted drug design guided by our previously reported crystal structure of PA-Nter in complex with luteolin (PDB entry 6YA5, 2.0 Å resolution) [37]. The structure revealed that the hydroxyl group at position C-7 forms a hydrogen bond with the Glu-26 residue of PA-Nter. The surface complementarity and the strong interaction of hydroxyls at the B-ring with metal ions contribute to the high affinity and inhibitory potency of luteolin. Thus, luteolin may serve as a useful scaffold to introduce modifications that improve the inhibitory potency and pharmacokinetic properties. Luteolin itself has low bioavailability [38,39] and is prone to oxidation. Therefore, we replaced the C-7 hydroxyl with other moieties capable of creating hydrogen bonds with Glu-26. Bio-isosteric replacement is a proven tool for modulating the drug-like properties of promising therapeutics [40]. The C-7 hydroxyl group has slightly higher acidity [41] compared to the other hydroxyls of luteolin. This allowed us to selectively modify the C-7 position using Pd-catalyzed cross couplings via the corresponding C-7 triflate.

We then continued to leverage the known structure–activity relationships (SAR) in 3′,4′-dihydroxyphenyl flavones. Moreover, we expanded our research effort to explore the chemical space around the C-8 position of the luteolin scaffold. Specifically, we set out to investigate whether moieties introduced at the C-8 position by Mannich reaction [42] would be tolerated or even enhance inhibitory potency. Our goal was to find additional points of interaction between luteolin derivatives and PA-Nter and, more importantly, to explain why vitexin exhibits moderate inhibitory potency even though it does not have the 3′,4′-dihydroxyphenyl motif. This ortho-hydroquinone motif was originally identified as the metal-binding pharmacophore and as such was considered indispensable for inhibition. That paradigm explains the lack of inhibitory potency of apigenin but fails to rationalize vitexin's moderate potency (see Figure 1).

## 2. Results and Discussion

### *2.1. Compound Synthesis*

Based on the SAR outlined in Figure 1, our initial efforts focused on exploring bio-isosterism at the C-7 moiety of luteolin. Guided by general knowledge of hydrogen bond formation and prior crystallographic study, we proposed that the hydroxyl group could be replaced with a small group featuring either N-H or O-H bonds. We also decided to introduce heterocyclic moieties that are not necessarily associated with textbook OH bio-isosteric replacement. Preparation of this C-7 series started from luteolin, which was per-acetylated. Compound **1** was then selectively mono-deacetylated at C-7 using previously reported conditions [43] (Scheme 1). This regioselective deprotection takes advantage of the higher acidity of the C-7 hydroxyl group in the luteolin scaffold caused by the electron-withdrawing pyrone carbonyl moiety in the para position. Therefore,

thiophenolate-mediated *O*-deacetylation selectively generates the corresponding phenolate (**2**), which was next treated with triflic anhydride to provide intermediate **3** in a decent yield.

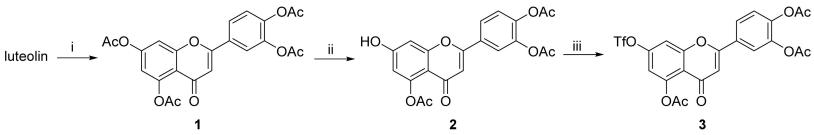


**Scheme 1.** Reagents and conditions: (i) $Ac_2O$, pyridine, 145 °C, 3 h, 77%; (ii) thiophenol, imidazole, NMP/THF (1:3), 0 °C to r.t., 5 h, 68%; (iii) $Tf_2O$, pyridine, DCM, 0 °C, 3.5 h, 41%.

Triflate **3** was subjected to a wide range of palladium-catalyzed cross-couplings. In addition to the desired products, certain reactions also yielded C-5 *O*-deacetylated analogues (Scheme 2). However, formation of such byproducts was not an obstacle, because we subsequently performed global deprotections of the flavone scaffolds. Hirao coupling [44] of **3** resulted in a high yield of diethyl phosphonate **4**. Subsequent standard dealkylation using trimethylsilyl bromide [45] resulted in phosphonic acid **5**. Molybdenum hexacarbonyl was used as a source of carbon monoxide for Pd-catalyzed methoxy-carbonylation. This approach was superior to methoxycarbonylation with dicobaltoctacarbonyl [46] in terms of yield and subsequent cleaning of the reaction apparatus. The pre-purified mixture of methyl esters **6** and **7** was subjected to hydrolysis and to different aminolysis reactions, which produced **8**, **9** and **10**.

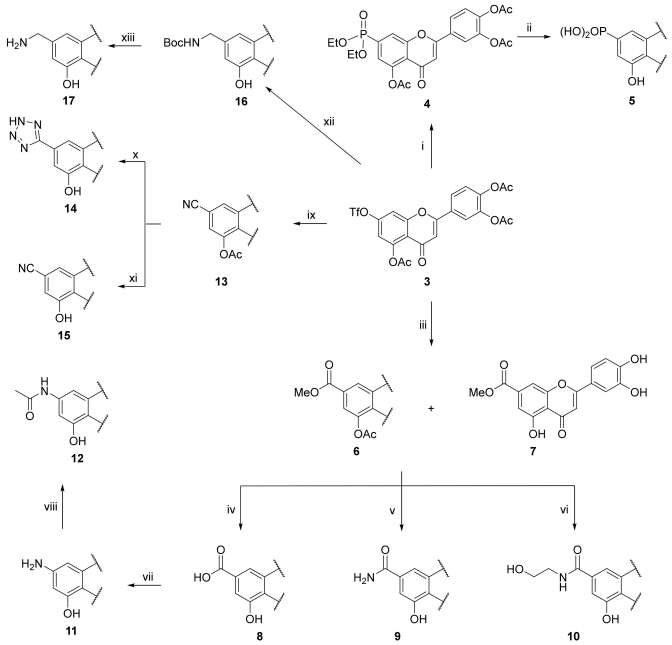


**Scheme 2.** Reagents and conditions: (i) $Pd(PPh_3)_4$, $(EtO)_2P(O)H$, DIPEA, MeCN, 70 °C, 3 h, 78%; (ii) (a) TMS-Br, DCM, r.t., 32 h, (b) MeOH, r.t., 1 h, (c) KOH, THF/MeOH, r.t., 1 h, 25%; (iii) $Mo(CO)_6$, $Pd(OAc)_2$, dppp, $Et_3N$, DMSO/MeOH (3:2), 70 °C, 20 h, 40% (**6**), 48% (**7**); (iv) 2M LiOH (aq.), THF, 45 °C, 1 h, 71%; (v) 7M $NH_3$ (MeOH), 50 °C, 4 d, 21%; (vi) 2-aminoethanol, $K_2CO_3$, EtOH, 50 °C, 24 h, 23%; (vii) a) DPPA, $Et_3N$, DMF, 100 °C, 16 h, b) $H_2O$, DMF, 100 °C, 3 h, 30%; (viii) AcOSu, $Et_3N$, DMF, r.t., 36 h, 23%; (ix) $Zn(CN)_2$, XantPhos Pd G2, DIPEA, DMF, 85 °C, 24 h, 61%; (x) $NaN_3$, AcOH, DMF, 130 °C, 3h, 38%; (xi) 2M LiOH (aq.), THF, r.t., 24 h, 46%; (xii) potassium [[(*t*-butoxycarbonyl)amino]methyl]trifluoroborate, SPhos Pd G2, $K_2CO_3$, THF/$H_2O$ (25:1), 100 °C, 2 h, 43%; (xiii) TFA, THF/$H_2O$ (4:1), 50 °C, 48 h, 73%.

One-pot Curtius rearrangement converted 3,4,5-trihydroxyflavone-7-carboxylic acid (**8**) to amino-derivative **11** in an acceptable yield of 30%. In general, electron rich anilines are prone to quick degradation, and thus the corresponding acetamide **12** was prepared from **11** using AcOSu. Palladium-catalyzed cyanation of triflate **3** by a modified Buchwald's procedure [47] gave rise to tetrazole derivative **14** and nitrile **15**. Amino-methyl transfer to triflate **3** was accomplished by protected potassium aminomethyltrifluoroborate under slightly modified conditions, reported by Molander [48]. The crude product of cross-coupling was then subjected to trifluoroacetic-acid-mediated de-tert-butylation, affording **17** as a homolog of amine **11**.

Our well-established method for preparation of the key intermediate **3** enabled us to execute heteroarylations of the flavone scaffold. We hypothesized that replacement of the hydroxyl group with pyrazole and azaindole could, in principle, ensure engagement of Glu-26 while improving the metabolic stability of the flavone. Synthesis of **18**–**20** was mediated by $Pd(PPh_3)_4$ or by Buchwald 2nd generation pre-catalysts. Regardless of which catalyst was used, **18**–**20** were obtained in low yields (Scheme 3).

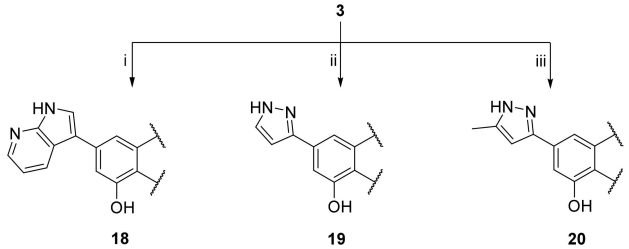


**Scheme 3.** Reagents and conditions: (i) 3-(4,4,5,5-tetramethyl-1,3,2-dioxaborolan-2-yl)-1*H*-pyrrolo[2,3-*b*]pyridine, $Pd(PPh_3)_4$, $Cs_2CO_3$, DMF, 90 °C, 16 h, 10%; (ii) (1*H*-pyrazol-3-yl)boronic acid, SPhos Pd G2, $K_2CO_3$, THF, 100 °C, 16 h, 25%; (iii) (5-methyl-1*H*-pyrazol-3-yl)boronic acid, SPhos Pd G2, $K_2CO_3$, THF/$H_2O$ (25:1), 100 °C, 16 h, 19%.

Although efficient Mannich reactions with luteolin [49] and quercetin [50,51] have been previously described, we found this type of C–C formation reaction very challenging. In our hands, formation of the desired products was in all cases accompanied by formation of C-6 regioisomers, contrary to reports in the literature. We also observed formation of other byproducts with a methylendioxy group on the B-ring serving as a 2:1 adduct of formalin to luteolin. The very limited solubility of luteolin further complicated our effort to optimize the Mannich reaction. Methanol worked least poorly among a variety of solvents screened (methanol, ethanol, propan-2-ol, trifluoroethanol, 1,4-dioxane and DMF). Room temperature and equimolar loading of formalin and the secondary amine with respect to luteolin efficiently suppressed the double Mannich reaction at both the C-6 and C-8 positions. To avoid issues with low regioselectivity and to exclude methylendioxy formation, we attempted Mannich reactions with tetraacetate **1** and triacetate **2**. These reactions led to complex reaction mixtures due to low conversions and the lability of acetates in the presence of secondary amines. According to HPLC analysis, subsequent methanolysis resulted in a simplified mixture of compounds, but yields of products were low (~15%). Considering the need to prepare triacetate **2**, this approach is clearly not advantageous to the Mannich reaction of parental luteolin in methanol. Data resulting from screening of the Mannich reaction with **1** and **2** are provided in the Supplementary Materials.

To explore the chemical space around C-8 as much as possible, we used structurally different secondary amines possessing additional functional groups (Scheme 4). Mannich reactions were stirred at room temperature overnight until almost all luteolin was consumed. The ratio between C-8 Mannich adduct and unwanted C-6 regioisomer ranged from 1.7:1 to 3.0:1. Since both regioisomers have similar retention factors, the purification of **21**–**32** was very laborious. Products were purified by multiple HPLC preparations

that further negatively influenced the yields. Alkyl esters of secondary amines were used for preparation of **30**–**32**, and after the Mannich reaction, these ester moieties were trans-formed into carboxylic acids.

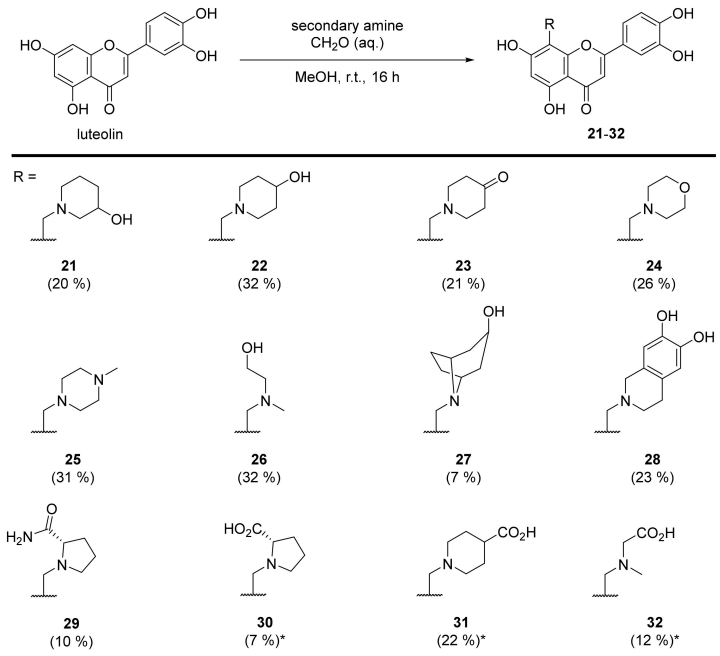


**Scheme 4.** Mannich reaction of luteolin with secondary amines in methanol. The asterisk indicates the overall yield of the Mannich reaction with subsequent acidic hydrolysis of corresponding alkyl esters.

### *2.2. Relationship between Chemical Structure and Inhibitory Potency*

The inhibition potencies of the prepared compounds were assessed by an assay that we recently developed for screening PA-Nter inhibitors based on the amplified luminescent proximity assay system (AlphaScreen) [37]. Examples of titration curves are shown in Figure 2A and Figure S1. The series of C-7 luteolin congeners displayed moderate inhibitory potencies with one- to two-order-of-magnitude higher $IC_{50}$ values compared to luteolin (Table 1).

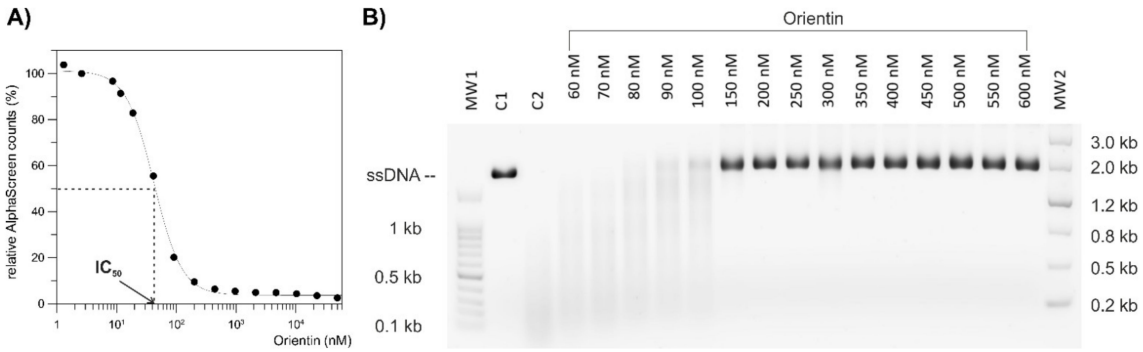


**Figure 2.** (**A**) Titration curve of orientin using the AlphaScreen assay, revealing an $IC_{50}$ value of 42 nM. (**B**) Inhibition of endonuclease activity by orientin, documented by a gel-based endonuclease inhibitory assay. The single-stranded circular DNA M13mp18 was used as substrate (lane C1). The substrate fully cleaved by endonuclease in the absence of inhibitor (lane C2) was used as a control. The GelPilot 100 bp Plus Ladder molecular weight marker (lane MW1) and the GelPilot Wide Range Ladder molecular weight marker (lane MW2) are shown for reference.

**Table 1.** Inhibition assay of influenza endonuclease. Structure-activity relationship of C-7 luteolin derivatives.

| Compound | Structure | $IC_{50}$ (μM) (AlphaScreen) |
|---|---|---|
| luteolin | 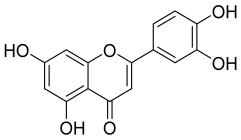 | 0.073 ± 0.003 |
| **5** | 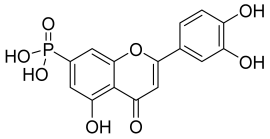 | 9.2 ± 2.3 |
| **8** | 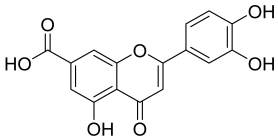 | 0.98 ± 0.13 |
| **9** | 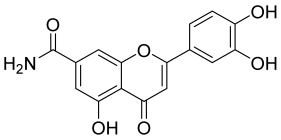 | 2.0 ± 0.6 |
| **10** | 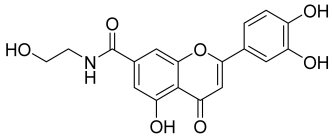 | 7.6 ± 1.2 |
| **11** | 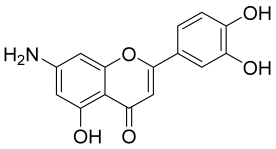 | 1.3 ± 0.2 |
| **12** | 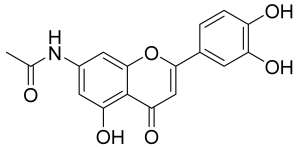 | 3.0 ± 0.4 |
| **14** | 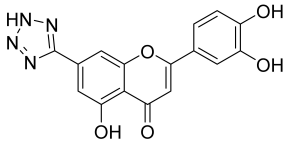 | 1.4 ± 0.3 |
| **15** | 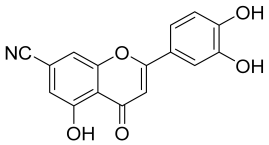 | 1.3 ± 0.3 |
| **17** | 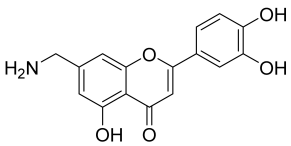 | 6.7 ± 0.8 |

**Table 1.** *Cont.*

| Compound | Structure | $IC_{50}$ (μM) (AlphaScreen) |
|---|---|---|
| **18** | 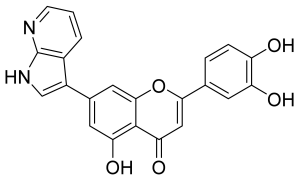 | 3.4 ± 0.6 |
| **19** | 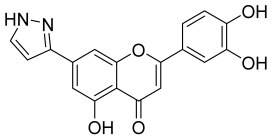 | 0.81 ± 0.12 |
| **20** | 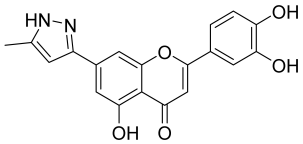 | 2.6 ± 0.3 |
| cynaroside | 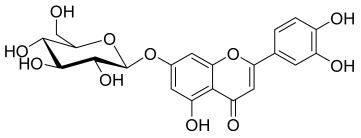 | 32 ± 3 |

Phosphonic acid **5** inhibited PA-Nter with an $IC_{50}$ of 9.2 μM, which was one of the weakest inhibitory potencies of the whole series. On the other hand, carboxylic acid **8** was a sub-micromolar inhibitor ($IC_{50}$ = 0.98 μM). Related amides **9** and **10** were less potent than **8** ($IC_{50}$ = 2.0 and 7.6 μM, respectively), which might indicate relatively confined C-7 proximal space. The amino derivative **11** had approximately 20-times weaker binding potency than luteolin. Clearly, the anticipated interaction between the C-7 amino group and side chain of Glu-26 did not result in superior binding. We speculate that solvation of the protonated amino group disrupted the effective formation of a salt bridge with Glu-26. Acetamide **12**, tetrazole derivative **14**, and nitrile **15** exhibited relatively flat SAR with $IC_{50}$ values of 3.0, 1.4 and 1.3 μM, respectively. Amino-methyl derivative **17** exhibited a significantly decreased inhibitory activity compared to luteolin ($IC_{50}$ = 6.7 μM). Apparently, neither strongly acidic nor basic moieties at C-7 are tolerated (see the inhibitory potencies of phosphonic acid **5** and aminomethyl derivative **17**). The relatively bulky azaindole congener **18** exhibited appreciable inhibitory potency with an $IC_{50}$ value of 3.4 μM. Pyrazoles **19** and **20** differed slightly in inhibitory potency; the former was more potent than its methylated analogue **20,** but both exhibited $IC_{50}$ values comparable with that of tetrazole **14** (0.81 and 2.6 versus 1.4 μM). Considering the almost identical half-maximal inhibitory concentrations of weakly basic pyrazoles **19** and **20** and acidic tetrazole **14**, we surmise that interaction with PA-Nter is not susceptible to the "proton affinity" of the moiety introduced at C-7. The inhibitory potencies of **5** and **17** further strengthen our hypothesis. On the other hand, it seems that steric effects play a key role in this specific point of interaction with the endonuclease. To confirm this, we screened cynaroside, a commercially available luteolin 7-*O*-β-D-glucoside. The introduction of a bulky glucose residue at C-7 led to an almost complete loss of inhibition ($IC_{50}$ = 32 ± 3 μM; three orders of magnitude worse than luteolin). We conclude that relocation of amino acids surrounding Glu-26 within PA-Nter and/or a clash with the Glu-26 side chain leads to a significant drop of inhibitory potency.

Next, we assessed the effect of C-8 substituents. As shown in Table 2, almost all aminomethylene moieties were well-tolerated. Compounds **21**, **23**–**25** and **29**–**32** exhibited inhibitory potencies roughly comparable to that of orientin ($IC_{50}$ = 0.042 μM). Moieties

with additional basic (**25**) or acidic residues (**30**–**32**) had $IC_{50}$ values within the same range. This suggests the lack of a PA-Nter amino acid featuring proton affinity in the chemical space around C-8. The bulky nor-tropine (**27**, $IC_{50}$ = 0.075 μM) and dihydroxytetrahydroisoquinoline (**28**, $IC_{50}$ = 0.12 μM) scaffolds were not found to be significantly unfavorable. It is likely that both bulky residues are oriented away from the PA-Nter active site and into the solvent. This hypothesis fits well with the findings presented in Section 2.3. 4-Hydroxypiperidine derivative **22** showed a slightly decreased potency in comparison with 3-hydroxy analogue **21** (0.14 *versus* 0.083 μM). However, the micromolar inhibitory potency of alcohol **26** ($IC_{50}$ = 1.2 μM) has no rational explanation based on the acquired SAR. Rather, we anticipated that **26**, as a cyclic analogue of **21**, would be a sub-micromolar inhibitor.

**Table 2.** Inhibition assay of influenza endonuclease. Structure–activity relationship of C-8 luteolin derivatives.

| Compound | Structure | $IC_{50}$ (μM) (AlphaScreen) |
|---|---|---|
| orientin | 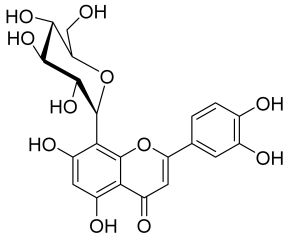 | 0.042 ± 0.002 |
| **21** | 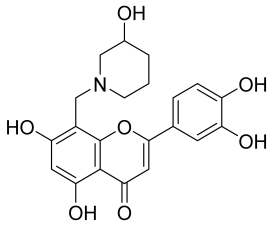 | 0.083 ± 0.009 |
| **22** | 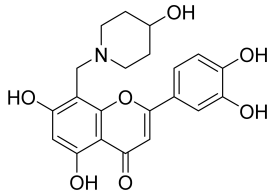 | 0.14 ± 0.01 |
| **23** | 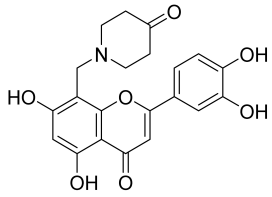 | 0.077 ± 0.013 |
| **24** | 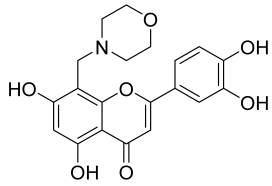 | 0.054 ± 0.009 |

**Table 2.** *Cont.*

| Compound | Structure | $IC_{50}$ (μM) (AlphaScreen) |
|---|---|---|
| **25** | 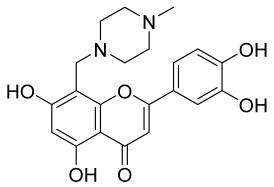 | 0.066 ± 0.009 |
| **26** | 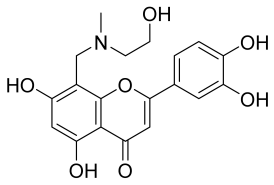 | 1.2 ± 0.2 |
| **27** | 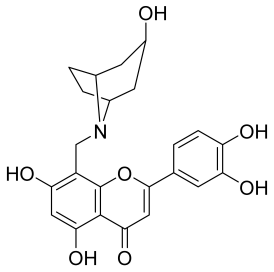 | 0.075 ± 0.015 |
| **28** | 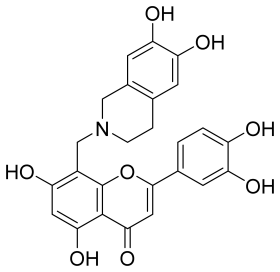 | 0.12 ± 0.02 |
| **29** | 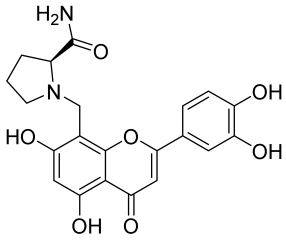 | 0.073 ± 0.012 |
| **30** | 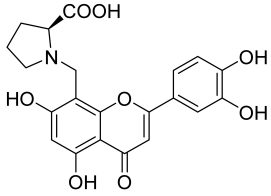 | 0.078 ± 0.013 |

**Table 2.** *Cont.*

| Compound | Structure | $IC_{50}$ (μM) (AlphaScreen) |
|---|---|---|
| **31** | 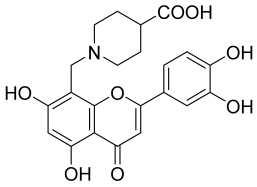 | 0.080 ± 0.022 |
| **32** | 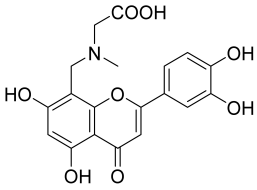 | 0.074 ± 0.008 |

To assess the inhibition of endonuclease activity by selected compounds by a direct mechanism-based method, we applied a gel-based endonuclease inhibitory assay (Figure 2B). This assay was performed for five selected ligands (orientin, baloxavir acid, luteolin, **21** and **30**) with wild-type PA-Nter (see Supplementary Materials, Figure S2). The analysis showed that orientin had a higher inhibitory potency than luteolin, in agreement with the AlphaScreen assay. The gel-based assay also confirmed similar inhibition activities for baloxavir acid, orientin, **21** and **30**. We also attempted this assay with the PA-Nter I38T variant, but the mutation of Ile-38 to Thr-38 led to complete loss of ssDNA cleavage ability (see Figure S3). Thus, we used a fluorescent-labelled ssRNA substrate and performed a FRET-based endonuclease assay with this variant. Compared to wild-type PA-Nter, the I38T variant had only 1.9% activity (see Figure S4) toward the ssRNA substrate and none for ssDNA. This result is in line with a recently reported observation of significantly reduced fitness and ssRNA nuclease activity of a virus harboring the I38T variant [26].

### *2.3. Crystal Structures of Wild-Type and I38T PA-Nter Domains in Complex with Orientin*

To reveal the structure of orientin bound to wild-type PA-Nter and the I38T mutant, we prepared both proteins for X-ray crystallographic studies. Thanks to its high inhibitory potency and aqueous solubility, orientin (PDBe ligand USE) was soaked into the unoccupied protein crystals. The structure of wild-type PA-Nter in complex with orientin was refined to 1.9 Å resolution (PDB ID 7NUG), and the I38T mutant complex (PDB ID 7NUH) was refined to 2.2 Å resolution. Both crystallographic models consisted of one protein molecule per asymmetric unit. Two metal ions were embedded in the endonuclease active site. Based on the strong anomalous signal observed, we speculate a mixed occupancy of $Mn^{2+}$ and $Mg^{2+}$ cations. The majority (0.8 occupancy) proximal ion was $Mn^{2+}$, coordinated by four protein atoms ($N^{\varepsilon 2}$His-41, $O^{\delta 2}$Asp-108, $O^{\varepsilon 2}$Glu-119, O Ile-120) and two hydroxyl groups from the 3′,4′-dihydroxyphenyl moiety of orientin. The distal octahedrally coordinated sphere was partially assigned as the central $Mg^{2+}$ cation (0.4 occupancy), which corresponds to lower anomalous scattering and is in agreement with previously reported PA-Nter complexes (Figure 3) [19,37].

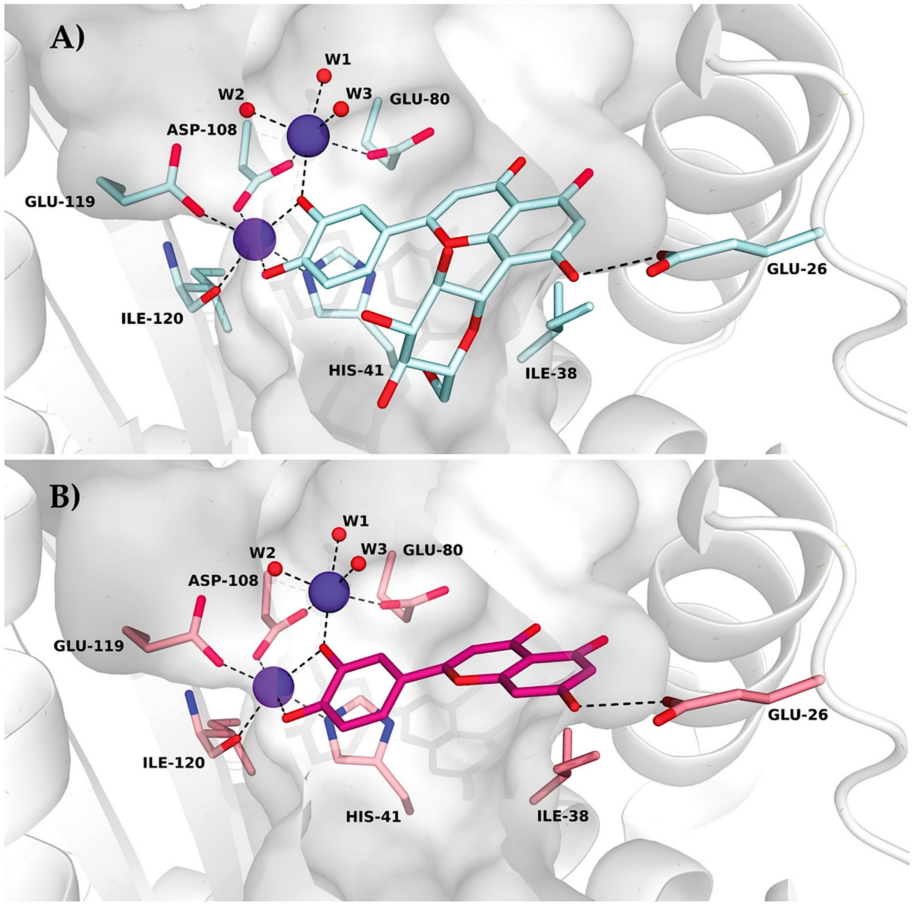


**Figure 3.** Comparison of crystal structures of PA-Nter in complex with orientin (**A**; PDB ID 7NUG) and luteolin (**B**; PDB ID 6YA5). The active site pocket containing two metal ions (purple-blue spheres) is presented as a grey surface. Interacting residues and ligands are in stick representation. Hydrogen bonds are shown as black dashes. Coordinating water molecules (W1, W2 and W3) are presented as red spheres.

The distal ion was coordinated by $O^{\varepsilon 2}$Glu-80, $O^{\delta 2}$Asp-108, the 4′-hydroxyl group of orientin, and three water molecules (W1, W2, W3). Unoccupied PA-Nter (PDB entry 5DES, not shown) harbors metal ions coordinated by two additional water molecules, which are replaced by the two hydroxyl groups from the flavonoid's B ring in our wild-type and I38T variant structures. Orientin adopts a similar position as luteolin in a previously described PA-Nter structure (PDB ID 6YA5) [37]. Ligands in both structures form a hydrogen bond with $O^{\varepsilon 2}$Glu-26 at the C-7 position. The previously observed high affinity of luteolin for PA-Nter is likely to be enhanced by the additional hydrogen bonding network surrounding orientin's glucosyl moiety. This was observed in both protein variants, as most of the water molecules in the first solvation shell are located at similar positions (Figure 4). However, there is a little ligand shift visible in the mutant variant. Wild-type Ile-38 moves orientin towards the solvent and differs from the mutant variant with an RMSD of 0.466 Å. Moreover, there is a visible movement of the Tyr-24 side chain in the mutant variant, likely to be due to the ligand shift.

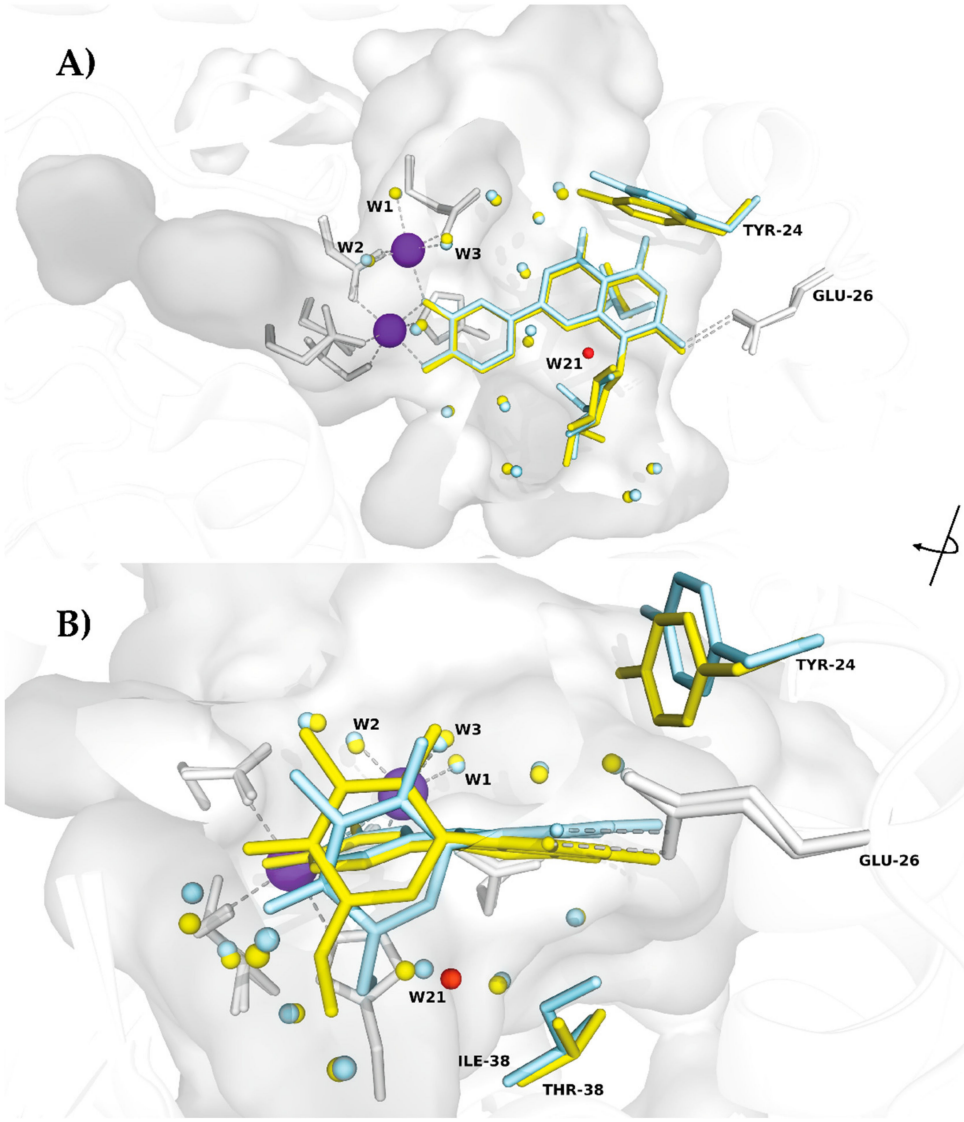


**Figure 4.** Structural alignment of wild-type PA-Nter (pale cyan) and its I38T mutant (yellow), both in complex with orientin (PDB ID 7NUG, 7NUH). The active site (**A**) containing two metal ions (purple-blue spheres) is presented as a surface cavity in grey. Closeup view, 90° clockwise rotated (**B**), onto interacting residues, Ile-38/Thr-38, and ligands (all in stick representation) reveals shift of the glucoside moiety. The hydrogen bond between ligand and the Glu-26 side chain is shown as a grey dash. Common waters contributing to protein-ligand binding, with a maximum distance of 3 Å from the ligand, are presented as spheres with color coding corresponding to each structure. Metal-coordinating water molecules (W1, W2 and W3) and W21 (red) are shown as spheres.

The side chain of Tyr-24 in the mutant variant approaches the active site pocket, whereas in the wild-type, Tyr-24 is pushed away from the cavity (RMSD of 0.029 Å for side chain atoms). Thr-38, which is one atom shorter than Ile-38, helps accommodate orientin. $O^{\gamma 1}$Thr-38 forms a hydrogen bond through W21 to the glucosyl moiety of the ligand (O6) (Figure 5). This is not observed in the wild-type, as Ile-38 does not contain a hydroxyl group capable of such interaction.

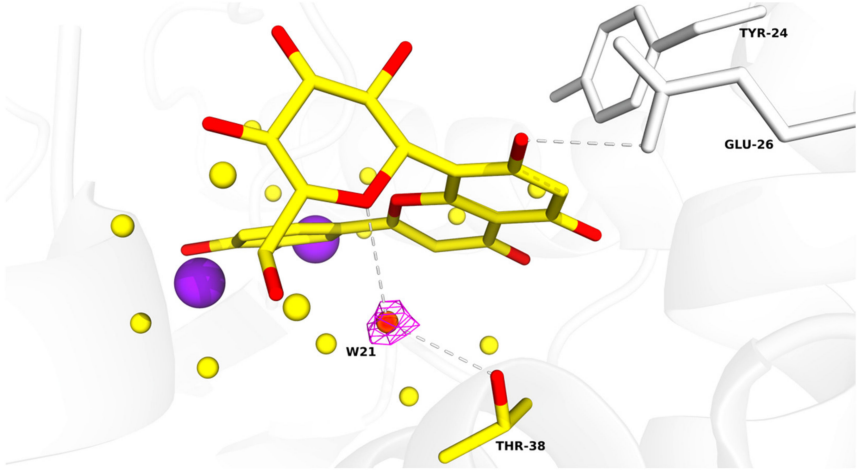


**Figure 5.** Closeup view of the active site pocket of I38T PA-Nter. Metal ions are shown as purple-blue spheres. Ligand and amino acid residues are shown in stick representation, where red represents oxygen atoms. The hydrogen bonds between the ligand and the Glu-26 side chain and between the ligand, W21, and the Thr-38 side chain are depicted as grey dashes. Water molecules are shown as yellow spheres, except for W21 which is shown as a red sphere with its 2Fo–Fc electron density map in magenta mesh contoured at 1.5 σ.

## 3. Materials and Methods

### *3.1. AlphaScreen Assay*

AlphaScreen experiments were performed using a Perkin Elmer Enspire plate reader in 96-well ProxiPlates. Biotinylated L-742.001 derivative [37] was captured on Streptavidin-coated donor beads (Perkin Elmer). Separately, GST-PA-Nter fusion protein was bound to GSH-coated acceptor beads (Perkin Elmer). These solutions were incubated for 60 min at room temperature in the dark and subsequently mixed and incubated for an additional 120 min. In experiments screening for endonuclease inhibitors, compounds were mixed with both types of beads prior to the 120-min incubation. The optimal concentrations of biotinylated L-742.001 derivative and GST-PA-Nter were 15 nM and 50 nM, respectively. The concentrations of donor and acceptor beads were 5 µg/mL each in a 50 µL reaction volume. All experiments were performed in 25 mM Tris-HCl, pH 7.4, 150 mM NaCl, 0.05% Tween20, 1 mM $MnCl_2$, 10 mM $MgCl_2$, and 1 mM 2-mercaptoethanol.

### *3.2. Cloning, Expression and Purification of Recombinant Proteins*

DNA encoding the first 196 amino acids of the N-terminal domain of the influenza polymerase acidic subunit (PA-Nter) from the viral strain A/California/07/2009 (H1N1) (GenBank accession No. CY121685.1) was prepared using GenScript USA Inx. The flexible loop (residues 51–72) was replaced with a GGS linker [52]. Constructs with affinity tags (GST-PA-Nter and $His_6$-SUMO-Nter) were prepared for both wild-type and I 38T PA-Nter. First, DNA encoding PA-Nter was inserted into the plasmid pGEX-1λT. Next, PA-Nter with a $(GS)_4$ linker and N-terminal extension was cloned into the plasmid pETM11-SUMO3 (EMBL, Heidelberg, Germany) using BamHI and XhoI sites. The I38T mutation was introduced into both GST- and $His_6$-SUMO-tagged constructs using the following primers for site-directed mutagenesis: 5′–CAAGTTTGCTGCAACATGCACACAT TTG–3′ and 5′–CAAATGTGTGCATGTTGCACAAACTTG–3′. All tagged PA-Nter constructs were expressed in *E. coli* BL21 (DE3) RIL. Cells were harvested and resuspended in lysis buffer (25 mM Tris/HCl, pH 7.5, 150 mM NaCl, 1 mM EDTA (GST) or 50 mM Tris/HCl, pH 8.0, 200 mM NaCl, 10 mM imidazole ($His_6$-SUMO)) and lysed with an EmulsiFlex device (Avestin, Ottawa, ON, Canada) at a pressure of 1200 bar. GST-tagged PA-Nter soluble proteins were loaded onto a glutathione-agarose column (ThermoFisher Scientific) and

eluted with elution buffer (50 mM Tris/HCl, pH 7.5, 150 mM NaCl, 10 mM reduced L glutathione, 1 mM EDTA). Analogously, $His_6$-SUMO PA-Nter was purified using Ni-NTA Agarose (Roche Diagnostics GmbH, Mannheim, Germany) and eluted with Ni-NTA elution buffer (50 mM Tris/HCl, pH 8.0, 200 mM NaCl, 250 mM imidazole). The $His_6$-SUMO tag was removed by the ULP1 protease. All proteins were purified on a Superdex 75 (GE Healthcare/Amersham Pharmacia, Uppsala, Sweden) gel filtration chromatography column, yielding >95% purity as estimated by SDS-PAGE.

### 3.3. Gel-Based Endonuclease Inhibitory Assay

To compare the endonuclease activities of wild-type and I38T PA-Nter in the presence of selected compounds (baloxavir acid, luteolin, orientin), we used a gel-based endonuclease inhibitory assay. The single-stranded DNA substrate M13mp18 (New England Biolabs) was cleaved in vitro by either protein. Each reaction (10 µL) contained 1 µM protein (GST-PA-Nter wild type/GST-PA-Nter I38T mutant) in digestion buffer (25 mM Tris-HCl, pH 7.4, 150 mM NaCl, 0.05% Tween20, 1 mM $MnCl_2$, 10 mM $MgCl_2$, 1 mM 2-mercaptoethanol) and was incubated with various concentrations of inhibitors (BXA/LU2/OTN/**21**/**30**). Reactions were initiated by the addition of 0.2 µg of M13mp18 plasmid. Reactions were incubated at 37 °C for 5 h and stopped by adding 1 µL of 0.2 M EDTA. Finally, cleavage of DNA substrate was visualized by agarose electrophoresis using 1% agarose gel stained with GelRed.

### 3.4. Crystallization and Diffraction Data Collection

Hexagonal bifrustum crystals of empty wild-type and I38T PA-Nter subunits were obtained by the hanging-drop vapor diffusion method. Protein solution (12 mg/mL) was mixed with crystallization reservoir solution (12.5% *w*/*v* PEG 1000, 12.5% *w*/*v* PEG 3350, 0.1% M MOPS/HEPES-Na pH 7.5, 0.06 M magnesium chloride, 0.06 M calcium chloride) and PA-Nter seed in a 1:1:0.2 ratio. Crystals grew at 18 °C until they reached approximately 0.2 mm in diameter. Ligands (100 mM solution in DMSO) were soaked in for 15 min (the final DMSO concentration did not exceed 5%). Crystals were harvested, flash-cooled by plunging into liquid nitrogen and stored at −196 °C.

Diffraction qualities were tested at BESSY II and data were collected at −173 °C on a home diffractometer (MicroMax-007 HF microfocus equipped with a PILATUS 300 K detector, Rigaku). The crystal of wild-type PA-Nter soaked with orientin diffracted to a resolution of up to 1.87 Å, and the I38T PA-Nter/orientin crystal diffracted up to 2.15 Å. Diffraction data were processed, integrated, and reduced using XDS [53] and scaled using XSCALE from the XDS suite [54]. Both crystals belonged to the $\boldsymbol{P}6_422$ space group and contained one molecule per asymmetric unit, with a solvent content of 47.5% (wild-type PA-Nter), and 48.2% (I38T PA-Nter). We observed anomalous signals up to a resolution of 3.0 Å for wild-type and 3.5 Å for the I38T variant. Therefore, the data were processed with unmerged Friedel pairs. Detailed crystal parameters and data collection statistics are given in Table S1.

### 3.5. Structure Determination and Analyses

Structures of wild-type and I38T PA-Nter were determined by molecular replacement with MOLREP [55] from the CCP4 package [56] using a previously reported structure of PA-Nter as a template (PDB entry 6YA5 [37]). The final step of complex structure polishing was carried out by cycles of manual adjustments using Coot software [57] followed by refinement in REFMAC 5.8.0103 [58]. MolProbity [59] was used to validate the quality of the final models. Refinement statistics are given in Table S1. All figures illustrating structural representations were prepared with PyMOL (The PyMOL Molecular Graphics System, Version 2.4.2 accessed on 10 March 2020; Schrödinger, LLC., New York, NY, USA). Atomic coordinates and experimental structure factors are deposited in the Protein Data Bank under codes 7NUG for wild-type PA-Nter in complex with orientin and 7NUH for I38T PA-Nter in complex with orientin.

### *3.6. Chemistry*

Unless otherwise noted, all reactions were carried out under argon in oven-dried glassware. Solvents were distilled from drying agents as indicated and transferred under nitrogen: THF (Na/benzophenone), toluene (Na/benzophenone), MeCN ($CaH_2$), and DCM ($CaH_2$). Chromatography was performed using a Teledyne ISCO Combi Flash Rf+ flash chromatography system with RediSep Rf Gold Silica or RediSep Rf Gold Reversed-phase C18 columns. All starting materials were used as purchased (Sigma Aldrich, Alfa Aesar, TCI, Fluorochem, Combi-Blocks), unless otherwise indicated. Compounds luteolin and orientin were purchased from Sigma-Aldrich (product numbers L9283 and O9765). All inhibitors were purified using an ECOM TOY18DAD800 compact preparative system [flow rate 15 mL/min; gradient 0–60% MeCN/$H_2O$ (0.1% trifluoroacetic acid) over 60 min], with a ProntoSIL 120-10-C18 ace-EPS column, 10 µm, 20 × 250 mm. The purity of compounds and composition of the reaction mixtures were tested on a Waters UPLC-MS Acquity with QDa Mass Detector (flow rate 0.5 mL/min, gradient 0–100 % MeCN/$H_2O$ (0.1% formic acid) over 7 min) with an ACQUITY UPLC BEH C18 Column, 130 Å, 1.7 µm, 2.1 mm × 100 mm with a 2.1 mm × 5 mm pre-column. The final inhibitors were of at least 90% purity. $^1$H-NMR spectra were recorded on Bruker instruments at 400, 500 or 600 MHz; $^{13}$C-NMR spectra were recorded at 100, 126 or 150 MHz. Chemical shifts are provided in $\delta$-scale; coupling constants $J$ are given in Hz. ESI high resolution mass spectra were recorded using a Thermo Scientific LTQ Orbitrap XL (Termo Fisher Scientific, Waltham, Massachusetts, USA) controlled by MassLynx software.

Compounds **1** and **2** were prepared according to literature procedures [43]. Analytical data for these compounds were in agreement with published data.

### *3.7. 4-(5,7-Diacetoxy-4-oxo-4H-chromen-2-yl)-1,2-phenylene Diacetate (**1**)*

Neat acetic anhydride (10 mL) was added to luteolin (1.43 g, 5.0 mmol), followed by the addition of pyridine (1.0 mL). The reaction mixture was heated to 145 °C for 3 h. The hot mixture was poured into ice and stirred for 30 min. The suspension was filtered off, and the solids were mixed with a boiling mixture of MeOH/$CHCl_3$ (9:1, 15 mL). The product was isolated by filtration from the cool suspension to furnish the desired compound **1** (1.75 g, 77%). $^1$H NMR (400 MHz, $CDCl_3$) $\delta$ = 7.74 (dd, $J$ = 8.4, 2.2 Hz, 1H), 7.70 (d, $J$ = 2.1 Hz, 1H), 7.38–7.32 (m, 2H), 6.85 (d, $J$ = 2.2 Hz, 1H), 6.61 (s, 1H), 2.44 (s, 3H), 2.35 (s, 6H), 2.33 (s, 3H) ppm. $^{13}$C NMR (101 MHz, $CDCl_3$) $\delta$ = 176.3, 169.5, 168.1, 167.9, 160.9, 157.7, 154.2, 150.4, 145.0, 142.8, 129.8, 124.6, 124.5, 121.8, 115.0, 114.0, 109.2, 109.1, 21.3, 21.2, 20.8, 20.8 ppm.

### *3.8. 4-(5-Acetoxy-7-hydroxy-4-oxo-4H-chromen-2-yl)-1,2-phenylene Diacetate (**2**)*

4-(5,7-Diacetoxy-4-oxo-4*H*-chromen-2-yl)-1,2-phenylene diacetate (**1**) (1.70 g, 3.7 mmol, 1.00 eq.) was dissolved in THF (56 mL) and NMP (19 mL). Then, imidazole (88.5 mg, 1.3 mmol, 0.35 eq.) was added at 0 °C followed by addition of thiophenol (0.45 mL, 4.4 mmol, 1.18 eq.) via septum under a nitrogen atmosphere at 0 °C. The reaction mixture was stirred and slowly warmed to room temperature over 2 h until the starting material was fully consumed (TLC, UPLC-MS). Volatiles were evaporated and the oily residue was dissolved in EtOAc (150 mL). The organic phase was washed with 5% HCl (aq., 5 × 45 mL), and organic solvents were evaporated. The solids were mixed with EtOH, and the product was isolated by filtration to furnish the desired compound **2** (1.05 g, 68%). $^1$H NMR (400 MHz, DMSO-$d_6$) $\delta$ = 11.17 (s, 1H), 8.08–7.95 (m, 2H), 7.49 (d, $J$ = 9.0 Hz, 1H), 6.97 (d, $J$ = 2.3 Hz, 1H), 6.80 (s, 1H), 6.60 (d, $J$ = 2.3 Hz, 1H), 2.35 (s, 3H), 2.34 (s, 3H), 2.32 (s, 3H) ppm. $^{13}$C NMR (101 MHz, DMSO-$d_6$) $\delta$ = 175.2, 168.9, 168.2, 168.0, 162.3, 159.4, 158.2, 150.1, 144.6, 142.5, 129.5, 124.8, 124.5, 121.7, 109.5, 108.8, 108.0, 101.0, 21.0, 20.4 (2C) ppm.

### *3.9. 4-(5-Acetoxy-4-oxo-7-(((trifluoromethyl)sulfonyl)oxy)-4H-chromen-2-yl)-1,2-phenylene Diacetate (**3**)*

A flask with 4-(5-acetoxy-7-hydroxy-4-oxo-4*H*-chromen-2-yl)-1,2-phenylene diacetate (**2**) (1.00 g, 2.4 mmol, 1.0 eq.) was purged with nitrogen. The solids were mixed with dry $CH_2Cl_2$ (12 mL) and the suspension was cooled to 0 °C. Pyridine (0.39 mL, 4.9 mmol, 2.0 eq.) was added dropwise. After 10 min, trifluoromethanesulfonic anhydride (0.53 mL, 3.2 mmol, 1.3 eq.) was added dropwise at 0 °C under a nitrogen atmosphere. The resulting red-colored reaction mixture was stirred for 3.5 h until the starting material was fully consumed (TLC, UPLC-MS). Then, the reaction mixture was diluted with additional $CH_2Cl_2$ (15 mL) and washed with sat. $NH_4Cl$ (aq., 1 × 10 mL), sat. $CuSO_4$ (aq., 2 × 10 mL) and water (1 × 10 mL). The organic phase was dried over anhydrous $MgSO_4$ and then evaporated under reduced pressure. The residue was purified by flash chromatography ($SiO_2$, cyclohexane/EtOAc = 100:0 → 50:50) to afford the desired triflate **3** (533 mg, 41%). $^1$H NMR (400 MHz, $CDCl_3$) $\delta$ = 7.74 (dd, *J* = 8.5, 2.3 Hz, 1H), 7.71 (d, *J* = 2.1 Hz, 1H), 7.44 (d, *J* = 2.4 Hz, 1H), 7.38 (d, *J* = 8.4 Hz, 1H), 6.99 (d, *J* = 2.4 Hz, 1H), 6.65 (s, 1H), 2.45 (s, 3H), 2.35 (s, 3H), 2.33 (s, 3H) ppm. $^{13}$C NMR (101 MHz, $CDCl_3$) $\delta$ = 175.6, 169.1, 168.1, 167.8, 161.3, 157.6, 151.6, 151.3, 145.3, 142.9, 129.2, 124.7, 124.6, 121.9, 120.4, 117.1, 113.6, 109.5, 109.4, 21.1, 20.8, 20.7 ppm. $^{19}$F NMR (376 MHz, $CDCl_3$) $\delta$ = −72.4 ppm. HRMS (ESI) *m/z* calcd for $C_{22}H_{16}F_3O_{11}S$ $[M+H^+]^+$ 545.0359, found 545.0356.

### *3.10. 4-(5-Acetoxy-7-(diethoxyphosphoryl)-4-oxo-4H-chromen-2-yl)-1,2-phenylene Diacetate (**4**)*

A tube with 4-(5-acetoxy-4-oxo-7-(((trifluoromethyl)sulfonyl)oxy)-4*H*-chromen-2-yl)-1,2-phenylene diacetate (**3**) (100 mg, 0.184 mmol, 1.0 eq.) and $Pd(PPh_3)_4$ (64 mg, 0.055 mmol, 0.3 eq.) was sealed, and the mixture was dissolved in anhydrous MeCN (1.8 mL) followed by an addition of diethylphosphite (30 µL, 0.221 mmol, 1.2 eq.) and DIPEA (42 µL, 0.240 mmol, 1.3 eq.) via septum. The mixture was degassed with a stream of argon for 15 min followed by heating to 70 °C for 3 h until the starting material was fully consumed (TLC, UPLC-MS). The reaction mixture was cooled to room temperature, filtered through Celite, and washed with EtOAc. Solvents were evaporated and the resulting mixture was purified by flash chromatography ($SiO_2$, cyclohexane/EtOAc = 100:0 → 0:100) to afford the desired phosphonate **4** (76 mg, 78%). $^1$H NMR (400 MHz, $CDCl_3$) $\delta$ = 7.93 (dd, *J* = 14.9, 1.3 Hz, 1H), 7.76–7.70 (m, 2H), 7.39–7.31 (m, 2H), 6.65 (s, 1H), 4.27–4.04 (m, 4H), 2.42 (s, 3H), 2.32 (s, 3H), 2.30 (s, 3H), 1.34 (td, *J* = 7.0, 0.6 Hz, 6H) ppm. $^{13}$C NMR (101 MHz, $CDCl_3$) $\delta$ = 176.3, 169.5, 168.0, 167.8, 161.2, 156.8 (d, *J* = 23.5 Hz), 149.6, 149.4, 145.1, 142.8, 135.9, 134.0, 129.4, 124.6, 124.5, 121.8, 121.5 (d, *J* = 9.5 Hz), 120.3 (d, *J* = 10.3 Hz), 119.4 (d, *J* = 2.6 Hz), 109.2, 63.1, 63.0, 21.1, 20.7, 20.6, 16.4, 16.4 ppm. $^{31}$P NMR (162 MHz, $CDCl_3$) $\delta$ = 16.58 ppm. HRMS (ESI) *m/z* calcd for $C_{25}H_{25}O_{11}PNa$ $[M+Na^+]^+$ 555.1026, found 555.1023.

### *3.11. (2-(3,4-Dihydroxyphenyl)-5-hydroxy-4-oxo-4H-chromen-7-yl)phosphonic Acid (**5**)*

4-(5-Acetoxy-7-(diethoxyphosphoryl)-4-oxo-4*H*-chromen-2-yl)-1,2-phenylene diacetate (**4**) (312 mg, 0.58 mmol, 1.0 eq.) was dissolved in dry $CH_2Cl_2$ (18 mL). Then, bromo-trimethylsilane (0.77 mL, 5.86 mmol, 10 eq.) was added dropwise under a nitrogen atmosphere. The reaction mixture was stirred for 31 h until the starting material was fully consumed (TLC, UPLC-MS). The solvent was evaporated and MeOH (3.1 mL) was added. The white suspension was allowed to stir for 1 h followed by evaporation of the solvent. THF (5.8 mL) was added, followed by an addition of 1 M KOH in MeOH (2.9 mL, 2.9 mmol, 5.0 eq). The reaction mixture was allowed to stir for 1 h. Solvent was evaporated, and the resulting mixture was purified by flash chromatography ($SiO_2$-$C_{18}$, $H_2O$ (0.1% TFA)/MeCN= 100:0 → 30:70) to afford the desired final phosphonic acid **5** (51 mg, 25%). $^1$H NMR (400 MHz, DMSO-$d_6$) $\delta$ = 12.83 (s, 1H), 7.51 (dd, *J* = 8.3, 2.3 Hz, 1H), 7.48 (d, *J* = 2.3 Hz, 1H), 7.34 (dd, *J* = 14.0, 1.2 Hz, 1H), 6.97 (dd, *J* = 13.7, 1.2 Hz, 1H), 6.91 (d, *J* = 8.3 Hz, 1H), 6.87 (s, 1H) ppm. $^{13}$C NMR (101 MHz, DMSO-$d_6$) $\delta$ = 183.1, 165.7, 159.9 (d, *J* = 19.7 Hz), 155.8, 155.6, 150.7, 146.3, 143.6, 141.9, 121.6, 120.0, 116.5, 114.2, 112.5 (d, *J* = 9.9 Hz), 111.5 (d, *J* = 2.6 Hz), 109.6 (d, *J* = 9.9 Hz), 104.2 ppm. $^{31}$P NMR (162 MHz, DMSO) $\delta$ = 11.98 ppm. HRMS (ESI) *m/z* calcd for $C_{15}H_{10}O_8P$ $[M-H^+]^-$ 349.0118, found 349.0118.

*3.12. Palladium-Catalyzed Methoxycarbonylation of Triflate* **3**

A tube with 4-(5-acetoxy-4-oxo-7-(((trifluoromethyl)sulfonyl)oxy)-4*H*-chromen-2-yl)-1,2-phenylene diacetate (**3**) (100 mg, 0.184 mmol, 1.0 eq.), 1,3-bis(diphenylphosphino)propane (7.50 mg, 0.018 mmol, 0.1 eq.), $Mo(CO)_6$ (24 mg, 0.092 mmol, 0.5 eq.) and palladium acetate (4.00 mg, 0.018 mmol, 0.1 eq.) was sealed, and dry DMSO (1.1 mL) and dry MeOH (0.7 mL) were added via septum. The mixture was degassed with a stream of argon for 15 min followed by addition of triethylamine (57 µL, 0.405 mmol, 2.2 eq.). The reaction mixture was heated to 70 °C for 20 h until the starting material was fully consumed (UPLC-MS). The reaction mixture was cooled to room temperature, diluted with MeOH (5 mL), and filtered through a syringe filter. The solvents were evaporated, and the residue was purified by flash chromatography ($SiO_2$-$C_{18}$, $H_2O$ (0.1% TFA)/MeCN = 100:0 → 20:80) to afford the desired monoacetylated ester **6** (28 mg, 40%) and deacetylated ester **7** (29 mg, 48%).

*3.13. Methyl 5-acetoxy-2-(3,4-dihydroxyphenyl)-4-oxo-4H-chromene-7-carboxylate (**6**)*

$^1$H NMR (401 MHz, DMSO-$d_6$) δ 9.98 (s, 1H), 9.37 (s, 1H), 8.12 (t, *J* = 1.5 Hz, 1H), 7.56 – 7.52 (m, 1H), 7.50 – 7.43 (m, 2H), 6.90 (d, *J* = 8.2 Hz, 1H), 6.69 (s, 1H), 3.92 (s, 3H), 2.33 (s, 3H) ppm. $^{13}$C NMR (101 MHz, DMSO-$d_6$) δ 175.2, 169.0, 164.2, 162.9, 156.4, 149.9, 148.8, 145.8, 133.9, 121.1, 119.3, 119.2, 118.8, 117.4, 116.0, 113.6, 106.2, 53.0, 20.9 ppm. HRMS (ESI) *m/z* calcd for $C_{19}H_{14}O_8Na$ $[M+Na^+]^+$ 393.0581, found 393.0580.

*3.14. Methyl 2-(3,4-dihydroxyphenyl)-5-hydroxy-4-oxo-4H-chromene-7-carboxylate (**7**)*

$^1$H NMR (401 MHz, DMSO-$d_6$) δ 12.91 (s, 1H), 10.11 (s, 1H), 9.42 (s, 1H), 7.64 (d, *J* = 1.6 Hz, 1H), 7.55 (dd, *J* = 8.4, 2.3 Hz, 1H), 7.51 (d, *J* = 2.3 Hz, 1H), 7.22 (d, *J* = 1.6 Hz, 1H), 6.93–6.91 (m, 2H), 3.91 (s, 3H) ppm. $^{13}$C NMR (101 MHz, DMSO-$d_6$) δ 182.9, 166.5, 165.3, 160.4, 156.0, 150.9, 146.3, 135.8, 121.4, 120.2, 116.5, 114.3, 113.0, 111.1, 108.7, 104.3, 53.3 ppm. HRMS (ESI) *m/z* calcd for $C_{17}H_{12}O_7$ $[M+H^+]^+$ 329.0656, found 329.0655.

*3.15. 2-(3,4-Dihydroxyphenyl)-5-hydroxy-4-oxo-4H-chromene-7-carboxylic acid (**8**)*

A solution of methyl 2-(3,4-dihydroxyphenyl)-5-hydroxy-4-oxo-4*H*-chromene-7- carboxylate (**7**) (136 mg, 0.41 mmol, 1.0 eq.) in THF (8.4 mL) was heated to 45 °C under a nitrogen atmosphere, followed by addition of 2 M aq. LiOH (4.2 mL, 8.3 mmol, 20 eq.) via septum. The reaction mixture was stirred for 1 h until the starting material was fully consumed (UPLC-MS). The solvents were evaporated and the residue was purified by flash chromatography ($SiO_2$-$C_{18}$, $H_2O$ (0.1% TFA)/MeCN= 100:0 → 20:80) to afford the desired final carboxylic acid **8** (93 mg, 71 %). $^1$H NMR (400 MHz, DMSO-$d_6$) $\delta$ = 12.87 (s, 1H), 10.09 (s, 1H), 9.43 (s, 1H), 7.61 (d, *J* = 1.3 Hz, 1H), 7.53 (dd, *J* = 8.4, 2.3 Hz, 1H), 7.49 (d, *J* = 2.3 Hz, 1H), 7.21 (d, *J* = 1.3 Hz, 1H), 6.91 (d, *J* = 9.0 Hz, 2H) ppm. $^{13}$C NMR (101 MHz, DMSO-$d_6$) $\delta$ = 182.6, 165.8, 165.6, 159.9, 155.5, 150.4, 145.9, 136.9, 121.1, 119.7, 116.1, 113.8, 112.3, 110.8, 108.2, 103.8 ppm. HRMS (ESI) *m/z* calcd for $C_{16}H_{10}O_7$ $[M-H^+]^-$ 313.0354, found 313.0351.

*3.16. 2-(3,4-Dihydroxyphenyl)-5-hydroxy-4-oxo-4H-chromene-7-carboxamide (**9**)*

A tube with a mixture of methyl 5-acetoxy-2-(3,4-dihydroxyphenyl)-4-oxo-4*H*-chromene-7-carboxylate (**6**) (21.5 mg, 0.058 mmol, 1.0 eq.) and methyl 2-(3,4-dihydroxyphenyl)-5-hydroxy-4-oxo-4*H*-chromene-7-carboxylate (**7**) (22 mg, 0.067 mmol, 1.15 eq.) was sealed, and 7 M ammonia in MeOH (10 mL) was added via septum. The reaction mixture was heated to 50 °C and stirred for 4 days until the starting materials were fully consumed (UPLC-MS). The solvents were evaporated and the residue was purified by preparative HPLC to obtain the final amide **9** (8.0 mg, 21%). $^1$H NMR (600 MHz, DMSO-$d_6$) $\delta$ = 12.82 (s, 1H), 10.07 (s, 1H), 9.45 (d, *J* = 2.5 Hz, 1H), 8.20 (s, 1H), 7.68 (s, 1H), 7.60 (d, *J* = 1.5 Hz, 1H), 7.51 (dd, *J* = 8.4, 2.3 Hz, 1H), 7.47 (d, *J* = 2.3 Hz, 1H), 7.25 (d, *J* = 1.3 Hz, 1H), 6.92 (d, *J* = 8.5 Hz, 1H), 6.89 (s, 1H) ppm. $^{13}$C NMR (151 MHz, DMSO-$d_6$) $\delta$ = 182.6, 166.1, 165.5, 159.8, 155.5, 150.3, 145.9, 140.7, 121.2, 119.5, 116.1, 113.7, 111.3, 109.6, 106.6, 103.8 ppm. HRMS (ESI) *m/z* calcd for $C_{16}H_{11}NO_6Na$ $[M+Na^+]^+$ 336.0479, found 336.0479.

*3.17. 2-(3,4-Dihydroxyphenyl)-5-hydroxy-N-(2-hydroxyethyl)-4-oxo-4H-chromene-7-carboxamide (***10***)*

Methyl 2-(3,4-dihydroxyphenyl)-5-hydroxy-4-oxo-4*H*-chromene-7-carboxylate (**7**) (70 mg, 0.213 mmol, 1.0 eq.) was mixed with dry EtOH (2 mL). Potassium carbonate (100 mg, 0.723 mmol, 3.4 eq.) was added, followed by 2-aminoethanol (0.6 mL). The reaction mixture was heated to 50 °C and stirred for 48 h until the starting materials was fully consumed (UPLC-MS). The solvents were evaporated and the residue was purified by preparative HPLC to obtain the final amide **10** (17 mg, 23%). $^{1}$H NMR (400 MHz, DMSO-$d_6$) $\delta$ = 12.81 (s, 1H), 10.07 (s, 1H), 9.45 (s, 1H), 8.68 (t, *J* = 5.6 Hz, 1H), 7.59 (d, *J* = 1.5 Hz, 1H), 7.51 (dd, *J* = 8.3, 2.3 Hz, 1H), 7.48 (d, *J* = 2.3 Hz, 1H), 7.23 (d, *J* = 1.5 Hz, 1H), 6.92 (d, *J* = 8.4 Hz, 1H), 6.89 (s, 1H), 3.53 (t, *J* = 6.1 Hz, 2H), 3.35 (q, *J* = 5.2, 4.4 Hz, 2H) ppm. $^{13}$C NMR (101 MHz, DMSO-$d_6$) $\delta$ = 182.6, 165.4, 164.6, 159.8, 155.5, 150.3, 145.9, 140.9, 121.2, 119.5, 116.1, 113.7, 111.2, 109.3, 106.4, 103.7, 59.5, 42.4 ppm. HRMS (ESI) *m/z* calcd for $C_{18}H_{15}NO_7Na$ $[M+Na^+]^+$ 380.0741, found 380.0742.

*3.18. 7-Amino-2-(3,4-dihydroxyphenyl)-5-hydroxy-4H-chromen-4-one (***11***)*

2-(3,4-Dihydroxyphenyl)-5-hydroxy-4-oxo-4*H*-chromene-7-carboxylic acid (**8**) (32 mg, 0.102 mmol, 1.0 eq.) was dissolved in dry DMF (1 mL) followed by dropwise addition of triethylamine (21 µL, 0.143 mmol, 1.4 eq.) and diphenylphosphoryl azide (31 µL, 0.143 mmol, 1.4 eq.) under a nitrogen atmosphere. The reaction mixture was heated to 100 °C and stirred for 16 h. Water (1 mL) was added and the reaction mixture was stirred for 3 h at 100 °C. The solvents were evaporated and the residue was purified by preparative HPLC to obtain the final amine **11** (8.7 mg, 30%). $^{1}$H NMR (500 MHz, DMSO-$d_6$) $\delta$ = 12.93 (s, 1H), 9.83 (s, 1H), 9.39 (s, 1H), $\delta$ = 7.36–7.33 (m, 2H), 6.87 (d, *J* = 8.1 Hz, 1H), 6.51 (s, 1H), 6.12 (d, *J* = 1.8 Hz, 1H), 5.92 (d, *J* = 2.0 Hz, 1H) ppm. $^{13}$C NMR (126 MHz, DMSO-$d_6$) $\delta$ = 181.1, 163.2, 161.6, 158.1, 156.3, 149.7, 146.1, 122.3, 119.0, 116.5, 113.6, 103.0, 101.5, 96.3, 90.7 ppm. HRMS (ESI) *m/z* calcd for $C_{15}H_{12}NO_5$ $[M+H^+]^+$ 286.0710, found 286.0710.

*3.19. N-(2-(3,4-Dihydroxyphenyl)-5-hydroxy-4-oxo-4H-chromen-7-yl)acetamide (***12***)*

7-Amino-2-(3,4-dihydroxyphenyl)-5-hydroxy-4*H*-chromen-4-one **(11)** (30 mg, 0.10 mmol, 1.0 eq.) was dissolved in dry DMF (0.5 mL), followed by addition of DIPEA (37 µL, 0.21 mmol, 2.0 eq.) and *N*-succinimidyl acetate (33 mg, 0.15 mmol, 1.5 eq.). The reaction mixture was allowed to stir at room temperature for 36 h until the starting material was fully consumed (UPLC-MS). The reaction mixture was directly purified by preparative HPLC to obtain the final product **12** (7.9 mg, 23%). $^{1}$H NMR (400 MHz, DMSO-$d_6$) $\delta$ = 10.57 (s, 1H), 7.78 (dd, *J* = 8.6, 2.3 Hz, 1H), 7.73 (d, *J* = 2.2 Hz, 1H), 7.06 (d, *J* = 8.6 Hz, 1H), 6.67 (s, 1H), 6.17 (d, *J* = 1.8 Hz, 1H), 5.94 (d, *J* = 2.0 Hz, 1H), 2.30 (s, 3H) ppm. $^{13}$C NMR (101 MHz, DMSO-$d_6$) $\delta$ = 180.6, 168.7, 161.7, 161.1, 157.6, 155.9, 152.5, 138.7, 125.2, 122.0, 121.5, 117.3, 103.2, 101.1, 95.9, 90.4, 20.6 ppm. HRMS (ESI) *m/z* calcd for $C_{17}H_{12}NO_6$ $[M-H^+]^-$ 326.0670, found 326.0671.

*3.20. 4-(5-Acetoxy-7-cyano-4-oxo-4H-chromen-2-yl)-1,2-phenylene Diacetate (***13***)*

A tube with 4-(5-acetoxy-4-oxo-7-(((trifluoromethyl)sulfonyl)oxy)-4*H*-chromen-2-yl)-1,2-phenylene diacetate (**3**) (100 mg, 0.184 mmol, 1.00 eq.), zinc cyanide (12.0 mg, 0.101 mmol, 0.55 eq.), and XantPhos Pd G2 (2.00 mg, 0.002 mmol, 0.01 eq.) was sealed and purged with nitrogen. Dry DMF (0.9 mL) and DIPEA (15 µL, 0.084 mmol, 0.15 eq.) were added. The reaction mixture was heated to 85 °C and stirred for 16 h until the starting material was fully consumed (TLC, UPLC-MS). Then the reaction mixture was cooled to room temperature, and EtOAc (5 mL) was added. The reaction mixture was washed with water (2 × 10 mL), and the organic phase was dried over anhydrous $MgSO_4$ and then evaporated under reduced pressure. The resulting mixture was purified by flash chromatography ($SiO_2$, cyclohexane/EtOAc = 100:0 → 60:40) to afford the desired nitrile **13** (47 mg, 61 %). $^{1}$H NMR (400 MHz, $CDCl_3$) $\delta$ = 7.79 (d, *J* = 1.5 Hz, 1H), 7.75 (d, *J* = 2.2 Hz, 1H), 7.73–7.71 (m, 1H), 7.38 (d, *J* = 8.4 Hz, 1H), 7.27 (d, *J* = 1.5 Hz, 1H), 6.67 (s, 1H), 2.46 (s, 3H), 2.35 (s, 3H), 2.34 (s, 3H) ppm. $^{13}$C NMR (101 MHz, $CDCl_3$) $\delta$ = 175.5, 169.2, 168.0, 167.7, 161.4, 156.8, 150.2, 145.3, 142.8, 128.9, 124.6, 124.5, 122.1, 121.8, 120.6, 120.2, 116.9, 116.2, 109.5, 21.0, 20.7, 20.6 ppm. HRMS (ESI) *m/z* calcd for $C_{22}H_{15}NO_8Na$ $[M+Na^+]^+$ 444.0690, found 444.0691.

*3.21. 2-(3,4-Dihydroxyphenyl)-5-hydroxy-7-(2H-tetrazol-5-yl)-4H-chromen-4-one (**14**)*

A tube with 4-(5-acetoxy-7-cyano-4-oxo-4*H*-chromen-2-yl)-1,2-phenylene diacetate (**13**) (58 mg, 0.134 mmol, 1.0 eq) and $NaN_3$ (36 mg, 0.562 mmol, 4.0 eq.) was sealed and the mixture was dissolved in dry DMF (0.5 mL). The mixture was degassed with a stream of argon for 10 min, followed by addition of glacial acetic acid (2 drops) via septum and the reaction mixture was heated to 130 °C for 16 h until the starting material was fully consumed (TLC, UPLC-MS). The reaction mixture was cooled to room temperature, and 4 M HCl was added until the pH reached 2. The solvents were evaporated, and the residue was purified by preparative HPLC to obtain the final tetrazole derivative **14** (18 mg, 38%). $^1$H NMR (400 MHz, DMSO-$d_6$) $\delta$ = 13.02 (s, 1H), 10.09 (s, 1H), 9.45 (s, 1H), 7.77 (d, *J* = 1.5 Hz, 1H), 7.52 (dd, *J* = 8.4, 2.4 Hz, 1H), 7.49 (d, *J* = 2.3 Hz, 1H), 7.39 (d, *J* = 1.6 Hz, 1H), 6.98 –6.86 (m, 2H) ppm. $^{13}$C NMR (101 MHz, DMSO-$d_6$) $\delta$ = 182.3, 165.4, 160.5, 156.1, 150.4, 145.9, 130.5, 121.0, 119.6, 116.1, 113.7, 111.2, 108.7, 105.8, 103.9 ppm. HRMS (ESI) *m/z* calcd for $C_{16}H_{11}N_4O_5$ $[M+H^+]^+$ 339.0724, found 339.0724.

*3.22. 2-(3,4-Dihydroxyphenyl)-5-hydroxy-4-oxo-4H-chromene-7-carbonitrile (**15**)*

4-(5-Acetoxy-7-cyano-4-oxo-4*H*-chromen-2-yl)-1,2-phenylene diacetate (**13**) (47 mg, 0.11 mmol, 1.0 eq.) was dissolved in THF (1.1 mL), followed by addition of 2 M aq. LiOH (0.33 mL, 0.66 mmol, 6.0 eq.). The reaction mixture was allowed to stir for 24 h at room temperature under a nitrogen atmosphere until the starting material was fully consumed (UPLC-MS). Then, solvents were evaporated and the residue was purified by preparative HPLC to obtain the final nitrile **15** (25 mg, 77%). $^1$H NMR (400 MHz, DMSO-$d_6$) $\delta$ = 13.12 (s, 1H), 10.15 (s, 1H), 9.46 (s, 1H), 7.72 (d, *J* = 1.3 Hz, 1H), 7.50 (dd, *J* = 8.3, 2.3 Hz, 1H), 7.46 (d, *J* = 2.3 Hz, 1H), 7.25 (d, *J* = 1.5 Hz, 1H), 6.94 (s, 1H), 6.91 (d, *J* = 8.3 Hz, 1H) ppm. $^{13}$C NMR (101 MHz, DMSO-$d_6$) $\delta$ = 182.3, 165.7, 160.3, 155.5, 150.6, 145.9, 120.8, 119.8, 117.4, 116.6, 116.0, 113.9, 112.8, 111.8, 104.2 ppm. HRMS (ESI) *m/z* calcd for $C_{16}H_{10}NO_5$ $[M+H^+]^+$ 296.0554, found 296.0551.

*3.23. Tert-Butyl ((2-(3,4-dihydroxyphenyl)-5-hydroxy-4-oxo-4H-chromen-7-yl)methyl)carbamate (**16**)*

A tube with 4-(5-acetoxy-4-oxo-7-(((trifluoromethyl)sulfonyl)oxy)-4*H*-chromen-2-yl)-1,2-phenylene diacetate (**3**) (100 mg, 0.184 mmol, 1.0 eq.), potassium (((*tert*-butoxy- carbonyl)amino)methyl)trifluoroborate (66 mg, 0.276 mmol, 1.5 eq.), $K_2CO_3$ (127 mg, 0.552 mmol, 3.0 eq.) and SPhos Pd G2 (15 mg, 0.018 mmol, 0.1 eq.) was sealed, and THF/water (25:1, 3.5 mL) was added via septum. The mixture was degassed with a stream of argon for 15 min, followed by heating to 100 °C for 2 h until the starting material was fully consumed (TLC, UPLC-MS). The reaction mixture was cooled to room temperature, diluted with EtOAc (2 mL), and filtered through a syringe filter. The solvents were evaporated and the residue was purified by flash chromatography ($SiO_2$-$C_{18}$, $H_2O$/MeCN= 100:0 → 0:100) to afford the desired carbamate **16** (32 mg, 43%). $^1$H NMR (400 MHz, DMSO-$d_6$) $\delta$ = 12.78 (s, 1H), 7.54 (t, *J* = 6.2 Hz, 1H), 7.47 (dd, *J* = 8.3, 2.3 Hz, 1H), 7.44 (d, *J* = 2.3 Hz, 1H), 6.98 (s, 1H), 6.91 (d, *J* = 8.3 Hz, 1H), 6.81 (s, 1H), 6.67 (d, *J* = 1.3 Hz, 1H), 4.21 (d, *J* = 6.1 Hz, 2H), 1.42 (s, 9H) ppm. $^{13}$C NMR (101 MHz, DMSO-$d_6$) $\delta$ = 183.0, 165.2, 160.2, 156.2, 150.7, 149.8, 146.3, 121.6, 119.8, 116.5, 113.9, 109.5, 109.1, 105.5, 103.8, 78.6, 43.9, 28.7 ppm. HRMS (ESI) *m/z* calcd for $C_{21}H_{22}NO_7$ $[M+H^+]^+$ 400.1391, found 400.1386.

*3.24. 7-(Aminomethyl)-2-(3,4-dihydroxyphenyl)-5-hydroxy-4H-chromen-4-one (**17**)*

Tert-butyl ((2-(3,4-dihydroxyphenyl)-5-hydroxy-4-oxo-4*H*-chromen-7-yl)methyl) carbamate (**16**) (25 mg, 0.063 mmol) was dissolved in THF/water (4:1, 1.5 mL), followed by addition of trifluoroacetic acid (0.6 mL). The reaction mixture was heated to 50 °C and allowed to stir for 48 h. The solvents were evaporated and the residue was purified by preparative HPLC to obtain the final amine **17** (19 mg, 73%). $^1$H NMR (400 MHz, DMSO-$d_6$) $\delta$ = 12.85 (s, 1H), 10.12 (s, 1H), 9.52 (s, 1H), 8.40 (s, 2H), 7.51–7.42 (m, 2H), 7.24 (d, *J* = 1.6 Hz, 1H), 6.97–6.90 (m, 2H), 6.87 (d, *J* = 1.8 Hz, 1H) ppm. $^{13}$C NMR (101 MHz, DMSO-$d_6$) $\delta$ = 182.5, 165.1, 159.9, 155.6, 150.3, 145.9, 142.1, 121.1, 119.3, 116.1, 113.6, 110.9, 109.5, 107.3, 103.7, 42.0 ppm. HRMS (ESI) *m/z* calcd for $C_{16}H_{14}NO_5$ $[M+H^+]^+$ 300.0867, found 300.0870.

*3.25. 2-(3,4-Dihydroxyphenyl)-5-hydroxy-7-(1H-pyrrolo[2 ,3-B]pyridin-3-yl)-4H-chromen-4-one (***18***)*

A tube with 4-(5-acetoxy-4-oxo-7-(((trifluoromethyl)sulfonyl)oxy)-4*H*-chromen-2-yl)-1,2-phenylene diacetate (**3**) (100 mg, 0.184 mmol, 1.0 eq.), 3-(4,4,5,5-tetramethyl-1,3,2-dioxaborolan-2-yl)-1*H*-pyrrolo[2,3-*b*]pyridine (54 mg, 0.221 mmol, 1.2 eq.), $Cs_2CO_3$ (240 mg, 0.736 mmol, 4.0 eq.) and $Pd(PPh_3)_4$ (21 mg, 0.018 mmol, 0.1 eq.) was sealed, and dry THF (3.5 mL) was added via septum. The mixture was degassed with a stream of argon for 15 min. then heated to 100 °C for 16 h until the starting material was fully consumed (TLC, UPLC-MS). The reaction mixture was cooled to room temperature, diluted with MeOH (5 mL), and filtered through a syringe filter. The solvents were evaporated and the residue was purified by preparative HPLC to obtain the final product **18** (6.6 mg, 10%). $^1$H NMR (400 MHz, DMSO-$d_6$) $\delta$ = 12.87 (s, 1H), 12.27 (s, 1H), 10.02 (s, 1H), 9.42 (s, 1H), 8.49 (dd, *J* = 8.1, 1.6 Hz, 1H), 8.34 (dd, *J* = 4.6, 1.6 Hz, 1H), 8.25 (d, *J* = 2.8 Hz, 1H), 7.60 – 7.43 (m, 3H), 7.28–7.23 (m, 1H), 7.20 (d, *J* = 1.5 Hz, 1H), 6.94 (d, *J* = 8.1 Hz, 1H), 6.81 (s, 1H) ppm. $^{13}$C NMR (101 MHz, DMSO-$d_6$) $\delta$ = 182.6, 165.1, 160.6, 156.9, 150.4, 149.5, 146.3, 143.7, 143.2, 128.5, 127.3, 122.0, 119.8, 117.6, 117.2, 116.4, 114.2, 113.3, 108.3, 108.2, 104.4, 103.8 ppm. HRMS (ESI) *m/z* calcd for $C_{22}H_{13}N_2O_5$ $[M-H^+]^-$ 385.0830, found 385.0827.

*3.26. 2-(3,4-Dihydroxyphenyl)-5-hydroxy-7-(1H-pyrazol-3-yl)-4H-chromen-4-one (***19***)*

A tube with 4-(5-acetoxy-4-oxo-7-(((trifluoromethyl)sulfonyl)oxy)-4*H*-chromen-2-yl)-1,2-phenylene diacetate (**3**) (100 mg, 0.184 mmol, 1.0 eq.), (1*H*-pyrazol-3-yl)boronic acid (31 mg, 0.276 mmol, 1.5 eq.), $K_2CO_3$ (127 mg, 0.920 mmol, 5.0 eq.), and SPhos Pd G2 (15 mg, 0.018 mmol, 0.1 eq.) was sealed, and dry THF (3.5 mL) was added via septum. The mixture was degassed with a stream of argon for 15 min, then heated to 100 °C for 16 h until the starting material was fully consumed (TLC, UPLC-MS). The reaction mixture was cooled to room temperature, diluted with MeOH (5 mL), and filtered through a syringe filter. The solvents were evaporated and the residue was purified by preparative HPLC to obtain the final product **19** (15 mg, 25%). $^1$H NMR (400 MHz, DMSO-$d_6$) $\delta$ = 12.84 (s, 1H), 7.83 (d, *J* = 2.3 Hz, 1H), 7.59 (d, *J* = 1.5 Hz, 1H), 7.52–7.46 (m, 2H), 7.27 (d, *J* = 1.5 Hz, 1H), 6.96 (d, *J* = 2.3 Hz, 1H), 6.92 (d, *J* = 8.2 Hz, 1H), 6.81 (s, 1H) ppm. $^{13}$C NMR (101 MHz, DMSO-$d_6$) $\delta$ = 182.4, 164.9, 160.1, 157.3, 156.3, 150.0, 147.3, 145.8, 140.1, 132.2, 121.4, 119.3, 116.0, 113.7, 109.0, 107.2, 103.6, 103.5 ppm. HRMS (ESI) *m/z* calcd for $C_{18}H_{13}N_2O5$ $[M+H^+]^+$ 337.0819, found 337.0819.

*3.27. 2-(3,4-Dihydroxyphenyl)-5-hydroxy-7-(5-methyl-1H-pyrazol-3-yl)-4H-chromen-4-one (***20***)*

A tube with 4-(5-acetoxy-4-oxo-7-(((trifluoromethyl)sulfonyl)oxy)-4*H*-chromen-2-yl)-1,2-phenylene diacetate (**3**) (100 mg, 0.184 mmol, 1.0 eq.), (5-methyl-1*H*-pyrazol-3-yl)boronic acid (35 mg, 0.276 mmol, 1.5 eq.), $K_2CO_3$ (127 mg, 0.920 mmol, 5 eq.), and SPhos Pd G2 (15 mg, 0.018 mmol, 0.1 eq.) was sealed, and THF/water (25:1, 3.5 mL) was added via septum. The mixture was degassed with a stream of argon for 15 min, then heated to 100 °C for 16 h until the starting material was fully consumed (TLC, UPLC-MS). The reaction mixture was cooled to room temperature, diluted with MeOH (5 mL), and filtered through a syringe filter. Then solvents were evaporated and the residue was purified by preparative HPLC to obtain the final product **20** (12 mg, 19%). $^1$H NMR (400 MHz, DMSO-$d_6$) $\delta$ = 7.51 (d, *J* = 1.5 Hz, 1H), 7.51–7.46 (m, 2H), 7.19 (d, *J* = 1.3 Hz, 1H), 6.92 (d, *J* = 8.2 Hz, 1H), 6.80 (s, 1H), 6.66 (d, *J* = 1.0 Hz, 1H), 2.28 (s, 3H) ppm. $^{13}$C NMR (101 MHz, DMSO-$d_6$) $\delta$ = 182.3, 164.8, 160.1, 158.4, 158.1, 156.2, 150.0, 145.8, 140.3, 121.4, 119.3, 116.0, 113.7, 108.9, 107.0, 103.5, 103.3, 102.7, 10.9 ppm. HRMS (ESI) *m/z* calcd for $C_{19}H_{15}N_2O_5$ $[M+H^+]^+$ 351.0976, found 351.0975.

*3.28. 2-(3,4-Dihydroxyphenyl)-5,7-dihydroxy-8-((3-hydroxypiperidin-1-yl)methyl)-4H-chromen -4-one (***21***)*

Luteolin (100 mg, 0.35 mmol, 1.0 eq.) was dissolved in MeOH (5 mL), followed by addition of 3-hydroxypiperidine (35 mg, 0.35 mmol, 1.0 eq.) and a 35% formalin solution (27 μL, 0.35 mmol, 1.0 eq.). The reaction mixture was allowed to stir at room temperature for 16 h. The solvents were evaporated and the residue was purified by preparative HPLC to obtain the final product **21** (27 mg, 20%). $^{1}$H NMR (500 MHz, DMSO-$d_6$, 330 K) $\delta$ = 13.27 (s, 1H), 9.89 (s, 1H), 9.35 (s, 1H), 7.47 (dd, *J* = 8.2, 2.3 Hz, 1H), 7.45 (d, *J* = 2.3 Hz, 1H), 6.94 (d, *J* = 8.2 Hz, 1H), 6.74 (d, *J* = 0.6 Hz, 1H), 6.39 (s, 1H), 5.33 (s, 1H), 4.63–4.29 (m, 2H), 4.01–2.80 (m, 5H), 2.11–1.31 (m, 4H) ppm. $^{13}$C NMR (126 MHz, DMSO-$d_6$, 330 K) $\delta$ = 181.7, 164.1, 163.7, 162.5, 156.5, 150.0, 145.9, 121.5, 119.3, 116.2, 113.7, 103.9, 103.2, 98.4, 95.5, 57.3, 51.9, 49.1 ppm. HRMS (ESI) *m/z* calcd for $C_{21}H_{20}NO_7$ $[M-H^+]^-$ 398.1245, found 398.1244.

*3.29. 2-(3,4-Dihydroxyphenyl)-5,7-dihydroxy-8-((4-hydroxypiperidin-1-yl)methyl)-4H-chromen-4-one (***22***)*

Luteolin (100 mg, 0.35 mmol, 1.0 eq.) was dissolved in MeOH (5 mL), followed by addition of 4-hydroxypiperidine (35 mg, 0.35 mmol, 1.0 eq.) and a 35% formalin solution (27 μL, 0.35 mmol, 1.0 eq.). The reaction mixture was allowed to stir at room temperature for 16 h. The solvents were evaporated and the residue was purified by preparative HPLC to obtain the final product **22** (58 mg, 32%). $^{1}$H NMR (400 MHz, DMSO-$d_6$) $\delta$ = 13.32 (s, 1H), 12.17 (br s, 1H), 10.12 (br s, 1H), 9.38 (br s, 1H), 7.56–7.44 (m, 2H), 6.95 (d, *J* = 9.0 Hz, 1H), 6.79 (s, 1H), 6.43 (s, 2H), 4.43 (br s, 2H), 3.91 (br s, 1H), 3.39 – 2.97 (m, 4H), 1.89–1.48 (m, 4H) ppm. $^{13}$C NMR (101 MHz, DMSO-$d_6$) $\delta$ = 182.2, 164.5, 164.2, 162.8, 156.8, 150.4, 146.3, 121.8, 119.7, 116.6, 113.8, 104.2, 103.5, 98.8, 96.1, 59.9, 51.1, 47.9, 31.7 ppm. HRMS (ESI) *m/z* calcd for $C_{21}H_{22}NO_7$ $[M+H^+]^+$ 400.1391, found 400.1387.

*3.30. 1-((2-(3,4-Dihydroxyphenyl)-5,7-dihydroxy-4-oxo-4H-chromen-8-yl)methyl)piperidin-4-one (***23***)*

Luteolin (100 mg, 0.35 mmol, 1.0 eq.) was dissolved in MeOH (5 mL), followed by addition of 4-piperidone monohydrate hydrochloride (54 mg, 0.35 mmol, 1.0 eq.), 35% formalin solution (27 μL, 0.35 mmol, 1.0 eq.), and triethylamine (49 μL, 0.35 mmol, 1.0 eq.). The reaction mixture was allowed to stir at room temperature for 16 h. Then, solvents were evaporated and the residue was purified by preparative HPLC to obtain the final product **23** as a 3:1 mixture of C-8 and C-6 regioisomers (38 mg, 21%). Spectral data includes the C-8 regioisomer only. $^{1}$H NMR (400 MHz, DMSO-$d_6$) $\delta$ = 13.09 (s, 1H), 7.49–7.45 m, 2H), 6.93–6.91 (m, 1H), 6.73 (s, 1H), 6.29 (s, 1H), 3.97 (s, 2H), 2.93 (t, *J* = 5.8 Hz, 4H), 2.41 (t, *J* = 6.1 Hz, 4H) ppm. $^{13}$C NMR (101 MHz, DMSO-$d_6$) $\delta$ = 208.1, 183.3, 164.2, 164.0, 161.0, 155.8, 150.2, 146.2, 122.2, 119.5, 116.5, 113.9, 104.1, 103.1, 98.9, 94.1, 52.5, 49.4, 40.8 ppm. HRMS (ESI) *m/z* calcd for $C_{21}H_{18}NO_7$ $[M-H^+]^-$ 396.1089, found 396.1085.

*3.31. 2-(3,4-Dihydroxyphenyl)-5,7-dihydroxy-8-(morpholinomethyl)-4H-chromen-4-one (***24***)*

Luteolin (100 mg, 0.35 mmol, 1.0 eq.) was dissolved in MeOH (5 mL), followed by addition of morpholine (30 μL, 0.35 mmol, 1.0 eq.) and a 35% formalin solution (27 μL, 0.35 mmol, 1.0 eq.). The reaction mixture was allowed to stir at room temperature for 16 h. Then, solvents were evaporated and the residue was purified by preparative HPLC to obtain the final product **24** (46 mg, 26%). $^{1}$H NMR (400 MHz, DMSO-$d_6$, 330 K) $\delta$ = 13.33 (s, 1H), 12.13 (br s, 1H), 10.07 (br s, 1H), 9.59 (br s, 1H), 7.51 (dd, *J* = 8.3, 2.3 Hz, 1H), 7.48 (d, *J* = 2.3 Hz, 1H), 6.93 (d, *J* = 8.3 Hz, 1H), 6.79 (s, 1H), 6.42 (s, 1H), 4.47 (s, 2H), 4.01–3.20 (m, 8H) ppm. $^{13}$C NMR (101 MHz, DMSO-$d_6$, 330 K) $\delta$ = 181.8, 164.1, 163.9, 162.5, 156.4, 150.0, 145.9, 121.3, 119.4, 116.2, 113.6, 103.7, 103.0, 98.4, 95.2, 63.2, 51.5, 48.9 ppm. HRMS (ESI) *m/z* calcd for $C_{20}H_{18}NO_7$ $[M-H^+]^-$ 384.1089, found 384.1087.

*3.32. 2-(3,4-Dihydroxyphenyl)-5,7-dihydroxy-8-((4-methylpiperazin-1-yl)methyl)-4H-chromen-4-one (***25***)*

Luteolin (100 mg, 0.35 mmol, 1.0 eq.) was dissolved in MeOH (5 mL), followed by addition of *N*-methyl-piperazine (40 µL, 0.35 mmol, 1.0 eq.) and a 35% formalin solution (27 µL, 0.35 mmol, 1.0 eq.). The reaction mixture was allowed to stir at room temperature for 16 h. Then, solvents were evaporated and the residue was purified by preparative HPLC to obtain the final product **25** (44 mg, 31%). $^{1}$H NMR (500 MHz, DMSO-$d_6$, 330 K) $\delta$ = 13.10 (br s, 1H), 7.46–7.41 (m, 2H), 6.93 (d, $J$ = 8.7 Hz, 1H), 6.68 (s, 1H), 6.34 (s, 1H), 4.01 (br s, 2H), 3.34–2.87 (m, 8H), 2.75 (s, 3H) ppm. $^{13}$C NMR (126 MHz, DMSO-$d_6$) $\delta$ = 181.9, 164.0, 163.3, 161.2, 155.9, 149.9, 145.9, 121.7, 119.1, 116.2, 113.6, 103.8, 102.9, 98.4, 51.9, 49.1, 48.4, 42.3 ppm. HRMS (ESI) *m/z* calcd for $C_{21}H_{21}N_2O_6$ $[M-H^+]^-$ 397.1405, found 397.1403.

*3.33. 2-(3,4-Dihydroxyphenyl)-5,7-dihydroxy-8-(((2-hydroxyethyl)(methyl)amino)methyl)-4H -chromen-4-one (***26***)*

Luteolin (100 mg, 0.35 mmol, 1.0 eq.) was dissolved in MeOH (5 mL), followed by addition of *N*-methylethanolamine (28 µL, 0.35 mmol, 1.0 eq.) and a 35% formalin solution (27 µL, 0.35 mmol, 1.0 eq.). The reaction mixture was allowed to stir at room temperature for 16 h. Then, solvents were evaporated and the residue was purified by preparative HPLC to obtain the final product **26** (42 mg, 32%). $^{1}$H NMR (400 MHz, DMSO-$d_6$) $\delta$ = 13.96 (s, 1H), 12.21 (br s, 1H), 10.08 (br s, 1H), 9.54 (br s, 1H), 7.47 – 7.41 (m, 2H), 6.91 (d, $J$ = 9.0 Hz, 1H), 6.76 (s, 1H), 6.65 (s, 1H), 5.34 (br s, 1H), 4.27 (br s, 2H), 3.80 (t, $J$ = 5.4 Hz, 2H), 3.25 (br s, 2H), 2.75 (s, 3H) ppm. $^{13}$C NMR (101 MHz, DMSO-$d_6$) $\delta$ = 181.8, 164.4, 163.5, 161.3, 157.6, 150.1, 145.9, 121.2, 119.2, 116.1, 113.5, 103.3, 102.9, 100.3, 93.5, 57.6, 55.4, 47.7, 40.5 ppm. HRMS (ESI) *m/z* calcd for $C_{19}H_{20}NO_7$ $[M+H^+]^+$ 374.1234, found 374.1235.

*3.34. 2-(3,4-Dihydroxyphenyl)-5,7-dihydroxy-8-((3-hydroxy-8-azabicyclo[3.2.1]octan-8-yl)methyl)-4Hn -chromen-4-one (***27***)*

Luteolin (100 mg, 0.35 mmol, 1.0 eq.) was dissolved in MeOH (5 mL), followed by an addition of nortropine hydrochloride (58 mg, 0.35 mmol, 1.0 eq.), a 35% formalin solution (27 µL, 0.35 mmol, 1.0 eq.), and triethylamine (49 µL, 0.35 mmol, 1.0 eq.). The reaction mixture was allowed to stir at room temperature for 16 h. Then, solvents were evaporated and the residue was purified by preparative HPLC to obtain the final product **27** (10 mg, 7%). $^{1}$H NMR (500 MHz, DMSO-$d_6$) $\delta$ = 13.27 (s, 1H), 11.94 (br s, 1H), 10.09 (br s, 1H), 9.51 (br s, 1H), 8.83 (br s, 1H), 7.48 (dd, $J$ = 8.3, 2.4 Hz, 1H), 7.43 (d, $J$ = 2.4 Hz, 1H), 6.93 (d, $J$ = 8.4 Hz, 1H), 6.81 (s, 1H), 6.38 (s, 1H), 4.95 (br s, 1H), 4.27 (s, 2H), 4.17–3.66 (m, 4H), 2.47–2.35 (m, 4H), 2.18 (br d, $J$ = 15.4 Hz, 2H), 1.88 (br d, $J$ = 14.3 Hz, 2H) ppm. $^{13}$C NMR (126 MHz, DMSO-$d_6$) $\delta$ = 181.9, 164.3, 163.7, 162.5, 156.6, 150.2, 146.1, 121.7, 119.5, 116.3, 113.8, 104.0, 103.4, 98.5, 96.7, 62.1, 60.6, 44.9, 37.2 (2C), 24.4 (2C) ppm. HRMS (ESI) *m/z* calcd for $C_{23}H_{22}NO_7$ $[M-H^+]^-$ 424.1402, found 424.1400.

*3.35. 8-((6,7-Dihydroxy-3,4-dihydroisoquinolin-2(1H)-yl)methyl)-2-(3,4-dihydroxyphenyl)-5,7-dihydroxy-4H-chromen-4-one (***28***)*

Luteolin (100 mg, 0.35 mmol, 1.0 eq.) was dissolved in MeOH (5 mL), followed by addition of 6,7-dihydroxy-1,2,3,4-tetrahydroisoquinolin-2-ium chloride (71 mg, 0.35 mmol, 1.0 eq.), a 35% formalin solution (27 µL, 0.35 mmol, 1.0 eq.), and triethylamine (49 µL, 0.35 mmol, 1.0 eq.). The reaction mixture was allowed to stir at room temperature for 16 h. Then, solvents were evaporated and the residue was purified by preparative HPLC to obtain the final product **28** (46 mg, 23 %). $^{1}$H NMR (400 MHz, DMSO-$d_6$) $\delta$ = 13.29 (s, 1H), 12.07 (br s, 1H), 10.07 (br s, 1H), 9.62 (br s, 1H), 9.12 (br s, 1H), 9.06 (s, 1H), 7.52–7.46 (m, 1H), 7.45 (d, $J$ = 2.3 Hz, 1H), 6.92 (d, $J$ = 8.3 Hz, 1H), 6.79 (s, 1H), 6.57 (s, 1H), 6.53 (s, 1H), 6.41 (s, 1H), 4.54 (s, 2H), 4.36 (s, 2H), 3.58 (br s, 2H), 2.91 (t, $J$ = 6.9 Hz, 2H) ppm. $^{13}$C NMR (101 MHz, DMSO-$d_6$) $\delta$ = 182.2, 164.4, 164.2, 162.8, 156.8, 150.4, 146.3, 145.9, 144.9, 121.8 (2C), 119.7, 118.9, 116.6, 115.3, 114.0, 113.5, 104.2, 103.4, 98.7, 96.1, 53.0, 49.8, 48.2, 24.8 ppm. HRMS (ESI) *m/z* calcd for $C_{25}H_{20}NO_8$ $[M-H^+]^-$ 462.1194, found 462.1193.

*3.36. (S)-1-((2-(3,4-Dihydroxyphenyl)-5,7-dihydroxy-4-oxo-4H-chromen-8-yl)methyl)pyrrolidine-2-carboxamide (***29***)*

Luteolin (100 mg, 0.35 mmol, 1.0 eq.) was dissolved in EtOH (5 mL), followed by an addition of L-prolinamide hydrochloride (71 mg, 0.35 mmol, 1.0 eq.), a 35% formalin solution (27 µL, 0.35 mmol, 1.0 eq.), and triethylamine (49 µL, 0.35 mmol, 1.0 eq.). The reaction mixture was allowed to stir at room temperature for 16 h. Then, solvents were evaporated and the residue was purified by preparative HPLC to obtain the final product **29** (19 mg, 10%). $^{1}$H NMR (400 MHz, DMSO-$d_6$) $\delta$ = 13.31 (s, 1H), 11.85 (br s, 1H), 10.08 (br s, 1H), 9.52 (br s, 1H), 9.38 (br s, 1H), 7.96 (s, 1H), 7.69 (s, 1H), 7.55 (dd, $J$ = 8.4, 2.3 Hz, 1H), 7.47 (d, $J$ = 2.3 Hz, 1H), 6.93 (d, $J$ = 8.4 Hz, 1H), 6.77 (s, 1H), 6.34 (s, 1H), 4.54 (d, $J_{gem}$ = 13.7 Hz, 1H), 4.48 (d, $J_{gem}$ = 13.7 Hz, 1H), 4.16 (br d, $J$ = 9.3 Hz, 1H), 3.56 (br s, 2H), 2.47–2.35 (m, 1H), 2.04–1.93 (m, 1H), 1.89–1.77 (m, 2H) ppm. $^{13}$C NMR (101 MHz, DMSO-$d_6$) $\delta$ = 181.8, 169.3, 164.1, 163.6, 162.4, 156.4, 150.0, 145.8, 121.3, 119.6, 116.0, 113.9, 103.7, 103.0, 98.3, 96.0, 65.9, 53.9, 45.5, 29.2, 22.3 ppm. HRMS (ESI) *m/z* calcd for $C_{21}H_{21}N_2O_7$ $[M+H^+]^+$ 413.1343, found 413.1344.

*3.37. ((2-(3,4-Dihydroxyphenyl)-5,7-dihydroxy-4-oxo-4H-chromen-8-yl)methyl)-*L*-proline (***30***)*

Luteolin (100 mg, 0.35 mmol, 1.0 eq.) was dissolved in EtOH (5 mL), followed by addition of *L*-proline tert-butyl ester hydrochloride (72 mg, 0.35 mmol, 1.0 eq.) and a 35% formalin solution (27 µL, 0.35 mmol, 1.0 eq.). The reaction mixture was stirred at room temperature for 16 h. The solvent was evaporated under reduced pressure and the residue was purified by preparative HPLC to obtain the monosubstituted luteolin C-8 derivative as tert-butyl ester (UPLC-MS: *m/z* = 470). The monosubstituted luteolin C-8 derivative was used in the next step without further characterization. The tert-butyl ester was dissolved in a mixture of TFA/DCM (1:1, 1 mL) with 1,3-dimethoxybenzene (25 µL, 0.19 mmol, 0.54 eq.) as a scavenger. The reaction mixture was allowed to stir at room temperature for 16 h. The reaction mixture was concentrated using a stream of nitrogen, and the product was precipitated with tert-butyl methyl ether. The precipitate was collected and purified by preparative HPLC to obtain the product **30** (9.5 mg, 7% – over two steps). $^{1}$H NMR (500 MHz, DMSO-$d_6$) $\delta$ = 13.25 (s, 1H), 9.91 (br s, 1H), 7.68 (d, $J$ = 2.3 Hz, 1H), 7.48 (dd, $J$ = 8.4, 2.3 Hz, 1H), 6.88 (d, $J$ = 8.2 Hz, 1H), 6.77 (s, 1H), 6.31 (s, 1H), 4.50 (d, $J_{gem}$ = 13.7 Hz, 1H), 4.39 (d, $J_{gem}$ = 13.7 Hz, 1H), 4.03 (m, 1H), 3.39 (m, 1H), 3.13–2.98 (m, 1H), 2.39–2.31 (m, 1H), 1.96 (m, 2H), 1.79 (m, 1H) ppm. $^{13}$C NMR (126 MHz, DMSO-$d_6$) $\delta$ = 181.9, 170.8, 164.0, 163.7, 161.9, 156.0, 149.8, 145.9, 121.2, 119.0, 116.1, 114.3, 103.7, 102.7, 98.3, 97.4, 67.0, 53.6, 46.1, 28.4, 22.5. HRMS (ESI) *m/z* calcd for $C_{21}H_{18}NO_8$ $[M-H^+]^-$ 412.1035, found 412.1037.

*3.38. 1-((2-(3,4-Dihydroxyphenyl)-5,7-dihydroxy-4-oxo-4H-chromen-8-yl)methyl)piperidine-4-carboxylic acid (***31***)*

Luteolin (143 mg, 0.50 mmol, 1.0 eq.) was dissolved in MeOH (7 mL), followed by addition of ethyl 4-piperidinecarboxylate (77 µL, 0.50 mmol, 1.0 eq.) and a 35% formalin solution (38 µL, 0.35 mmol, 1.0 eq.). The reaction mixture was allowed to stir at room temperature for 16 h. The solvent was evaporated under reduced pressure and the residue was purified by flash chromatography ($SiO_2$-$C_{18}$, $H_2O$ (0.1% TFA)/MeCN= 100:0 $\rightarrow$ 20:80) to obtain the monosubstituted luteolin C-8 derivative as an ethyl ester (UPLC-MS: *m/z* = 456). The monosubstituted luteolin C-8 derivative was used in the next step without further characterization. The ethyl ester was dissolved in THF (2 mL) and 5% aq. HCl (2 mL) was added. The reaction mixture was allowed to stir at 70 °C for 7 h until the starting material was fully consumed (UPLC-MS). Then, solvents were evaporated and the residue was purified by preparative HPLC to obtain the final product **31** (60 mg, 22% – over 2 steps). $^{1}$H NMR (400 MHz, DMSO-$d_6$) $\delta$ = 13.31 (s, 1H), 12.07 (br s, 1H), 10.09 (br s, 1H), 9.56 (br s, 1H), 7.49 (dd, $J$ = 8.3, 2.3 Hz, 1H), 7.46 (d, $J$ = 2.2 Hz, 1H), 6.93 (d, $J$ = 8.3 Hz, 1H), 6.79 (s, 1H), 6.40 (s, 1H), 4.41 (s, 2H), 3.73–3.37 (m, 4H), 3.28–3.08 (m, 1H), 2.13–1.69 (m, 4H) ppm. $^{13}$C NMR (101 MHz, DMSO-$d_6$) $\delta$ = 181.8, 174.7, 164.1, 163.8, 162.5, 156.4, 150.0,

145.9, 121.3, 119.3, 116.2, 113.6, 103.8, 103.1, 98.4, 95.6, 51.5 (2C), 48.7, 37.6, 25.4 (2C) ppm. HRMS (ESI) *m/z* calcd for $C_{22}H_{20}NO_8$ $[M-H^+]^-$ 426.1194, found 426.1190.

### *3.39. N-((2-(3,4-Dihydroxyphenyl)-5,7-dihydroxy-4-oxo-4H-chromen-8-yl)methyl)-N-methylglycine (**32**)*

Luteolin (143 mg, 0.50 mmol, 1.0 eq.) was dissolved in MeOH (7 mL), followed by addition of sarcosine methyl ester hydrochloride (70 mg, 0.50 mmol, 1.0 eq.), a 35% formalin solution (38 µL, 0.35 mmol, 1.0 eq.), and triethylamine (70 µL, 0.50 mmol, 1.0 eq.). The reaction mixture was allowed to stir at room temperature for 16 h. The solvent was evaporated under reduced pressure and the residue was purified by flash chromatography ($SiO_2$-$C_{18}$, $H_2O$ (0.1% TFA)/MeCN= 100:0 → 40:60) to obtain the monosubstituted luteolin C-8 derivative as a methyl ester (UPLC-MS: *m/z* = 402). The monosubstituted luteolin C-8 derivative was used in the next step without further characterization. The methyl ester was dissolved in THF (2 mL) and 5% aq. HCl (2 mL) was added. The reaction mixture was allowed to stir at 70 °C for 3 days until the starting material was fully consumed (UPLC-MS). The solvents were evaporated and the residue was purified by preparative HPLC to obtain the final product **32** (29 mg, 12% – over 2 steps). $^1$H NMR (400 MHz, DMSO-$d_6$) $\delta$ = 13.30 (s, 1H), 10.09 (br s, 1H), 9.54 (br s, 1H), 7.52 (dd, *J* = 8.3, 2.3 Hz, 1H), 7.49 (d, *J* = 2.3 Hz, 1H), 6.92 (d, *J* = 8.3 Hz, 1H), 6.76 (s, 1H), 6.35 (s, 1H), 4.49 (s, 2H), 4.00 (s, 2H), 2.75 (s, 3H) ppm. $^{13}$C NMR (101 MHz, DMSO-$d_6$) $\delta$ = 181.8, 168.1, 164.0 (2C), 162.3, 156.4, 149.9, 145.9, 121.3, 119.3, 116.0, 113.8, 103.8, 103.0, 98.4, 96.1, 55.5, 48.2, 40.9 ppm. HRMS (ESI) *m/z* calcd for $C_{19}H_{18}NO_8$ $[M+H^+]^+$ 388.1027, found 388.1026.

## 4. Conclusions

Bio-isosteric replacement of the hydroxyl group at C-7 failed to provide luteolin congeners with comparable inhibitory potency against the influenza PA-Nter domain. However, the introduction of diverse substituents at C-8 increased the binding affinity of the resulting compounds. Crystallographic study of the orientin complex with I38T PA-Nter revealed an additional point of interaction of the flavonoid with Thr-38 mediated by a water molecule.

**Supplementary Materials:** Supplementary materials can be found at https://www.mdpi.com/article/10.3390/ijms22147735/s1.

**Author Contributions:** Synthesis of compounds, R.R. and V.Z.; structural work, K.R., J.B.; $IC_{50}$ determination, M.K. (Michal Kráľ); supervision, P.M.; NMR experiments, M.D.; funding acquisition, J.K.; original draft preparation, M.K. (Milan Kožíšek) and A.M. All authors have read and agreed to the published version of the manuscript.

**Funding:** This research was funded by EATRIS-CZ (grant No. LM2018133) from the Ministry of Education of the Czech Republic and by the European Regional Development Fund; OP RDE; Project: "Chemical biology for drugging undruggable targets (ChemBioDrug)" (No. CZ.02.1.01/0.0/0.0/16_019/0000729).

**Institutional Review Board Statement:** Not applicable.

**Informed Consent Statement:** Not applicable.

**Data Availability Statement:** The data presented in this study are available in the article.

**Acknowledgments:** The authors thank Radko Souček for HPLC analyses as well as Hillary Hoffman and Joshua Smith for proofreading of the manuscript.

**Conflicts of Interest:** The authors declare no conflict of interest.

## References

1. Iuliano, A.D.; Roguski, K.M.; Chang, H.H. Estimates of global seasonal influenza-associated respiratory mortality: A modelling study. *Lancet* **2018**, *391*, 1285–1300. [CrossRef]
2. Fodor, E. The RNA polymerase of influenza A virus: Mechanisms of viral transcription and replication. *Acta Virol.* **2013**, *57*, 113–122. [CrossRef]

3. Eisfeld, A.J.; Neumann, G.; Kawaoka, Y. At the centre: Influenza A virus ribonucleoproteins. *Nat. Rev. Microbiol.* **2015**, *13*, 28–41. [CrossRef]
4. Ortin, J.; Martin-Benito, J. The RNA synthesis machinery of negative-stranded RNA viruses. *Virology* **2015**, *479*, 532–544. [CrossRef]
5. Dias, A.; Bouvier, D.; Crepin, T.; McCarthy, A.A.; Hart, D.J.; Baudin, F.; Cusack, S.; Ruigrok, R.W.H. The cap-snatching endonuclease of influenza virus polymerase resides in the PA subunit. *Nature* **2009**, *458*, 914–918. [CrossRef] [PubMed]
6. Walker, A.P.; Fodor, E. Interplay between influenza virus and the host RNA polymerase II transcriptional machinery. *Trends Microbiol.* **2019**, *27*, 398–407. [CrossRef] [PubMed]
7. De Vlugt, C.; Sikora, D.; Pelchat, M. Insight into influenza: A virus cap-snatching. *Viruses* **2018**, *10*, 641. [CrossRef] [PubMed]
8. Guilligay, D.; Tarendeau, F.; Resa-Infante, P.; Coloma, R.; Crepin, T.; Sehr, P.; Lewis, J.; Ruigrok, R.W.H.; Ortin, J.; Hart, D.J.; et al. The structural basis for cap binding by influenza virus polymerase subunit PB2. *Nat. Struct. Mol. Biol.* **2008**, *15*, 500–506. [CrossRef]
9. Credille, C.V.; Dick, B.L.; Morrison, C.N.; Stokes, R.W.; Adamek, R.N.; Wu, N.C.; Wilson, I.A.; Cohen, S.M. Structure-activity relationships in metal-binding pharmacophores for influenza endonuclease. *J. Med. Chem.* **2018**, *61*, 10206–10217. [CrossRef] [PubMed]
10. Bouloy, M.; Plotch, S.J.; Krug, R.M. Globin messenger-RNAs are primers for transcription of influenza viral-RNA In Vitro. *Proc. Natl. Acad. Sci. USA* **1978**, *75*, 4886–4890. [CrossRef] [PubMed]
11. Hayden, F.G.; Shindo, N. Influenza virus polymerase inhibitors in clinical development. *Curr. Opin. Infect. Dis.* **2019**, *32*, 176–186. [CrossRef]
12. Stevaert, A.; Naesens, L. The influenza virus polymerase complex: An update on its structure, functions, and significance for antiviral drug design. *Med. Res. Rev.* **2016**, *36*, 1127–1173. [CrossRef]
13. Clark, M.P.; Ledeboer, M.W.; Davies, I.; Byrn, R.A.; Jones, S.M.; Perola, E.; Tsai, A.; Jacobs, M.; Nti-Addae, K.; Bandarage, U.K.; et al. Discovery of a novel, first-in-class, orally bioavailable azaindole inhibitor (VX-787) of influenza PB2. *J. Med. Chem.* **2014**, *57*, 6668–6678. [CrossRef] [PubMed]
14. Byrn, R.A.; Jones, S.M.; Bennett, H.B.; Bral, C.; Clark, M.P.; Jacobs, M.D.; Kwong, A.D.; Ledeboer, M.W.; Leeman, J.R.; McNeil, C.F.; et al. Preclinical activity of VX-787, a first-in-class, orally bioavailable inhibitor of the influenza virus polymerase PB2 subunit. *Antimicrob. Agents Chemother.* **2015**, *59*, 1574–1587. [CrossRef] [PubMed]
15. Sugiyama, K.; Obayashi, E.; Kawaguchi, A.; Suzuki, Y.; Tame, J.R.H.; Nagata, K.; Park, S.Y. Structural insight into the essential PB1-PB2 subunit contact of the influenza virus RNA polymerase. *EMBO J.* **2009**, *28*, 1803–1811. [CrossRef]
16. He, X.J.; Zhou, J.; Bartlam, M.; Zhang, R.G.; Ma, J.Y.; Lou, Z.Y.; Li, X.M.; Li, J.J.; Joachimiak, A.; Zeng, Z.H.; et al. Crystal structure of the polymerase PA(C)-PB1(N) complex from an avian influenza H5N1 virus. *Nature* **2008**, *454*, 1123–1126. [CrossRef] [PubMed]
17. Hejdanek, J.; Radilova, K.; Pachl, P.; Hodek, J.; Machara, A.; Weber, J.; Rezacova, P.; Konvalinka, J.; Kozisek, M. Structural characterization of the interaction between the C-terminal domain of the influenza polymerase PA subunit and an optimized small peptide inhibitor. *Antivir. Res.* **2021**, *185*, 104971. [CrossRef]
18. Ju, H.; Zhang, J.; Huang, B.S.; Kang, D.W.; Huang, B.; Liu, X.Y.; Zhan, P. Inhibitors of influenza virus polymerase acidic (PA) endonuclease: Contemporary developments and perspectives. *J. Med. Chem.* **2017**, *60*, 3533–3551. [CrossRef]
19. Kowalinski, E.; Zubieta, C.; Wolkerstorfer, A.; Szolar, O.H.J.; Ruigrok, R.W.H.; Cusack, S. Structural analysis of specific metal chelating inhibitor binding to the endonuclease domain of influenza pH1N1 (2009) polymerase. *PLoS Pathog.* **2012**, *8*, e1002831. [CrossRef]
20. Chen, A.Y.; Adamek, R.N.; Dick, B.L.; Credille, C.V.; Morrison, C.N.; Cohen, S.M. Targeting metalloenzymes for therapeutic intervention. *Chem. Rev.* **2019**, *119*, 1323–1455. [CrossRef]
21. Rouffet, M.; Cohen, S.M. Emerging trends in metalloprotein inhibition. *Dalton Trans.* **2011**, *40*, 3445–3454. [CrossRef]
22. Riccardi, L.; Genna, V.; De Vivo, M. Metal-ligand interactions in drug design. *Nat. Rev. Chem.* **2018**, *2*, 100–112. [CrossRef]
23. Yang, Y.; Hu, X.Q.; Li, Q.S.; Zhang, X.X.; Ruan, B.F.; Xu, J.; Liao, C.Z. Metalloprotein inhibitors for the treatment of human diseases. *Curr. Top. Med. Chem.* **2016**, *16*, 384–396. [CrossRef] [PubMed]
24. Kikuchi, T.; Watanabe, A. Baloxavir heralds a new era in influenza virus biology. *Respir. Investig.* **2019**, *57*, 1–2. [CrossRef] [PubMed]
25. Noshi, T.; Kitano, M.; Taniguchi, K.; Yamamoto, A.; Omoto, S.; Baba, K.; Hashimoto, T.; Ishida, K.; Kushima, Y.; Hattori, K.; et al. In Vitro characterization of baloxavir acid, a first-in-class cap-dependent endonuclease inhibitor of the influenza virus polymerase PA subunit. *Antivir. Res.* **2018**, *160*, 109–117. [CrossRef]
26. Omoto, S.; Speranzini, V.; Hashimoto, T.; Noshi, T.; Yamaguchi, H.; Kawai, M.; Kawaguchi, K.; Uehara, T.; Shishido, T.; Naito, A.; et al. Characterization of influenza virus variants induced by treatment with the endonuclease inhibitor baloxavir marboxil. *Sci. Rep.* **2018**, *8*, 1–15. [CrossRef] [PubMed]
27. Hastings, J.C.; Selnick, H.; Wolanski, B.; Tomassini, J.E. Anti-influenza virus activities of 4-substituted 2,4-dioxobutanoic acid inhibitors. *Antimicrob. Agents Chemother.* **1996**, *40*, 1304–1307. [CrossRef]
28. Liao, Y.X.; Ye, Y.L.; Li, S.M.; Zhuang, Y.L.; Chen, L.Y.; Chen, J.X.; Cui, Z.N.; Huo, L.J.; Liu, S.W.; Song, G.P. Synthesis and SARs of dopamine derivatives as potential inhibitors of influenza virus PA(N) endonuclease. *Eur. J. Med. Chem.* **2020**, *189*, 112048. [CrossRef]

29. Sagong, H.Y.; Bauman, J.D.; Patel, D.; Das, K.; Arnold, E.; LaVoie, E.J. Phenyl substituted 4-Hydroxypyridazin-3(2H)-ones and 5-Hydroxypyrimidin-4(3H)-ones: Inhibitors of influenza A endonuclease. *J. Med. Chem.* **2014**, *57*, 8086–8098. [CrossRef]
30. Parhi, A.K.; Xiang, A.; Bauman, J.D.; Patel, D.; Vijayan, R.S.K.; Das, K.; Arnold, E.; LaVoie, E.J. Phenyl substituted 3-hydroxypyridin-2(1H)-ones: Inhibitors of influenza A endonuclease. *Bioorg. Med. Chem.* **2013**, *21*, 6435–6446. [CrossRef]
31. Credille, C.V.; Chen, Y.; Cohen, S.M. Fragment-based identification of influenza endonuclease inhibitors. *J. Med. Chem.* **2016**, *59*, 6444–6454. [CrossRef] [PubMed]
32. Tomassini, J.E.; Davies, M.E.; Hastings, J.C.; Lingham, R.; Mojena, M.; Raghoobar, S.L.; Singh, S.B.; Tkacz, J.S.; Goetz, M.A. A novel antiviral agent which inhibits the endonuclease of influenza viruses. *Antimicrob. Agents Chemother.* **1996**, *40*, 1189–1193. [CrossRef] [PubMed]
33. Kuzuhara, T.; Iwai, Y.; Takahashi, H.; Hatakeyama, D.; Echigo, N. Green tea catechins inhibit the endonuclease activity of influenza A virus RNA polymerase. *PLoS Curr.* **2009**, *1*, RRN1052. [CrossRef] [PubMed]
34. Song, J.M.; Lee, K.H.; Seong, B.L. Antiviral effect of catechins in green tea on influenza virus. *Antivir. Res.* **2005**, *68*, 66–74. [CrossRef] [PubMed]
35. Sagong, H.Y.; Parhi, A.; Bauman, J.D.; Patel, D.; Vijayan, R.S.K.; Das, K.; Arnod, E.; LaVoie, E.J. 3-Hydroxyquinolin-2(1H)-ones as inhibitors of influenza A endonuclease. *ACS Med. Chem. Lett.* **2013**, *4*, 547–550. [CrossRef]
36. Carcelli, M.; Rogolino, D.; Gatti, A.; De Luca, L.; Sechi, M.; Kumar, G.; White, S.W.; Stevaert, A.; Naesens, L. N-acylhydrazone inhibitors of influenza virus PA endonuclease with versatile metal binding modes. *Sci. Rep.* **2016**, *6*, 1–14. [CrossRef]
37. Zima, V.; Radilova, K.; Kozisek, M.; Albinana, C.B.; Karlukova, E.; Brynda, J.; Fanfrlik, J.; Flieger, M.; Hodek, J.; Weber, J.; et al. Unraveling the anti-influenza effect of flavonoids: Experimental validation of luteolin and its congeners as potent influenza endonuclease inhibitors. *Eur. J. Med. Chem.* **2020**, *208*, 112754. [CrossRef]
38. Sarawek, S.; Derendorf, H.; Butterweck, V. Pharmacokinetics of luteolin and metabolites in rats. *Nat. Prod. Commun.* **2008**, *3*, 2029–2036. [CrossRef]
39. Thilakarathna, S.H.; Rupasinghe, H.P.V. Flavonoid bioavailability and attempts for bioavailability enhancement. *Nutrients* **2013**, *5*, 3367–3387. [CrossRef]
40. Patani, G.A.; LaVoie, E.J. Bioisosterism: A rational approach in drug design. *Chem. Rev.* **1996**, *96*, 3147–3176. [CrossRef] [PubMed]
41. Li, M.; Han, X.W.; Yu, B. Facile synthesis of flavonoid 7-O-glycosides. *J. Org. Chem.* **2003**, *68*, 6842–6845. [CrossRef]
42. Subramaniapillai, S.G. Mannich reaction: A versatile and convenient approach to bioactive skeletons. *J. Chem. Sci.* **2013**, *125*, 467–482. [CrossRef]
43. Li, Y.Q.; Yang, F.; Wang, L.; Cao, Z.; Han, T.J.; Duan, Z.A.; Li, Z.; Zhao, W.J. Phosphoramidate protides of five flavones and their antiproliferative activity against HepG2 and L-O2 cell lines. *Eur. J. Med. Chem.* **2016**, *112*, 196–208. [CrossRef] [PubMed]
44. Hirao, T.; Masunaga, T.; Ohshiro, Y.; Agawa, T. A Novel synthesis of dialkyl arenephosphonates. *Synthesis* **1981**, *1*, 56–57. [CrossRef]
45. Albinana, C.B.; Machara, A.; Rezacova, P.; Pachl, P.; Konvalinka, J.; Kozisek, M. Kinetic, thermodynamic and structural analysis of tamiphosphor binding to neuraminidase of H1N1 (2009) pandemic influenza. *Eur. J. Med. Chem.* **2016**, *121*, 100–109. [CrossRef]
46. Huang, H.; Song, C.J.; Wang, Z.; Li, M.Y.; Chang, J.B. Total synthesis of tanshinone IIA. *Tetrahedron Lett.* **2020**, *61*. [CrossRef]
47. Cohen, D.T.; Buchwald, S.L. Mild palladium-catalyzed cyanation of (hetero)aryl halides and triflates in aqueous media. *Org. Lett.* **2015**, *17*, 202–205. [CrossRef] [PubMed]
48. Molander, G.A.; Shin, I. Synthesis and Suzuki-Miyaura cross-coupling reactions of potassium Boc-protected aminomethyltrifluoroborate with aryl and hetaryl halides. *Org. Lett.* **2011**, *13*, 3956–3959. [CrossRef]
49. Wen, G.; Liu, Q.; Hu, H.B.; Wang, D.M.; Wu, S. Design, synthesis, biological evaluation, and molecular docking of novel flavones as H3R inhibitors. *Chem. Biol. Drug Des.* **2017**, *90*, 580–589. [CrossRef]
50. Helgren, T.R.; Sciotti, R.J.; Lee, P.; Duffy, S.; Avery, V.M.; Igbinoba, O.; Akoto, M.; Hagen, T.J. The synthesis, antimalarial activity and CoMFA analysis of novel aminoalkylated quercetin analogs. *Bioorg. Med. Chem. Lett.* **2015**, *25*, 327–332. [CrossRef]
51. Joshi, D.; Field, J.; Murphy, J.; Abdelrahim, M.; Schonherr, H.; Sparrow, J.R.; Ellestad, G.; Nakanishi, K.; Zask, A. Synthesis of antioxidants for prevention of age-related macular degeneration. *J. Nat. Prod.* **2013**, *76*, 450–454. [CrossRef] [PubMed]
52. DuBois, R.M.; Slavish, P.J.; Baughman, B.M.; Yun, M.K.; Bao, J.; Webby, R.J.; Webb, T.R.; White, S.W. Structural and biochemical basis for development of influenza virus inhibitors targeting the PA endonuclease. *PLoS Pathog.* **2012**, *8*, e1002830. [CrossRef] [PubMed]
53. Kabsch, W. Xds. *Acta Crystallogr. D* **2010**, *66*, 125–132. [CrossRef] [PubMed]
54. Kabsch, W. Integration, scaling, space-group assignment and post-refinement. *Acta Crystallogr. D* **2010**, *66*, 133–144. [CrossRef]
55. Vagin, A.; Teplyakov, A. MOLREP: An automated program for molecular replacement. *J. Appl. Crystallogr.* **1997**, *30*, 1022–1025. [CrossRef]
56. Winn, M.D.; Ballard, C.C.; Cowtan, K.D.; Dodson, E.J.; Emsley, P.; Evans, P.R.; Keegan, R.M.; Krissinel, E.B.; Leslie, A.G.W.; McCoy, A.; et al. Overview of the CCP4 suite and current developments. *Acta Crystallogr. Sect. D Struct. Biol.* **2011**, *67*, 235–242. [CrossRef]
57. Emsley, P.; Cowtan, K. Coot: Model-building tools for molecular graphics. *Acta Crystallogr. Sect. D Struct. Biol.* **2004**, *60*, 2126–2132. [CrossRef]

58. Murshudov, G.N.; Skubak, P.; Lebedev, A.A.; Pannu, N.S.; Steiner, R.A.; Nicholls, R.A.; Winn, M.D.; Long, F.; Vagin, A.A. REFMAC5 for the refinement of macromolecular crystal structures. *Acta Crystallogr. Sect. D Struct. Biol.* **2011**, *67*, 355–367. [CrossRef]
59. Chen, V.B.; Arendall, W.B.; Headd, J.J.; Keedy, D.A.; Immormino, R.M.; Kapral, G.J.; Murray, L.W.; Richardson, J.S.; Richardson, D.C. MolProbity: All-atom structure validation for macromolecular crystallography. *Acta Crystallogr. Sect. D Struct. Biol.* **2010**, *66*, 12–21. [CrossRef] [PubMed]

## 4. CONCLUSION AND DISCUSSION

As influenza remains a serious viral infection with pandemic potential, searching for a new antiviral drug is ongoing. Several viral drug targets have been identified. We have focused on two targets placed within the heterotrimeric influenza RNA-dependent RNA polymerase, both within the PA subunit.

The intersubunit PA-PB1 interaction, located on the C-terminus of PA, is a highly conserved region. Moreover, this PPI is essential for the heterotrimer assembly, therefore the viral cycle itself. As the first structure of PB1 N-terminus derived peptide was crystallized within the CPA binding pocket, we have started a project to explore the peptide and its derivates PPI inhibitory potency. Generally, the development of PPI inhibitors represents challenging targets for small-molecule inhibitors as the shared interface is most often wide and flat. However, this interaction is formed by a quite small hydrophobic pocket and an oligopeptide forming a $3_{10}$ helix. As the wild-type PA N-terminus derived peptide was 14 amino acids long (**PB1-0**, MDVNPTLLFLKIPA), we generated, and in publication **I.** analyzed a truncation peptide set by sequentially removing amino acids from each terminus. We expressed, purified influenza A CPA, and developed a high-throughput screening assay that enabled the biochemical characterization and determination of potent PA-PB1 peptide inhibitors. In the first generation of peptides, the truncation from both the C-terminus and the N-terminus exposed the oligopeptide interacting core and confirmed the importance of the internal $3_{10}$ helix. Truncation of the C-terminus amino acids was tolerated up to the Lys-11. When the peptide was cut shorter, the $IC_{50}$ value worsened dramatically. Analogously we truncated the N-terminus up to Pro-5. These deletions were tolerated only to Asn-2, otherwise the half-maximal inhibitory concentration dropped in the order of magnitude. Minimal peptide **PB1-10** (DVNPTLLFLK) was identified as a low micromolar inhibitor ($IC_{50}$ = 3 400 nM). Being inspired by a published peptide array, we introduced substitutions at “hot-spots” to enhance peptide affinity. Two substitutions (V3Y and T6Y) improved the inhibition activity, resulting in decapeptide **PB1-11** (D<u>Y</u>NP<u>Y</u>LLFLK) of $IC_{50}$ of 13 nM. To evaluate if the decapeptide binding is structurally consistent with the wild-type, I have co-crystallized the CPA with this inhibitor. Crystals of CPA/**PB1-11** diffracted up to 1.6 Å resolution in $P\,2_12_12_1$ symmetry. **PB1-11** was located at nearly the same position as the wild-type PB1-derived peptide. This high-resolution crystal structure also revealed a structural basis for the affinity increase. The introduction of two tyrosine residues into the inhibitor sequence resulted in the formation of two water-mediated hydrogen bonds with the CPA Cys-415, Arg-638, Ser-659, and Asn-703. This was not observed for the wild-type peptide of PB1. We have also tried to improve the intracellular delivery of

peptides. For this, we have joined the **PB1-11** peptide with the commonly used cell-penetrating Tat-sequence. However, this strategy did not help to deliver the linear decapeptide inside the cell and therefore failed to have an antiviral effect *in vivo*. This might also be due to the cell lines used in the assay. HEK293T and MDCK are generally known to struggle with cell-penetrating peptide-based delivery.

To follow up on the results from publication **I.**, we further modified and optimized the decapeptide to enhance its inhibitory potency and intracellular delivery in publication **II.**. Although many of the prepared oligopeptides were tested as nanomolar inhibitors, there were several subsequent issues needed to be overcome. Not mentioned above, the solubility of the first peptide set was very poor. Truncated, modified peptides, as well as the native **PB1-0** peptide, precipitated/aggregated in higher concentrations in an aqueous solution. We prepared a second set of decapeptides with modified hot-spots. One modification of all three hot-spots led to a decapeptide **PB1-19** (DYNPYLLYLK) with $IC_{50}$ of 5.5 nM. Its maximal solubility was over 200 μM. This enabled us to perform the first thermodynamic analysis of the PA-PB1 peptide inhibitor. The binding of **PB1-19** to the CPA was enthalpy-driven with a dissociation constant $K_D$ of 1.7 nM. This suggested a high degree of van der Waals interactions and favorable hydrogen bonding between the decapeptide and CPA. Conformational changes which are coupled to the binding process resulted in unfavorable entropy change. I have co-crystallized the protein-decapeptide complex. Crystals of CPA/**PB1-19** diffracted up to 1.9 Å resolution again in the $P\,2_12_12_1$ symmetry. Using the X-ray crystallography, I have found additional water-mediated hydrogen bonds in the binding pocket (PDB code **7ZPY**), compared to the previously described decapeptide **PB1-11** (PDB code **6SYI**). These new water molecules binding between the CPA and hydroxyl from the introduced F9Y side chain shifted two CPA alpha helices α11 and α12 of RMSD of 0.84 Å for corresponding 332 atoms. To improve peptide intracellular delivery, we have employed a reversible bicyclic strategy approach. Both peptides **PB1-11** and **PB1-19** were fused with a short CPP motif (cyclo(RRRRØF), where Ø is L-2-naphtylalanine) and formed into the bicyclic peptide by the creation of two disulfide bonds. Hypothetically, the bicyclic peptide **PB1-11B**/**PB1-19B** would enter the cell via endocytosis and escape the early endosome into the cytosol. A PA-PB1 inhibiting linear peptide would be then released after the intracellular glutathione reduces the pair of disulfide bonds. To observe the peptide delivery, we have labelled the **PB1-11** and **PB1-11B** with rhodamine B (RB) and naphtofluororescein (NF). We have treated HeLa cells with those peptides and visualized them on the confocal microscope. The pH-insensitive RB-labelled peptides were observed through the entire range of pH. But the fluorescence of NF-labelled peptides was detected only in the

cytosol, due to the pH sensitivity of the label. Comparing labelled linear and bicyclic peptides, the formation of bicyclic peptides enhanced the transmembrane transport, as well as the escape from the early endosome. We have further characterized the effect of bicyclic peptides targeting PA-PB1 interaction in cell cultures. Two approaches applied on HEK293T and MDCK cell lines, the mini-replicon assay and the cytopathic effect (CPE) reduction assay were used. In both, the introduction of the bicyclic strategy improved the inhibitory potency of bicyclic peptides. The **PB1-19B** was determined as a low micromolar RdRp inhibitor ($EC_{50}$ of 1 μM, 2 μM respectively). All peptides were cell-tolerated up to 100 μM concentration. Moreover, the peptides were tested for their stability in human plasma. The bicyclization prolonged the peptide's half-lives over ten times.

To conclude the CPA project, we developed a novel high-throughput method and tested two sets of peptide-based inhibitors of the PA-PB1 interaction. We optimized a selected decapeptide and structurally characterized its binding into the CPA pocket. This resulted in two structures of protein-peptide complexes with PDB codes **6SYI** and **7ZPY**. Thanks to the increased solubility of **PB1-19**, the very first ITC of this interaction was performed. In combination with the reversible bicyclic strategy, we have significantly improved the peptide stability and inhibition in cell-based assays. This could provide a starting point for a structure-based development of compounds targeting the protein-protein interaction between PA and PB1 subunits.

Our second project was focused on the PA endonuclease domain, located at the N-terminus (NPA). This domain can be considered a first-thought drug target, as it is a bridged metalloenzyme with a solvent-exposed binding pocket. Several compounds were designed to chelate the two manganese ions in the active site. Promising NPA inhibitors include the phytochemicals from the catechol derivatives, such as the epigallocatechin gallate (EGCG) and its congener epicatechin gallate. Both are contained in green tea and have exhibited some inhibitory potency against endonuclease activity. Other flavonoids share some structural similarities with EGCG. From the protein-inhibitor crystal structure (**4AWM**, Kowalinski et al., 2012), we have considered compounds of this class as promising compounds to target NPA. Besides being part of a daily diet, flavonoids were studied for their potential benefits for human health. One of them, quercetin was described to have some inhibitory effect on viruses including influenza. Several *in vitro* and *in vivo* experiments in mice had been previously performed. However, no structure-based proof of protein target was revealed. To test if quercetin and its derivatives act on the NPA, we have prepared DNA encoding the first 196 amino acids of NPA.

The sequence was optimized for crystallization as a flexible loop region was replaced by a GGS linker. We have expressed the NPA domain and purified it. For the testing of prepared compounds, we have developed a novel high-throughput AlphaScreen-based assay. This assay allowed us to confirm the NPA as a quercetin protein target. We have studied the SAR of flavonoids and their analogs in the endonuclease active site. A series of 83 compounds was prepared and tested (publication **III.**). The results from AlphaScreen were further verified by the *in vitro* cleavage endonuclease gel-based assay. To support our hypothesis, that the binding site is the endonuclease active site of the NPA, I have crystallized the NPA domain. When hexagonal bifrustum crystals were formed, luteolin, quambalarine B, and myricetin were soaked in. Due to the flavonoid's natural colorful character, the crystal color change could be observed over time. All crystals belonged to the *P* $6_422$ space group and had a clear anomalous signal. Crystal of NPA/luteolin complex diffracted up to 2.0 Å and NPA/quambalarine B up to 2.5 Å. Luteolin chelated the manganese ions in a bidentate binding mode **A** and formed an additional hydrogen bond via hydroxyl at C7 to the NPA Glu-26. On the other hand, quambalarine B exhibited the tridentate binding mode **B**. Atomic coordinates and experimental structure factors were deposited in the Protein Data Bank under codes **6YA5** and **6YEM**. I obtained crystal structures of NPA in complex with luteolin and quambalarine B. The position of myricetin could not be determined from the electron density map. This was maybe due to myricetin flexibility within the active site. We have used rough estimates of myricetin position from the X-ray structure for molecular modelling. To conclude, we found that flavonoids target the NPA domain of influenza RdRp. Furthermore, we established a novel method for high-throughput screening assay, which was correlated to the gel-based assay. For the first time, we identified the molecular mode-of-action of flavonoids bound to the endonuclease active site of the influenza RdRp. This could be a set off in a rational design of the NPA endonuclease next-generation inhibitors.

We continued to map the protein chemical space around the flavonoid ligand. In publication **IV.**, we studied the next generation of luteolin-derived compounds. Specifically changes at the C-7 and C-8 positions. Another set of 24 prepared compounds was tested for its inhibitory potency of NPA endonuclease. Analogously to the previous work, we have utilized the AlphaScreen technology, as well as the generally used gel-based *in vitro* endonuclease cleavage assay. Moieties introduced to the C-7 position did not have any advantageous effect on the inhibitory potency. The C-8 derivatives exhibited generally decent submicromolar half-maximal inhibitory concentration. The most promising NPA inhibitor of the set was orientin ($IC_{50}$ of 42 nM), a C-8-glucose derivative of luteolin. In patients, a point mutation I38T of NPA

within the active site was observed, as a response to the treatment with an FDA-approved endonuclease inhibitor Xofluza (baloxavir marboxil). Therefore, we included this mutant variant in the endonuclease assay. We found out that this mutation in the endonuclease active site led to a complete loss of ssDNA cleavage ability. Nevertheless, the influenza polymerase is RNA-dependent. We have used a fluorescent-labelled ssRNA substrate for a FRET-based endonuclease assay to test the ssRNA cleavage. Compared to the wild-type NPA, the I38T variant had only 1.9% activity toward the ssRNA substrate. This observation was in correlation with a report of significantly reduced fitness and ssRNA nuclease activity of a virus carrying the I38T mutation. To characterize orientin in the active site, I have crystallized the protein of wild type NPA along with the I38T mutant variant. Both protein crystals exhibited the same $P\,6_422$ symmetry. Orientin was consequently soaked into empty crystals in a short period of time. The complex of wild type NPA/orientin diffracted up to 1.9 Å resolution (**7NUG**), and I38T/orientin up to 2.2 Å resolution (**7NUH**). In both structures, the ligands were clearly visible with the electron density map well defined. Orientin was bound to two manganese ions almost identically to the luteolin scaffold in our previous structure. It also remained the C-7 hydroxyl-mediated hydrogen bond to the Glu-26. The introduction of the I38T mutation did not lead to any major changes in the binding mode of orientin. The enhanced affinity of orientin was likely due to the additional hydrogen bonding network surrounding orientin's glucosyl moiety. This was observed in both protein variants as a vast majority of the water molecules in the first solvation shell were located at similar positions. One of only two differences was a small ligand shift in the mutant variant with an RMSD of 0.446 Å. The second one was an evident movement of Tyr-24. Its side chain was pushed away from the cavity with an RMSD of 0.029 Å. The Thr-38 is one atom shorter than Ile-38 and better lodged the inhibitor in the active site and formed an additional hydrogen bond to an extra water molecule via its $O^{\gamma 1}$. This suggested that this clinically relevant mutation should not affect the orientin binding into the NPA endonuclease domain.

To conclude, the presented publications in this dissertation closely examine two different drug targets located within the influenza PA subunit. I must mention that I was lucky to obtain six X-ray structures with bound inhibitors altogether. This contributed to a detailed exploration of their interactions with binding sites of protein targets and follow up optimizations. Optimized minimal peptidic inhibitors derived from the PB1 subunit were found to be potent RdRp inhibitors. Any of the peptide-based inhibitors are considered as an attractive alternative to small molecule drugs. They can be specific, more efficient, and most importantly better tolerated. Generally, to translate peptide-based inhibitors into clinical application, they must be

potent, stable, and have good bioavailability. Improving these features may lead to a highly potent anti-influenza drug. One way to obtain such compound could be through their cyclization, which should possibly prevent their degradation in human plasma. This modification can also be considered as a first step towards synthetic inhibitor specifically targeting a viral protein. However, the peptide cyclization can negatively affect its inhibitory potency, as the binding site in the PA subunit is relatively closed. Another approach for an intracellular delivery and stability enhancement could be using a carrier systems, such as nanoparticles with inhibitory peptides as a cargo. A different way is the utilization of chemically synthesized non-peptidic compounds, which mimic the $3_{10}$ helix structure. Nonetheless, such inhibitor might act differently, and may not be advantageous for intracellular delivery. Altogether, any of the suggested compounds can stand a chance in the development of novel influenza virostatics and could be classed beside other currently used therapeutic peptides.

Biological effects of substances obtained from plants have been known for centuries. Natural products represent a huge reservoir of bioactive chemical diversity and a potential drug leading to new therapeutics for many human diseases. One class, the flavonoids, showed beneficial effects on the human health. Beside many others, the antiviral effect was mentioned. Although there were several proposals of their mechanism of action, there was no clear consensus for the protein target. For the first time, we present the structural characterization of this plant-derived compound as a nonspecific influenza inhibitor. Luteolin and its derivatives inhibit the influenza endonuclease by chelating its embedded metal ions. These observations of the active site with bound flavonoids may serve for the development of more potent influenza RdRp endonuclease inhibitors derived from this scaffold.

RNA viruses typically adapt rapidly to new hosts. Their mutation rate is high, also caused by the impreciseness of the RNA-dependent RNA polymerase, which is prone to translation and replication errors. From past pandemics, it is clear that the emergence of antiviral-resistant influenza viruses is not easily predictable. The development of virostatics against all RNA viruses would need to be considered a suitable target. So far, the RdRp appears to be one of the promising ones. The above-presented targets in the PA subunit have the advantage of their essential role within the viral life cycle, and the C-terminal PPI is especially suitable for its highly conserved region within influenza viruses. The general therapeutic nucleoside analogue, favipiravir, targets not only influenza viruses. Though, it has severe negative side effects and did not pass the development of resistant mutations. It might be that a universal virostatic recquires a different approach. One of those may represent the targeted protein degradation or a novel class of optimized nucleoside analogues.

## 5. SUMMARY

Influenza virus causes acute infection of the respiratory system among humans and presents a year-round disease burden. As the influenza virus is constantly mutating and has pandemic potential, new antiviral drugs need to be developed. Currently used antivirals in the majority target the viral surface protein neuraminidase and are used with limitations. In the past twenty years, several viral drug targets have been identified. This thesis focuses on the two of them, both located within the viral heterotrimeric RNA-dependent RNA polymerase (RdRp). The first is the PA subunit C-terminal domain (CPA) harboring the protein-protein interaction (PPI) with the PB1 subunit. The second is the PA subunit N-terminal domain (NPA), carrying the endonuclease active site. Revealing their structure with novel inhibitors would bring new aspects to rational structure-based drug development.

The PA-PB1 PPI is mediated by the small $3_{10}$ helix from the PB1 N-terminus inside the CPA hydrophobic pocket. The structure with a 25 amino acids long peptide inhibiting the assembly of RdRp heterotrimer was previously published. Therefore, we have decided to map the chemical space around the peptide,and to truncate and modify the peptide inhibitor maintaining the inhibitory potency. To study the first set of peptide inhibitors, we expressed the CPA domain and developed an AlphaScreen assay. Utilizing this assay, we tested ten peptides and selected one peptide to be modified according to the peptide array. This resulted in a nanomolar inhibitory potency of peptide **PB1-11** (DYNPYLLFLK), and a high-resolution crystal structure of the CPA with bound peptide (publication **I.**). However, using the generally used cell-penetrating Tat sequence connected to the peptide inhibitor did not improve the intracellular delivery of the inhibitory peptide. Therefore, the antiviral *in vivo* effect was not observed. To overcome this, we have further employed the recently published strategy, where the bicyclic peptide contains a cell-penetrating peptide in one cycle and the inhibitor peptide in the other cycle. The bicyclic strategy improved the intracellular delivery, and we were able to observe the peptide endosomal escape. Moreover, we have optimized the **PB1-11** peptide to the final **PB1-19** peptide (DYNPYLLYLK), resulting in a vastly improved solubility of the peptide in higher concentrations, allowing the first isothermal titration calorimetry (ITC) of this PA-PB1 interaction (publication **II.**). The **PB1-19** peptide was characterized as a low nanomolar inhibitor of the PA-PB1 PPI and was also observed from the X-ray protein crystallography data within the hydrophobic pocket of the CPA. These results may serve as a starting point for further peptide optimization or the design of non-peptidic PA-PB1 PPI inhibitors.

The NPA endonuclease is essential for viral transcription, as it cleaves the primer from host mRNA. The enzyme embeds two solvent-exposed metal ions in the active site. Currently, there

is one FDA approved compound, the baloxavir marboxil (BAM), targeting the NPA endonuclease. In the other part of this thesis, we were exploring the inhibitory potency of phytochemicals flavonoids and their derivatives against the NPA endonuclease domain. We have developed a high-throughput assay and tested over 80 compounds. Some of them were characterized as submicromolar inhibitors of the NPA, including luteolin and quambalarine B. The NPA endonuclease was identified as the target protein of those compounds which are broadly used as supplements during influenza viral infection. We crystallized the NPA with selected compounds and observed two binding modes (bidentate and tridentate) of the compounds to the metal ions in the active site. The molecular mode-of-action of flavonoids towards the influenza virus was revealed for the first time (publication **III.**). We continued to explore the structure-activity relationship (SAR) of luteolin derivatives. The second set of 21 compounds was prepared and tested. Orientin is a luteolin derivative with the C-8 introduced glucose moiety. It was characterized as a nanomolar inhibitor of the NPA endonuclease. Its glucose moiety formed an additional water-mediated net of hydrogen bonds, while maintaining the luteolin binding mode. Moreover, we prepared a mutant variant carrying the substitution of Ile-38 to Thr-38, which emerged during the BAM clinical trials. Although it reduced the susceptibility to BAM 30- to 50-fold, it did not affect the binding of orientin to the NPA. From the analyses of the I38T mutant variant crystal structure, the mutation occurred at a distant region of the endonuclease active site (publication **IV.**). Even though subsequent optimizations of the chemical structure of the flavonoid derivatives are needed to enhance their bioavailability, the protein-compound structure analysis brought additional insights into the protein inhibitor interactions.

# 6. SOUHRN

Virus chřipky způsobuje akutní infekci respiračního systému u lidí a představuje riziko onemocnění v rámci celého roku. Jelikož virus chřipky neustále mutuje a zároveň má pandemický potenciál, je potřeba vyvíjet stále nová antivirotika. V současnosti se většinou používají léky cílící na povrchový protein viru, neuraminidasu, a jsou užívány s určitou limitací. V posledních dvaceti letech bylo na viru identifikováno několik možných cílů pro antivirotické léky. Tato práce se zaměřuje na dva z nich, oba obsažené ve virové RNA-dependentní RNA polymerase (RdRp). Prvním z nich je C-koncová doména PA podjednotky (CPA) obsahující protein-proteinovou interakci (PPI) s podjednotkou PB1. Druhým z nich je N-koncová doména PA podjednotky (NPA), která obsahuje endonukleasovou doménu. Pokud by se získala jejich trojrozměrná struktura s navázaným inhibitorem, přineslo by to důležitý poznatek do racionálního vývoje léků založeného na struktuře.

PPI mezi PA a PB1 podjednotkou je zprostředkovaná malým $3_{10}$ helixem, odvozeným z N-koncové části PB1 podjednotky, který se váže do hydrofobní kapsy uvnitř CPA. Již dříve byla zveřejněna struktura peptidu dlouhého 25 aminokyselin, který inhiboval zkompletování celého RdRp heterotrimeru. Na základě této práce jsme se rozhodli zmapovat chemický prostor kolem peptidu a dále zkrátit a upravit peptidový inhibitor tak, aby si stále zachoval inhibiční potenci. V bakteriích jsme vyprodukovali CPA doménu, abychom mohli studovat první sérii peptidových inhibitorů, a zároveň vyvinuli AlphaScreen metodu na testování inhibitorů. Pomocí této metody jsme testovali deset peptidů, z nichž jsme jeden dále modifikovali. Výsledkem byl nanomolární peptidový inhibitor **PB1-11** (DYNPYLLFLK). Z krystalu komplexu s CPA jsme byli schopni určit jejich strukturu ve vysokem rozlišení (publikace **I.**). Ačkoliv jsme využili obecně používanou metodu, kdy se na peptid připojí Tat sekvence, nezlepšil nám tento přístup přenos peptidu přes buněčnou membránu. Kvůli špatné biologické dostupnosti jsme nepozorovali antivirový efekt *in vivo*. Abychom obešli prostupnost inhibitorů přes membránu, použili jsme nedávno publikovanou strategii využívající bicyklické peptidy. Jeden cyklus je tvořený peptidovou sekvencí, která prostupuje buněčnou membránou a druhý, který nese sekvenci peptidového inhibitoru. Tento příštup zlepšil dostupnost peptidového inhibitoru do buňky a zároveň jsme byli schopni sledovat únik peptidu z endosomu. Dále jsme optimalizovali **PB1-11** peptid na výsledný peptid **PB1-19** (DYNPYLLYLK), který byl daleko rozpustnější, což nám umožnilo vůbec první mikrokalorimetrickou charakterizaci vazby inhibitoru PA-PB1 interakce pomocí isotermální titrační kalorimetrii (ITC) (publikace **II.**). Peptid **PB1-19** byl charakterizován jako nanomolární inhibitor PA-PB1 PPI, a současně jsme získali trojrozměrnou strukturu s CPA pomocí rentgenové krystalografie. Tyto výsledky mohou

sloužit jako výchozí bod pro další optimalizaci peptidu, nebo pro design nepeptidových inhibitorů PA-PB1 interakce.

Endonukleasa v N-koncové části PA podjednotky (NPA) je nezbytná pro transkripci viru, jelikož vytváří primer z mRNA hositelské buňky. V aktivní části enzymu jsou usazené dva kovové ionty, které jsou vystavené do solventu. V současné době je dostupná jedna látka cílící na NPA endonukeasu, baloxavir marboxil (BAM). V druhé části disertační práce jsme zkoumali inhibiční možnosti rostlinných látek flavonoidů a z nich odvozených sloučenin proti NPA endonukleasové doméně. Vyvinuli jsme esej pro vysokokapacitní testování sloučenin a pomocí ní otestovali přes 80 látek. Některé z nich byly charakterizované jako submikromolární inhibitory NPA, včetně luteolinu a quambalarinu B. NPA endonukleasa byla identifikovaná jako cílový protein těchto sloučenin, které jsou běžně užívané při infekci způsobené virem chřipky. Povedlo se nám vykrystalizovat NPA protein s vybranými sloučeninami a ze struktury jsme identifikovali dva vazebné módy látek na kovové ionty v aktivním místě enzymu. Tímto jsme poprvé odhalili molekulární podstatu vazby flavonoidů proti viru chřipky (publikace **III.**). Nadále jsme pokračovali s prozkoumáváním vztahu mezi strukturou a aktivitou derivátů luteolinu. Připravili jsme a otestovali druhou série o 21 sloučeninách. Orientin je derivát luteolinu, který má na uhlíku C-8 glukosový zbytek. Byl charakterizovaný jako nanomolární inhibitor NPA endonukleasy. Glukosová část tvoří dodatečnou síť vodíkových vazeb s vedlejšími řetězci v aktivním místě, zprostředkovanou molekulami vody, zatímco si zachovává obdobný vazebný mód jako luteolin. V klinických studiích BAM se objevila varianta NPA proteinu, která nese substituci Ile-38 na Thr-38, a která zhoršila citlivost viru na BAM inhibitor 30- až 50-krát. Variantu I38T jsme rovněž připravili a otestovali, ale nijak neovlivnila vazbu orientinu do NPA aktivního místa. Z analýzy krystalové struktury vyplývá, že se mutace nachází na odlehlém místě aktivního místa endonukleasy od vazebného místa orientinu (publikace **IV.**). Další optimalizace chemické struktury flavonoidových derivátů budou potřeba, aby se zlepšila jejich biodostupnost. I přesto přinesla analýza struktur komplexu proteinu se sloučeninami nová porozumění jejich vzájemných interakcí.

## 7. REFERENCES


Air, G. M. (2012). Influenza neuraminidase. *Influenza and Other Respiratory Viruses*, *6*(4), 245–256. https://doi.org/10.1111/j.1750-2659.2011.00304.x

Akarsu, H., Burmeister, W. P., Petosa, C., Petit, I., Müller, C. W., Ruigrok, R. W. H., & Baudin, F. (2003). Crystal structure of the M1 protein-binding domain of the influenza A virus nuclear export protein (NEP/NS2). *EMBO Journal*, *22*(18), 4646–4655. https://doi.org/10.1093/emboj/cdg449

Amorim, M. J., Bruce, E. A., Read, E. K. C., Foeglein, Á., Mahen, R., Stuart, A. D., & Digard, P. (2011). A Rab11- and Microtubule-Dependent Mechanism for Cytoplasmic Transport of Influenza A Virus Viral RNA. *Journal of Virology*, *85*(9), 4143–4156. https://doi.org/10.1128/jvi.02606-10

Antipov, E. A., & Pokryshevskaya, E. B. (2019). The effects of adverse drug reactions on patients' satisfaction: Evidence from publicly available data on Tamiflu (oseltamivir). *International Journal of Medical Informatics*, *125*(February), 30–36. https://doi.org/10.1016/j.ijmedinf.2019.02.005

Area, E., Martin-Benito, J., Gastaminza, P., Torreira, E., Valpuesta, J. M., Carrascosa, J. L., & Ortin, J. (2004). 3D structure of the influenza virus polymerase complex: Localization of subunit domains. *Proceedings of the National Academy of Sciences*, *101*(1), 308–313. https://doi.org/10.1073/pnas.0307127101

Arranz, R., Coloma, R., Chichón, F. J., Conesa, J. J., Carrascosa, J. L., Valpuesta, J. M., Ortín, J., & Martín-Benito, J. (2012). The Structure of Native Influenza Virion Ribonucleoproteins. *Science*, *338*(6114), 1634–1637. https://doi.org/10.1126/science.1228172

Ayllon, J., & García-Sastre, A. (2014). The NS1 Protein: A Multitasking Virulence Factor. In *Assessment & Evaluation in Higher Education* (Vol. 37, Issue October, pp. 73–107). https://doi.org/10.1007/82_2014_400

Banerjee, I., Yamauchi, Y., Helenius, A., & Horvath, P. (2013). High-Content Analysis of Sequential Events during the Early Phase of Influenza A Virus Infection. *PLoS ONE*, *8*(7), 1–9. https://doi.org/10.1371/journal.pone.0068450

Bantia, S., Arnold, C. S., Parker, C. D., Upshaw, R., & Chand, P. (2006). Anti-influenza virus activity of peramivir in mice with single intramuscular injection. *Antiviral Research*, *69*(1), 39–45. https://doi.org/10.1016/j.antiviral.2005.10.002

Barman, S., Adhikary, L., Chakrabarti, A. K., Bernas, C., Kawaoka, Y., & Nayak, D. P. (2004). Role of Transmembrane Domain and Cytoplasmic Tail Amino Acid Sequences of Influenza A Virus Neuraminidase in Raft Association and Virus Budding. *Journal of Virology*, *78*(10), 5258–5269. https://doi.org/10.1128/JVI.78.10.5258-5269.2004

Barroso, L., Treanor, J., Gubareva, L., & Hayden, F. G. (2005). Efficacy and tolerability of the oral neuraminidase inhibitor peramivir in experimental human influenza: Randomized, controlled trials for prophylaxis and treatment. *Antiviral Therapy*, *10*(8), 901–910. https://doi.org/10.1177/135965350501000805

Barry, J. M. (2004). The site of origin of the 1918 influenza pandemic and its public health implications. *Journal of Translational Medicine*, *2*(1), 3. https://doi.org/10.1186/1479-5876-2-3

Bauman, J. D., Patel, D., Baker, S. F., Vijayan, R. S. K., Xiang, A., Parhi, A. K., Martínez-Sobrido, L., LaVoie, E. J., Das, K., & Arnold, E. (2013). Crystallographic Fragment Screening and Structure-Based Optimization Yields a New Class of Influenza Endonuclease Inhibitors. *ACS Chemical Biology*, *8*(11), 2501–2508. https://doi.org/10.1021/cb400400j

Biswas, S. K., & Nayak, D. P. (1994). Mutational analysis of the conserved motifs of influenza A virus polymerase basic protein 1. *Journal of Virology*, *68*(3), 1819–1826. https://doi.org/10.1128/jvi.68.3.1819-1826.1994

Bos, T. J., Davis, A. R., & Nayak, D. P. (1984). NH2-terminal hydrophobic region of influenza virus neuraminidase provides the signal function in translocation. *Proceedings of the National Academy of Sciences of the United States of America*, *81*(8 I), 2327–2331. https://doi.org/10.1073/pnas.81.8.2327

Bossart-Whitaker, P., Carson, M., Babu, Y. S., Smith, C. D., Laver, W. G., & Air, G. M. (1993). Three-dimensional structure of influenza a N9 neuraminidase and its complex with the inhibitor 2-deoxy 2,3-dehydro-N-acetyl neuraminic acid. In *Journal of Molecular Biology* (Vol. 232, Issue 4, pp. 1069–1083). https://doi.org/10.1006/jmbi.1993.1461

Bruenn, J. A. (2003). A structural and primary sequence comparison of the viral RNA-dependent RNA polymerases. *Nucleic Acids Research*, *31*(7), 1821–1829. https://doi.org/10.1093/nar/gkg277

Brundage, J. F., & Shanks, G. D. (2007). What Really Happened during the 1918 Influenza Pandemic? The Importance of Bacterial Secondary Infections. *The Journal of Infectious Diseases*, *196*(11), 1717–1718. https://doi.org/10.1086/522355

Bui, M, Whittaker, G., & Helenius, A. (1996). Effect of M1 protein and low pH on nuclear transport of influenza virus ribonucleoproteins. *Journal of Virology*, *70*(12), 8391–8401. https://doi.org/10.1128/jvi.70.12.8391-8401.1996

Bui, Matthew, Wills, E. G., Helenius, A., & Whittaker, G. R. (2000). Role of the Influenza Virus M1 Protein in Nuclear Export of Viral Ribonucleoproteins. *Journal of Virology*, *74*(4), 1781–1786. https://doi.org/10.1128/JVI.74.4.1781-1786.2000

Bullough, P. A., Hughson, F. M., Skehel, J. J., & Wiley, D. C. (1994). Structure of influenza HA at the pH of membrane fusion. *Nature*, *371*(6492), 37–43. https://www.nature.com/articles/371037a0.pdf

Cady, S. D., Luo, W., Hu, F., & Hong, M. (2009). Structure and function of the influenza A M2 proton channel. *Biochemistry*, *48*(31), 7356–7364. https://doi.org/10.1021/bi9008837

Carrique, L., Fan, H., Walker, A. P., Keown, J. R., Sharps, J., Staller, E., Barclay, W. S., Fodor, E., & Grimes, J. M. (2020). Host ANP32A mediates the assembly of the influenza virus replicase. *Nature*, *587*(7835), 638–643. https://doi.org/10.1038/s41586-020-2927-z

Cass, L. M. R., Efthymiopoulos, C., & Bye, A. (1999). Pharmacokinetics of zanamivir after intravenous, oral, inhaled or intranasal administration to healthy volunteers. *Clinical Pharmacokinetics*, *36*(SUPPL. 1), 1–11. https://doi.org/10.2165/00003088-199936001-00001

Chase, G. P., Rameix-Welti, M. A., Zvirbliene, A., Zvirblis, G., Götz, V., Wolff, T., Naffakh, N., & Schwemmle, M. (2011). Influenza virus ribonucleoprotein complexes gain preferential access to cellular export machinery through chromatin targeting. *PLoS Pathogens*, *7*(9). https://doi.org/10.1371/journal.ppat.1002187

Chen, J., Skehel, J. J., & Wiley, D. C. (1999). N- and C-terminal residues combine in the fusion-pH influenza hemagglutinin HA2 subunit to form an N cap that terminates the triple-stranded coiled coil. *Proceedings of the National Academy of Sciences of the United States of America*, *96*(16), 8967–8972. https://doi.org/10.1073/pnas.96.16.8967

Choi, H. J., Song, J. H., Park, K. S., & Kwon, D. H. (2009). Inhibitory effects of quercetin 3-rhamnoside on influenza A virus replication. *European Journal of Pharmaceutical Sciences*, *37*(3–4), 329–333. https://doi.org/10.1016/j.ejps.2009.03.002

Cianci, C., Chung, T. D. Y., Meanwell, N., Putz, H., Hagen, M., Colonno, R. J., & Krystal, M. (1996). Identification of N-Hydroxamic Acid and N-Hydroxyimide Compounds that Inhibit the Influenza Virus Polymerase. *Antiviral Chemistry and Chemotherapy*, *7*(6), 353–360. https://doi.org/10.1177/095632029600700609

Clark, M. P., Ledeboer, M. W., Davies, I., Byrn, R. A., Jones, S. M., Perola, E., Tsai, A., Jacobs, M., Nti-Addae, K., Bandarage, U. K., Boyd, M. J., Bethiel, R. S., Court, J. J., Deng, H., Duffy, J. P., Dorsch, W. A., Farmer, L. J., Gao, H., Gu, W., … Charifson, P. S. (2014). Discovery of a Novel, First-in-Class, Orally Bioavailable Azaindole Inhibitor (VX-787) of Influenza PB2. *Journal of Medicinal Chemistry*, *57*(15), 6668–6678. https://doi.org/10.1021/jm5007275

Coleman, M. T., Dowdle, W. R., Pereira, H. G., Schild, G. C., & Chang, W. K. (1968). The Hong Kong-68 influenza A2 variant. *Lancet*, *2*(7583), 1384–1386. https://doi.org/10.1016/s0140-6736(68)92683-4

Coloma, R., Arranz, R., de la Rosa-Trevín, J. M., Sorzano, C. O. S., Munier, S., Carlero, D., Naffakh, N., Ortín, J., & Martín-Benito, J. (2020). Structural insights into influenza A virus ribonucleoproteins reveal a processive helical track as transcription mechanism. *Nature Microbiology*, *5*(5), 727–734. https://doi.org/10.1038/s41564-020-0675-3

Cros, J. F., García-Sastre, A., & Palese, P. (2005). An Unconventional NLS is Critical for the Nuclear Import of the Influenza A Virus Nucleoprotein and Ribonucleoprotein. *Traffic*, *6*(3), 205–213. https://doi.org/10.1111/j.1600-0854.2005.00263.x

D'Agostino, I., Giacchello, I., Nannetti, G., Fallacara, A. L., Deodato, D., Musumeci, F., Grossi, G., Palù, G., Cau, Y., Trist, I. M., Loregian, A., Schenone, S., & Botta, M. (2018). Synthesis and biological evaluation of a library of hybrid derivatives as inhibitors of influenza virus PA-PB1 interaction. *European Journal of Medicinal Chemistry*, *157*, 743–758. https://doi.org/10.1016/j.ejmech.2018.08.032

Daniels, R., Kurowski, B., Johnson, A. E., & Hebert, D. N. (2003). N-linked glycans direct the cotranslational folding pathway of Influenza hemagglutinin. *Molecular Cell*, *11*(1), 79–90. https://doi.org/10.1016/S1097-2765(02)00821-3

Dawood, F. S., Iuliano, A. D., Reed, C., Meltzer, M. I., Shay, D. K., Cheng, P.-Y., Bandaranayake, D., Breiman, R. F., Brooks, W. A., Buchy, P., Feikin, D. R., Fowler, K. B., Gordon, A., Hien, N. T., Horby, P., Huang, Q. S., Katz, M. A., Krishnan, A., Lal, R., … Widdowson, M.-A. (2012). Estimated global mortality associated with the first 12 months of 2009 pandemic influenza A H1N1 virus circulation: a modelling study. *The Lancet Infectious Diseases*, *12*(9), 687–695. https://doi.org/10.1016/S1473-3099(12)70121-4

De Vlieger, D., Ballegeer, M., Rossey, I., Schepens, B., & Saelens, X. (2018). Single-Domain Antibodies and Their Formatting to Combat Viral Infections. *Antibodies*, *8*(1), 1. https://doi.org/10.3390/antib8010001

Deng, T., Vreede, F. T., & Brownlee, G. G. (2006). Different De Novo Initiation Strategies Are Used by Influenza Virus RNA Polymerase on Its cRNA and Viral RNA Promoters during Viral RNA Replication. *Journal of Virology*, *80*(5), 2337–2348. https://doi.org/10.1128/jvi.80.5.2337-2348.2006

Desantis, J., Nannetti, G., Massari, S., Barreca, M. L., Manfroni, G., Cecchetti, V., Palù, G., Goracci, L.,

Loregian, A., & Tabarrini, O. (2017). Exploring the cycloheptathiophene-3-carboxamide scaffold to disrupt the interactions of the influenza polymerase subunits and obtain potent anti-influenza activity. *European Journal of Medicinal Chemistry*, *138*, 128–139. https://doi.org/10.1016/j.ejmech.2017.06.015

Dias, A., Bouvier, D., Crépin, T., McCarthy, A. A., Hart, D. J., Baudin, F., Cusack, S., & Ruigrok, R. W. H. (2009). The cap-snatching endonuclease of influenza virus polymerase resides in the PA subunit. *Nature*, *458*(7240), 914–918. https://doi.org/10.1038/nature07745

Dou, D., Revol, R., Östbye, H., Wang, H., & Daniels, R. (2018). Influenza A Virus Cell Entry, Replication, Virion Assembly and Movement. *Frontiers in Immunology*, *9*(JUL), 1–17. https://doi.org/10.3389/fimmu.2018.01581

Dowdle, W. R. (1999). Influenza A virus recycling revisited. *Bulletin of the World Health Organization*, *77*(10), 820–828. http://www.ncbi.nlm.nih.gov/pubmed/10593030

DuBois, R. M., Slavish, P. J., Baughman, B. M., Yun, M.-K., Bao, J., Webby, R. J., Webb, T. R., & White, S. W. (2012). Structural and Biochemical Basis for Development of Influenza Virus Inhibitors Targeting the PA Endonuclease. *PLoS Pathogens*, *8*(8), e1002830. https://doi.org/10.1371/journal.ppat.1002830

Eisfeld, A. J., Kawakami, E., Watanabe, T., Neumann, G., & Kawaoka, Y. (2011). RAB11A Is Essential for Transport of the Influenza Virus Genome to the Plasma Membrane. *Journal of Virology*, *85*(13), 6117–6126. https://doi.org/10.1128/jvi.00378-11

Eisfeld, A. J., Neumann, G., & Kawaoka, Y. (2015). At the centre: Influenza A virus ribonucleoproteins. *Nature Reviews Microbiology*, *13*(1), 28–41. https://doi.org/10.1038/nrmicro3367

Ellis, D., Lederhofer, J., Acton, O. J., Tsybovsky, Y., Kephart, S., Yap, C., Gillespie, R. A., Creanga, A., Olshefsky, A., Stephens, T., Pettie, D., Murphy, M., Sydeman, C., Ahlrichs, M., Chan, S., Borst, A. J., Park, Y.-J., Lee, K. K., Graham, B. S., … Kanekiyo, M. (2022). Structure-based design of stabilized recombinant influenza neuraminidase tetramers. *Nature Communications*, *13*(1), 1825. https://doi.org/10.1038/s41467-022-29416-z

Elton, D., Simpson-Holley, M., Archer, K., Medcalf, L., Hallam, R., McCauley, J., & Digard, P. (2001). Interaction of the influenza virus nucleoprotein with the cellular CRM1-mediated nuclear export pathway. *Journal of Virology*, *75*(1), 408–419. https://doi.org/10.1128/JVI.75.1.408-419.2001

Engelhardt, O. G., Smith, M., & Fodor, E. (2005). Association of the Influenza A Virus RNA-Dependent RNA Polymerase with Cellular RNA Polymerase II. *Journal of Virology*, *79*(9), 5812–5818. https://doi.org/10.1128/jvi.79.9.5812-5818.2005

Fan, H., Walker, A. P., Carrique, L., Keown, J. R., Serna Martin, I., Karia, D., Sharps, J., Hengrung, N., Pardon, E., Steyaert, J., Grimes, J. M., & Fodor, E. (2019). Structures of influenza A virus RNA polymerase offer insight into viral genome replication. *Nature*, *573*(7773), 287–290. https://doi.org/10.1038/s41586-019-1530-7

Fudo, S., Yamamoto, N., Nukaga, M., Odagiri, T., Tashiro, M., & Hoshino, T. (2016). Two Distinctive Binding Modes of Endonuclease Inhibitors to the N-Terminal Region of Influenza Virus Polymerase Acidic Subunit. *Biochemistry*, *55*(18), 2646–2660. https://doi.org/10.1021/acs.biochem.5b01087

Furuta, Y., Gowen, B. B., Takahashi, K., Shiraki, K., Smee, D. F., & Barnard, D. L. (2013). Favipiravir (T-705), a novel viral RNA polymerase inhibitor. *Antiviral Research*, *100*(2), 446–454. https://doi.org/10.1016/j.antiviral.2013.09.015

Gagnon, A., Miller, M. S., Hallman, S. A., Bourbeau, R., Herring, D. A., Earn, D. J. D., & Madrenas, J. (2013). Age-Specific Mortality During the 1918 Influenza Pandemic: Unravelling the Mystery of High Young Adult Mortality. *PLoS ONE*, *8*(8). https://doi.org/10.1371/journal.pone.0069586

Gansukh, E., Kazibwe, Z., Pandurangan, M., Judy, G., & Kim, D. H. (2016). Probing the impact of quercetin-7-O-glucoside on influenza virus replication influence. *Phytomedicine*, *23*(9), 958–967. https://doi.org/10.1016/j.phymed.2016.06.001

Garten, R. J., Davis, C. T., Russell, C. A., Shu, B., Lindstrom, S., Balish, A., Sessions, W. M., Xu, X., Skepner, E., Deyde, V., Okomo-Adhiambo, M., Gubareva, L., Barnes, J., Smith, C. B., Emery, S. L., Hillman, M. J., Rivailler, P., Smagala, J., de Graaf, M., … Cox, N. J. (2009). Antigenic and Genetic Characteristics of Swine-Origin 2009 A(H1N1) Influenza Viruses Circulating in Humans. *Science*, *325*(5937), 197–201. https://doi.org/10.1126/science.1176225

Ghanem, A., Mayer, D., Chase, G., Tegge, W., Frank, R., Kochs, G., García-Sastre, A., & Schwemmle, M. (2007). Peptide-Mediated Interference with Influenza A Virus Polymerase. *Journal of Virology*, *81*(14), 7801–7804. https://doi.org/10.1128/JVI.00724-07

Goldhill, D. H., te Velthuis, A. J. W., Fletcher, R. A., Langat, P., Zambon, M., Lackenby, A., & Barclay, W. S. (2018). The mechanism of resistance to favipiravir in influenza. *Proceedings of the National Academy of Sciences*, *115*(45), 11613–11618. https://doi.org/10.1073/pnas.1811345115

Gottschalk, A. (1957). Neuraminidase: the specific enzyme of influenza virus and Vibrio cholerae. *Biochimica et Biophysica Acta*, *23*(C), 645–646. https://doi.org/10.1016/0006-3002(57)90389-X

Goujon, M., McWilliam, H., Li, W., Valentin, F., Squizzato, S., Paern, J., & Lopez, R. (2010). A new

bioinformatics analysis tools framework at EMBL-EBI. *Nucleic Acids Research*, *38*(SUPPL. 2), 695–699. https://doi.org/10.1093/nar/gkq313

Gu, W., Gallagher, G. R., Dai, W., Liu, P., Li, R., Trombly, M. I., Gammon, D. B., Mello, C. C., Wang, J. P., & Finberg, R. W. (2015). Influenza A virus preferentially snatches noncoding RNA caps. *Rna*, *21*(12), 2067–2075. https://doi.org/10.1261/rna.054221.115

Guilligay, D., Tarendeau, F., Resa-Infante, P., Coloma, R., Crepin, T., Sehr, P., Lewis, J., Ruigrok, R. W. H., Ortin, J., Hart, D. J., & Cusack, S. (2008). The structural basis for cap binding by influenza virus polymerase subunit PB2. *Nature Structural & Molecular Biology*, *15*(5), 500–506. https://doi.org/10.1038/nsmb.1421

Guo, Z., Chen, L. M., Zeng, H., Gomez, J. A., Plowden, J., Fujita, T., Katz, J. M., Donis, R. O., & Sambhara, S. (2007). NS1 protein of influenza A virus inhibits the function of intracytoplasmic pathogen sensor, RIG-I. *American Journal of Respiratory Cell and Molecular Biology*, *36*(3), 263–269. https://doi.org/10.1165/rcmb.2006-0283RC

Hay, A. J., Wolstenholme, A. J., Skehel, J. J., & Smith, M. H. (1985). The molecular basis of the specific anti-influenza action of amantadine. *The EMBO Journal*, *4*(11), 3021–3024. https://doi.org/10.1002/j.1460-2075.1985.tb04038.x

Hayashi, T., MacDonald, L. A., & Takimoto, T. (2015). Influenza A Virus Protein PA-X Contributes to Viral Growth and Suppression of the Host Antiviral and Immune Responses. *Journal of Virology*, *89*(12), 6442–6452. https://doi.org/10.1128/JVI.00319-15

Hayden, F. G., Sugaya, N., Hirotsu, N., Lee, N., de Jong, M. D., Hurt, A. C., Ishida, T., Sekino, H., Yamada, K., Portsmouth, S., Kawaguchi, K., Shishido, T., Arai, M., Tsuchiya, K., Uehara, T., & Watanabe, A. (2018). Baloxavir Marboxil for Uncomplicated Influenza in Adults and Adolescents. *New England Journal of Medicine*, *379*(10), 913–923. https://doi.org/10.1056/NEJMoa1716197

He, X., Zhou, J., Bartlam, M., Zhang, R., Ma, J., Lou, Z., Li, X., Li, J., Joachimiak, A., Zeng, Z., Ge, R., Rao, Z., & Liu, Y. (2008). Crystal structure of the polymerase PA(C)-PB1(N) complex from an avian influenza H5N1 virus. *Nature*, *454*(7208), 1123–1126. https://doi.org/10.1038/nature07120

Hejdánek, J., Radilová, K., Pachl, P., Hodek, J., Machara, A., Weber, J., Řezáčová, P., Konvalinka, J., & Kožíšek, M. (2021). structural characterization of the interaction between the C-terminal domain of the influenza polymerase PA subunit and an optimized small peptide inhibitor. *Antiviral Research*, *185*(August 2020), 104971. https://doi.org/10.1016/j.antiviral.2020.104971

Hengrung, N., El Omari, K., Serna Martin, I., Vreede, F. T., Cusack, S., Rambo, R. P., Vonrhein, C., Bricogne, G., Stuart, D. I., Grimes, J. M., & Fodor, E. (2015). Crystal structure of the RNA-dependent RNA polymerase from influenza C virus. *Nature*, *527*(7576), 114–117. https://doi.org/10.1038/nature15525

Hirsch, E. F., & Mckinney, M. (1919). An Epidemic of Pneumococcus Bronchopneumonia. *Journal of Infectious Diseases*, *24*(6), 594–617. https://doi.org/10.1093/infdis/24.6.594

Huang, S., Chen, J., Chen, Q., Wang, H., Yao, Y., Chen, J., & Chen, Z. (2013). A Second CRM1-Dependent Nuclear Export Signal in the Influenza A Virus NS2 Protein Contributes to the Nuclear Export of Viral Ribonucleoproteins. *Journal of Virology*, *87*(2), 767–778. https://doi.org/10.1128/jvi.06519-11

Huet, S., Avilov, S. V., Ferbitz, L., Daigle, N., Cusack, S., & Ellenberg, J. (2010). Nuclear Import and Assembly of Influenza A Virus RNA Polymerase Studied in Live Cells by Fluorescence Cross-Correlation Spectroscopy. *Journal of Virology*, *84*(3), 1254–1264. https://doi.org/10.1128/JVI.01533-09

Hull, J. D., Gilmore, R., Lamb, R. A., & Biology, C. (1988). Integration of a Small Integral Membrane Protein,. *Journal of Cell Biology*, *106*(May), 1489–1498. http://www.ncbi.nlm.nih.gov/pubmed/2836432%0Ahttp://www.pubmedcentral.nih.gov/articlerender.fcgi?artid=PMC2115032

Hutchinson, E. C., Charles, P. D., Hester, S. S., Thomas, B., Trudgian, D., Martínez-Alonso, M., & Fodor, E. (2014). Conserved and host-specific features of influenza virion architecture. *Nature Communications*, *5*(1), 4816. https://doi.org/10.1038/ncomms5816

Ikematsu, H., & Kawai, N. (2011). Laninamivir octanoate: a new long-acting neuraminidase inhibitor for the treatment of influenza. *Expert Review of Anti-Infective Therapy*, *9*(10), 851–857. https://doi.org/10.1586/eri.11.112

Influenza Vaccine: Quickly Produce Here to Combat Asian Type. (1957, July 7). *The New York Times*, 119. https://nyti.ms/3z6ZyY0

Ishizuka, H., Yoshiba, S., Okabe, H., & Yoshihara, K. (2010). Clinical pharmacokinetics of laninamivir, a novel long-acting neuraminidase inhibitor, after single and multiple inhaled doses of its prodrug, CS-8958, in healthy male volunteers. *Journal of Clinical Pharmacology*, *50*(11), 1319–1329. https://doi.org/10.1177/0091270009356297

Itzstein Von, M. (2007). The war against influenza : discovery and development of sialidase inhibitors. *Nature Reviews. Drug Discovery*, *6*(dECEMBEr), 967–974.

Iuliano, A. D., Roguski, K. M., Chang, H. H., Muscatello, D. J., Palekar, R., Tempia, S., Cohen, C., Gran, J. M.,

Schanzer, D., Cowling, B. J., Wu, P., Kyncl, J., Ang, L. W., Park, M., Redlberger-Fritz, M., Yu, H., Espenhain, L., Krishnan, A., Emukule, G., … Mustaquim, D. (2018). Estimates of global seasonal influenza-associated respiratory mortality: a modelling study. *The Lancet*, *391*(10127), 1285–1300. https://doi.org/10.1016/S0140-6736(17)33293-2

Jagger, B. W., Wise, H. M., Kash, J. C., Walters, K.-A., Wills, N. M., Xiao, Y.-L., Dunfee, R. L., Schwartzman, L. M., Ozinsky, A., Bell, G. L., Dalton, R. M., Lo, A., Efstathiou, S., Atkins, J. F., Firth, A. E., Taubenberger, J. K., & Digard, P. (2012). An Overlapping Protein-Coding Region in Influenza A Virus Segment 3 Modulates the Host Response. *Science*, *337*(6091), 199–204. https://doi.org/10.1126/science.1222213

Kamal, R., Alymova, I., & York, I. (2017). Evolution and Virulence of Influenza A Virus Protein PB1-F2. *International Journal of Molecular Sciences*, *19*(1), 96. https://doi.org/10.3390/ijms19010096

Keown, J. R., Zhu, Z., Carrique, L., Fan, H., Walker, A. P., Serna Martin, I., Pardon, E., Steyaert, J., Fodor, E., & Grimes, J. M. (2022). Mapping inhibitory sites on the RNA polymerase of the 1918 pandemic influenza virus using nanobodies. *Nature Communications*, *13*(1), 251. https://doi.org/10.1038/s41467-021-27950-w

Khaperskyy, D. A., Schmaling, S., Larkins-Ford, J., McCormick, C., & Gaglia, M. M. (2016). Selective Degradation of Host RNA Polymerase II Transcripts by Influenza A Virus PA-X Host Shutoff Protein. *PLOS Pathogens*, *12*(2), e1005427. https://doi.org/10.1371/journal.ppat.1005427

Kilbourne, E. D. (2006). Influenza Pandemics of the 20th Century. *Emerging Infectious Diseases*, *12*(1), 9–14. https://doi.org/10.3201/eid1201.051254

Kim, H., Webster, R. G., & Webby, R. J. (2018). Influenza Virus: Dealing with a Drifting and Shifting Pathogen. *Viral Immunology*, *31*(2), 174–183. https://doi.org/10.1089/vim.2017.0141

Klenk, H. D., Rott, R., Orlich, M., & Blödorn, J. (1975). Activation of influenza A viruses by trypsin treatment. *Virology*, *68*(2), 426–439. https://doi.org/10.1016/0042-6822(75)90284-6

Koppstein, D., Ashour, J., & Bartel, D. P. (2015). Sequencing the cap-snatching repertoire of H1N1 influenza provides insight into the mechanism of viral transcription initiation. *Nucleic Acids Research*, *43*(10), 5052–5064. https://doi.org/10.1093/nar/gkv333

Kouba, T., Drncová, P., & Cusack, S. (2019). Structural snapshots of actively transcribing influenza polymerase. *Nature Structural and Molecular Biology*, *26*(6), 460–470. https://doi.org/10.1038/s41594-019-0232-z

Kowalinski, E., Zubieta, C., Wolkerstorfer, A., Szolar, O. H. J., Ruigrok, R. W. H., & Cusack, S. (2012). Structural Analysis of Specific Metal Chelating Inhibitor Binding to the Endonuclease Domain of Influenza pH1N1 (2009) Polymerase. *PLoS Pathogens*, *8*(8), e1002831. https://doi.org/10.1371/journal.ppat.1002831

Landeras-Bueno, S., Jorba, N., Pérez-Cidoncha, M., & Ortín, J. (2011). The splicing factor proline-glutamine rich (SFPQ/PSF) is involved in influenza virus transcription. *PLoS Pathogens*, *7*(11). https://doi.org/10.1371/journal.ppat.1002397

Le Sage, V., Nanni, A., Bhagwat, A., Snyder, D., Cooper, V., Lakdawala, S., & Lee, N. (2018). Non-Uniform and Non-Random Binding of Nucleoprotein to Influenza A and B Viral RNA. *Viruses*, *10*(10), 522. https://doi.org/10.3390/v10100522

Lee, N., Le Sage, V., Nanni, A. V., Snyder, D. J., Cooper, V. S., & Lakdawala, S. S. (2017). Genome-wide analysis of influenza viral RNA and nucleoprotein association. *Nucleic Acids Research*, *45*(15), 8968–8977. https://doi.org/10.1093/nar/gkx584

Li, M. L., Rao, P., & Krug, R. M. (2001). The active sites of the influenza cap-dependent endonuclease are on different polymerase subunits. *The EMBO Journal*, *20*(8), 2078–2086. https://doi.org/10.1093/emboj/20.8.2078

Li, X., & Palese, P. (1994). Characterization of the polyadenylation signal of influenza virus RNA. *Journal of Virology*, *68*(2), 1245–1249. https://doi.org/10.1128/jvi.68.2.1245-1249.1994

Liu, M., Lo, C. Y., Wang, G., Chow, H. F., Ngo, J. C. K., Wan, D. C. C., Poon, L. L. M., & Shaw, P. C. (2017). Identification of influenza polymerase inhibitors targeting polymerase PB2 cap-binding domain through virtual screening. *Antiviral Research*, *144*, 186–195. https://doi.org/10.1016/j.antiviral.2017.06.009

Liu, Z., Zhao, J., Li, W., Shen, L., Huang, S., Tang, J., Duan, J., Fang, F., Huang, Y., Chang, H., Chen, Z., & Zhang, R. (2016). Computational screen and experimental validation of anti-influenza effects of quercetin and chlorogenic acid from traditional Chinese medicine. *Scientific Reports*, *6*(June 2015), 1–9. https://doi.org/10.1038/srep19095

Lo, C. Y., Li, O. T. W., Tang, W. P., Hu, C., Wang, G. X., Ngo, J. C. K., Wan, D. C. C., Poon, L. L. M., & Shaw, P. C. (2018). Identification of influenza polymerase inhibitors targeting C-terminal domain of PA through surface plasmon resonance screening. *Scientific Reports*, *8*(1), 1–13. https://doi.org/10.1038/s41598-018-20772-9

Long, J. S., Giotis, E. S., Moncorgé, O., Frise, R., Mistry, B., James, J., Morisson, M., Iqbal, M., Vignal, A., Skinner, M. A., & Barclay, W. S. (2016). Species difference in ANP32A underlies influenza A virus polymerase host restriction. *Nature*, *529*(7584), 101–104. https://doi.org/10.1038/nature16474

Luk, J., Gross, P., & Thompson, W. W. (2001). Observations on Mortality during the 1918 Influenza Pandemic. *Clinical Infectious Diseases*, *33*(8), 1375–1378. https://doi.org/10.1086/322662

Lukarska, M., Fournier, G., Pflug, A., Resa-Infante, P., Reich, S., Naffakh, N., & Cusack, S. (2017). Structural basis of an essential interaction between influenza polymerase and Pol II CTD. *Nature*, *541*(7635), 117–121. https://doi.org/10.1038/nature20594

Mahy, B. W., Hastie, N. D., & Armstrong, S. J. (1972). Inhibition of influenza virus replication by -amanitin: mode of action. *Proceedings of the National Academy of Sciences of the United States of America*, *69*(6), 1421–1424. https://doi.org/10.1073/pnas.69.6.1421

Mänz, B., Götz, V., Wunderlich, K., Eisel, J., Kirchmair, J., Stech, J., Stech, O., Chase, G., Frank, R., & Schwemmle, M. (2011). Disruption of the Viral Polymerase Complex Assembly as a Novel Approach to Attenuate Influenza A Virus. *Journal of Biological Chemistry*, *286*(10), 8414–8424. https://doi.org/10.1074/jbc.M110.205534

Martín-Benito, J., Area, E., Ortega, J., Llorca, O., Valpuesta, J. M., Carrascosa, J. L., & Ortín, J. (2001). Three-dimensional reconstruction of a recombinant influenza virus ribonucleoprotein particle. *EMBO Reports*, *2*(4), 313–317. https://doi.org/10.1093/embo-reports/kve063

Massari, S., Goracci, L., Desantis, J., & Tabarrini, O. (2016). Polymerase Acidic Protein–Basic Protein 1 (PA–PB1) Protein–Protein Interaction as a Target for Next-Generation Anti-influenza Therapeutics. *Journal of Medicinal Chemistry*, *59*(17), 7699–7718. https://doi.org/10.1021/acs.jmedchem.5b01474

McGowan, D. C., Balemans, W., Embrechts, W., Motte, M., Keown, J. R., Buyck, C., Corbera, J., Funes, M., Moreno, L., Cooymans, L., Tahri, A., Eymard, J., Stoops, B., Strijbos, R., Van den Berg, J., Fodor, E., Grimes, J. M., Koul, A., Jonckers, T. H. M., … Guillemont, J. (2019). Design, Synthesis, and Biological Evaluation of Novel Indoles Targeting the Influenza PB2 Cap Binding Region. *Journal of Medicinal Chemistry*, *62*(21), 9680–9690. https://doi.org/10.1021/acs.jmedchem.9b01091

McKimm-Breschkin, J., Trivedi, T., Hampson, A., Hay, A., Klimov, A., Tashiro, M., Hayden, F., & Zambon, M. (2003). Neuraminidase sequence analysis and susceptibilities of influenza virus clinical isolates to zanamivir and oseltamivir. *Antimicrobial Agents and Chemotherapy*, *47*(7), 2264–2272. https://doi.org/10.1128/AAC.47.7.2264-2272.2003

Memorandum, W. H. O. (1980). A revision of the system of nomenclature for influenza viruses: a WHO memorandum. *Bulletin of the World Health Organization*, *58*(4), 585–591. http://www.ncbi.nlm.nih.gov/pubmed/6969132

Mibayashi, M., Martínez-Sobrido, L., Loo, Y.-M., Cárdenas, W. B., Gale, M., & García-Sastre, A. (2007). Inhibition of Retinoic Acid-Inducible Gene I-Mediated Induction of Beta Interferon by the NS1 Protein of Influenza A Virus. *Journal of Virology*, *81*(2), 514–524. https://doi.org/10.1128/jvi.01265-06

Momose, F., Kikuchi, Y., Komase, K., & Morikawa, Y. (2007). Visualization of microtubule-mediated transport of influenza viral progeny ribonucleoprotein. *Microbes and Infection*, *9*(12–13), 1422–1433. https://doi.org/10.1016/j.micinf.2007.07.007

Morens, D. M., & Taubenberger, J. K. (2011). Pandemic influenza: certain uncertainties. *Reviews in Medical Virology*, *21*(5), n/a-n/a. https://doi.org/10.1002/rmv.689

Nagata, T., Lefor, A. K., Hasegawa, M., & Ishii, M. (2015). Favipiravir: A New Medication for the Ebola Virus Disease Pandemic. *Disaster Medicine and Public Health Preparedness*, *9*(1), 79–81. https://doi.org/10.1017/dmp.2014.151

Nannetti, G., Massari, S., Mercorelli, B., Bertagnin, C., Desantis, J., Palù, G., Tabarrini, O., & Loregian, A. (2019). Potent and broad-spectrum cycloheptathiophene-3-carboxamide compounds that target the PA-PB1 interaction of influenza virus RNA polymerase and possess a high barrier to drug resistance. *Antiviral Research*, *165*(February), 55–64. https://doi.org/10.1016/j.antiviral.2019.03.003

Neumann, G., Hughes, M. T., & Kawaoka, Y. (2000). Influenza A virus NS2 protein mediates vRNP nuclear export through NES-independent interaction with hCRM1. *EMBO Journal*, *19*(24), 6751–6758. https://doi.org/10.1093/emboj/19.24.6751

Noshi, T., Kitano, M., Taniguchi, K., Yamamoto, A., Omoto, S., Baba, K., Hashimoto, T., Ishida, K., Kushima, Y., Hattori, K., Kawai, M., Yoshida, R., Kobayashi, M., Yoshinaga, T., Sato, A., Okamatsu, M., Sakoda, Y., Kida, H., Shishido, T., & Naito, A. (2018). In vitro characterization of baloxavir acid, a first-in-class cap-dependent endonuclease inhibitor of the influenza virus polymerase PA subunit. *Antiviral Research*, *160*(June), 109–117. https://doi.org/10.1016/j.antiviral.2018.10.008

O'Neil, B., Ison, M. G., Hallouin-Bernard, M. C., Nilsson, A. C., Torres, A., Wilburn, J. M., van Duijnhoven, W., Van Dromme, I., Anderson, D., Deleu, S., Kosoglou, T., Vingerhoets, J., Rossenu, S., & Leopold, L. (2022). A Phase 2 Study of Pimodivir (JNJ-63623872) in Combination With Oseltamivir in Elderly and Nonelderly Adults Hospitalized With Influenza A Infection: OPAL Study. *The Journal of Infectious Diseases*, *226*(1), 109–118. https://doi.org/10.1093/infdis/jiaa376

O'Neill, R. E., Talon, J., & Palese, P. (1998). The influenza virus NEP (NS2 protein) mediates the nuclear export of viral ribonucleoproteins. *EMBO Journal*, *17*(1), 288–296. https://doi.org/10.1093/emboj/17.1.288

Obayashi, E., Yoshida, H., Kawai, F., Shibayama, N., Kawaguchi, A., Nagata, K., Tame, J. R. H., & Park, S. (2008). The structural basis for an essential subunit interaction in influenza virus RNA polymerase. *Nature*, *454*(7208), 1127–1131. https://doi.org/10.1038/nature07225

Omoto, S., Speranzini, V., Hashimoto, T., Noshi, T., Yamaguchi, H., Kawai, M., Kawaguchi, K., Uehara, T., Shishido, T., Naito, A., & Cusack, S. (2018). Characterization of influenza virus variants induced by treatment with the endonuclease inhibitor baloxavir marboxil. *Scientific Reports*, *8*(1), 9633. https://doi.org/10.1038/s41598-018-27890-4

Oymans, J., & te Velthuis, A. J. W. (2018). A Mechanism for Priming and Realignment during Influenza A Virus Replication. *Journal of Virology*, *92*(3). https://doi.org/10.1128/jvi.01773-17

Parhi, A. K., Xiang, A., Bauman, J. D., Patel, D., Vijayan, R. S. K., Das, K., Arnold, E., & LaVoie, E. J. (2013). Phenyl substituted 3-hydroxypyridin-2(1H)-ones: Inhibitors of influenza A endonuclease. *Bioorganic & Medicinal Chemistry*, *21*(21), 6435–6446. https://doi.org/10.1016/j.bmc.2013.08.053

Pauly, M. D., Procario, M. C., & Lauring, A. S. (2017). A novel twelve class fluctuation test reveals higher than expected mutation rates for influenza A viruses. *ELife*, *6*(45), 11613–11618. https://doi.org/10.7554/eLife.26437

Pautus, S., Sehr, P., Lewis, J., Fortuné, A., Wolkerstorfer, A., Szolar, O., Guilligay, D., Lunardi, T., Décout, J.-L., & Cusack, S. (2013). New 7-Methylguanine Derivatives Targeting the Influenza Polymerase PB2 Cap-Binding Domain. *Journal of Medicinal Chemistry*, *56*(21), 8915–8930. https://doi.org/10.1021/jm401369y

Peng, Q., Liu, Y., Peng, R., Wang, M., Yang, W., Song, H., Chen, Y., Liu, S., Han, M., Zhang, X., Wang, P., Yan, J., Zhang, B., Qi, J., Deng, T., Gao, G. F., & Shi, Y. (2019). Structural insight into RNA synthesis by influenza D polymerase. *Nature Microbiology*, *4*(10), 1750–1759. https://doi.org/10.1038/s41564-019-0487-5

Pflug, A., Gaudon, S., Resa-Infante, P., Lethier, M., Reich, S., Schulze, W. M., & Cusack, S. (2018). Capped RNA primer binding to influenza polymerase and implications for the mechanism of cap-binding inhibitors. *Nucleic Acids Research*, *46*(2), 956–971. https://doi.org/10.1093/nar/gkx1210

Pflug, A., Guilligay, D., Reich, S., & Cusack, S. (2014). Structure of influenza A polymerase bound to the viral RNA promoter. *Nature*, *516*(7531), 355–360. https://doi.org/10.1038/nature14008

Poon, L. L. M., Pritlove, D. C., Fodor, E., & Brownlee, G. G. (1999). Direct Evidence that the Poly(A) Tail of Influenza A Virus mRNA Is Synthesized by Reiterative Copying of a U Track in the Virion RNA Template. *Journal of Virology*, *73*(4), 3473–3476. https://doi.org/10.1128/jvi.73.4.3473-3476.1999

Principi, N., Camilloni, B., & Esposito, S. (2018). Influenza immunization policies: Which could be the main reasons for differences among countries? *Human Vaccines and Immunotherapeutics*, *14*(3), 684–692. https://doi.org/10.1080/21645515.2017.1405188

Radilová, K., Zima, V., Kráľ, M., Machara, A., Majer, P., Hodek, J., Weber, J., Brynda, J., Strmeň, T., Konvalinka, J., & Kožíšek, M. (2022). Thermodynamic and structural characterization of an optimized peptide-based inhibitor of the influenza polymerase PA-PB1 subunit interaction. *Antiviral Research*, 105449. https://doi.org/10.1016/j.antiviral.2022.105449

Reguera, J., Gerlach, P., & Cusack, S. (2016). Towards a structural understanding of RNA synthesis by negative strand RNA viral polymerases. *Current Opinion in Structural Biology*, *36*, 75–84. https://doi.org/10.1016/j.sbi.2016.01.002

Reiberger, R., Radilová, K., Kráľ, M., Zima, V., Majer, P., Brynda, J., Dračínský, M., Konvalinka, J., Kožíšek, M., & Machara, A. (2021). Synthesis and In Vitro Evaluation of C-7 and C-8 Luteolin Derivatives as Influenza Endonuclease Inhibitors. *International Journal of Molecular Sciences*, *22*(14), 7735. https://doi.org/10.3390/ijms22147735

Reich, S., Guilligay, D., Pflug, A., Malet, H., Berger, I., Crépin, T., Hart, D., Lunardi, T., Nanao, M., Ruigrok, R. W. H., & Cusack, S. (2014). Structural insight into cap-snatching and RNA synthesis by influenza polymerase. *Nature*, *516*(7531), 361–366. https://doi.org/10.1038/nature14009

Reid, A. H., Fanning, T. G., Hultin, J. V., & Taubenberger, J. K. (1999). Origin and evolution of the 1918 "Spanish" influenza virus hemagglutinin gene. *Proceedings of the National Academy of Sciences*, *96*(4), 1651–1656. https://doi.org/10.1073/pnas.96.4.1651

Reilly, P. T., Yu, Y., Hamiche, A., & Wang, L. (2014). Cracking the ANP32 whips: Important functions, unequal requirement, and hints at disease implications. *BioEssays*, *36*(11), 1062–1071. https://doi.org/10.1002/bies.201400058

Robert, X., & Gouet, P. (2014). Deciphering key features in protein structures with the new ENDscript server. *Nucleic Acids Research*, *42*(W1), 320–324. https://doi.org/10.1093/nar/gku316

Roch, F. F., Hinterkörner, G., Menke, J., Tang, G. Q., Cusack, S., Butzendobler, B., Buschmann, H., Datta, K., & Wolkerstorfer, A. (2015). An RNA Hybridization Assay for Screening Influenza A Virus Polymerase Inhibitors Using the Entire Ribonucleoprotein Complex. *Assay and Drug Development Technologies*, *13*(8), 488–506. https://doi.org/10.1089/adt.2015.668

Rust, M. J., Lakadamyali, M., Zhang, F., & Zhuang, X. (2004). Assembly of endocytic machinery around

individual influenza viruses during viral entry. *Nature Structural and Molecular Biology*, *11*(6), 567–573. https://doi.org/10.1038/nsmb769
Sakaguchi, A., Hirayama, E., Hiraki, A., Ishida, Y. I., & Kim, J. (2003). Nuclear export of influenza viral ribonucleoprotein is temperature-dependently inhibited by dissociation of viral matrix protein. *Virology*, *306*(2), 244–253. https://doi.org/10.1016/S0042-6822(02)00013-2
Salk, J. E., Pearson, H. E., Brown, P. N., & Francis, T. (1944). Protective Effect of Vaccination Against Induced Influenza B. *Experimental Biology and Medicine*, *55*(2), 106–107. https://doi.org/10.3181/00379727-55-14478P
Sangawa, H., Komeno, T., Nishikawa, H., Yoshida, A., Takahashi, K., Nomura, N., & Furuta, Y. (2013). Mechanism of Action of T-705 Ribosyl Triphosphate against Influenza Virus RNA Polymerase. *Antimicrobial Agents and Chemotherapy*, *57*(11), 5202–5208. https://doi.org/10.1128/AAC.00649-13
Sano, K., Ainai, A., Suzuki, T., & Hasegawa, H. (2017). The road to a more effective influenza vaccine: Up to date studies and future prospects. *Vaccine*, *35*(40), 5388–5395. https://doi.org/10.1016/j.vaccine.2017.08.034
Satterly, N., Tsai, P. L., Van Deursen, J., Nussenzveig, D. R., Wang, Y., Faria, P. A., Levay, A., Levy, D. E., & Fontoura, B. M. A. (2007). Influenza virus targets the mRNA export machinery and the nuclear pore complex. *Proceedings of the National Academy of Sciences of the United States of America*, *104*(6), 1853–1858. https://doi.org/10.1073/pnas.0610977104
Schrödinger, LLC. (2015). *The {PyMOL} Molecular Graphics System, Version~1.8*.
Serna Martin, I., Hengrung, N., Renner, M., Sharps, J., Martínez-Alonso, M., Masiulis, S., Grimes, J. M., & Fodor, E. (2018). A Mechanism for the Activation of the Influenza Virus Transcriptase. *Molecular Cell*, *70*(6), 1101-1110.e4. https://doi.org/10.1016/j.molcel.2018.05.011
Shi, L., Summers, D. F., Peng, Q., & Galarza, J. M. (1995). Influenza A Virus RNA Polymerase Subunit PB2 Is the Endonuclease Which Cleaves Host Cell mRNA and Functions Only as the Trimeric Enzyme. *Virology*, *208*(1), 38–47. https://doi.org/10.1006/viro.1995.1127
Shimizu, T., Takizawa, N., Watanabe, K., Nagata, K., & Kobayashi, N. (2011). Crucial role of the influenza virus NS2 (NEP) C-terminal domain in M1 binding and nuclear export of vRNP. *FEBS Letters*, *585*(1), 41–46. https://doi.org/10.1016/j.febslet.2010.11.017
Shiraki, K., & Daikoku, T. (2020). Favipiravir, an anti-influenza drug against life-threatening RNA virus infections. *Pharmacology & Therapeutics*, *209*, 107512. https://doi.org/10.1016/j.pharmthera.2020.107512
Sievers, F., Wilm, A., Dineen, D., Gibson, T. J., Karplus, K., Li, W., Lopez, R., McWilliam, H., Remmert, M., Söding, J., Thompson, J. D., & Higgins, D. G. (2011). Fast, scalable generation of high-quality protein multiple sequence alignments using Clustal Omega. *Molecular Systems Biology*, *7*(539). https://doi.org/10.1038/msb.2011.75
Smith, W., Andrewes, C. H., & Laidlaw, P. P. (1933). A Virus Obtained from Influenza Patients. *The Lancet*, *222*(5732), 66–68.
Song, M.-S., Kumar, G., Shadrick, W. R., Zhou, W., Jeevan, T., Li, Z., Slavish, P. J., Fabrizio, T. P., Yoon, S.-W., Webb, T. R., Webby, R. J., & White, S. W. (2016). Identification and characterization of influenza variants resistant to a viral endonuclease inhibitor. *Proceedings of the National Academy of Sciences*, *113*(13), 3669–3674. https://doi.org/10.1073/pnas.1519772113
Stevaert, A., Dallocchio, R., Dessì, A., Pala, N., Rogolino, D., Sechi, M., & Naesens, L. (2013). Mutational Analysis of the Binding Pockets of the Diketo Acid Inhibitor L-742,001 in the Influenza Virus PA Endonuclease. *Journal of Virology*, *87*(19), 10524–10538. https://doi.org/10.1128/jvi.00832-13
Stevaert, A., & Naesens, L. (2016). The Influenza Virus Polymerase Complex: An Update on Its Structure, Functions, and Significance for Antiviral Drug Design. *Medicinal Research Reviews*, *36*(6), 1127–1173. https://doi.org/10.1002/med.21401
Stewart, M. (2007). Molecular mechanism of the nuclear protein import cycle. *Nature Reviews Molecular Cell Biology*, *8*(3), 195–208. https://doi.org/10.1038/nrm2114
Stieneke-Grober, A., Vey, M., Angliker, H., Shaw, E., Thomas, G., Roberts, C., Klenk, H. D., & Garten, W. (1992). Influenza virus hemagglutinin with multibasic cleavage site is activated by furin, a subtilisin-like endoprotease. *EMBO Journal*, *11*(7), 2407–2414. https://doi.org/10.1002/j.1460-2075.1992.tb05305.x
Stouffer, A. L., Acharya, R., Salom, D., Levine, A. S., Di Costanzo, L., Soto, C. S., Tereshko, V., Nanda, V., Stayrook, S., & DeGrado, W. F. (2008). Structural basis for the function and inhibition of an influenza virus proton channel. *Nature*, *451*(7178), 596–599. https://doi.org/10.1038/nature06528
Sugiura, A., Ueda, M., & Enomoto, C. (1969). The effect of actinomycin D on the synthesis of influenza virus-specific RNA. *Archiv Für Die Gesamte Virusforschung*, *26*(1–2), 105–117. https://doi.org/10.1007/BF01241180
Takahashi, K., Furuta, Y., Fukuda, Y., Kuno, M., Kamiyama, T., Kozaki, K., Nomura, N., Egawa, H., Minami, S., & Shiraki, K. (2003). In vitro and in vivo activities of T-705 and oseltamivir against influenza virus. *Antiviral Chemistry and Chemotherapy*, *14*(5), 235–241. https://doi.org/10.1177/095632020301400502

Takashita, E., Ejima, M., Ogawa, R., Fujisaki, S., Neumann, G., Furuta, Y., Kawaoka, Y., Tashiro, M., & Odagiri, T. (2016). Antiviral susceptibility of influenza viruses isolated from patients pre- and post-administration of favipiravir. *Antiviral Research*, *132*, 170–177. https://doi.org/10.1016/j.antiviral.2016.06.007

Tanaka, T., Kamiyama, T., Daikoku, T., Takahashi, K., Nomura, N., Kurokawa, M., & Shiraki, K. (2017). T-705 (Favipiravir) suppresses tumor necrosis factor α production in response to influenza virus infection: A beneficial feature of T-705 as an anti-influenza drug. *Acta Virologica*, *61*(1), 48–55. https://doi.org/10.4149/av_2017_01_48

Tarendeau, F., Boudet, J., Guilligay, D., Mas, P. J., Bougault, C. M., Boulo, S., Baudin, F., Ruigrok, R. W. H., Daigle, N., Ellenberg, J., Cusack, S., Simorre, J.-P., & Hart, D. J. (2007). Structure and nuclear import function of the C-terminal domain of influenza virus polymerase PB2 subunit. *Nature Structural & Molecular Biology*, *14*(3), 229–233. https://doi.org/10.1038/nsmb1212

Taubenberger, J. K., Reid, A. H., Lourens, R. M., Wang, R., Jin, G., & Fanning, T. G. (2005). Characterization of the 1918 influenza virus polymerase genes. *Nature*, *437*(7060), 889–893. https://doi.org/10.1038/nature04230

te Velthuis, A. J. W., Grimes, J. M., & Fodor, E. (2021). Structural insights into RNA polymerases of negative-sense RNA viruses. *Nature Reviews Microbiology*, *19*(5), 303–318. https://doi.org/10.1038/s41579-020-00501-8

Te Velthuis, A. J. W., Robb, N. C., Kapanidis, A. N., & Fodor, E. (2016). The role of the priming loop in influenza A virus RNA synthesis. *Nature Microbiology*, *1*(5). https://doi.org/10.1038/nmicrobiol.2016.29

Thierry, E., Guilligay, D., Kosinski, J., Bock, T., Gaudon, S., Round, A., Pflug, A., Hengrung, N., El Omari, K., Baudin, F., Hart, D. J., Beck, M., & Cusack, S. (2016). Influenza Polymerase Can Adopt an Alternative Configuration Involving a Radical Repacking of PB2 Domains. *Molecular Cell*, *61*(1), 125–137. https://doi.org/10.1016/j.molcel.2015.11.016

Thomaston, J. L., Polizzi, N. F., Konstantinidi, A., Wang, J., Kolocouris, A., & Degrado, W. F. (2018). Inhibitors of the M2 Proton Channel Engage and Disrupt Transmembrane Networks of Hydrogen-Bonded Waters. *Journal of the American Chemical Society*, *140*(45), 15219–15226. https://doi.org/10.1021/jacs.8b06741

Tomassini, J. E., Davies, M. E., Hastings, J. C., Lingham, R., Mojena, M., Raghoobar, S. L., Singh, S. B., Tkacz, J. S., & Goetz, M. A. (1996). A novel antiviral agent which inhibits the endonuclease of influenza viruses. *Antimicrobial Agents and Chemotherapy*, *40*(5), 1189–1193. https://doi.org/10.1128/AAC.40.5.1189

Trevejo, J. M., Asmal, M., Vingerhoets, J., Polo, R., Robertson, S., Jiang, Y., Kieffer, T. L., & Leopold, L. (2018). Pimodivir Treatment in Adult Volunteers Experimentally Inoculated with Live Influenza Virus: A Phase IIa, Randomized, Double-Blind, Placebo-Controlled Study. *Antiviral Therapy*, *23*(4), 335–344. https://doi.org/10.3851/IMP3212

Trifonov, V., Khiabanian, H., Greenbaum, B., & Rabadan, R. (2009). The origin of the recent swine influenza A(H1N1) virus infecting humans. *Eurosurveillance*, *14*(17), 19193. https://doi.org/10.2807/ese.14.17.19193-en

Trist, I. M. L., Nannetti, G., Tintori, C., Fallacara, A. L., Deodato, D., Mercorelli, B., Palù, G., Wijtmans, M., Gospodova, T., Edink, E., Verheij, M., De Esch, I., Viteva, L., Loregian, A., & Botta, M. (2016). 4,6-Diphenylpyridines as Promising Novel Anti-Influenza Agents Targeting the PA-PB1 Protein-Protein Interaction: Structure-Activity Relationships Exploration with the Aid of Molecular Modeling. *Journal of Medicinal Chemistry*, *59*(6), 2688–2703. https://doi.org/10.1021/acs.jmedchem.5b01935

Turrell, L., Lyall, J. W., Tiley, L. S., Fodor, E., & Vreede, F. T. (2013). The role and assembly mechanism of nucleoprotein in influenza A virus ribonucleoprotein complexes. *Nature Communications*, *4*, 1–11. https://doi.org/10.1038/ncomms2589

Uyeki, T. M., Bernstein, H. H., Bradley, J. S., Englund, J. A., File, T. M., Fry, A. M., Gravenstein, S., Hayden, F. G., Harper, S. A., Hirshon, J. M., Ison, M. G., Johnston, B. L., Knight, S. L., McGeer, A., Riley, L. E., Wolfe, C. R., Alexander, P. E., & Pavia, A. T. (2019). Clinical Practice Guidelines by the Infectious Diseases Society of America: 2018 Update on Diagnosis, Treatment, Chemoprophylaxis, and Institutional Outbreak Management of Seasonal Influenzaa. *Clinical Infectious Diseases*, *68*(6), 895–902. https://doi.org/10.1093/cid/ciy874

Valleron, A.-J., Cori, A., Valtat, S., Meurisse, S., Carrat, F., & Boëlle, P.-Y. (2010). Transmissibility and geographic spread of the 1889 influenza pandemic. *Proceedings of the National Academy of Sciences*, *107*(19), 8778–8781. https://doi.org/10.1073/pnas.1000886107

Varghese, J. N., & Colman, P. M. (1991). Three-dimensional structure of the neuraminidase of influenza virus A/Tokyo/3/67 at 2·2 Å resolution. *Journal of Molecular Biology*, *221*(2), 473–486. https://doi.org/10.1016/0022-2836(91)80068-6

Varghese, Joseph N., McKimm-Breschkin, J. L., Caldwell, J. B., Kortt, A. A., & Colman, P. M. (1992). The structure of the complex between influenza virus neuraminidase and sialic acid, the viral receptor.

*Proteins: Structure, Function, and Bioinformatics*, *14*(3), 327–332. https://doi.org/10.1002/prot.340140302
Wandzik, J. M., Kouba, T., Karuppasamy, M., Pflug, A., Drncova, P., Provaznik, J., Azevedo, N., & Cusack, S. (2020). A Structure-Based Model for the Complete Transcription Cycle of Influenza Polymerase. *Cell*, *181*(4), 877-893.e21. https://doi.org/10.1016/j.cell.2020.03.061
Wang, C., Takeuchi, K., Pinto, L. H., & Lamb, R. A. (1993). Ion channel activity of influenza A virus M2 protein: characterization of the amantadine block. *Journal of Virology*, *67*(9), 5585–5594. https://doi.org/10.1128/JVI.67.9.5585-5594.1993
Watanabe, K., Ishikawa, T., Otaki, H., Mizuta, S., Hamada, T., Nakagaki, T., Ishibashi, D., Urata, S., Yasuda, J., Tanaka, Y., & Nishida, N. (2017). Structure-based drug discovery for combating influenza virus by targeting the PA-PB1 interaction. *Scientific Reports*, *7*(1), 1–12. https://doi.org/10.1038/s41598-017-10021-w
Webster, R. G., Laver, W. G., Air, G. M., & Schild, G. C. (1982). Molecular mechanisms of variation in influenza viruses. *Nature*, *296*(5853), 115–121. https://doi.org/10.1038/296115a0
Webster, Robert G., Wright, S. M., Castrucci, M. R., Bean, W. J., & Kawaoka, Y. (1993). Influenza – A Model of an Emerging Virus Disease. *Intervirology*, *35*(1–4), 16–25. https://doi.org/10.1159/000150292
Wilson, I. A., Skehel, J. J., & Wiley, D. C. (1981). Structure of the haemagglutinin membrane glycoprotein of influenza virus at 3 Å resolution. *Nature*, *289*(5796), 366–373. https://doi.org/10.1038/289366a0
Wise, H. M., Foeglein, A., Sun, J., Dalton, R. M., Patel, S., Howard, W., Anderson, E. C., Barclay, W. S., & Digard, P. (2009). A Complicated Message: Identification of a Novel PB1-Related Protein Translated from Influenza A Virus Segment 2 mRNA. *Journal of Virology*, *83*(16), 8021–8031. https://doi.org/10.1128/JVI.00826-09
World Health Organization. (2019). Global influenza strategy 2019-2030. In *World Health Organization*. https://www.cdc.gov/coronavirus/2019-ncov/hcp/guidance-postmortem-specimens.html%0Ahttps://apps.who.int/iris/bitstream/handle/10665/311184/9789241515320-eng.pdf?ua=1
Wunderlich, K., Juozapaitis, M., Ranadheera, C., Kessler, U., Martin, A., Eisel, J., Beutling, U., Frank, R., & Schwemmle, M. (2011). Identification of High-Affinity PB1-Derived Peptides with Enhanced Affinity to the PA Protein of Influenza A Virus Polymerase. *Antimicrobial Agents and Chemotherapy*, *55*(2), 696–702. https://doi.org/10.1128/AAC.01419-10
Wunderlich, K., Mayer, D., Ranadheera, C., Holler, A.-S., Mänz, B., Martin, A., Chase, G., Tegge, W., Frank, R., Kessler, U., & Schwemmle, M. (2009). Identification of a PA-Binding Peptide with Inhibitory Activity against Influenza A and B Virus Replication. *PLoS ONE*, *4*(10), e7517. https://doi.org/10.1371/journal.pone.0007517
Xiao, S., Klein, M. L., LeBard, D. N., Levine, B. G., Liang, H., MacDermaid, C. M., & Alfonso-Prieto, M. (2014). Magnesium-Dependent RNA Binding to the PA Endonuclease Domain of the Avian Influenza Polymerase. *The Journal of Physical Chemistry B*, *118*(4), 873–889. https://doi.org/10.1021/jp408383g
Ye, Z. P., Pal, R., Fox, J. W., & Wagner, R. R. (1987). Functional and antigenic domains of the matrix (M1) protein of influenza A virus. *Journal of Virology*, *61*(2), 239–246. https://doi.org/10.1128/jvi.61.2.239-246.1987
Yuan, P., Bartlam, M., Lou, Z., Chen, S., Zhou, J., He, X., Lv, Z., Ge, R., Li, X., Deng, T., Fodor, E., Rao, Z., & Liu, Y. (2009). Crystal structure of an avian influenza polymerase PAN reveals an endonuclease active site. *Nature*, *458*(7240), 909–913. https://doi.org/10.1038/nature07720
Yuan, S., Chu, H., Singh, K., Zhao, H., Zhang, K., Kao, R. Y. T., Chow, B. K. C., Zhou, J., & Zheng, B. J. (2016). A novel small-molecule inhibitor of influenza A virus acts by suppressing PA endonuclease activity of the viral polymerase. *Scientific Reports*, *6*(March), 1–12. https://doi.org/10.1038/srep22880
Yuan, S., Chu, H., Ye, J., Singh, K., Ye, Z., Zhao, H., Kao, R. Y. T., Chow, B. K. C., Zhou, J., & Zheng, B. J. (2017). Identification of a novel small-molecule compound targeting the influenza A virus polymerase PB1-PB2 interface. *Antiviral Research*, *137*, 58–66. https://doi.org/10.1016/j.antiviral.2016.11.005
Zhang, J., Hu, Y., Foley, C., Wang, Y., Musharrafieh, R., Xu, S., Zhang, Y., Ma, C., Hulme, C., & Wang, J. (2018). Exploring Ugi-Azide Four-Component Reaction Products for Broad-Spectrum Influenza Antivirals with a High Genetic Barrier to Drug Resistance. *Scientific Reports*, *8*(1), 1–14. https://doi.org/10.1038/s41598-018-22875-9
Zhang, J., Hu, Y., Wu, N., & Wang, J. (2020). Discovery of Influenza Polymerase PA-PB1 Interaction Inhibitors Using an in Vitro Split-Luciferase Complementation-Based Assay. *ACS Chemical Biology*, *15*(1), 74–82. https://doi.org/10.1021/acschembio.9b00552
Zhang, K., Xie, Y., Muñoz-Moreno, R., Wang, J., Zhang, L., Esparza, M., García-Sastre, A., Fontoura, B. M. A., & Ren, Y. (2019). Structural basis for influenza virus NS1 protein block of mRNA nuclear export. *Nature Microbiology*, *4*(10), 1671–1679. https://doi.org/10.1038/s41564-019-0482-x
Zhao, C., Lou, Z., Guo, Y., Ma, M., Chen, Y., Liang, S., Zhang, L., Chen, S., Li, X., Liu, Y., Bartlam, M., &

Rao, Z. (2009). Nucleoside Monophosphate Complex Structures of the Endonuclease Domain from the Influenza Virus Polymerase PA Subunit Reveal the Substrate Binding Site inside the Catalytic Center. *Journal of Virology*, *83*(18), 9024–9030. https://doi.org/10.1128/JVI.00911-09

Zhirnov, O. P., & Klenk, H. D. (1997). Histones as a target for influenza virus matrix protein M1. *Virology*, *235*(2), 302–310. https://doi.org/10.1006/viro.1997.8700

Zhu, W., Zhu, Y., Qin, K., Yu, Z., Gao, R., Yu, H., Zhou, J., & Shu, Y. (2012). Mutations in polymerase genes enhanced the virulence of 2009 pandemic H1N1 influenza virus in mice. *PLoS ONE*, *7*(3). https://doi.org/10.1371/journal.pone.0033383

## 8. SUPPLEMENTARY MATERIAL

**S1. Sequence alignments of the RdRp of various influenza viruses**

The four influenza types (A – D) were selected for the sequence alignments: pandemic influenza A virus (A/California/07/2009 (H1N1)), pandemic influenza A virus (A/Brevig Mission/1/1918 (H1N1)), pandemic influenza A virus (A/Northern Territory/60/1968 (H3N2)), influenza A virus (A/bat/Guatemala/060/202(H17N10), influenza B virus (B/Panama/45/1990), influenza C virus (C/Johannesburh/1/1966), and influenza D virus (D/bovine/Mississippi/C00046N/2014). The influenza D virus lacks the PA subunit, instead it contains the complementary P3 subunit. Multiple sequence alignment was performed using the Clustal Omega (Goujon et al., 2010; Sievers et al., 2011) and visualised using ESPript, with the **4WSB** (Reich et al., 2014) and **7NHX** (Keown et al., 2022) as a secondary structure models (Robert & Gouet, 2014).

### 8.1. PA SUBUNITs alignment

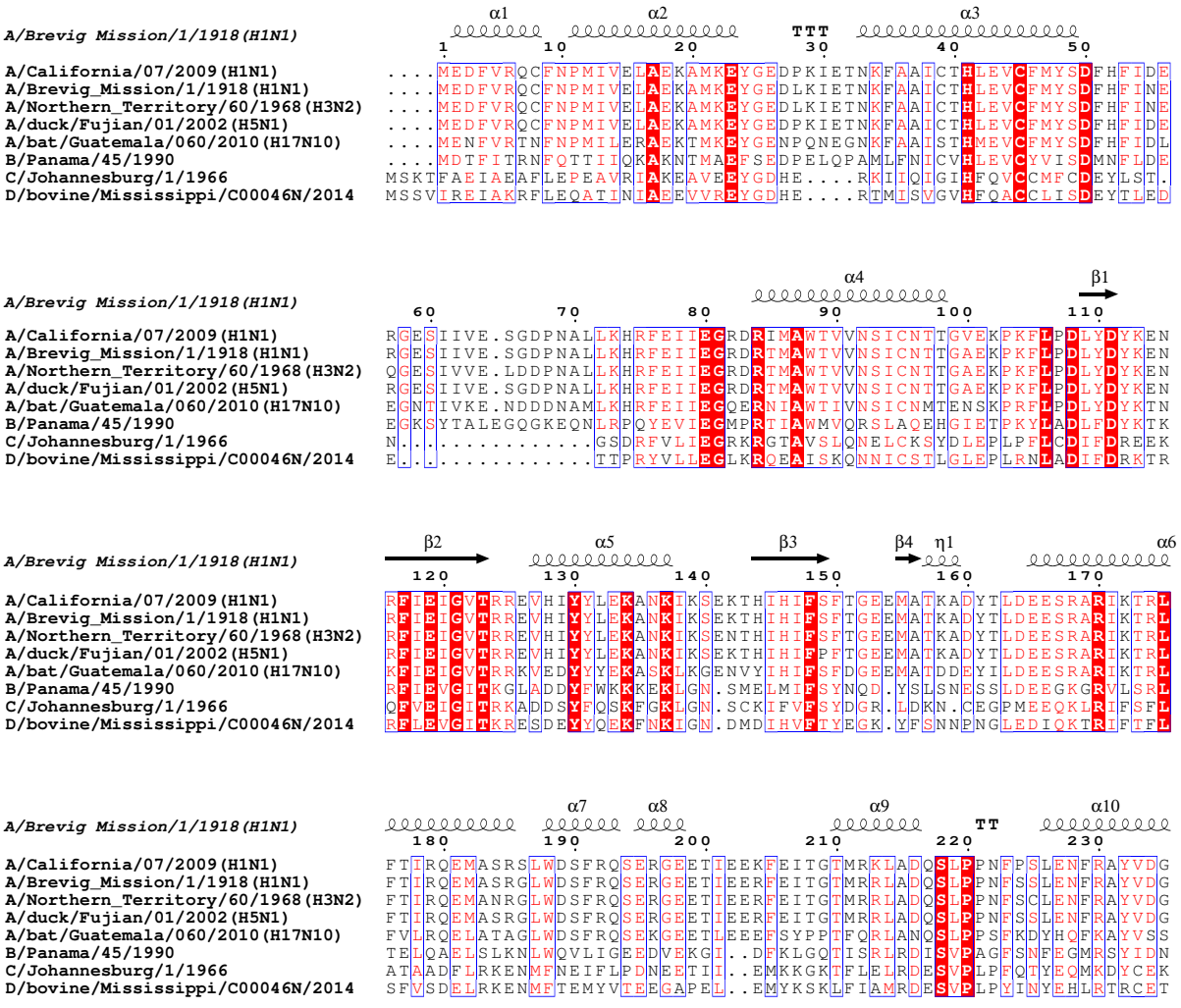

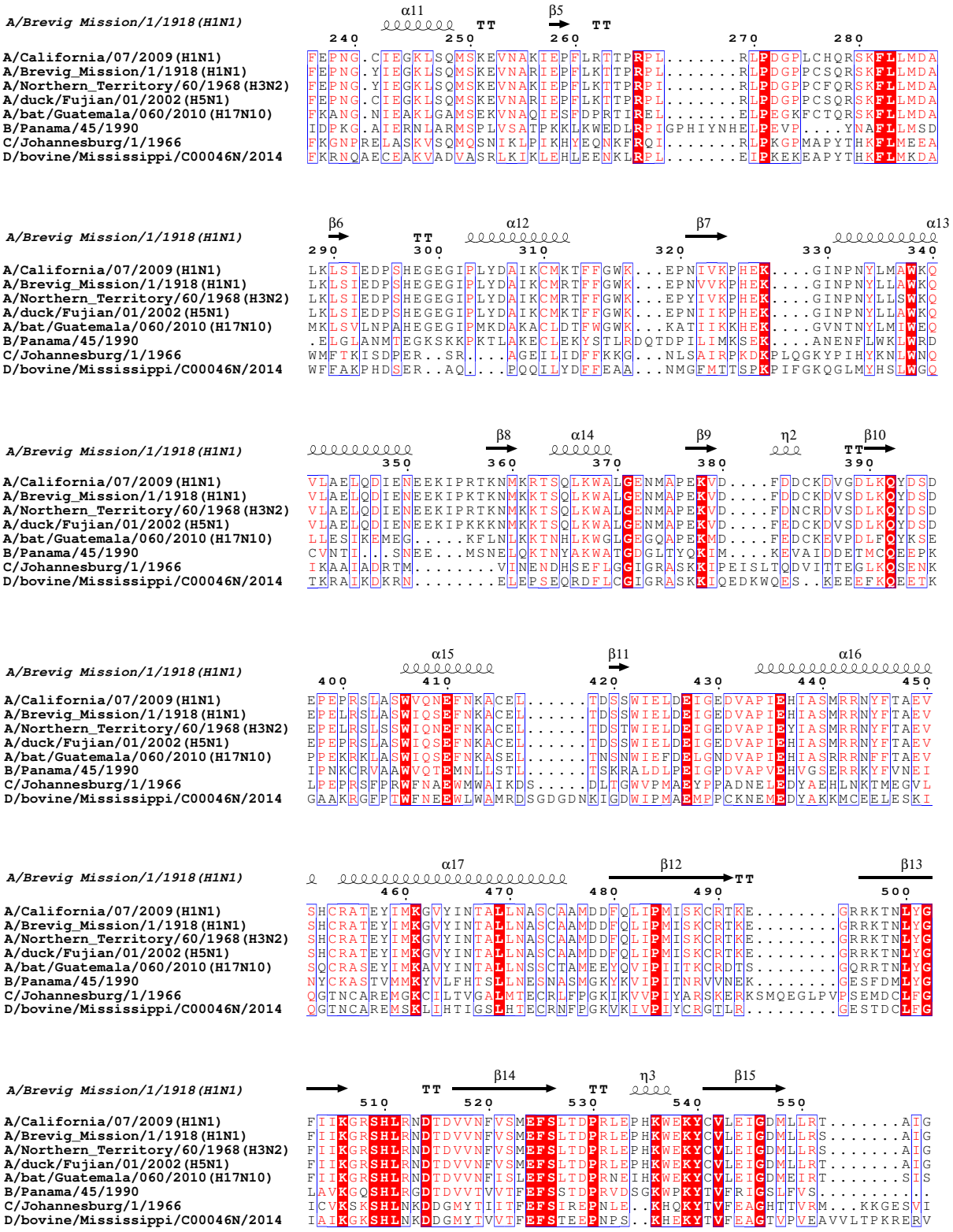
A/Brevig Mission/1/1918(H1N1)
A/California/07/2009(H1N1)
A/Brevig_Mission/1/1918(H1N1)
A/Northern_Territory/60/1968(H3N2)
A/duck/Fujian/01/2002(H5N1)
A/bat/Guatemala/060/2010(H17N10)
B/Panama/45/1990
C/Johannesburg/1/1966
D/bovine/Mississippi/C00046N/2014

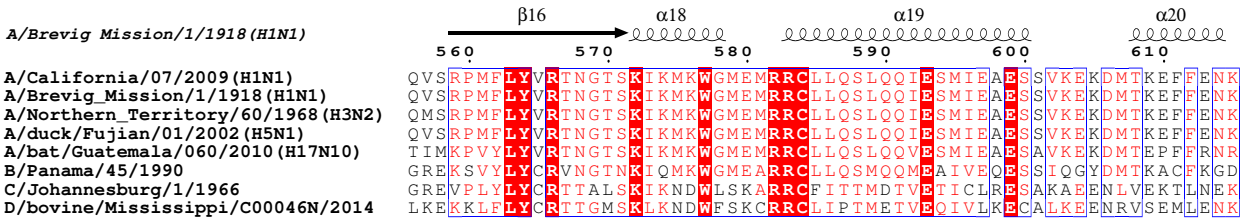


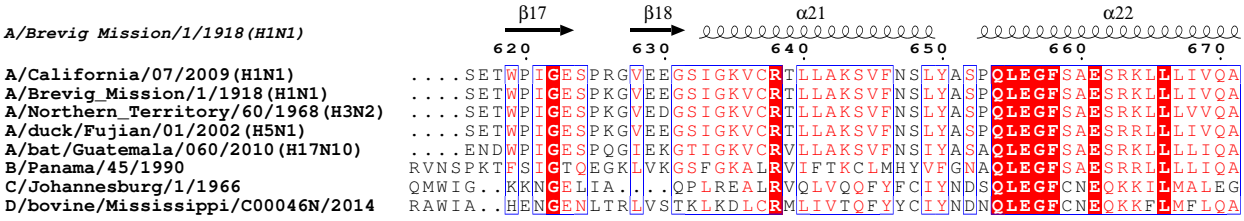


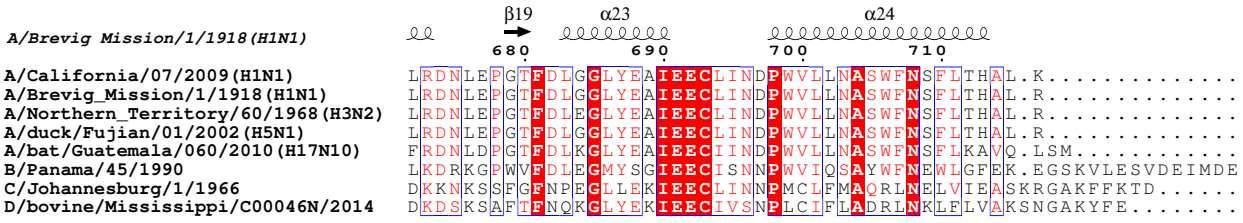


## 8.2. PB1 SUBUNITs alignment

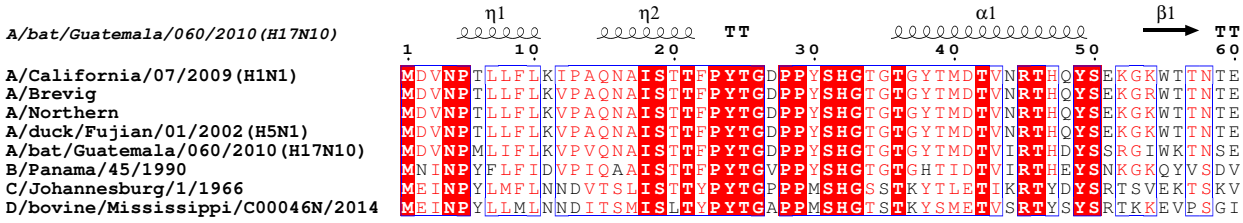


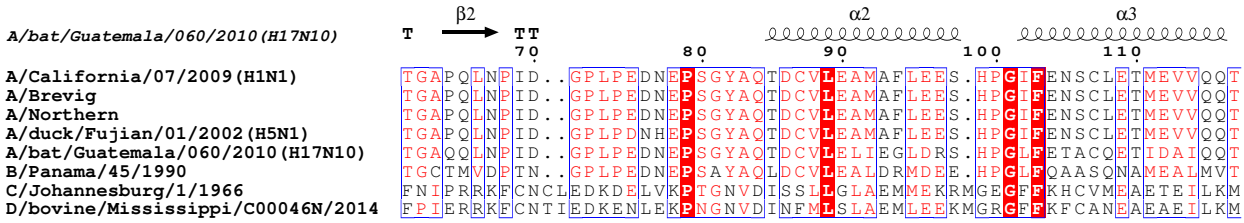

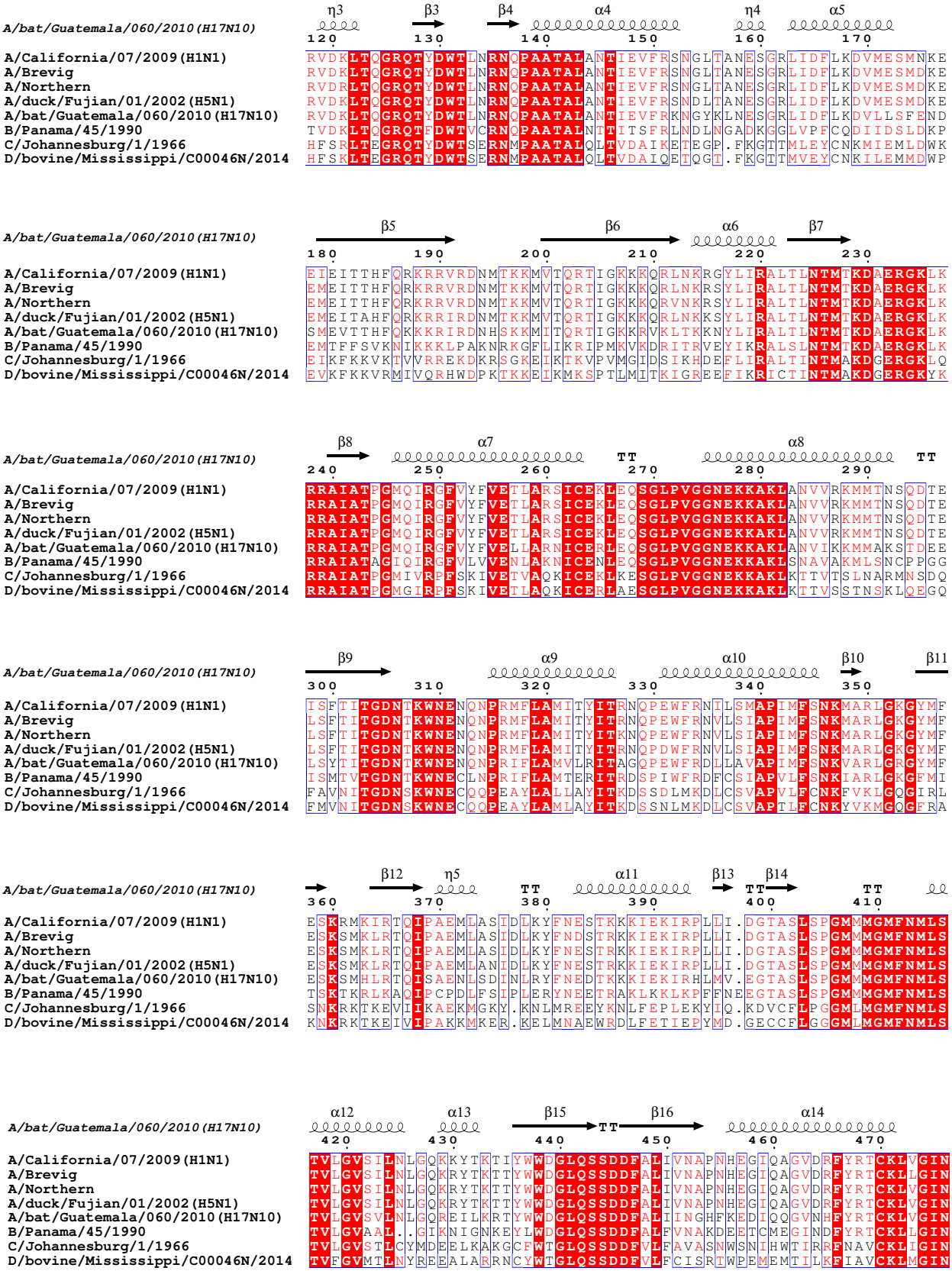
A/bat/Guatemala/060/2010(H17N10)
A/California/07/2009(H1N1)
A/Brevig
A/Northern
A/duck/Fujian/01/2002(H5N1)
A/bat/Guatemala/060/2010(H17N10)
B/Panama/45/1990
C/Johannesburg/1/1966
D/bovine/Mississippi/C00046N/2014

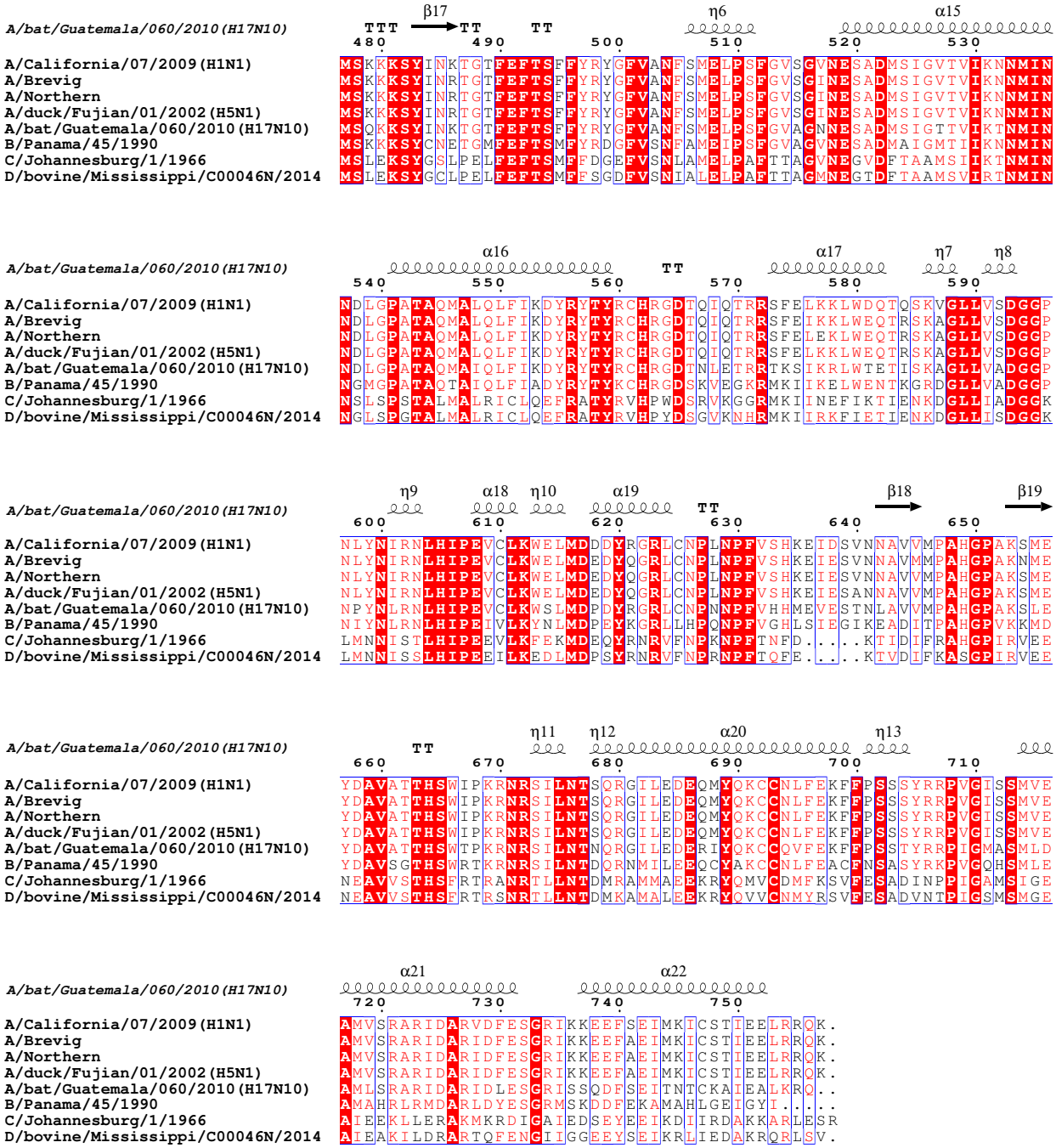
A/bat/Guatemala/060/2010(H17N10)
A/California/07/2009(H1N1)
A/Brevig
A/Northern
A/duck/Fujian/01/2002(H5N1)
A/bat/Guatemala/060/2010(H17N10)
B/Panama/45/1990
C/Johannesburg/1/1966
D/bovine/Mississippi/C00046N/2014

## 8.3. PB2 SUBUNITs alignment

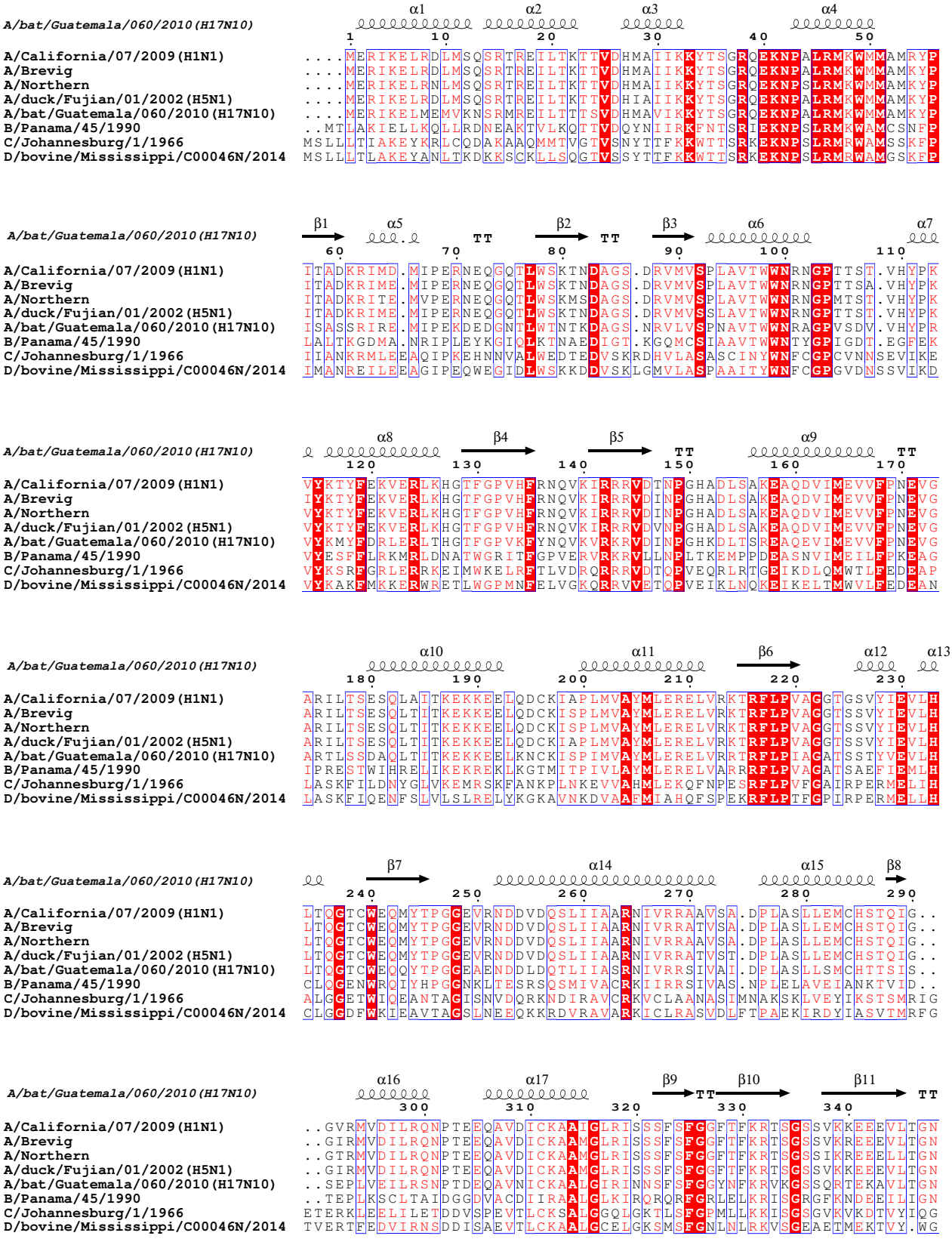

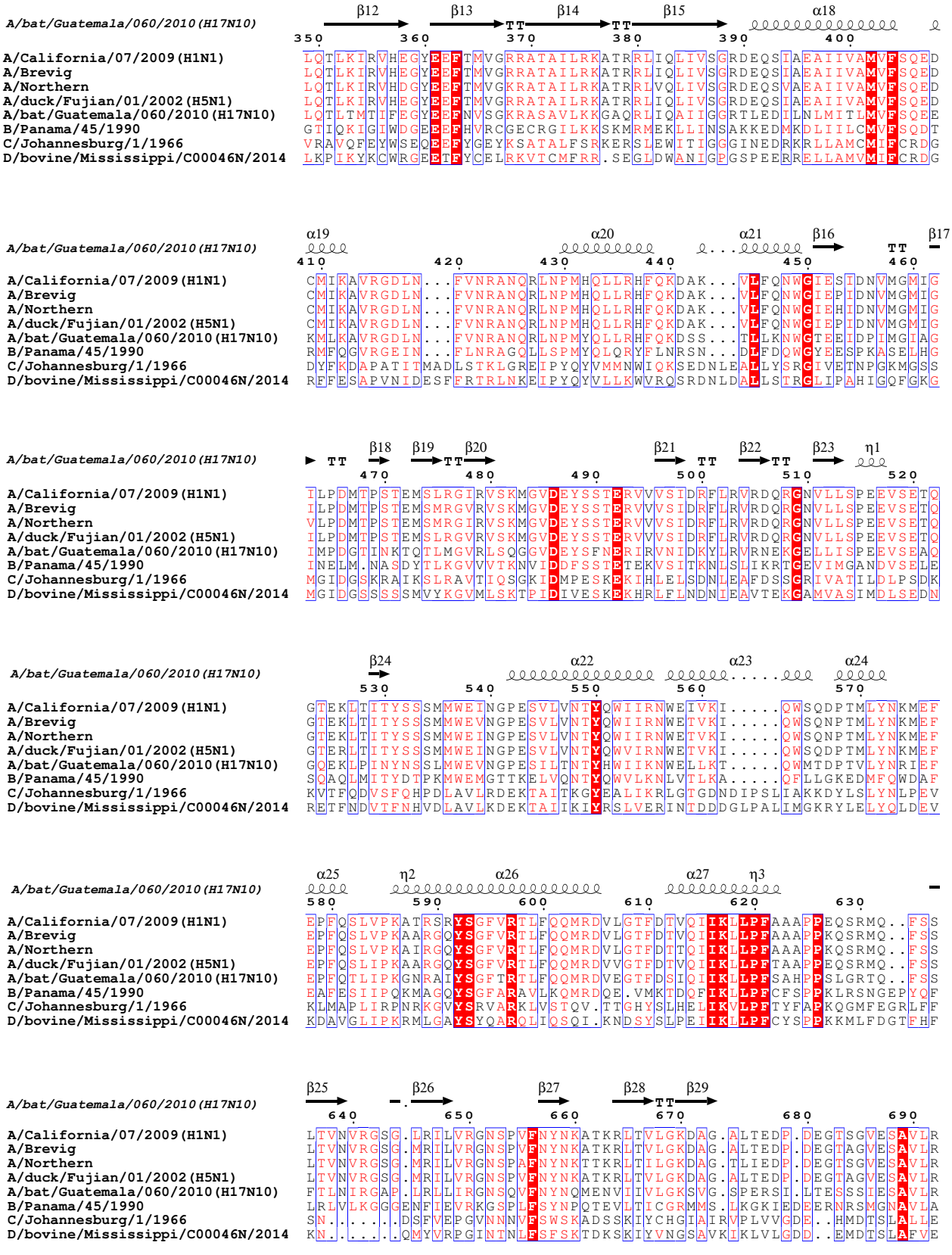
A/bat/Guatemala/060/2010(H17N10)
A/California/07/2009(H1N1)
A/Brevig
A/Northern
A/duck/Fujian/01/2002(H5N1)
A/bat/Guatemala/060/2010(H17N10)
B/Panama/45/1990
C/Johannesburg/1/1966
D/bovine/Mississippi/C00046N/2014

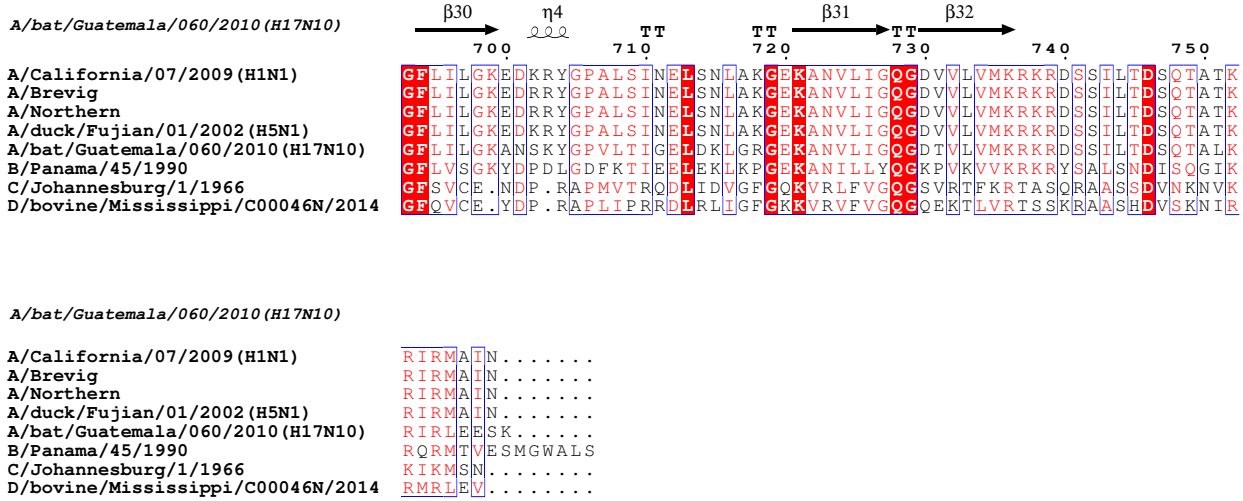
A/bat/Guatemala/060/2010(H17N10)
β30
η4
β31
β32
700
710
720
730
740
750
A/California/07/2009(H1N1)
A/Brevig
A/Northern
A/duck/Fujian/01/2002(H5N1)
A/bat/Guatemala/060/2010(H17N10)
B/Panama/45/1990
C/Johannesburg/1/1966
D/bovine/Mississippi/C00046N/2014


A/bat/Guatemala/060/2010(H17N10)
A/California/07/2009(H1N1)
A/Brevig
A/Northern
A/duck/Fujian/01/2002(H5N1)
A/bat/Guatemala/060/2010(H17N10)
B/Panama/45/1990
C/Johannesburg/1/1966
D/bovine/Mississippi/C00046N/2014